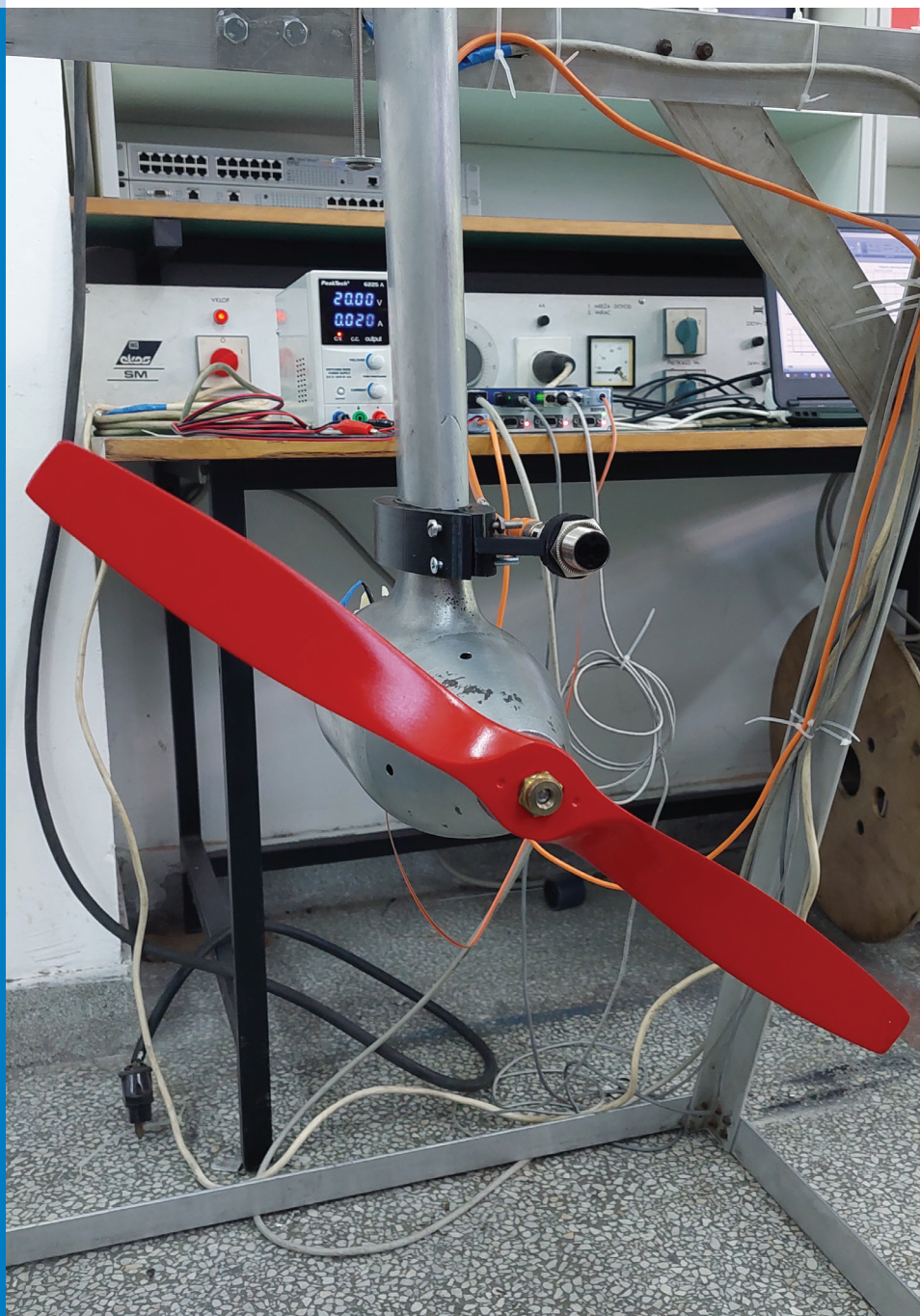




# Strojniški vestnik

## Journal of Mechanical Engineering



no. **5-6**

year **2023**

volume **69**

# Strojniški vestnik – Journal of Mechanical Engineering (SV-JME)

## Aim and Scope

The international journal publishes original and (mini)review articles covering the concepts of materials science, mechanics, kinematics, thermodynamics, energy and environment, mechatronics and robotics, fluid mechanics, tribology, cybernetics, industrial engineering and structural analysis.

The journal follows new trends and progress proven practice in the mechanical engineering and also in the closely related sciences as are electrical, civil and process engineering, medicine, microbiology, ecology, agriculture, transport systems, aviation, and others, thus creating a unique forum for interdisciplinary or multidisciplinary dialogue.

The international conferences selected papers are welcome for publishing as a special issue of SV-JME with invited co-editor(s).

## Editor in Chief

Vincenc Butala  
University of Ljubljana, Faculty of Mechanical Engineering, Slovenia

## Technical Editor

Pika Škraba  
University of Ljubljana, Faculty of Mechanical Engineering, Slovenia

## Founding Editor

Bojan Kraut  
University of Ljubljana, Faculty of Mechanical Engineering, Slovenia

## Editorial Office

University of Ljubljana, Faculty of Mechanical Engineering  
SV-JME, Aškerčeva 6, SI-1000 Ljubljana, Slovenia  
Phone: 386 (0)1 4771 137  
Fax: 386 (0)1 2518 567  
info@sv-jme.eu, <http://www.sv-jme.eu>

**Print:** Demat d.o.o., printed in 240 copies

## Founders and Publishers

University of Ljubljana, Faculty of Mechanical Engineering,  
Slovenia  
University of Maribor, Faculty of Mechanical Engineering,  
Slovenia  
Association of Mechanical Engineers of Slovenia  
Chamber of Commerce and Industry of Slovenia,  
Metal Processing Industry Association

## President of Publishing Council

Mihael Sekavčnik  
University of Ljubljana, Faculty of Mechanical Engineering, Slovenia

## Vice-President of Publishing Council

Bojan Dolšak  
University of Maribor, Faculty of Mechanical Engineering, Slovenia

## International Editorial Board

Kamil Arslan, Karabuk University, Turkey  
Hafiz Muhammad Ali, King Fahd U. of Petroleum & Minerals, Saudi Arabia  
Josep M. Bergada, Politechnical University of Catalonia, Spain  
Anton Bergant, Litostroj Power, Slovenia  
Miha Boltežar, University of Ljubljana, Slovenia  
Filippo Cianetti, University of Perugia, Italy  
Janez Diaci, University of Ljubljana, Slovenia  
Anselmo Eduardo Diniz, State University of Campinas, Brazil  
Igor Emri, University of Ljubljana, Slovenia  
Imre Felde, Obuda University, Faculty of Informatics, Hungary  
Imre Horvath, Delft University of Technology, The Netherlands  
Aleš Hribernik, University of Maribor, Slovenia  
Soichi Ibaraki, Kyoto University, Department of Micro Eng., Japan  
Julius Kaplunov, Brunel University, West London, UK  
Iyas Khader, Fraunhofer Institute for Mechanics of Materials, Germany  
Jernej Klemenc, University of Ljubljana, Slovenia  
Milan Kljajin, J.J. Strossmayer University of Osijek, Croatia  
Peter Krajnc, Chalmers University of Technology, Sweden  
Janez Kušar, University of Ljubljana, Slovenia  
Gorazd Lojen, University of Maribor, Slovenia  
Darko Lovrec, University of Maribor, Slovenia  
Thomas Lübben, University of Bremen, Germany  
George K. Nikas, KADMOS Engineering, UK  
Tomaž Pepelnjak, University of Ljubljana, Slovenia  
Vladimir Popović, University of Belgrade, Serbia  
Franci Pušavec, University of Ljubljana, Slovenia  
Mohammad Reza Safaei, Florida International University, USA  
Marco Sortino, University of Udine, Italy  
Branko Vasić, University of Belgrade, Serbia  
Arkady Voloshin, Lehigh University, Bethlehem, USA

## General information

Strojniški vestnik – Journal of Mechanical Engineering is published in 6 double issues per year.

Institutional prices include print & online access: institutional subscription price and foreign subscription €100,00 (the price of a single issue is €10,00); general public subscription and student subscription €50,00 (the price of a single issue is €5,00). Prices are exclusive of tax. Delivery is included in the price. The recipient is responsible for paying any import duties or taxes. Legal title passes to the customer on dispatch by our distributor. Single issues from current and recent volumes are available at the current single-issue price. To order the journal, please complete the form on our website. For submissions, subscriptions and all other information please visit: <http://www.sv-jme.eu>.

You can advertise on the inner and outer side of the back cover of the journal. The authors of the published papers are invited to send photos or pictures with short explanation for cover content.

We would like to thank the reviewers who have taken part in the peer-review process.



**Cover:**  
The use of low-powered aircraft as “expendable” material is the reality we live in, but ensuring the safety of their use is the primary goal of the authors who deal with this issue. A test bench for quantification of thrust, torque and vibration of a small unmanned aerial vehicles (UAV) vehicle propeller is presented. Obtained results realistically describe the complex behavior of propellers in operation.

*Image Courtesy:*  
The Authors,  
University of Belgrade,  
Faculty of Mechanical Engineering,  
Belgrade, Serbia

ISSN 0039-2480, ISSN 2536-2948 (online)

© 2023 with Authors.

SV-JME is indexed / abstracted in: SCI-Expanded, Compendex, Inspec, ProQuest-CSA, SCOPUS, TEMA. The list of the remaining bases, in which SV-JME is indexed, is available on the website.

The journal is subsidized by Slovenian Research Agency.

Strojniški vestnik - Journal of Mechanical Engineering is available on <https://www.sv-jme.eu>.

# Contents

**Strojniški vestnik - Journal of Mechanical Engineering**  
**volume 69, (2023), number 5-6**  
**Ljubljana, May-June 2023**  
**ISSN 0039-2480**

**Published every two months**

## Papers

Goran Vorotović, Jela Burazer, Aleksandar Bengin, Časlav Mitrović, Miloš Januzović, Nebojša Petrović, Đorđe Novković: A Case Study of a Methodological Approach to the Verification of UAV Propeller Performance	199
Ali Celik, Bayram Sahin, Eyüphan Manay, Abit Balin: A Study Using the Hybrid Fuzzy AHP&TOPSIS Method in the Conversion of a LEED-Certified Education Building into a Nearly Zero-Energy Building in a Cold Climate	208
Ava A.K. Mohammed, Gailan Ismail Hassan, Younis Khalid Khdir: The Dynamic Behaviour of Symmetrical Laminated Nano-composite Containing Equal Numbers of Glass and Carbon Fibre Layers	224
Linlin Li, Sanmin Wang: Experimental Study and Numerical Analysis on Windage Power Loss Characteristics of Aviation Spiral Bevel Gear with Oil Injection Lubrication	235
Sumit Kumar, Pardeep Gupta: Prioritizing the Key Actors of an Organization for Business Excellence Using the Efficient Interpretive Ranking Process	248
Teng Wang, Youfu Tang, Tao Wang, Na Lei: An Improved MSCNN and GRU Model for Rolling Bearing Fault Diagnosis	261
Haiter Lenin Allasi, Vettivel SingaravelChidambaranathan, Mary Vasanthi Soosaimariyan: Wear Behaviour of a Cu-Ni-Sn Hybrid Composite Reinforced with B <sub>4</sub> C prepared by Powder Metallurgy Technique	275
Igor Grabec, Nikolaj Sok: Diffusion Equation Generalized for Modeling of Chladni Patterns	284





# A Case Study of a Methodological Approach to the Verification of UAV Propeller Performance

Goran Vorotović\* – Jela Burazer – Aleksandar Bengin – Časlav Mitrović –  
Miloš Januzović – Nebojša Petrović – Đorđe Novković

University of Belgrade, Faculty of Mechanical Engineering, Serbia

*Understanding the behaviour of propeller-driven aircraft has been the primary goal of aviation since the brothers Orville and Wilbur Wright. Traction characteristics, which have over time become dominant in the field of aviation in addition to thrust, both examined and analysed, nevertheless represent a sort of oxymoron in modern aviation. In this sense, the authors of the paper present the possibilities of static performance characteristics and vibrations of aircraft propellers through the analysis of low-powered aircraft. The use of low-powered aircraft as “expendable” material is the reality we live in, but ensuring the safety of their use is the primary goal of the researchers who deal with this issue. Accordingly, the authors of this paper present indications of the methodology of testing the blades of low-power aircraft in the atmosphere with an observation that the same indications can be used with aircraft of higher power, as well as with the aircraft on celestial bodies that have not been tested or available. A test bench for the quantification of thrust force, torque, and vibration of small unmanned aerial vehicles’ (UAV) vehicle propellers is presented. The obtained results realistically describe the complex behaviour of propellers in operation.*

**Keywords:** propeller, traction-dynamic characteristics, oscillations, acquisition, dynamics

## Highlights

- A test bench for testing the propellers of low-power UAV vehicles was designed.
- A complete methodology for testing low-power UAV propellers using simple measuring techniques was developed.
- The acquired experimental data realistically describe the complex behaviour of propellers in operation.

## 0 INTRODUCTION

Small unmanned aerial vehicles (UAV) propeller design should reflect the optimal choice of aerodynamics, structural analysis, dynamic analysis, material selection, production technology, cost and dynamic traction characteristics. The aerodynamic design of the propeller is based on the choice of airfoil, chord, and pitch-angle radial distributions.

Particular attention is paid to the reliability, the noise level, the aesthetic appearance of the blade, the functional dependence of traction forces, the torques, the number of revolutions and the power of the power unit for all test conditions. One of the important requirements when designing a propeller is the maximum reliability of the structure in all modes of exploitation. Such optimization requires the inclusion of all parameters through aerodynamic and structural modelling and the adoption of all major components of the system that include the use of propellers.

An error that would appear in the production of the propeller would have the effect of endangering the safety and reliability of the operation of the unmanned aerial vehicle due to an increase in stress and deformations, a loss of traction force, and even breakage of the propeller. Less extreme consequences include reduced efficiency and performance of

the drone, shortened service life, and increased maintenance costs.

There are several theories that can be used for the determination of the aerodynamic characteristics of small UAVs: blade element theory (BET) [1] and [2], vortex methods [3] and computational fluid dynamics (CFD) [4] to [7]. Each of them has some disadvantages. Specifically, the BET and vortex methods have low or medium accuracy on the near-flow solution. Additionally, maximum values of lift and viscous drag coefficients cannot be calculated [8] and [9]. These values are important parameters for UAV design, flight control and performance studies. CFD is gaining popularity in the development of modern UAVs [10]. The numerical verification of UAV propeller performance using computational fluid dynamics (CFD), although of high accuracy, is dependent on the selected turbulence model and the selected mesh and is computationally expensive. Furthermore, numerical models require experimental validation. Experimental verification of UAV propeller performance can be done using wind tunnels [11] and dynamic testing, including model analysis and structural testing [12]. In addition to laboratory testing, verification of UAV propeller performance can be done using flight testing and data analysis [13].

Because unmanned aerial vehicles are currently viewed as devices for “one-time” use only, the

\*Corr. Author's Address: University of Belgrade, Faculty of Mechanical Engineering, Kraljice Marije 16, 11120 Belgrade 35, Serbia, gvorotovic@mas.bg.ac.rs

testing of the components of such aircraft, including propellers, has been relegated to the background to the detriment of the safety of air traffic and elements on the ground. As propellers are the only propulsion source for UAVs, any problem that would appear on the propeller would affect the UAV as a whole [14]. In this context, safety is set as a primary task; accordingly, an increasing number of manufacturers and institutions dealing with this issue have decided to build test benches for testing the static performance characteristics and vibrations of propellers of small unmanned aircraft. Some of these results are presented in [15] and [16].

The subject of this paper is the presentation of a methodology for low-power UAV propeller testing, taking into account their dynamic traction characteristics. More precisely, the research aims to determine the value of thrust force and vibration level, as well as the functional dependence of forces, revolutions per minute  $RPM$  [ $\text{min}^{-1}$ ], power, and torque by applying simple measuring techniques.

## 1 TEST BENCH DESCRIPTION

The test bench for testing the static performance characteristics and vibrations of small UAV propellers is made of aluminium construction (Fig. 1) that can safely test propellers with a diameter of up to 550 mm. The supporting construction of the test bench in question is made of aluminium L profiles with dimensions of  $30 \text{ mm} \times 50 \text{ mm} \times 5 \text{ mm}$ . Preliminary calculations of the structure's static and dynamic load-bearing capacities have shown satisfactory results that are in accordance with positive engineering practice related to statics and dynamics as a whole, with a degree of safety of 1.6.

The power group consists of one 250 W alternating current motor (2), controlled by a precise alternating current regulator (8) in the range from 0 V to 300 V. The regulator is a torus type and ensures a continuous change of the operating voltage. The motor is installed in an aerodynamic formwork made of aluminium, which is placed on an aerodynamic

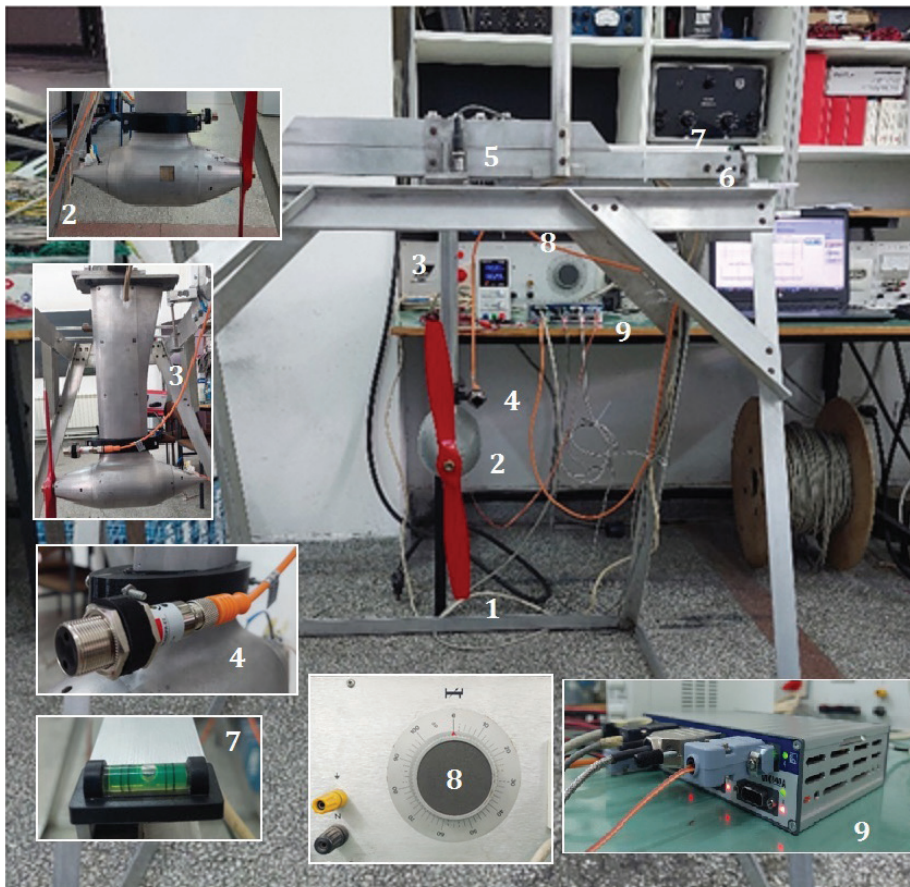


**Fig. 1.** Experimental rig: 1 propeller, 2 motor, 3 pylon, 4 optical encoder, 5 and 6 accelerometers, 7 scale, 8 alternating current regulator, and 9 central acquisition unit

support, a pylon (3). For fine adjustment of the zero-balance position of the propeller, a precision scale (7) is used, which is an integral part of the test bench.

The propeller is placed on the test bench by means of a conical holder on the drive shaft, which is secured with a self-locking nut. It is important to note that any propeller imbalance will be detected by the vibration detection system that is an integral part of the test bench and will be described later.



Fig. 2. Load cell for thrust force measurement

The HBM QuantumX MX-840A central acquisition unit (9) is a multifunctional model of receiving analogue and digital signals with the parallel tracing of the input quantities flow, an integrated microcomputer, offloading the acquisition bus with a higher-level system and enabling the transient flow of signals from specific “smart sensors” directly to the control unit.

The acquisition unit is equipped with a LAN and FireWire bus for distributing information to a higher-order system (acquisition computer) as well as for expanding the number of measurement points by direct connection to several Quantum devices. HBM QuantumX MX840A is a multi-channel acquisition unit intended for static and dynamic parallel measurements. Due to the integration with a personal computer as a higher-order system, the measurement process is extremely simple, and the complete acquisition system is compact and small in size. This eight-channel acquisition unit provides 20,000 measurements per second per channel with 24-bit resolution. All 8 A/D converters work synchronously and monitor the transformation of physical quantities into a digital signal in real time.

To measure the thrust force, a console-type force transducer, shown in Fig. 2, was used. It was placed at a distance of  $a = 105$  mm from the central axis of the pylon (see Fig. 3). The force transmitter is made of aluminium, and two  $120 \Omega$  strain gauges are placed on it in the axial direction of the transmitter. Two  $120$

$\Omega$  resistors are placed on the transducer to form a full Wheatstone bridge. The transmitter is connected to the acquisition unit according to the manufacturer’s factory specification [17]. The measuring bridge is supplied with a DC input voltage  $V_I$ , while the output voltage  $V_O$  depends on the changes in the resistance of the strain gauges due to their deformations and is proportional to the value of the bending force acting on the transducer. By changing the voltage using the voltage regulator, the value of the number of revolutions of the propeller changes and thus the traction force. The maximum load value on the force sensor is 100 N.

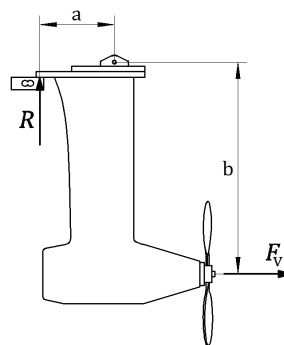


Fig. 3. Forces on the test bench

Fig. 3 shows that the thrust force is the result of the rotation of the propeller, which is mounted on two different arm lengths, with the arm of the pylon  $b$  being longer than the arm of the measuring device component. With this in mind, the real thrust force is calculated by applying the expression:

$$F_v = \frac{a}{b} R = \frac{105}{442} R = 0.237R. \quad (1)$$

A LANELO PR18-BC40DPR-E2 optical digital encoder (position (4) in Fig. 1) with a maximum response speed of 400 Hz was used to measure the number of revolutions, which provided a range of revolutions measuring up to 12000  $\text{min}^{-1}$ . The digital encoder is placed on an aerodynamic support that follows the contour of the pylon and has the ability to change the distance of the sensor in relation to the propeller for precise adjustments of the measured response.

Two accelerometers are used for vibration measurements: MONITRAN MTN/7100-50 (position (6) in Fig. 1) with a measurement range of  $-50$  g to  $+50$  g and a response speed of 1000 Hz, and HBM 1-B12/200 (position (5) in Fig. 1) with a measurement range of  $-20$  g to  $+20$  g with a response speed of 100 Hz. These accelerometers are placed on two



predefined points on the structure itself (Fig. 4). One is placed on the part of the bench that is affected by the thrust force of the propeller (i.e., the non-fixed part of the construction), while the other is placed on the fixed part of the test bench.

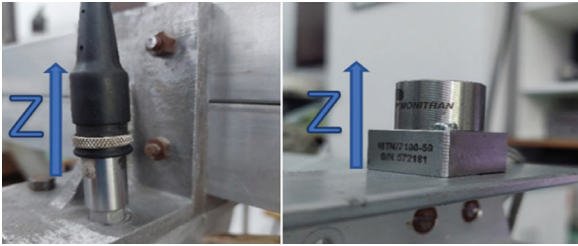


Fig. 4. Accelerometers (HBM and Monitran) with orientation of the z-axis

A special console support for torque measurement is designed and manufactured. Two 120  $\Omega$  strain gauges are mounted on this support and are connected to the acquisition device with a Wheatstone half-bridge (Fig. 5).

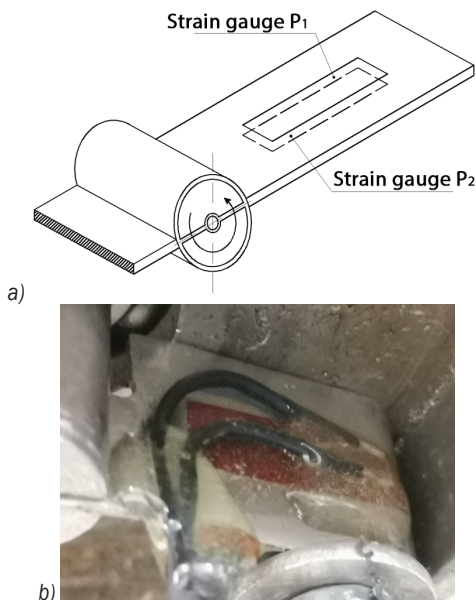


Fig. 5. Strain gauge on the console support; a) schematic and b) real

All previously mentioned sensors are calibrated before putting the test bench into operation, and their characteristics are entered into the CATMAN EASY acquisition software database. The calibration of the digital encoders is regulated by a simple display of counters per unit of time, while the calibrations of force and torque transmitters are done by entering loads with standard weights and using the HIOS HP-20 torque calibrator, respectively. Calibration of the

accelerometers is performed by placing the sensor in three positions (two sensors placed in the direction of the g component and one directed in that direction).

## 2 TESTING METHODOLOGY

A propeller that is prepared for testing is placed on the drive shaft of a motor by means of a conical holder and is secured with a self-locking nut. Since this test bench can be used for the testing of propellers of a wide range of diameters, which are of different geometries, they also differ in their mass. This is why this test bench has scales (7), by means of which we adjust the position of the non-fixed part of the structure to be in perfect balance. In that way, we are absolutely sure that the propeller is in its zero-level position and that once it starts to rotate, the produced thrust force will be immediately transferred to the load cell shown in Fig. 2. Once the test bench is set in zero balance with the testing propeller mounted on the motor driving shaft, we can proceed to data acquisition.

The sensors connected to the QuantumX acquisition unit are thrust force transducer, fixed and non-fixed accelerometer, strain gauge for torque measurement and optical encoder for *RPM* measurement. In order to avoid any error accumulation that could emerge on the sensor, the output of force and torque sensors in the sensor list are set to zero before the actual measurement session.

Fig. 6 shows the working screen of the CATMAN EASY software during propeller testing. For a defined *RPM*, changes are monitored on the transmitters of thrust force, torque, and vibrations, whose signals are incorporated into the corresponding graphic displays. The vibrations diagram that can be seen in Fig. 6 corresponds to the accelerometer that is placed on the non-fixed part of the test bench. The green button on the right monitors the signals from both accelerometers. In the case of a resonance of these two sensors, the green button becomes red, and the experiment is terminated.

In this manner, in case of any unforeseen circumstances, uncontrolled and unexpected increase/decrease of some of the observed quantities, or in the case of a resonant behaviour in the test bench, the experiment is terminated in a timely manner. All values can be exported in files of different formats (xlsx, ASCII, Matlab, etc.) for further analysis.

This test bench is located in an underground facility within a wind tunnel. This means that the test conditions have an environmental temperature of 20 °C and air humidity of 50 %. The values of these

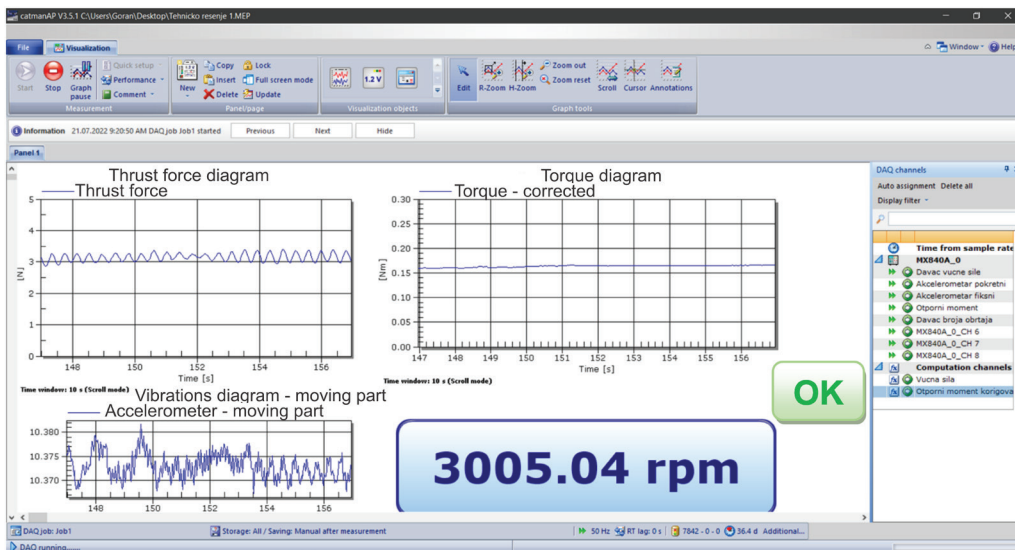


Fig. 6. CATMAN EASY working environment

two parameters are monitored constantly and are constant in time.

### 3 RESULTS AND DISCUSSION

Confirmation of the proposed methodology was carried out using measurements on the propeller shown in Fig. 7, whose characteristics are given in Table 1.

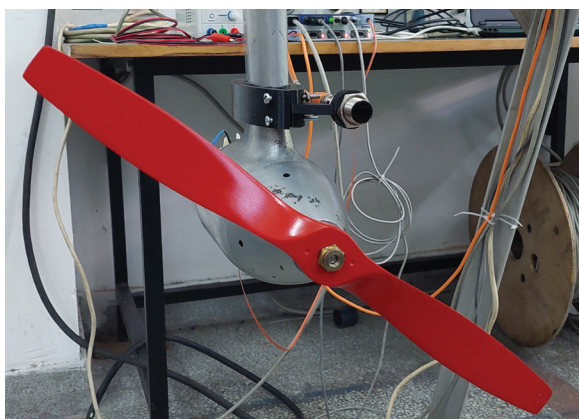


Fig. 7. Propeller on the test bench

During the trial measurements, it was determined that at a higher RPM, significantly greater vibrations occur in the system. Taking that into consideration and keeping in mind the safety of the experiment, it was decided to test the propeller in question for the four values of the RPM shown in the Table 2.

Table 1. Test propeller characteristics

Diameter, $D$	420 mm
Number of blades	2
Airfoil	Clark-Y
Reference pitch angle at $3/4D$	$19^\circ$

Table 2. RPM in the experiment

$RPM_1$ [min <sup>-1</sup> ]	$RPM_2$ [min <sup>-1</sup> ]	$RPM_3$ [min <sup>-1</sup> ]	$RPM_4$ [min <sup>-1</sup> ]
1000	2000	3000	3200

Data processing was performed with a maximum sampling rate of 20 kHz per channel. For the test in question, the sampling rate was 50 Hz. A Butterworth filter at 50 Hz with fully digital-to-analogue conversion distributed over a 400 MB/s fire-wire protocol is used.

Fig. 8 shows the diagrams of the comparative time dependence of the signal from the vibration transmitter and the optical encoder used to measure the RPM of the propeller. For all series of measurements, it is observable that increased vibrations occur at 2000 min<sup>-1</sup>, which indicates the asymmetry of the tested propeller.

The diagram of the dependence of the thrust force on the RPM is shown in Fig. 9, from which it can be concluded that the repeatability of the results is at a high level, which was verified by calculating the degree of correlation. For each of the series of measurements, the achieved degree of correlation was 0.98.



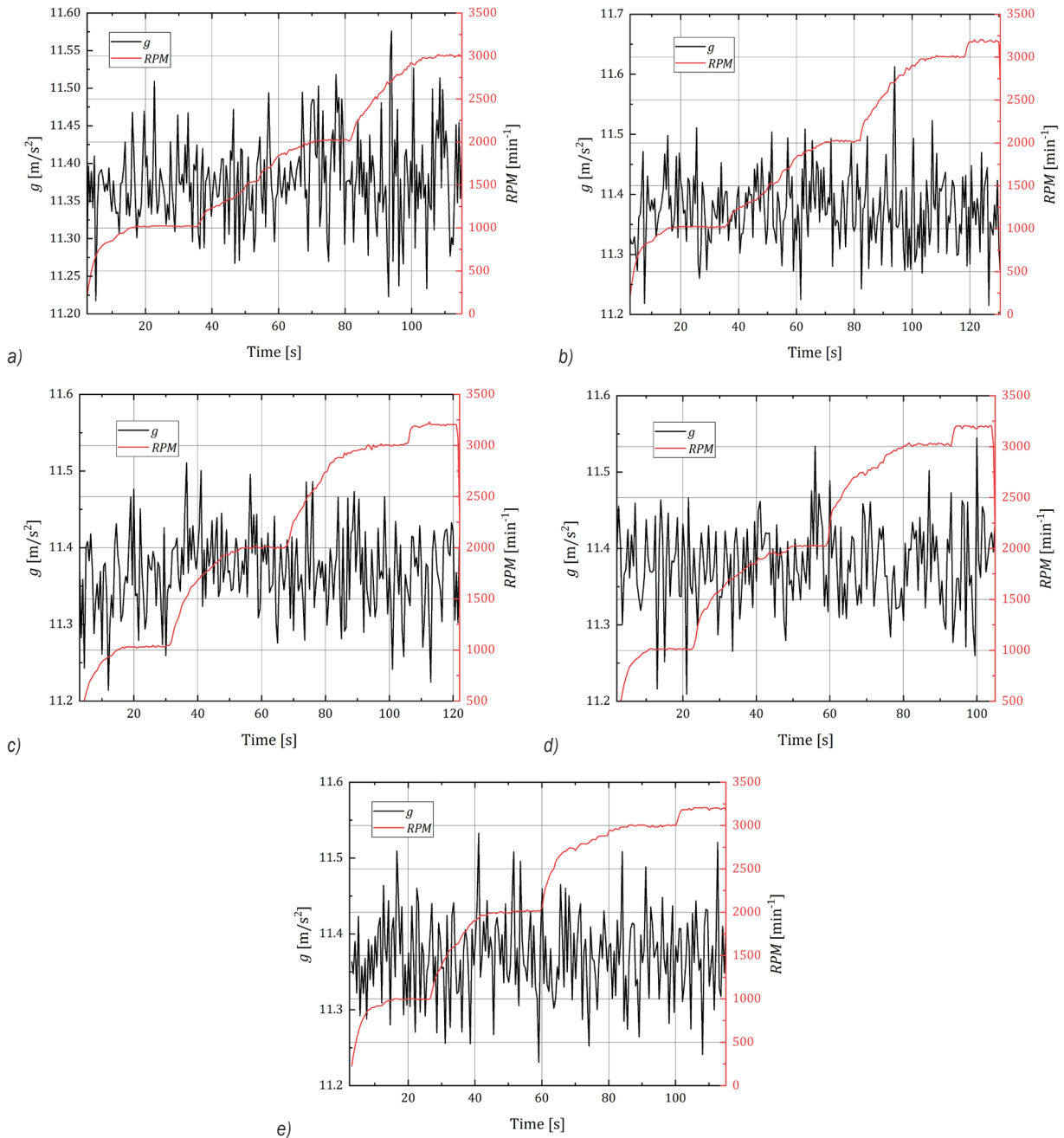


**Fig. 8.** Signal from accelerometer with the change in RPM: a) series 1, b) series 2, c) series 3, d) series 4, and e) series 5:  $g$  [ $m/s^2$ ] – acceleration

Two accelerometers are used in order to identify the interference between the operation of the propeller and the supporting structure. The experiment showed that there is no even linear dependence between the propeller's rpm and the response of the thrust force transducer. The pylon is of aerodynamic form and, as such, its geometry calms the airflow after the propeller.

As can be seen from Fig. 9, the thrust force is a square function of the RPM, as predicted by theory. With an increase in RPM, the thrust force is increased, since the propeller blades rotate faster, thus increasing the air mass flow rate flowing against them. The consequence of this is the increase of the forward load applied to the propeller that acts as a moving force forward. Due to the construction of the test bench and

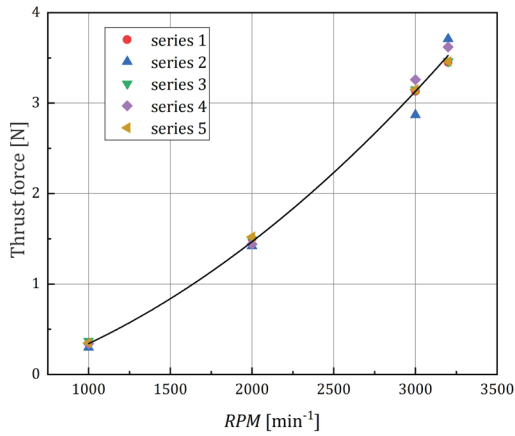


Fig. 9. Thrust force for different values of RPM

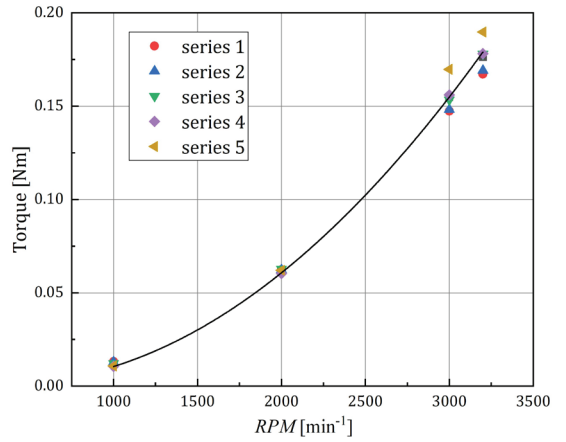


Fig. 10. Torque for different values of RPM

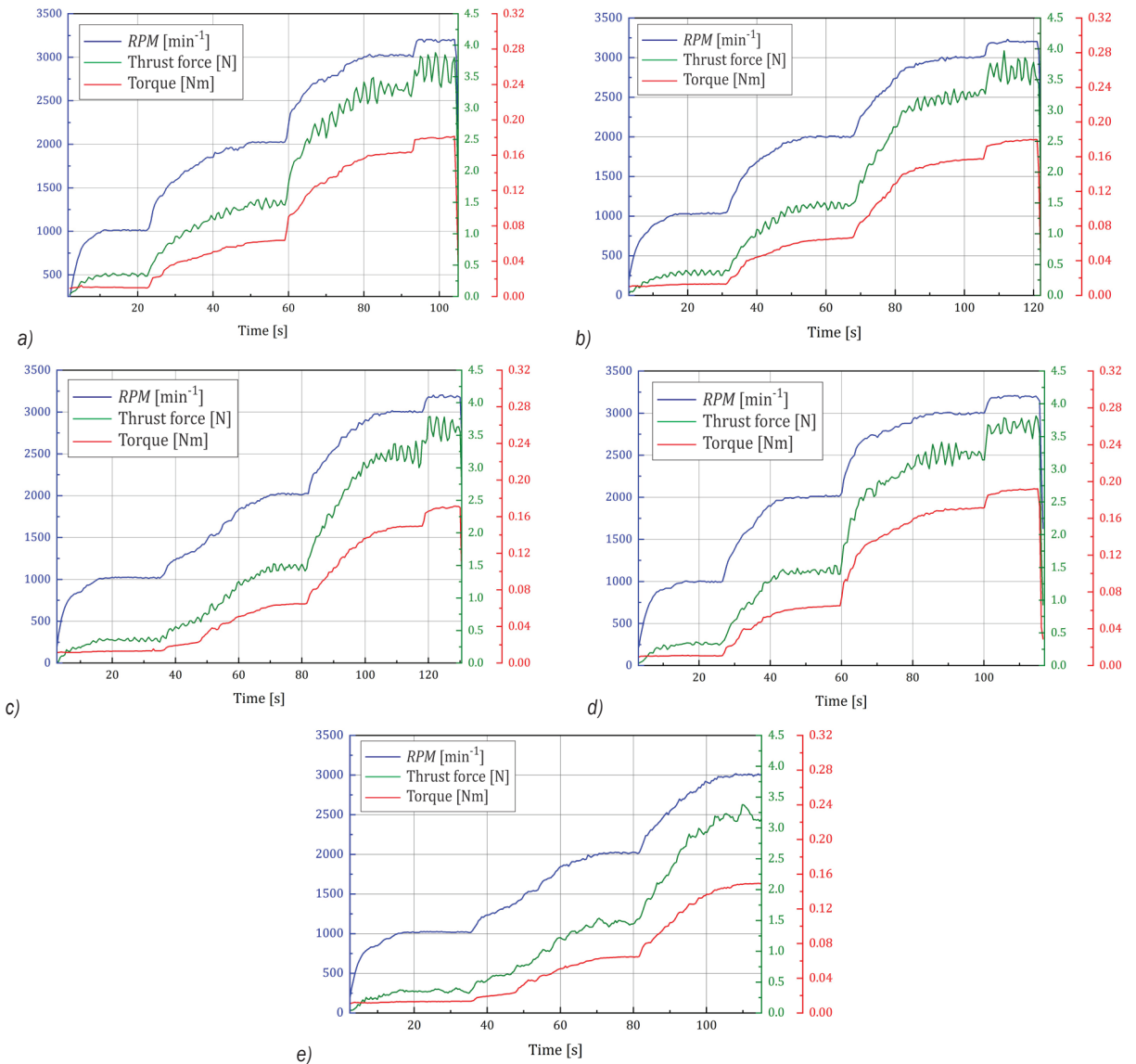


Fig. 11. Time evolution of RPM, thrust and torque: a) series 1, b) series 2, c) series 3, d) series 4, and e) series 5

the position of the load cell, this motion is restricted by the load cell itself. Hence, the load cell is “perceiving” the thrust force acting on the propeller. Fig. 10 shows the dependence of the resistance torque on the *RPM*. A slightly higher dispersion of the measured values is observed here, with a degree of correlation of 0.96.

The main discrepancy in the results is for higher *RPMs*. This behaviour of the value of the torque can be attributed to the inadequate stiffness of the console support on which the strain gauges are placed, which is reflected in conditions of increased vibration of the test bench. Therefore, these results are another indicator of the quality of the propeller under the test.

Fig. 11 shows the time dependences of the signals from the traction force sensor and the resistive torque sensor for all realized *RPM* and all series of measurements. A trend of global “tracking” of the values of both traction force and torque with the change in the number of revolutions is noticeable. Instability is also observed on the signal of the traction force sensor in the areas of the number of revolutions over 2000  $\text{min}^{-1}$ , which is a consequence of increased vibrations on the test table due to the imperfection of the tested propeller.

From the previously presented results, it can be concluded that the test table that is the subject of this technical solution can be used both for testing the static performance characteristics and vibrations and for balancing the propellers of unmanned aerial vehicles.

#### 4 CONCLUSIONS

This test aims to define the static performance characteristics and vibrations of propellers and to determine the functional dependence of force, *RPM*, power, torque, as well as the vibration level, especially from the point of view of use by propeller manufacturers in terms of quality checking, load capacity and traction-dynamic characteristics. In contrast, the results of vibro-diagnostic parameters are significant in terms of their balance and potential resonance. Not less significant is the educational and scientific research aspect from the point of view of aviation and information technologies development. The applied methodology represents a high-quality process of evaluating propeller parameters both in real conditions of exploitation and in laboratory conditions.

After testing, the acquired experimental data realistically describe the complex behaviour of propellers in operation. The experimental results represent the basis for finding the parameters that

cause the improper operation of propellers, as well as the quality characterization procedures for determining the service life of propellers from the aspect of dynamic traction characteristics in the initial phase of development.

The results of the research indicate the need to verify the obtained results in real operating conditions, where the combination of hardware and software components would provide the possibility of verifying analytical and experimental results from the test bench with real parameters in real operating conditions. In this sense, the authors are of the opinion that a real confirmation of the results on real aircraft in all atmospheric conditions is needed, regardless of the planet on which the experiment is performed.

#### 5 ACKNOWLEDGEMENTS

This research was funded by a grant from the Ministry of Education, Science and Technological Development, Republic of Serbia, under Contract No. 2022451-03-68/2022-14/200105 (subprojects TR35046, TR35045, and TR35040).

#### 6 REFERENCES

- [1] Evdokimov, I. (2015.) Blade element theory in the UAV multirotor blade optimization, *International CAE Conference*, p. 19-20.
- [2] Kuitche, M.A.J., Botez, R.M., Viso, R., Maunand, J.C., Moyao, O.C. (2020). Blade element momentum new methodology and wind tunnel test performance evaluation for the UAS-S45 Balaam propeller. *CEAS Aeronautical Journal*, vol. 11, no. 4, p. 937-953, DOI:10.1007/s13272-020-00462-x.
- [3] Moffitt, B., Bradley, T., Parekh, D., Mavris, D. (2008). Validation of vortex propeller theory for UAV design with uncertainty analysis. *46th AIAA Aerospace Sciences Meeting and Exhibit*, DOI:10.2514/6.2008-406.
- [4] Vargas Loureiro, E., Oliveira, N.L., Hallak, P.H., de Souza Bastos, F., Rocha, L.M., Grande Pancini Delmonte, R., de Castro Lemonge, A.C. (2021). Evaluation of low fidelity and CFD methods for the aerodynamic performance of a small propeller. *Aerospace Science and Technology*, vol. 108, art. ID 106402, DOI:10.1016/j.ast.2020.106402.
- [5] Figat, M., Piątkowska, P. (2021). Numerical investigation of mutual interaction between a pusher propeller and a fuselage. *Proceedings of the Institution of Mechanical Engineers, Part G: Journal of Aerospace Engineering*, vol. 235, no. 1, p. 40-53, DOI:10.1177/0954410020932796.
- [6] Erkan, O., Özkan, M., Karakoç, T.H., Garrett, S.J., Thomas, P.J. (2020). Investigation of aerodynamic performance characteristics of a wind-turbine-blade profile using the finite-volume method. *Renewable Energy*, vol. 161, p. 1359-1367, DOI:10.1016/j.renene.2020.07.138.
- [7] Viola, I.M., Chapin, V.G., Speranza, N., Biancolini, M.E. (2018). Optimal airfoil shapes by high-fidelity CFD. *Aircraft Engineering*

- and *Aerospace Technology*, vol. 90, no. 6, p. 1000-1011, DOI:10.1108/AEAT-09-2017-0210.
- [8] Karali, H., Inalhan, G., Demirezen, M.U., Yukselen, M.A. (2021). A new nonlinear lifting line method for aerodynamic analysis and deep learning modeling of small unmanned aerial vehicles. *International Journal of Micro Air Vehicles*, vol. 13, p. 1-24, DOI:10.1177/17568293211016817.
- [9] Ostler, J.N., Bowman, W.J., Snyder, D.O., McLain, T.W. (2009). Performance flight testing of small, electric powered unmanned aerial vehicles. *International Journal of Micro Air Vehicles*, vol. 1, p. 155-171, DOI:10.1260/175682909789996177.
- [10] Paz, C., Suárez, E., Gil, C., Vence, J. (2021). Assessment of the methodology for the CFD simulation of the flight of a quadcopter UAV. *Journal of Wind Engineering and Industrial Aerodynamics*, vol. 218, art. ID 104776, DOI:10.1016/j.jweia.2021.104776.
- [11] Zhao, A., Zhang, J., Li, K., Wen, D. (2021). Design and implementation of an innovative airborne electric propulsion measure system of fixed-wing UAV. *Aerospace Science and Technology*, vol. 109, art. ID 106357, DOI:10.1016/j.ast.2020.106357.
- [12] Cruzatty, C., Sarmiento, E., Valencia, E., Cando, E. (2022) Design methodology of a UAV propeller implemented in monitoring activities. *Materials Today: Proceedings*, vol. 49, p. 115-121, DOI:10.1016/j.matpr.2021.07.481.
- [13] Chipade, V.S., Abhishek, Kothari, M., Chaudhari, R.R. (2018) Systematic design methodology for development and flight testing of a variable pitch quadrotor biplane VTOL UAV for payload delivery. *Mechatronics*, vol. 55, p. 94-114, DOI:10.1016/j.mechatronics.2018.08.008.
- [14] Anemaat, W.A.J., Schuurman, M., Liu, W., Karwas, A. (2017). Aerodynamic design, analysis and testing of propellers for small unmanned aerial vehicles. *AIAA SciTech Forum*, 55<sup>th</sup> AIAA Aerospace Sciences Meeting, DOI:10.2514/6.2017-0721.
- [15] Asson, K.M., Dunn, P.F. (1992). Compact dynamometer system that can accurately determine propeller performance. *Journal of Aircraft*, vol. 29, no. 1, p. 8-9, DOI:10.2514/3.46118.
- [16] Marchent, M.P. (2004). *Propeller Performance Measurement for Low Reynolds Number Unmanned Aerial Vehicle Applications*. MSc. Thesis, Wichita State University, Wichita
- [17] QuantumX, (2015). Operating Manual, HBM, from: <https://www.hbm.com/fileadmin/mediapool/hbmdoc/technical/A03031.pdf>, accessed on 2022-11-01.

# A Study Using the Hybrid Fuzzy AHP&TOPSIS Method in the Conversion of a LEED-Certified Education Building into a Nearly Zero-Energy Building in a Cold Climate

Ali Celik<sup>1,\*</sup> – Bayram Sahin<sup>2</sup> – Eyüphan Manay<sup>1</sup> – Abit Balin<sup>3</sup>

<sup>1</sup> Erzurum Technical University, Department of Mechanical Engineering, Turkey

<sup>2</sup> Istanbul Technical University, Faculty of Mechanical Engineering, Turkey

<sup>3</sup> Istanbul University, School of Transportation and Logistics, Turkey

*In cold climate regions, it is essential to design and manufacture energy-efficient buildings for both economic benefits and the reduction of environmental effects by controlling energy consumption. This study aimed to increase the cost-effective energy performance and approach the nearly zero energy building (nZEB) by taking the leadership in energy and environmental design (LEED) in the cold climate region of Turkey as a model. The results of single and mixed scenarios that increase energy efficiency were determined by making energy modelling of the building. By applying single and mixed energy efficiency scenarios, a maximum saving of 85.60 % per year in terms of primary energy, an improvement of 83.6 % in terms of global costs and a reduction of 86.4 % in CO<sub>2</sub> emissions were obtained compared to the reference building. The payback period of the scenarios is between 3.8 years and 14.53 years. The most suitable single and mixed scenario was determined by a systematic hybrid model, in which the fuzzy analytical hierarchy process (FAHP) and technique for order of preference by similarity to ideal solution (TOPSIS) methods among multi-criteria decision-making methods are used together. The results showed that economic criteria were decisive in determining the most suitable scenario for cold climate regions. The results of this study revealed that there can be a realistic decision-support model for the creation of energy-efficient buildings for countries without the need for foreign certification.*

**Keywords:** green building, nearly zero energy building, energy and cost-optimal analysis, fuzzy analytic hierarchy process (FAHP), TOPSIS

## Highlights

- By increasing the cost-effective energy performance, a LEED-certified educational building has been brought closer to the nZEB.
- Energy cost analysis of single and mixed scenarios that increase energy efficiency has been made.
- FAHP and TOPSIS methods from multi-criteria decision-making methods have been used together to determine the most appropriate single and mixed scenarios.
- With a value of 5.08 kg CO<sub>2</sub> m<sup>2</sup>/year, net zero carbon emissions in buildings are approached.

## 0 INTRODUCTION

The need for energy is gradually increasing due to technological developments and population density. Therefore, it has become essential to use energy efficiently and in a planned way. In many countries, a large part of the total energy is used in buildings, and energy consumption rates are often parallel to the European Union (EU) countries. It has been determined that approximately 40 % of total energy consumption [1] and 36 % of CO<sub>2</sub> emissions originate from buildings in many countries in Europe [2]. Therefore, energy efficiency has become an critical issue for many countries in terms of energy dependence and economic development [2]. Furthermore, it is estimated that the energy consumption of buildings will increase by 50 % until 2060, and thus carbon emissions will also increase [3]. Within the scope of the Paris Agreement, many countries have included targets for increasing energy efficiency and low-carbon economic growth in their

long-term plans [4]. For example, while China aims to become carbon neutral by 2060, the United States and the United Kingdom have promised net zero greenhouse gas emissions by 2050 [5].

One of the important steps for energy efficiency in the building sector is the Energy Performance of Buildings Directive (EPBD) recast, which was published in 2002 and revised in 2010 [1]. The concepts of cost-optimal energy efficiency and nearly zero-energy building have come to the fore with this directive. Buildings should consume very little energy to approach the nearly zero energy building (nZEB), and most of it should be met by renewable energy sources [6]. Although the definition and requirements of the nZEB differ between countries, the common goal is to minimize energy consumption and greenhouse gas emissions throughout the service life of the building.

Since Turkey is dependent on foreign sources in terms of energy, it is essential to use energy effectively and efficiently. Foreign dependency on energy brings



great risks both in terms of economy and security. In Turkey, the building sector is responsible for 30 % of the total final energy consumption as the second largest energy consuming sector due to the increasing population and technological developments [7]. It is clearly seen that the measures to be taken in this sector will contribute to the national economy. Compared to countries in Europe, studies on nZEBs in Turkey remain in their early stages. Considering all these developments, it is necessary to determine cost-optimal energy levels in buildings in Turkey. In the subsequent period, reaching the level of nearly zero-energy buildings with cost-effective improvements in buildings is expected.

There is a need for a systematic method to evaluate the scenarios used to increase the cost-effective energy performance of buildings with many conflicting criteria. The absence of such an internationally accepted method indicates a gap in the literature that needs to be explored. According to the literature review, there has been no comprehensive internationally accepted method based on national conditions in cold climate regions without the need for foreign certification until the present day. This study has determined the parameters that would guide legal regulations using multi-criteria decision-making (MCDM) methods in identifying the cost-optimum nearly zero energy level. The present study is important for constructing cost-effective energy performance buildings on university campuses.

The nZEB aims to reduce energy consumption in buildings by using energy efficient technologies and renewable energy solutions [7] and [8]. Wang and Zhao [9] investigated the effect of external walls and roofs with different heat transfer coefficients ( $U$ ) on building energy consumption and determined that increasing energy efficiency in the building envelope affected energy saving. Zhao and Du [10] aimed to approach education buildings nZEB by optimizing national technologies in China and using four recommended technologies for the four main climate regions. They also determined that the total energy saving rate in very cold regions increased by 70.74 % compared to the current national standards and approximately 60 % of the total energy saving rate could be improved in cold regions. Sağlam et al. [11] made cost-optimal energy efficiency calculations for the existing multi-story buildings in cold climate regions. The sensitivity of the results to economic data and changes in initial investment costs was analysed. It was revealed that cost-optimal energy efficiency data varied depending on economic indicators. A new approach taking into account hourly, daily, and monthly consumption

and evaluating the former energy use and renewable energy generation for all buildings of the University of Lleida (Spain) was presented [12]. This analysis constitutes a basis for energy improvements and comparisons to be made in buildings. It also enables determining the difference between actual energy data at the building and campus levels and the nZEB levels specified for non-residential buildings in the European Union. The results show that there is a wide range of energy use between campus buildings, ranging from 50 to 470 kWh/m<sup>2</sup> years. The energy use is reduced with the inclusion of renewable energy generation. This analysis revealed that the average primary energy consumption in Spain was approximately four times higher than the EU nZEB levels.

Kalaycıoğlu and Yılmaz [13] determined single or mixed measures to increase energy efficiency in accordance with the method proposed by the EPBD methodology. They also found the optimal cost and nearly zero energy levels at the settlement scale with energy and cost analyses for these measures. It was revealed that the analysis results depended on countries' economic data, the laws related to buildings, and their political and financial targets. Valancius et al. [14] proposed a methodological approach that addressed both energy and environmental factors in bringing buildings to nearly zero energy (nZEB) levels under the climatic conditions of Lithuania. With this method, several energy-efficiency increasing scenarios were applied in a case study. The results of primary energy savings and CO<sub>2</sub> gas emissions over a 60-year period and the most reasonable thermal insulation materials for building insulation in terms of energy and ecology were provided. A four-star hotel operating in Faro (Portugal) was taken as a reference, and technical and economic analyses were performed to determine nZEB levels in three European cities with different climates. The energy modelling of the reference building was done using the DesignBuilder/EnergyPlus software, and cost-optimal energy efficiency-increasing measures were determined. Considering the climatic and economic realities for the three cities, it was indicated that the most suitable measure to increase energy efficiency should be selected [15].

Ferrari and Becalli [16] proposed strategies for the conversion of the building on the campus of Politecnico di Milano University, Italy into a nZEB. The aim was to achieve cost-effective energy savings and reduce greenhouse gas emissions with energy performance-increasing scenarios. Furthermore, it was determined that net energy consumption could be close to zero when on-site renewable energy sources

were used. The energy and carbon payback periods of the scenarios that would increase energy performance were evaluated to bring a school building in Torino, Northern Italy closer to the nZEB [17]; it was revealed that energy efficiency scenarios for nZEB had energy and carbon paybacks that were shorter than the building's life cycle. The measurement and analysis of the two-year energy consumption values of a nearly zero-energy building in the cold regions of China are presented in this study [18]. It was emphasized that nZEBs created a more comfortable indoor environment with less energy demand and would contribute to achieving climate change targets with less carbon emissions.

In this study, the analytical hierarchy process (AHP) and multi-criteria optimization method of complex systems VIKOR (multi-criteria optimization and compromise solution) method were employed together to determine the most suitable improvement scenarios used to increase the energy performance of old buildings [19]. Three scenarios showing the (nZEB) level were determined. They are common solution scenarios that include high energy potential on-site generation, medium energy potential mechanical/electrical system, and low energy potential building envelope components. Another study [20] presented an integrated approach requiring multi-objective optimization in the preference of passive and active design parameters that conflicted with each other instead of conventional methods in the process of designing a high-rise office building as zero energy building (ZEB) in the Mediterranean climate with hot summers in Athens, Greece. The targets set in this approach were aimed at reducing energy consumption and increasing energy generation and thermal comfort. With the implementation of this integrated approach, it was aimed to make conscious decisions in determining the design strategy to achieve ZEB.

The present study presents an approach toward constructing energy-efficient education buildings in cold climate regions in accordance with nZEB without the need for foreign certification in order to protect countries' energy resources and economic interests. Since the energy saving potential is high in cold climate regions, different nZEB scenario combinations can both reduce carbon emissions and help achieve climate change targets.

Natural gas and electricity field measurements of the reference building in 2017 to 2019 are made and the impact factors on the aim of obtaining approximately zero energy are analysed. The aim was to reach cost-optimal energy efficiency levels with the scenarios to reduce the energy demand of the leadership in energy

and environmental design (LEED)-certified Faculty of Engineering and Architecture building at Erzurum Technical University, Turkey. It is obligatory to determine which criteria should be used to determine the most appropriate scenario to increase energy efficiency. Many different and contradictory factors, such as technical, economic, and environmental, make it difficult for decision makers. To overcome this difficulty, a systematic hybrid decision method that takes all factors into account has been developed. The most suitable energy efficiency scenario, which would represent the optimal cost and nearly zero energy level, was determined using the fuzzy AHP (FAHP) technique and the technique for order of preference by similarity to ideal solution (TOPSIS) methods together.

## 1 MATERIAL AND METHODS

The present study investigated the conversion of Erzurum Technical University Faculty of Engineering and Architecture building, located in the cold climate region and having a SILVER certificate according to the LEED criteria [21], into a nZEB.

The conversion of the reference building into a nearly zero-energy building consists of six steps, and the flow chart is presented in Fig. 1.

Step 1: Description of the characteristics of the reference building (RB) and the climatic conditions of the region where it is located.

Step 2: Calculation of primary energy consumption and emission amount of the reference building with a LEED-SILVER certificate.

Step 3: Determining single scenarios increasing energy efficiency and conducting energy and cost analyses.

Step 4: Determining mixed scenarios and making energy and cost analyses to reduce the energy consumption of the reference building.

Step 5: Calculating the carbon emission amount and payback periods of energy efficiency increasing scenarios.

Step 6: Evaluation of the results of energy efficiency scenarios by multi-criteria decision-making methods.

### 1.1. Characteristics and Climatic Conditions of the Reference Building

The Faculty of Engineering and Architecture building on the campus of Erzurum Technical University was taken as a reference in the study; it has a closed area of 25245 m<sup>2</sup>. It has the LEED-Silver certificate, which

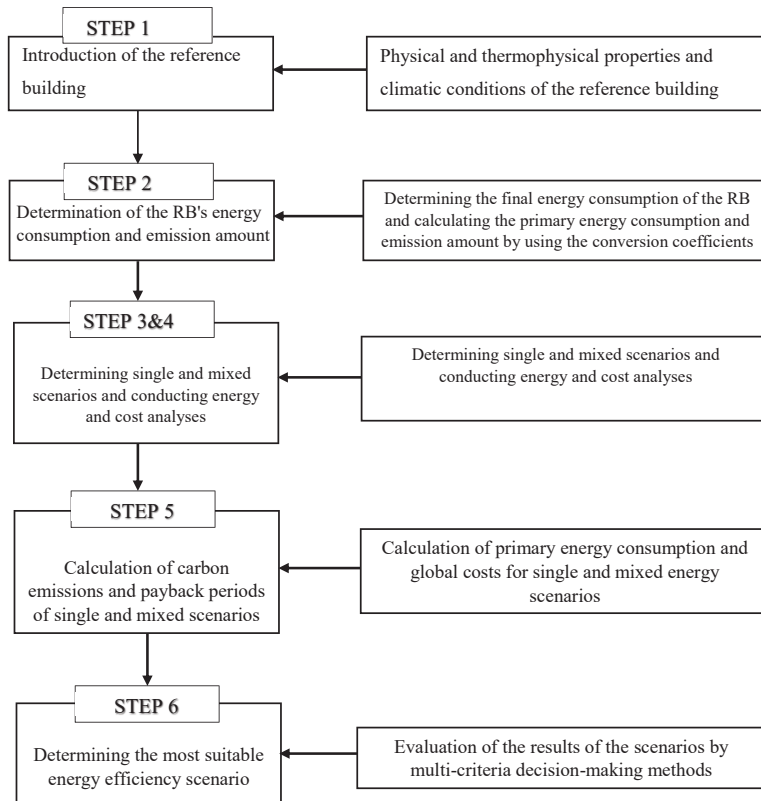


Fig. 1. Research flow chart

is commonly used throughout the world [22]. The reference building consists of a total of 5 blocks (Fig. 2). There are offices of faculty members in the 1<sup>st</sup>, 2<sup>nd</sup>, and 3<sup>rd</sup> blocks, classrooms in the 4<sup>th</sup> block, and dean's offices in the 5<sup>th</sup> block.

The building's envelope consists of external walls, floors, roofs, and glass surfaces. The facade of the reference building consists of a granite mechanical cladding system and a cladding glass system with a light transmittance of 35 % and a

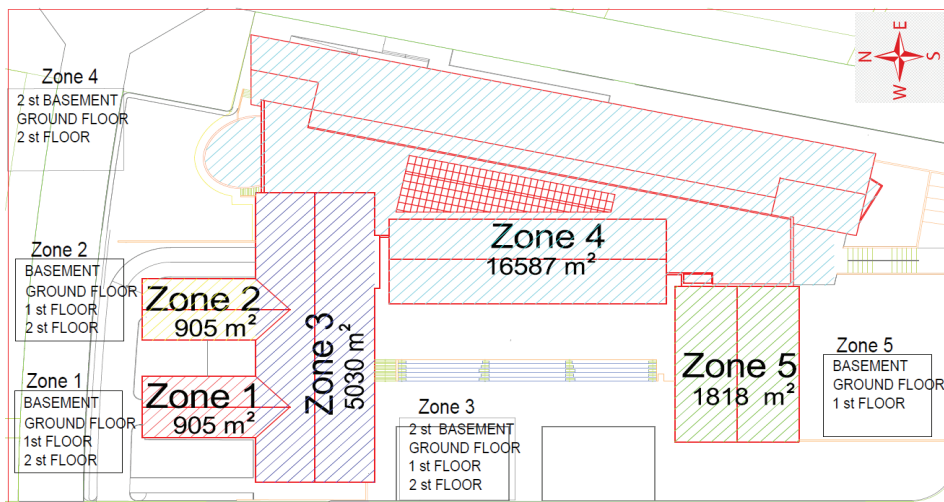


Fig. 2. Under study building's site plan

solar heat transmission coefficient of 0.24. The roof covering has dyed steel sheet cladding. The total heat transmission coefficients ( $U$ ), [ $W/m^2K$ ] according to the construction materials that make up the reference building's envelope and their thickness and the recommended heat transmission coefficients according to Turkish Thermal Insulation Standard TS 825-2013 [23] are presented in Table 1.

**Table 1.** Heat transmission coefficients of the reference building's envelope construction elements

Building's materials	Exterior wall (Curtain)	Exterior wall (Brick)	Roof	Ground floor	Glazing system
Current U-value [ $W/(m^2K)$ ]	0.260	0.235	0.177	0.367	1.1
According to TS 825 U-value [ $W/(m^2K)$ ]	0.370	0.324	0.209	0.367	2.2

In the heating system of the reference building, four high-efficiency natural gas boilers, each with a capacity of approximately 500 kW, were used. Heating in the reference building was done with radiators, air appliances and heating, ventilation, and air conditioning (HVAC) systems. Since the heating load of the reference building is very high, the saving measures to be applied to reduce the heat energy are of great importance. To achieve the comfort temperature determined according to TS825-2013, the set temperatures in the building are between 20 °C to 22 °C on the sites [23]. The operating times and operating temperatures of the heating system in the reference building are programmed according to the course hours on weekdays and weekends.

Cooling is provided by an air-source variable refrigerant volume (VRV) and air handling unit on certain sites depending on the climate and usage conditions in the reference building. The requirements of the American Society of Heating and Air- Conditioning Engineers ASHRAE 90.1-2010 [24] standard were prioritized using efficient heating, cooling, and ventilation systems in the RB.

The amount of fresh air given to the sites was kept above the ASHRAE 62.1 [25] standard in order to increase indoor air quality, low-emission materials were preferred, and the conditions for thermal comfort were monitored.

Fluorescent lighting was used for lighting on all sites in the reference building. The operating hours of the lighting systems are programmed according to course hours on weekdays and weekends.

Erzurum, where the RB is located, is in the cold climate zone [26]. According to the results

of the observations for approximately 80 years at meteorological stations, it was found that while the mean temperature of the coldest month was -8.6 °C, the mean temperature of the hottest month was 19.6 °C, and the lowest and highest temperatures were -35 °C and 35 °C, respectively. In winter, snowfall is about 50 days and the number of days covered with snow is 114 days [27]. Erzurum's total solar radiation (between 2011 and 2022) is between approximately 1400 kWh/m<sup>2</sup> to 1700 kWh/m<sup>2</sup> per year, and the monthly average daily radiation intensity value coming to the horizontal surface is between 1.48 kWh/m<sup>2</sup> to 6.83 kWh/m<sup>2</sup> [28] and [29].

## 1.2 Calculation of the RB's Energy Consumption and Carbon Emissions

Natural gas and electricity average consumption values for 2017, 2018, and 2019 were used as references in the calculations since the pandemic started at the beginning of 2020 and education and training activities were continued remotely. Primary energy consumption and emission amounts are determined by multiplying these consumption values by conversion coefficients. With regard to primary energy conversion coefficients in Turkey, the coefficients of 2.36 for electricity and 1 for natural gas and other fuels are used. The carbon emission conversion factors are also considered to be 0.626 (kg equivalent CO<sub>2</sub>/kWh) for electricity, 0.234 (kg equivalent CO<sub>2</sub>/kWh) for natural gas [30].

Total primary energy ( $TBE$ ) and annual carbon emissions for the reference building were calculated with the following equations.

$$TBE = [E_{natural\ gas}] + [E_{electricity} \times 2.36], \quad (1)$$

$$E_{CO_2} = (0.234 \times e_{natural\ gas}) + (0.626 \times e_{electricity}), \quad (2)$$

where  $TBE$  is total primary energy consumption, [kWh/m<sup>2</sup> year];  $E_{natural\ gas}$  is total natural gas energy consumption, [kWh/year];  $E_{electricity}$  is total electricity energy consumption, [kWh/year];  $E_{CO_2}$  is total CO<sub>2</sub> emission [kg m<sup>2</sup>/year].

## 1.3 Determination of Single and Mixed Scenarios Increasing Energy Efficiency

Since the reference building was built according to LEED-Silver green building certification standards, measures to increase energy performance are limited. As a result of evaluating the reference building's energy analysis, improvement scenarios for the use of lighting, heating systems, and renewable energy



systems were determined. The average electricity consumption values of the reference building from 2017 to 2019 were taken into account for determining the capacity of the gas engine micro-cogeneration system (Table 6). The purpose of using that system is to meet a remarkable part of the electrical energy consumption of the reference building with the electrical energy (75 kW) to be produced. In addition, it is intended to support the heating system of the reference building with the heat energy (116 kW) to be produced by the micro-cogeneration system. In the design of the water source heat pump, the average natural gas consumption values of the reference building in 2017, 2018, and 2019 were taken as reference (Table 6). It is intended to support the heating system with the heat energy (2300 kW) to be produced by the water source heat pump system. The descriptions of single scenarios increasing energy efficiency are given in Table 2.

**Table 2.** Description of single improvement scenarios

Scenario	Description
S1	Installation of 1151 photovoltaic (PV) panel systems with a power of 425.84 kWp on the south-facing roofs
S2	Installation of 2220 PV panel systems with a power of 821.40 kWp on the south + east + west facing roofs
S3	Replacing the existing compact fluorescent lamps with light-emitting diode (LED) lamps
S4	Establishment of a gas engine micro cogeneration system with 75 kWe electricity and 116 kW heat energy power generation capacity
S5	Installation of a 2300 kW water source heat pump system in the heating system

The aim was also to reduce global costs, primary energy consumption and payback periods through mixed energy efficiency scenarios. The triple mixed energy efficiency scenarios were selected from the scenarios with low global costs. The determined mixed energy efficiency scenarios are explained in Table 3.

Two different analyses, energy analysis and cost analysis, were used to determine the nearly zero energy level of the reference building. Energy analysis was conducted according to actual energy consumption and simulation data. The measurement and calculation methods used to determine the energy performance (heating and electrical energy consumption) of the reference building comply with the ISO 52016-1(2017) standard [31]. The purpose of the energy analysis is to determine the annual total energy consumption (heat energy and electrical energy)

and reveal how much energy consumption can be reduced with saving measures and renewable energy sources that will reduce consumption. Furthermore, the remaining electrical energy from consumption will be supplied to the grid. The EN 15459 Economic Evaluation Standard for Building Energy Systems, which is also guided by EU legislation, was used in the cost analysis [32].

**Table 3.** Description of mixed improvement scenarios

Scenario	Description
S1 + S3	Installation of 1151 PV panel systems with a power of 425.84 kWp on the south-facing roofs Replacing the existing compact fluorescent lamps with LED lamps
S1 + S4	Installation of 1151 PV panel systems with a power of 425.84 kWp on the south-facing roofs Establishment of a gas engine micro cogeneration system with 75 kWe electricity and 116 kW heat energy power generation capacity
S1 + S5	Installation of 1151 PV panel systems with a power of 425.84 kWp on the south-facing roofs Installation of a 2300 kW water source heat pump system in the heating system
S2+S3	Installation of 2220 PV panel systems with a power of 821.40 kWp on the south + east + west facing roofs Replacing the existing compact fluorescent lamps with LED lamps
S2+S4	Installation of 2220 PV panel systems with a power of 821.40 kWp on the south + east + west facing roofs Establishment of a gas engine micro cogeneration system with 75 kWe electricity and 116 kW heat energy power generation capacity
S5 + S3	Installation of a 2300 kW water source heat pump system in the heating system Replacing the existing compact fluorescent lamps with LED lamps
S3 + S4	Replacing the existing compact fluorescent lamps with LED lamps Establishment of a gas engine micro cogeneration system with 75 kWe electricity and 116 kW heat energy power generation capacity
S2+ S3 + S4	Installation of 2220 PV panel systems with a power of 821.40 kWp on the south + east + west facing roofs Replacing the existing compact fluorescent lamps with LED lamps Establishment of a gas engine micro cogeneration system with 75 kWe electricity and 116 kW heat energy power generation capacity
S1+ S3 + S4	Installation of 1151 PV panel systems with a power of 425.84 kWp on the south-facing roofs Replacing the existing compact fluorescent lamps with LED lamps Establishment of a gas engine micro cogeneration system with 75 kWe electricity and 116 kW heat energy power generation capacity



For the conversion of the reference building into a nearly zero-energy form, energy consumption and carbon emission amounts of the single and mixed scenarios were determined by using HAP 5.11 dynamic simulation software. It has a weather data library covering more than seven hundred cities around the world. The building model should be validated by comparing the consumption data obtained as a result of building energy modelling with the building's actual consumption data. As stated in the ASHRAE Guideline 14 [33], the coefficient of variation of the root mean square error (CV\_RMSE) value should be less than 15 % and the normalized mean bias error (NMBE) value should be less than 5 % for the building energy simulation data in monthly evaluations. The validation of the model after preparing the building energy model is important in terms of showing the reality of the applied energy-saving scenarios [34]. Next, the global cost analysis of the scenarios was performed, and the optimal cost and primary energy consumption of the scenarios were compared.

The formulae used in the global cost calculations of all scenarios were taken from EN 15459 [35], stated as the most reliable cost calculation method by the European Union. The net present value method, which expresses the present value of each investment by multiplying the projected earnings and costs for the coming years with the discount factor of the current year, is used in this procedure.

In the calculations, the lifetime of the systems to increase building energy efficiency was taken as approximately 20 years [36], and the scrap values were not taken into account. According to the EPBD-recast, the cost calculation period for non-residential buildings has been proposed as 20 years. The Construction and Installation Unit Prices of The Ministry of Environment, Urbanization and Climate Change, Turkey for 2021 were used in the initial investment costs to be used in global cost calculations [37]. Market prices for 2021 were used in the initial investment costs of energy improvement measures not defined in the unit price book (such as PV and LED lighting systems).

Cost calculations were made in Turkish lira (TL) and then the results were converted to US dollars (\$). In the calculations, euro €/TL was taken as 10.40 and \$/TL was taken as 8.74 [38] in the conversion of prices in foreign currency. The inflation rate was taken as 16.59 % [39] per annum in May 2021, the discount rate was taken as 1 %, and the interest rate was taken as 19 % [40] per annum. For Erzurum, the natural

gas unit price was taken as 0.193 TL/kWh [41], and electricity unit price was taken as 0.953 TL/kWh [42].

#### 1.4 Determination of Payback Periods of the Single and Mixed Scenarios Increasing Energy Efficiency

It is the period during which the sum of savings of single and mixed scenarios increasing energy efficiency reaches the initial investment cost. With the payback period, it is decided whether the investment is rational or not. The payback period is calculated with the following formula [43]:

$$IPP = \frac{II}{CFPP}. \quad (3)$$

In the Eq. (3), the terms of *IPP*, *II* and *CFPP* represent investment payback period [Year], initial investment [US dollar], cash flow per period [US dollar], respectively.

Energy efficiency scenarios with a payback period of not more than 10 years as the baseline scenario and energy efficiency scenarios with a payback period of not more than 20 years as the deep renovation scenario were proposed within the scope of this study.

#### 1.5 Multi-Criteria Decision-Making

MCDM is the process of selection, ranking, or evaluation using at least two of the evaluated criteria, in which more than one criterion or target is addressed together. One of the frequently used multi-criteria decision-making methods is the AHP, which was developed by Thomas L. Saaty in 1980 [44]. The AHP is a multi-criteria decision-making method based on comparing the significance levels of the criteria affecting the decision as a result of pairwise comparisons through a decision hierarchy. The FAHP method was developed by combining fuzzy logic and AHP in order to facilitate decision-making when there is incomplete and imprecise information in AHP. In pairwise comparisons in FAHP; Linguistic variables and fuzzy numbers replace the real numbers used in Saaty's AHP method. In general, trapezoidal and triangular fuzzy numbers are used in pairwise comparisons. In this method, fuzzy weight and performance values are obtained by using the geometric mean. The importance scale used in pairwise comparisons in FAHP is given in Table 4 [45].

Linguistic expressions and triangular fuzzy numbers are given in Table 5 in the evaluation of alternatives to help experts make more realistic decisions.

**Table 4.** Linguistic variables for importance weights

Linguistic expression	Scale of fuzzy numbers
Absolutely strong (as)	(7.00, 9.00, 9.00)
Very strong (vs)	(5.00, 7.00, 9.00)
Fairly strong (fs)	(3.00, 5.00, 7.00)
Slightly strong (ss)	(1.00, 3.00, 5.00)
Equally (E)	(1.00, 1.00, 3.00)
Slightly weak (sw)	(0.20, 0.33, 1.00)
Fairly weak (fw)	(0.14, 0.20, 0.33)
Very weak (vw)	(0.11, 0.14, 0.20)
Absolutely weak (aw)	(0.11, 0.11, 0.14)

**Table 5.** Fuzzy evaluation scores for the alternatives

Linguistic expressions	Fuzzy score
Very poor (VP)	(0.00, 0.00, 1.00)
Poor (P)	(0.00, 1.00, 3.00)
Medium poor (MP)	(1.00, 3.00, 5.00)
Fair (F)	(3.00, 5.00, 7.00)
Medium good (MG)	(5.00, 7.00, 9.00)
Good (G)	(7.00, 9.00, 10.00)
Very good (VG)	(9.00, 10.00, 10.00)

The study consists of the steps of determining the criteria by applying Buckley’s approach, evaluating the significance levels of the criteria relative to each other by experts, and determining the most suitable energy efficiency scenario by using the obtained results. According to the Buckley approach, the FAHP method consists of four steps [46] and [47].

Step 1: Fuzzy pairwise comparison matrix was obtained after pairwise comparison. This pairwise comparison matrix has been created with the data from surveys answered by experts.

This matrix contains the degree of importance between the criteria. An example of a pairwise comparison matrix is as follows:

$$\tilde{A} = \begin{bmatrix} \tilde{d}_{11} & \tilde{d}_{12} & \dots & \tilde{d}_{1n} \\ \vdots & \ddots & & \vdots \\ \tilde{d}_{m1} & \tilde{d}_{m2} & \dots & \tilde{d}_{mn} \end{bmatrix}. \tag{4}$$

Step 2: The geometric mean of each criterion  $i$  is found with the following equation:

$$\tilde{r}_i = \left( \prod_{j=1}^n \tilde{d}_{ij} \right)^{1/n} \quad i = 1, 2, \dots, n. \tag{5}$$

Step 3: The fuzzy weight of the criteria is calculated.

$$\tilde{w}_i = \tilde{r}_i \otimes (\tilde{r}_1 \otimes \tilde{r}_2 \otimes \dots \otimes \tilde{r}_n)^{-1}, \tag{6}$$

where  $lw_i$ ,  $mw_i$ ,  $uw_i$  values are determined,  $lw_i$  the lower weight of the criterion,  $mw_i$  is the middle weight of the criterion, and  $uw_i$  is the top weight of the criterion.

Step 4: Defuzzification of fuzzy numbers  $\tilde{w}_i$ ;

$$M_i = \frac{lw_i + mw_i + uw_i}{3}, \tag{7}$$

where  $M_i$  numbers are normalized with Eq. (7) and the weights of each criterion or alternative ( $N_i$ ) are calculated.

$$N_i = \frac{M_i}{\sum_{i=1}^n M_i}, \tag{8}$$

TOPSIS, a method developed by Hwang and Yoon [48] in 1981, is widely used in multi-criteria decision-making problems. In the TOPSIS method, the ranking is determined according to whether the alternative chosen for the criteria is the closest to the positive ideal solution and the farthest from the negative ideal solution [49]. The algorithm of this method has been created according to the principle that the solution option is the closest to the positive-ideal solution and the farthest from the negative-ideal solution [50]. With the TOPSIS method, the distances to the positive and negative ideal solutions are calculated and ideal and non-ideal solutions are determined. The TOPSIS method consists of six steps:

Step 1: A decision matrix containing the numerical values of the alternatives according to the criteria is created.

$$A_{ij} = \begin{bmatrix} X_{11} & \dots & X_{1j} \\ \vdots & \ddots & \vdots \\ X_{i1} & \dots & X_{ij} \end{bmatrix}, \tag{9}$$

where  $i$  is the number of alternatives,  $j$  is the number of criteria and  $X_{ij}$  is the numerical value of alternative  $i$  according to the  $j$  criterion.

Step 2: Obtaining the normalized decision matrix ( $N_{ij}$ );

$$r_{ij} = \frac{X_{ij}}{\sqrt{\sum_{j=1}^i X_{ij}^2}}, \tag{10}$$

$$N_{ij} = \begin{bmatrix} r_{11} & \cdots & r_{1j} \\ \vdots & \ddots & \vdots \\ r_{i1} & \cdots & r_{ij} \end{bmatrix}, \quad (11)$$

Step 3: Weighted normalized decision matrix ( $V_{ij}$ ) is created by multiplying the weight ( $w_j$ ) of each criterion with the normalized decision matrix.

$$V_{ij} = r_{ij} \cdot xw_{j..} \quad (12)$$

Step 4: Constructing solutions for the positive ideal ( $A^*$ ) and the negative ideal ( $A^-$ );

The maximum and minimum values are calculated for each criterion by Eqs. (13) and (14):

$$A^* = \left\{ (max_i V_{ij} | j \in J), (min_i V_{ij} | j \in J') \right\}, \quad (13)$$

$$A^- = \left\{ (min_i V_{ij} | j \in J), (max_i V_{ij} | j \in J') \right\}, \quad (14)$$

where  $J$  is the benefit (maximization) and  $J'$  is the loss (minimization).

Step 5: Calculation of separation measures: ( $S_i^+, S_i^-$ );

Distances from the positive ideal solution:

$$S_i^+ = \sqrt{\sum_{j=1}^n (v_{ij} - v_j^+)^2}, \quad (15)$$

Distances from the negative ideal solution:

$$S_i^- = \sqrt{\sum_{j=1}^n (v_{ij} - v_j^-)^2}, \quad (16)$$

are calculated.

Step 6: The relative closeness ( $C_i^*$ ) of the alternatives to the ideal solution is calculated:

$$C_i^* = \frac{S_i^-}{S_i^+ + S_i^-}, \quad 0 < C_i^* < 1. \quad (17)$$

Evaluation of  $C_i^*$  is based on its value between 0 and 1. The relative closeness values of the alternatives to the ideal solution are ordered from the largest to the smallest.

This study determined the most suitable scenarios to increase energy efficiency by applying the FAHP and TOPSIS hybrid model, among the multi-criteria decision-making methods. The significance levels of the criteria that are effective in the selection of applied energy efficiency scenarios are analysed with Buckley's approach from fuzzy AHP methods. The weight value showing the importance of each criterion determined by Buckley's approach, one of the FAHP methods, was used in the TOPSIS method to rank the alternatives.

## 2 RESULTS AND DISCUSSION

### 2.1 Validating the Building Energy Model

The monthly measured natural gas consumption values of the building were used to validate the energy model of the reference building with the HAP 5.11 dynamic simulation software, which is widely used and accepted at the project stage, to design an energy efficient building. As a result of the calculation according to ASHRAE Guideline 14 [33], the Coefficient of Variation of the Root Mean Square Error ( $CV_{RMSE}$ ) and the Normalized Mean Bias Error ( $NMBE$ ) were calculated as 10.42 and 3.85 respectively. These values are within the limits recommended in the standard. The mentioned results show that the margins of error in the energy model are acceptable, and the building model can represent the actual building due to its accuracy.

### 2.2 Energy Analysis of the Reference Building

The energy consumption distribution of Erzurum Technical University Faculty of Engineering and Architecture, Turkey showing the average natural gas and electricity consumption for 2017 to 2019 is presented in Table 6. According to these data, the annual total energy consumption of the reference building is 2,857,723.23 kWh. This consumption consists of 76 % natural gas and 24 % electricity.

**Table 6.** Energy consumption distribution of the reference building

Average natural gas and electricity consumption (2017 to 2019)				
Electricity [kWh/year]	Ratio	Natural gas [kWh/year]	Ratio	Annual total energy consumption [kWh]
693,002.50	24 %	2,164,720.73	76 %	2,857,723.23

After converting the actual consumption values into primary energy consumption, the energy consumption data calculated per unit area will be used as a reference in the comparison. The annual total primary energy consumption of the reference building is 3,800,206.63 kWh/year. The share of total primary energy consumption per unit area is 150.54 kWh/m<sup>2</sup> per year. It is observed that this value is much lower than the recommended 450 kWh/m<sup>2</sup> year for education buildings specified in Appendix 4A [23] of the Thermal Insulation Rules in Buildings in force in Turkey and more efficient by 66.6 %.

The type of fuel used in the generation of energy has a significant effect on the quantity of carbon emissions. The total carbon emission calculated

according to the energy consumption amounts of the reference building is 940,364.22 kg CO<sub>2</sub>/year, and the carbon emission per unit area is 37.25 kg CO<sub>2</sub>/m<sup>2</sup>year.

### 2.3 Analyses of Single Energy Efficiency Scenarios

The primary energy consumption and global costs of the scenarios of energy efficiency measures and the reference building are presented in Table 7. While the total primary energy consumption of the reference building was 150.54 kWh/(m<sup>2</sup>year), the primary energy consumption in the lowest S2 scenario achieved with improvements was calculated as 64.83 kWh/(m<sup>2</sup>year) (Table 7). With this scenario, it was possible to save 57 % of primary energy compared to the reference building. Upon evaluating the global costs of the energy efficiency scenarios, the primary energy consumption of scenario S2 was the lowest, although its global cost was the highest. It was observed that the lowest global cost was in scenario S3 (Table 7). The improvement of this scenario compared to the reference building's global cost was 83.6 %.

Global costs and primary energy consumption should be compared simultaneously to determine the cost-optimal energy efficiency scenario. With this analysis, the optimal cost solution and nearly zero-

energy solution are determined among the energy efficiency scenarios. Scenarios S3 and S2 represent the optimal cost and the nearly zero energy level, respectively (Fig. 3). With scenario S3, 11.4 % savings in primary energy and 83.5 % savings in global costs were achieved. Scenario S2, which shows nearly zero energy, was efficient by 57.3% in terms of primary energy and by 37 % in terms of global cost.

**Table 7.** Primary energy consumptions and global costs for energy efficiency scenarios

Scenario	Global cost [\$/m <sup>2</sup> ]	Primary energy consumption [kWh/(m <sup>2</sup> year)]
Reference Building	658.66	150.54
S1	256.35	102.40
S2	414.86	64.83
S3	108.12	133.40
S4	114.57	129.65
S5	317.30	85.37

While the total CO<sub>2</sub> emission of the reference building was 37.25 kg CO<sub>2</sub> m<sup>2</sup>/year, the total CO<sub>2</sub> emission of scenario S2 with the lowest primary energy consumption was calculated as 15.17 kg CO<sub>2</sub> m<sup>2</sup>/year (Fig. 4). It was observed that this scenario emitted 59.3 % less CO<sub>2</sub> than the reference building.

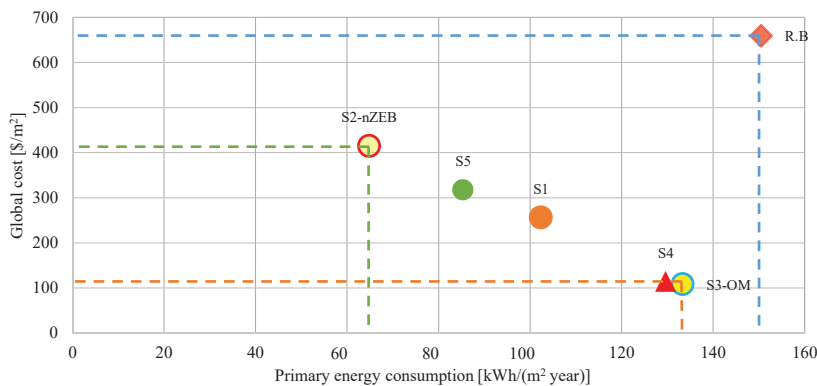


**Fig. 3.** Optimal cost and nearly zero energy levels for single energy efficiency scenarios

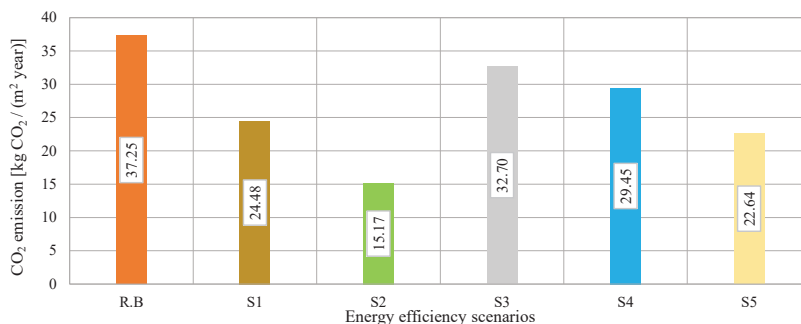


**Fig. 4.** CO<sub>2</sub> emission amounts for single energy efficiency scenarios

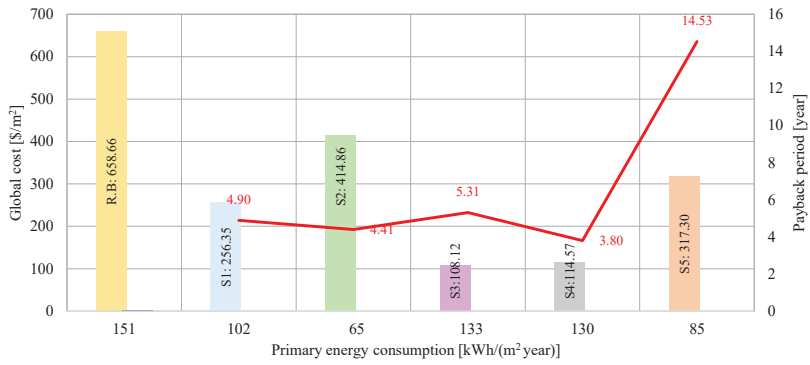


Fig. 5. Primary energy consumption and global costs and payback periods of the single scenarios

It was found that while the payback period of the optimal cost scenario S3 was 5.31 years, the payback period of scenario S2 showing nearly zero energy was 4.41 years (Fig. 5). According to these results, although scenario S3 resulted in the lowest cost, it had the highest primary energy consumption and CO<sub>2</sub> emissions. Although scenario S4 was advantageous in terms of payback period, it was not advantageous in terms of global cost, primary energy consumption, and CO<sub>2</sub> emissions (Fig. 5). When the global costs were analysed, the global costs of optimal cost and nearly zero energy levels all remained below the reference building levels, which indicated that the investments were economically beneficial in addition to energy consumption in the long run.

#### 2.4 Analyses of Mixed Energy Efficiency Scenarios

Among the mixed energy efficiency scenarios, the scenario with the lowest primary energy consumption of 21.69 kWh/m<sup>2</sup> years and the highest global cost of 610.67 \$/m<sup>2</sup> was S2+S3+S4 (Table 8). This scenario

shows the nearly zero energy level (Fig. 6) and saves primary energy by 85.60 % and global cost by 7.3 %. Although this scenario provided minimum energy consumption, it was observed that its cost did not result in minimum cost by moving away from the optimum point, which was due to the higher initial investment cost of the relevant scenario compared to the others.

The lowest global cost was 208.51 \$/m<sup>2</sup> in scenario S3+S4 (Table 7). The improvement of this scenario compared to the reference building's global cost was 68.4 %, indicating the optimal cost solution level (Fig. 6). However, this scenario had the highest primary energy consumption and saved primary energy consumption by 31.7 %.

Among the mixed energy efficiency scenarios, scenario S2+S3+S4 provided the lowest CO<sub>2</sub> emission by 5.08 kg CO<sub>2</sub> m<sup>2</sup>/year (Fig. 7). This mixed energy efficiency scenario had 86.40 % less CO<sub>2</sub> emissions compared to the reference building. It was observed that the amount of carbon emissions decreased in the

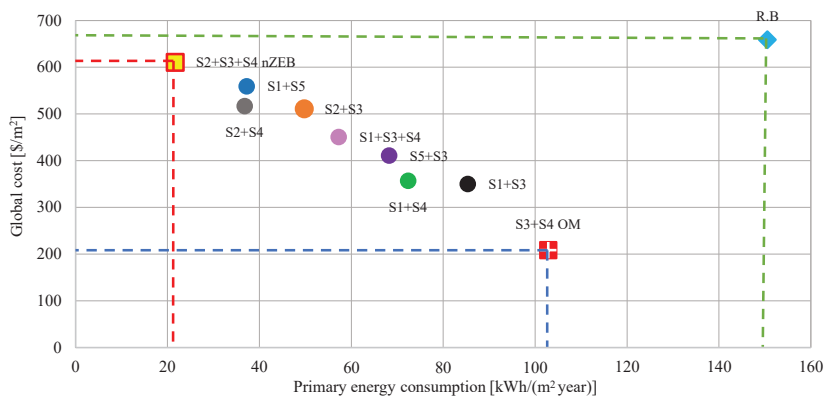


Fig. 6. Optimal cost and nearly zero energy levels for mixed energy efficiency scenarios



reference building at the rate of effective measures to reduce energy consumption.

**Table 8.** Primary energy consumptions and global costs for energy efficiency scenarios

Scenario	Global cost [\$/m <sup>2</sup> ]	Primary energy consumption [kWh/(m <sup>2</sup> year)]
R. B	658.65	150.54
S1+S3	350.28	85.32
S1+S4	356.74	72.36
S2+S3	511.12	49.74
S2+S4	516.93	36.79
S1+S5	559.14	37.22
S5+S3	410.91	68.23
S3+S4	208.51	102.86
S2+S3+S4	610.67	21.69
S1+S3+S4	450.68	57.27

Among the mixed energy efficiency scenarios, the payback period of the scenarios showing the optimal cost solution (S3+S4) and the nearly zero energy level (S2+S3+S4) was the same and determined as 4.41 years (Table 9). The payback period varies depending on annual savings. The ratios of the initial investment costs to the annual savings of scenario S3+S4 and scenario S2+S3+S4 were equal.

**Table 9.** Payback periods of the mixed energy efficiency scenarios

Scenarios	S1+S3	S1+S4	S2+S3	S2+S4	S1+S5
Payback periods (year)	5.01	4.52	4.55	4.27	7.75

Scenarios	S5+S3	S3+S4	S2+S3+S4	S1+S3+S4
Payback periods (year)	10.30	4.41	4.41	4.67

### 2.5 Evaluation of Energy Efficiency Scenarios by the FAHP & TOPSIS Hybrid Method

The determination of the significance level of main criteria and sub-criteria that are effective in the selection of applied energy efficiency scenarios is analysed with Buckley’s approach among FAHP methods. The criteria effective in the preference of energy efficiency increasing scenarios in buildings were determined based on the experiences of experts in the field of energy efficiency and quantitative information based on studies in the literature, rather than subjective and imprecise opinions.

The criteria consist of three main criteria: technical, economic, and environmental. Each main criterion consists of sub-criteria (Table 10).

**Table 10.** Order of sub-criteria

Main criteria	Sub criteria codes	Sub-criteria
Economic (C1)	C11	Global cost
	C12	Return on investment
	C13	Initial investment cost
	C14	Energy unit price
	C15	Economic life of investment
	C16	Real interest reduction
Technical (C2)	C21	Primary energy consumption
	C22	Energy efficiency
Environmental (C3)	C31	Carbon emission

A questionnaire study including the pairwise comparison of sub-criteria was conducted with engineers and academics who were experts in the field of energy efficiency in buildings, and consistency analysis was also performed for the results. Defuzzification was performed for determining the importance weights of the experts in the decisions and

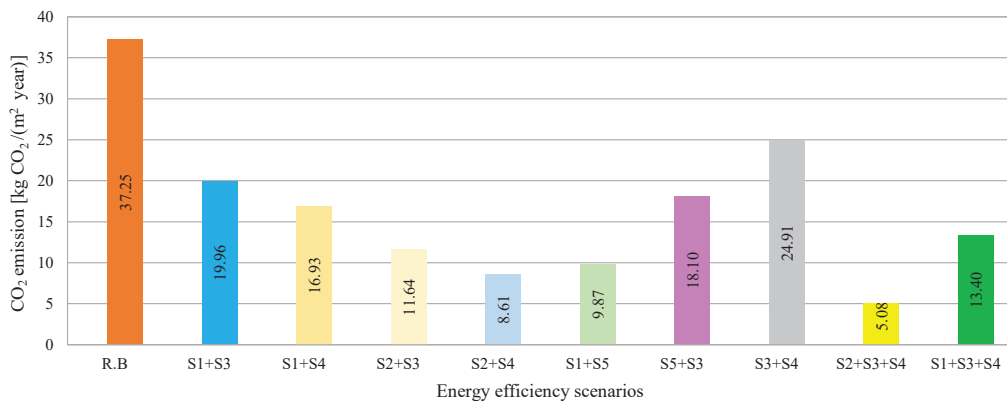


**Fig. 7.** CO<sub>2</sub> emission amounts for mixed energy efficiency scenarios

**Table 11.** Weight values (W) of sub-criteria, best real number value (BNP), and ranking

Main criteria	Sub criteria codes	W	BNP	Ranking		
Economic (C1)	C11	0.167	0.163	0.154	0.162	2
	C12	0.105	0.114	0.117	0.112	4
	C13	0.099	0.105	0.113	0.106	5
	C14	0.120	0.118	0.121	0.120	3
	C15	0.088	0.081	0.080	0.083	7
	C16	0.083	0.072	0.073	0.076	9
Technical (C2)	C21	0.174	0.190	0.180	0.181	1
	C22	0.085	0.080	0.086	0.084	6
Environmental (C3)	C31	0.078	0.076	0.076	0.077	8

for the combined decision matrix to yield meaningful results. To this end, the Best Non-fuzzy Performance (BNP) defuzzification method was employed. In the study, the weight of each criterion was calculated using the FAHP method, and the weights obtained were added to the TOPSIS method to determine the best alternative. Also, the hierarchical structure of the defined MCDM problem is given in Fig. 8.

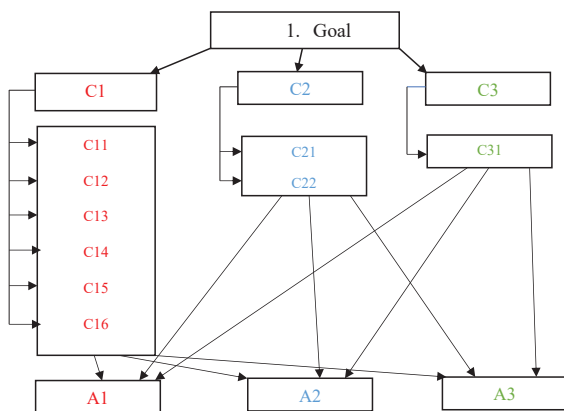


**Fig. 8.** Hierarchical structure of the study

According to the FAHP method, the criteria effective in choosing scenarios were determined in line with the experts' opinions. Considering Table 11, it was observed that criterion C21 (Primary Energy Consumption) was the most effective criterion. Criterion C11 (Global Cost) and criterion C14 (Energy Unit Price) were the second and third effective criteria, respectively. The order of importance of all criteria was obtained as C21> C11> C14> C12> C13> C22> C15> C31> C16.

Alternative scenarios were ranked using the weight value showing the importance of each criterion, which was determined by the FAHP method, in the TOPSIS method. In the ranking of the scenarios implemented to increase the energy efficiency of

the reference building, the distance values from the positive ideal solution and negative ideal solution of each scenario were calculated by creating positive ideal (S<sup>+</sup>) and negative ideal (S<sup>-</sup>) solution sets. The relative closeness of single and mixed scenarios to the ideal solution is shown in Table 12.

**Table 12.** Ideal solution values

Scenarios	C (The degree of proximity)	Ranking	
Single scenarios	S1	0.6156	3
	S2	0.4553	4
	S3	0.7178	2
	S4	0.7480	1
	S5	0.2981	5
Mixed scenarios	S1+S3	0.4981	7
	S1+S4	0.5658	4
	S2+S3	0.4628	8
	S2+S4	0.5950	1
	S1+S5	0.5667	3
	S5+S3	0.3788	9
	S3+S4	0.5202	6
	S2+S3+S4	0.5693	2
	S1+S3+S4	0.5642	5

As a result of using the FAHP-TOPSIS hybrid method, S4 was found to be the most suitable single energy efficiency scenario with a high C value and the closest to the ideal solution by ordering the closeness degrees from the largest to the smallest (Table 12). The scenario that must be in the last place was S5. It was revealed that the most suitable scenario was S2+S4 by ordering the closeness degrees of the mixed energy efficiency scenarios from the largest to the smallest. According to the FAHP-TOPSIS method, while the preference order of single scenarios was calculated as S4>S3>S1>S2>S5, the preference order of the mixed scenarios was calculated as S2+S4>S2+S3+S4>S1+S5>S1+S4>S1+S3+S4>S3+S4>S1+S3>S2+S3>S5+S3

(Table 12). Scenario S3, which provided the optimal cost solution among single scenarios, was the second most suitable scenario. Scenario S2, which showed the nearly zero energy level, was in the last place. In the mixed energy efficiency scenarios, scenario S2+S3+S4, which showed the nearly zero energy level, was the second most suitable scenario. Scenario S3+S4, which provided the optimal cost solution, was among the less suitable scenarios.

### 3 CONCLUSION

This study determined the most advantageous method in obtaining high-performance nZEB-compliant buildings in terms of energy, economy, and carbon emissions at universities located in cold climate regions. To this end, the criteria were prioritized in order to achieve high energy savings in education buildings with intense energy use in cold climate regions. Concerning its results, this study can guide both those who determine the energy policies of countries and those who conduct scientific studies. The results constitute a realistic decision support model in the selection of energy efficiency increasing scenarios in buildings in Turkey.

It was found that an improvement of 57 % to 75.3 % was achieved in the total energy consumption per unit area through the scenarios used to increase the cost-effective energy performance of the green building-certified education building. These results show that there is an energy saving potential even in certified buildings with criteria that prioritize energy efficiency. The use of this potential will contribute to achieving both energy efficiency and economic savings. It was determined that carbon emissions decreased by 59.3 % and 73.6 % by increasing the energy performance of the buildings compared to the reference building. It was lower than the predicted value of the EU, which aims to reduce greenhouse gas emissions by 55 % by 2030. In the EPBD recast, only energy-related costs are considered in the global cost in the definition of energy efficient cost. The life cycle cost and carbon emissions should also be taken into account for a full life cycle assessment of buildings. The results showed that the mixed application of energy efficiency increasing scenarios was more effective in terms of energy efficiency, CO<sub>2</sub> emissions, and payback period.

The most suitable scenarios showing the optimal cost and nearly zero energy levels that brought the buildings closer to nZEB were not the same. It was also revealed that these scenarios differed in terms of both CO<sub>2</sub> emission and payback period. Many

criteria are effective in determining the most suitable energy efficiency scenario according to both national and global developments. It was found that the use of multi-criteria decision-making methods in determining the most suitable energy efficiency increasing scenarios was more effective in terms of the results. According to the opinions of experts with the FAHP & TOPSIS methodology employed in the study, the most important criterion in the selection of scenarios was primary energy consumption. The global cost ranked second, followed by the energy unit price. The experts observed that the rates of increase in interest, inflation, and energy unit prices in the country were effective in determining the effective criteria in the scenario. The findings also demonstrated that the results determined by a hybrid method were consistent and reliable.

The results of this study showed that the use of renewable energy was effective in achieving high savings at nearly zero energy levels. In fact, net energy consumption may be close to zero in some scenarios using renewable energy sources. Thus, it was determined that the use of renewable energy systems was complementary in achieving the European Commission's energy efficiency and carbon emission targets. However, in nearly zero-energy scenarios, global costs may be higher than in other scenarios depending on the renewable energy investment. It should not be forgotten that costs are an important parameter in the decision-making phase when realizing investments.

This study revealed that countries should make a clear definition of country-specific nearly zero-energy building, which prioritizes countries' geographical, cultural, ecological, and economic characteristics without the need for foreign certifications.

### 4 REFERENCES

- [1] European Union (2010). Directive 2010/31/EU of the European Parliament and of the Council of 19 May 2010 on the Energy Performance of Buildings (recast), from <https://eur-lex.europa.eu/LexUriServ/LexUriServ.do?uri=OJ:L:2010:153:0013:0035:EN:PDF>, accessed on 2022-06-12.
- [2] European Union (2018). Directive 2018/844/EU of the European Parliament and of the Council of 30 May 2018 amending Directive 2010/31/EU on the Energy Performance of Buildings and Directive 2012/27/EU on energy efficiency, from <http://data.europa.eu/eli/dir/2018/844/oj>, accessed on 2022-06-12.
- [3] Liu, J., Chen, X., Yang, H., Shan, K. (2021). Hybrid renewable energy applications in zero-energy buildings and communities integrating battery and hydrogen vehicle storage. *Applied Energy*, vol. 290, art. ID 116733, DOI:10.1016/j.apenergy.2021.116733.

- [4] Bodansky, D. (2016). The Paris climate change agreement: a new hope? *The American Journal of International Law*, vol. 110, no. 2, p. 288-319, DOI:10.5305/amerjintelaw.110.2.0288.
- [5] Nature (2021). Net-zero carbon pledges must be meaningful to avert climate disaster (Editorials). *Nature*, vol. 592, no. 2, DOI:10.1038/d41586-021-00864-9.
- [6] Li, D.H.W., Liu, Y., Lam, J.C. (2013). Zero energy buildings and sustainable development implications a review. *Energy*, vol. 54, p. 1-10, DOI:10.1016/j.energy.2013.01.070.
- [7] EIGM Reports (2021). Energy investments, from <https://enerji.gov.tr/eigm-raporlari>, accessed on 2021-12-12. (in Turkish)
- [8] Attia, S., Eleftheriou, P., Xenii, F., Morlot, R., Ménézo, C., Kostopoulos, V., Betsi, M., Kalaitzoglou, I., Pagliano, L., Cellura, M., Almeida, M., Ferreira, M., Baracu, T., Badescu, V., Crutescu, C., Hidalgo-Betanzos, M.H. (2017). Overview and future challenges of nearly zero energy buildings (nZEB) design in Southern Europe. *Energy and Buildings*, vol. 155, p. 439-458, DOI:10.1016/j.enbuild.2017.09.043.
- [9] Wang, Z.X., Zhao, J. (2018). Optimization of passive envelop energy efficient measures for office buildings in different climate regions of China based on modified sensitivity analysis. *Sustainability*, vol. 10, no: 4, p.1-28, DOI:10.3390/su10040907.
- [10] Zhao, J., Du, Y. (2019). A study on energy-saving technologies optimization towards nearly zero energy educational buildings in four major climatic regions of China. *Energies*, vol. 12, no. 24, art. ID 4734, DOI:10.3390/en12244734.
- [11] Sağlam, N.G., Yılmaz, A.Z., Corgnati, S.P. (2017). Sensitivity analyses for cost optimal levels of residential buildings in cold climatic region. *Energy Performance in Buildings Symposium, 13th National Plumbing Engineering Congress*.
- [12] Medrano, M., Martí, J.M., Rincón, L., Mor, G., Cipriano, J., Farid, M. (2018). Assessing the nearly zero-energy building gap in university campuses with a feature extraction methodology applied to a case study in Spain. *International Journal of Energy and Environmental Engineering*, vol. 9, p.227 - 247, DOI:10.1007/s40095-018-0264-x.
- [13] Kalaycıoğlu, E., Yılmaz, A.Z. (2017). A new approach for the application of nearly zero energy concept at district level to reach EPBD recast requirements through a case study in Turkey. *Energy and Building*, vol. 152, p. 680-700, DOI:10.1016/j.enbuild.2017.07.040.
- [14] Valančius, K., Vilutiene, T., Rogoža, A. (2018). Analysis of the payback of primary energy and CO2 emissions in relation to the increase of thermal resistance of a building. *Energy and Buildings*, vol. 179, p. 39-48, DOI:10.1016/j.enbuild.2018.08.037.
- [15] Cunha, F. O., Oliveira, A. C. (2020). Comparison of nZEB indicators for hotel renovations under different European climatic conditions. *International Journal of Low-Carbon Technologies*, vol. 16, no.1, p. 246- 257, DOI:10.1093/ijlct/ctaa059.
- [16] Ferrari, S., Beccali, M. (2017). Energy-environmental and cost assessment of a set of strategies for retrofitting a public building toward nearly zero-energy building target. *Sustainable Cities and Society*, vol. 32, p. 226-234, DOI:10.1016/j.scs.2017.03.010.
- [17] Asdrubali, F., Ballarini, I., Corrado, V., Evangelisti, L., Grazieschi, G., Guattari, C. (2019). Energy and environmental payback times for an NZEB retrofit. *Building and Environment*, vol. 147, p. 461-472, DOI:10.1016/j.buildenv.2018.10.047.
- [18] Liu, Z., Zhou, Q., Yin, H., Xu, W., Yang, X., Gao, J. (2021). Indoor environmental quality and energy consumption real-time assessment: A field measurement of a nearly zero-energy building in cold region of China. *Energy and Buildings*, vol. 246, art. ID 111093, DOI:10.1016/j.enbuild.2021.111093.
- [19] Ongpeng, J.M.C., Rabe, B.I.B., Razon, L.F., Aviso, K.B., Tan, R.R. (2022). A multi-criterion decision analysis framework for sustainable energy retrofit in buildings. *Energy*, vol. 239, art. ID 122315, DOI:10.1016/j.energy.2021.122315.
- [20] Giouri, E.D., Tenpierik, Turrin, M. (2020). Zero energy potential of a high-rise office building in a Mediterranean climate: Using multi-objective optimization to understand the impact of design decisions towards zero-energy high-rise buildings. *Energy and Buildings*, vol. 209, art. ID 109666, DOI:10.1016/j.enbuild.2019.109666.
- [21] U.S. Green Building Council (2022). LEED-certified green buildings are better buildings, from <https://www.usgbc.org/leed>, accessed on 2022-06-07.
- [22] LEED certification (2014). Information and Documents About LEED, from [http://www.xn--leedsertifikas-jgc.com/leed-v4-\(2014\).html](http://www.xn--leedsertifikas-jgc.com/leed-v4-(2014).html), accessed on 2022-07-07.
- [23] TS 825 (2013). Thermal insulation requirements for buildings, Turkish Standardization Institute, Ankara. (in Turkish)
- [24] ASHRAE 90.1-2007. (2007). *Energy Standard for Buildings Except Low-Rise Residential Buildings*, American Society of Heating, Refrigerating and Air-Conditioning Engineers, Atlanta.
- [25] ANSI/ASHRAE standard 62.1 (2013). *Ventilation for Acceptable Indoor Air Quality*. American Society of Heating, Refrigerating and Air-Conditioning Engineers, Atlanta.
- [26] Koca, Ö. (2006). *An Approach For Determining Energy Efficient Settlement And Building Design Principles In Hot Dry And Hot Humid Climate Zones*. MSc. Thesis, Istanbul Technical University Faculty of Architecture, Istanbul.
- [27] Bakırcı, K., Özyurt, Ö., Yılmaz, M., Erdoğan, S. (2006). Climate and Meteorology Data for Erzurum Province Energy Studies. *Climate and Meteorology Data for Erzurum Province Energy Studies*, vol. 95, p. 19-26. (in Turkish)
- [28] Ministry of Environment, Urbanization and Climate Change, General Directorate of Meteorology (2022). <https://www.mgm.gov.tr/FILES/resmi-istatistikler/parametreAnalizi/2022-yillik-gunes-radyasyonu.pdf>, accessed on 2022-06-115. (in Turkish)
- [29] Weather Spark (2022). Climate in Erzurum region, from <https://tr.weatherspark.com/y/102045/Erzurum>, accessed on 2022-09-07.
- [30] Turkish green building council (CEDBIK) (2013). *Green Building Certification Guide for New Houses*. Ankara
- [31] ISO 52016-1 (2017). Energy performance of buildings - Energy needs for heating and cooling, internal temperatures and sensible and latent heat loads - Part 1: Calculation procedures, from <https://standards.iteh.ai/catalog/standards/iso/923e198d-1636-4616-b426-54fa1e28eb7e/iso-52016-1-2017>, accessed on 2021-09.10.

- [32] DIN EN 15459-1 (2017). Energy performance of buildings - Economic evaluation procedure for energy systems in buildings - Part 1: Calculation procedures, Module M1-14, from <https://www.en-standard.eu/din-en-15459-1-energy-performance-of-buildings-economic-evaluation-procedure-for-energy-systems-in-buildings-part-1-calculation-procedures-module-m1-14>, accessed on 2021-09-20.
- [33] ASHRAE (2014). *ASHRAE Guideline 14: Measurement of Energy, Demand, and Water Savings*, Atlanta.
- [34] Ruiz, G.A., Bandera, C.F. (2017). Validation of calibrated energy models: Common errors. *Energies*, vol. 10, no. 10, art. ID 1587, DOI:10.3390/en10101587.
- [35] CEN/TR 15459-2 (2017). *Energy Performance of Buildings - Economic Evaluation Procedure for Energy Systems in Buildings*, European Committee for Standardization (CEN), Brussels.
- [36] Ministry of Environment, Urbanization and Climate Change (2021). Guide to Energy Efficient Renovation of Public Buildings, from <https://meslekihizmetler.csb.gov.tr/kamubinalarinin-enerji-verimli-yenilemesine-yonelik-rehber-i-99595>, accessed on 2021-08-05. (in Turkish)
- [37] Ministry of Environment, Urbanization and Climate Change (2021). <https://webdosya.csb.gov.tr/db/yfk/icerikler/bf-2021-turkce-20210809122111.pdf>, accessed on 2021-08-05. (in Turkish)
- [38] Central Bank of Turkey (2021). Indicative Exchange Rates, from <https://www.tcmb.gov.tr/kurlar/202106/29062021.xml>, accessed on 2021-06-29.
- [39] TurkStat (2021). Consumer Price Index, from <https://data.tuik.gov.tr/Bulten/Index?p=Tuketici-Fiyat-Endeksi-Mayis-2021-37383>, accessed on 2021-06-29.
- [40] Central Bank of the Republic of Turkey Administrative Center (2021). Press Release on Interest Rates (2021-21) from <https://www.tcmb.gov.tr/wps/wcm/connect/tr/tcmb+tr/main+menu/duyurular/basin/2021/duy2021-21>, accessed on 2021-06-17. (in Turkish)
- [41] Palen (2021). From <https://www.palen.com.tr/evsel-musteri/satis-tarifeleri>, accessed on 2021-05-31. (in Turkish)
- [42] Turkish Statistical Institute (2021). <https://data.tuik.gov.tr/Bulten/Index?p=Elektrik-ve-Dogal-Gaz-Fiyatlari-II.-Donem:-Temmuz-Aralik-2021-45566>, accessed on 2021-05-31.
- [43] Harker, P.T., Vargas, L.G. (1987). The theory of ratio scale estimation: Saaty's analytic hierarchy process. *Management Science*, vol. 33, no. 11, p. 1383-1403, DOI:10.1287/mnsc.33.11.1383.
- [44] Demirel, H., Şener, B., Yildiz, B., Balin, A. (2020). A real case study on the selection of suitable roll stabilizer type for motor yachts using hybrid fuzzy AHP and VIKOR methodology. *Ocean Engineering*, v. 217, p. 108125, DOI:10.1016/j.oceaneng.2020.108125.
- [45] Balin, A., Demirel, H., Alarcin, F. (2015). A hierarchical structure for ship diesel engine troubleshooting problem using fuzzy AHP and fuzzy VIKOR hybrid methods. *Shipbuilding*, vol. 66, no. 1, p. 54-65.
- [46] Buckley, J.J. (1985). Fuzzy hierarchical analysis. *Fuzzy Sets and Systems*, vol. 17, no. 3, p. 233-247, DOI:10.1016/0165-0114(85)90090-9.
- [47] Hwang, C.L., Yoon, K. (1981). Methods for Multiple Attribute Decision Making. *Multiple Attribute Decision Making. Lecture Notes in Economics and Mathematical Systems*, vol. 186, Springer, Berlin, Heidelberg, DOI:10.1007/978-3-642-48318-9\_3.
- [48] Afonso, P., Cunha, J. (2009). Determinants of the use of capital investment appraisal methods: evidence from the field. *European Applied Business Research Conference*.
- [49] Chen, C. (2000). Extensions of the TOPSIS for group decision-making under fuzzy environment. *Fuzzy Sets and Systems*, vol. 114, no. 1, p. 1-9, DOI:10.1016/S0165-0114(97)00377-1.
- [50] Li, H., Adeli, H., Sun, J., Han, J.-G. (2011). Hybridizing principles of TOPSIS with case-based reasoning for business failure prediction. *Computers and Operations Research*, vol. 38, no. 2, p. 409-41, DOI:10.1016/j.cor.2010.06.008.



# The Dynamic Behaviour of Symmetrical Laminated Nano-composite Containing Equal Numbers of Glass and Carbon Fibre Layers

Ava A.K. Mohammed\* – Gailan Ismail Hassan – Younis Khalid Khdir

Erbil Polytechnic University, Erbil Technical Engineering College,  
Department of Technical Mechanical and Energy Engineering, Erbil 44001, Iraq

*Fibre-reinforced polymer composite has many uses in structural components that required high strength, stiffness, and damping capacity. Cross and quasi-laminated epoxy composites with and without nano  $Al_2O_3$  were used in this investigation to determine flexural modulus, natural frequency, damping ratio, and mode shapes by using analytical, experimental, and numerical (ANSYS) methods. It was demonstrated that adding 2 % nano  $Al_2O_3$  improved the flexural modulus and the damping ratio while decreased the natural frequency. Cross number 2 and quasi number 2 had the highest natural frequency for cross and quasi laminate groups which are equal to 23.5 Hz and 20.25 Hz experimentally, respectively. On the other hand, the higher damping ratio was achieved for cross number 1 with nano  $Al_2O_3$  and quasi number 2 with nano  $Al_2O_3$  for both cross and quasi laminates, which are equal to 0.707 % and 0.693 %, respectively. The flexural modulus and damping ratio are inversely related to each other. However, the novelty in this article is that by adding two glass plies at the outer surface of quasi group laminate the flexural modulus, natural frequency, and damping ratio are increased simultaneously, as in the configurations quasi number 2 and quasi number 2 with nano  $Al_2O_3$  in comparison with quasi number 1 and quasi number 1 with nano  $Al_2O_3$ .*

**Key words:** cross laminate, quasi laminate, natural frequency, damping ratio, nano $Al_2O_3$

## Highlights

- Adding 2 % nano  $Al_2O_3$  decreases natural frequency and increases damping capacity and flexural modulus.
- Adding two glass plies at the outer surface of all laminated composite increases flexural modulus and natural frequency, but the damping ratio is also increased jointly in the quasi-laminated group.
- Comparison between analytical, experimental, and numerical natural frequency for eight configurations of laminated composites.

## 0 INTRODUCTION

Multifunctional fibre-reinforced laminated polymer composites have been utilized in recent decades in structural applications, including automobiles, shafts, aircraft, bicycle frames, and tennis rackets, due to their superior properties, such as low density (low weight), high strength, high stiffness, and high damping capacity. The vibration energy dissipation of fibre-reinforced polymer composite (FRPC) can be achieved via increasing its viscoelastic behaviour [1]. FRPC damping capacity can be enhanced by increasing the numbers of interfacial regions, either by adding fibres or nano-fillers to its viscoelastic matrix, which then causes the vibrating energy to be dissipated by friction between the matrix and reinforcement. Hybridization is one of the means to increase the damping capacity of FRPC by adding high elongation to low elongation fibres [2] and [3].

Natural frequency and damping ratio represent the dynamic behaviour of materials. Glass and carbon fibres are widely use in structural applications. Researchers [4] to [8] have illustrated that the carbon fibre has a higher natural frequency than glass fibre

due to the high bending modulus value of carbon fibre in a polymer matrix. In contrast, glass fibre has a higher damping ratio than carbon fibre in a polymer matrix, as shown in Table 1. The mechanical and dynamic properties of materials are related to each other. Zhang et al. [9] and Swolfs et al. [10] illustrated that a laminated fibre composite with equal numbers of glass and carbon fibres gives the best flexural strength and modulus. The high flexural modulus and low strain to failure carbon fabric is added to the low flexural modulus and high strain to failure glass fabric in order to benefit from the advantages of each ingredient and exclude the disadvantages of them. The natural frequency is related to the flexural modulus of the materials, increased with increasing flexural modulus, while the damping ratio is inversely related to the bending modulus. In order to increase interfacial boundary regions, nano-filler is added to the epoxy matrix of interply (G+C) hybrid fibre-reinforced composite, so that more friction will occur when it vibrates; consequently, the damping ratio is increased.

Zhang et al. [11] investigated the tensile properties and damping characteristics in both

vacuum and air environments of nine conditions of E-glass/polyurethane laminate composites by changing glass volume fraction ( $V_f$ ) 50 %, 55 %, 60 % and angle of orientation 0°, 45°, and 90°. They deduced that the best damping capacity was for lower glass ( $V_f$ ) with a greater angle of orientation, which leads to lower tensile strength. The damping capacity in air is higher compared to that in vacuum for the same laminate. Navaneeth et al. [12] studied the tensile, flexural, and damping properties of woven glass/epoxy laminated composites with three different glass volume fractions: 50 %, 60 %, and 70 %. From collected experimental data, they found that the laminate with 60 % glass ( $V_f$ ) obtained the best tensile and flexural properties (strength and stiffness), while the laminate with 70 % glass ( $V_f$ ) obtained the highest natural frequency and lowest damping ratio. Hossein et al. [13] researched the effect of adding 1 %, 2 %, 3 %, 5 %, and 7 % nano clay filler to 12-layer woven glass laminated epoxy composite and concluded that increasing the weight percentage of nano-filler to 5 % increased the natural frequency; after that, it decreased, but the damping ratio increased to 7 %. Khahaba [14] researched the impact of adding 1.5 % nano SiC and 1.5 % nano Al<sub>2</sub>O<sub>3</sub> on the damping properties of quasi-isotropic laminates with two stacking sequences [0/±45/90] and [90/±45/0]. They proved that the highest damping capacity is obtained for the second stacking configuration with and without nano glass/epoxy composite because the 90° first layer reduces the stiffness of the composites. Pujar et al. [15] examined the effect of introducing 0.1 %, 0.5 %, and 1 % nano-graphene oxide on the damping properties of glass/epoxy composite by utilizing 0° and 45° fibre orientation and two boundary conditions (cantilever and free). They found that adding nano-GO improves damping capacity, whereas 0.5 % GO gives the highest damping ratio. Increasing the angle of fibre orientation between 0° and 45° leads to decrease natural frequency and increase damping ratio for cantilever boundary condition and vice versa for free condition.

**Table 1.** Comparative dynamic behaviour of glass and carbon fibre reinforced polymer composite [4] to [7]

FRPC	Natural frequency [Hz]	Damping ratio [%]
CFRPC	High	Low
GFRPC	low	High

Researchers [4] to [8], [16] to [19] investigated the mechanical and dynamic behaviour of hybrid glass/carbon laminated composite. Murrugan et al.

[4] concluded that the presence of carbon fibre in the middle of the laminated composite H1[GCCG] increases tensile strength, tensile modulus, and damping ratio, while the presence of carbon fibre in the outer surface of the laminated composite H2[CGGC] increases flexural strength, flexural modulus, and natural frequency for (50 % carbon: 50 % glass) fibre addition. Suman et al. [5] found that the interply hybridization of equal numbers of glass and carbon fibre in laminated composite affects the dynamic properties. As a result, the arrangement GC1[G/C/G/C/G/C/G/C]<sub>s</sub> has a natural frequency of 46 Hz and a damping ratio of 0.095. In contrast, altering the arrangement by putting the carbon fibre on the external surface for the arrangement CC1[C/G/C/G/C/G/C/G]<sub>s</sub> will slightly reduce both the natural frequency and damping ratio to 45 Hz and 0.088, respectively. Pujar et al. [6] investigated the tensile and dynamic properties for laminated composite that is fabricated from 80 % glass and 20 % carbon. They found that H3[G/G/G/G/C]<sub>s</sub> has maximum tensile strength and modulus because of the presence of one carbon ply in the middle of the laminate. The dynamic properties were accumulated for free FFFF and cantilever CFFF boundary conditions. In the FFFF condition, a higher natural frequency was found in H1[C/G/G/G/G]<sub>s</sub> hybrid condition in the presence of one carbon fibre at the outer surface of the laminate. On the other hand, higher damping ratio was found in H3 hybrid condition in the presence of one carbon fibre in the middle of the laminate. In the CFFF condition, the natural frequency and damping ratio dropped in comparison with FFFF, with the higher natural frequency for first hybrid condition H1, while the higher damping ratio for H2[G/G/C/G/G]<sub>s</sub> condition in which one carbon fibre is present after two glass fibres from the outer surface. Adyin et al. [7] predicted the dynamic properties for non-hybrid, interlayer, and intralayer hybrid composites for carbon, glass, and aramid fibre reinforced in an epoxy matrix and taking the angle of orientation, stacking sequence, and number of plies into consideration. They found the best arrangement of fibres for higher dynamic properties by using the Taguchi program. Karthik et al. [16] investigated the damping properties of E-glass chopped mat/woven carbon hybrid with four different volume fractions in epoxy matrix and polyester matrix. They demonstrated that the damping capacity increased with increasing glass volume fraction for both matrices; furthermore, the addition of 5 % carbon fibre gave the best damping behaviour and natural frequency for structural composite. Utomo et al. [17] studied the effect of increasing carbon layers and its

position in eight-layer hybrid glass/carbon laminated unsaturated polyester composite and concluded that with increasing numbers of carbon layers near the outer surface of the laminate, the natural frequency increased and damping capacity ( $\xi$ ) decreased. In contrast, by positioning carbon layers toward the centre of the laminate, the natural frequency decreased while the damping capacity increased. Finally, the natural frequency and flexural stiffness are directly proportional to each other. Singh et al [18] studied the effect of stacking sequence and angle of orientations on the natural frequency and damping ratio of four-layer glass/carbon epoxy laminates and found that the laminate  $[0c/90g]_s$  acquired the highest natural frequency, while  $[90c/0g]_s$  obtained the lowest one. The highest damping ratio is attained for both laminates  $[90g/90c]_s$  and  $[90c/90g]_s$ , while the laminate  $[0c/0g]_s$  obtained the lowest damping ratio. Pingulkar et al. [19] utilized ANSYS software package to evaluate natural frequency and mode shapes of eight-layer glass/carbon hybrid laminated cantilever plates and concluded that important change in natural frequency can be obtained by hybridization, change of angle of orientation, and stacking sequence more than change in volume fraction. Bulut et al. [20] inspected the effect of adding Kevlar fibre into the glass fibre in hybrid laminated epoxy composite with various hybrid ratios through tensile and damping tests. They deduced that H4 (G2K8) had maximum tensile strength and maximum damping capacity; both factors improved, by 124 % and 145 %, respectively, in comparison with glass/epoxy laminate. Alsaadi et al. [21] studied the effect of adding (0.5 %, 1 %, 1.5 %, 2.5 % and 3%) nano-SiO<sub>2</sub> on the tensile, flexural, and damping properties of carbon/Kevlar intraply hybrid epoxy composite. They obtained that the highest tensile modulus and flexural modulus are at 0.5 % nano SiO<sub>2</sub>, while the highest tensile strength and flexural strength at 3 % and 1.5 % nano SiO<sub>2</sub>, respectively. The flexural modulus and natural frequency are directly related to each other. Therefore, the highest natural frequency at 0.5 % nano-silica which gave 20.5 % improvement, while the damping capacity (damping ratio) decreased by 37 %. Fairlie and Njuguna [22] investigated the impact of stacking sequence and angle of orientation on the tensile and damping capacity of interply hybrid carbon/flax epoxy laminated composite and attained that the outer layer in the laminate is the important layer to control the damping capacity of the laminate. By adding one flax layer at the exterior of the carbon/epoxy laminate, the damping ratio increased by 53.6 % and by adding two flax layers, it increased by 94 %. Alexander et al. [23] studied the effect of boundary

conditions, material properties, and laminate thickness on the natural frequency of glass/epoxy and basalt/epoxy laminated composite and reached to the conclusion that the damping capacity of basalt/epoxy composite is higher than that for glass/epoxy composite. Erkliđ, et al. [8] inspected the dynamic behaviour of interply FRPC by using carbon, Kevlar, and glass fibres and determined that  $[(0G/90G)3]_s$  and  $[(0C/90C)3]_s$  had minimum and maximum natural frequencies, respectively. The laminates  $[(0C/90C)3]_s$  and  $[(0K/90K)3]_s$  had the minimum and maximum damping capacity, respectively. To increase natural frequency, add higher stiffness fibre at the outer surface, like carbon; however, to increase the damping ratio of the structure, add higher viscoelastic fibre at the surface like Kevlar. Hybrid  $[(0C/90C)/(0K/90K)/(0G/90G)]_s$  had the maximum natural frequency compared to other hybrids, and the  $[(0/90)3]_s$  fibre orientation had the maximum natural frequency compared to other orientations. Moreover, [24] showed that the large cut-out size decreases the natural frequency, while the small cut-out size had a trivial effect on the natural frequency. Bulut et al. [25] investigated the influence of adding S-glass interply to woven carbon-aramid intraply on the natural frequency and found that higher natural frequency can be obtained by positioning glass in the middle and (C+A) at the outer surface of the laminate, where the configuration  $[CA2G2]_s$  had the highest natural frequency. Kröger et al. [26] increased the damping capacity of unidirectional carbon fibre/epoxy laminate by adding vectran, aramid, and cellulose in intraply form. In contrast, tensile, flexural strength, and stiffness were reduced.

SenthamaraiKannan and Ramesh [27] decided to increase the damping capacity of woven carbon laminated structure by adding 11 % nano SiO<sub>2</sub> with 9 % micro CTBN rubber to the epoxy matrix, despite the slight drop in tensile and flexural modulus. Bulut et al. [28] investigated the dynamic behaviour of basalt/epoxy laminated composite by adding (0.1, 0.2, and 0.3) nano-graphene and determined that 0.1 % and 0.2 % of nano-pellets increased the natural frequency and damping ratio, but 0.3 % decreased both of them.

According to the above literature review, it is clear that increasing flexural modulus is accompanied by increasing the natural frequency and decreasing the damping ratio. One way to increase flexural modulus is by adding equal numbers of glass and carbon fibre layers to the composite matrix and then rearranging them to obtain a higher damping capacity. Another way to increase flexural modulus and damping

capacity is by adding nearly 2 % nano-filler to the matrix of fibre-reinforced polymer composite.

The aim of this investigation is to increase flexural modulus, natural frequency, and damping capacity simultaneously by using a new special arrangement of glass and carbon fibres that are different from the cited studies and by adding 2 % nano Al<sub>2</sub>O<sub>3</sub> to the epoxy matrix of G/C hybrid composite. Eight configurations for eight layers of glass/carbon epoxy laminated composite with and without nano Al<sub>2</sub>O<sub>3</sub> were fabricated. Analytical, experimental, and numerical (ANSYS) methods were used to evaluate the flexural modulus, natural frequencies, damping ratio, and shape modes, in addition to compare between them.

### 1 ANALYTICAL WORK

Knowledge of the dynamic properties of FRPC is just as important as that of the static ones. It is suitable to utilize static stiffness to estimate the natural frequency of laminated composite [2]. Classical laminate plate theory (CLPT) was used to evaluate the theoretical flexural modulus and fundamental natural frequency for all laminates (shown in Table 2) by using the mechanical properties for unidirectional glass and carbon fibres with and without nano-Al<sub>2</sub>O<sub>3</sub> (shown in Table 3).

The flexural stiffness matrix and theoretical flexural modulus for each laminate can be calculated by using Eqs. (1) and (2) [29].

$$D_{ij} = \frac{1}{3} \sum_{k=1}^n [(Q_{ij})_k] (h_k^3 - h_{k-1}^3), \quad (1)$$

$$E_b = \frac{12}{h^3 D_{11}^*}. \quad (2)$$

**Table 2.** Stacking sequence G: C configuration of hybrid laminated epoxy composite

Symbol	Laminates	Stacking sequences	Hybrid ratio G:C
C1	Cross no. 1	[G0/C90/C0/G90] <sub>s</sub>	4:4
C1WN	Cross no. 1 with nano Al <sub>2</sub> O <sub>3</sub>	[G0/C90/C0/G90] <sub>s</sub>	4:4
C2	Cross no. 2	[G0/G90/C0/C90] <sub>s</sub>	4:4
C2WN	Cross no. 2 with nano Al <sub>2</sub> O <sub>3</sub>	[G0/G90/C0/C90] <sub>s</sub>	4:4
Q1	Quasi no. 1	[G0/C90/C45/G-45] <sub>s</sub>	4:4
Q1WN	Quasi no. 1 with nano Al <sub>2</sub> O <sub>3</sub>	[G0/C90/C45/G-45] <sub>s</sub>	4:4
Q2	Quasi no. 2	[G0/G90/C45/C-45] <sub>s</sub>	4:4
Q2WN	Quasi no. 2 with nano Al <sub>2</sub> O <sub>3</sub>	[G0/G90/C45/C-45] <sub>s</sub>	4:4

Table 4 demonstrates the [D] matrix, theoretical flexural modulus E<sub>b</sub>, and fundamental natural

frequency ωn for all laminated epoxy composites. The fundamental frequency is the smallest frequency for the structure; for the case of a cantilever beam, ωn can be calculated from Eq. (3) [30]

$$\omega n = \frac{1}{2\pi} \left( \frac{1.875}{l} \right)^2 \sqrt{\frac{E_b I_{yy}}{\rho A}}. \quad (3)$$

**Table 3.** The mechanical properties of unidirectional glass and carbon with and without nano alumina

Laminates	Density [kg/m <sup>3</sup> ]	E <sub>1</sub> [MPa]	E <sub>2</sub> [MPa]	ν <sub>12</sub>	G <sub>12</sub> [MPa]
UD glass/epoxy	1658	31802	12804	0.22	4271
UD carbon/epoxy	1484	99438	6273	0.25	4031
UD glass/epoxy Al <sub>2</sub> O <sub>3</sub>	1883	33507	13344	0.27	4500
UD carbon/epoxy Al <sub>2</sub> O <sub>3</sub>	1574	105044	6626	0.3	4260

The results in Table 4 show that cross-laminate has higher flexural modulus than quasi-laminate, similar to the results of [7] and [17]. It is apparent that C2WN and Q2WN laminates have maximum flexural modulus E<sub>b</sub> in the cross and quasi groups, respectively. In spite of the presence of two glass layers on the exterior of both laminates, it is in contrast with the results of [16] because of the effect of element Q11, Q12, and Q66 in [Q<sub>ij</sub>] matrix of the 90° glass layer. By adding 2 % nano Al<sub>2</sub>O<sub>3</sub>, the natural frequency for all laminates slightly dropped despite the increase in flexural modulus, similar to the results of research [14]. The maximum natural frequency had been obtained for C2 in the cross-group, while in the quasi-group, Q2 had the maximum natural frequency.

### 2 EXPERIMENTAL

#### 2.1 Materials

The matrix material used in this study is the laminating epoxy resin MGS L285 with hardener H285 in a 100:40 mixing ratio (resin: hardener), for which the density for resin and hardener are equal to 1.18 g/cm<sup>3</sup> to 1.23 g/cm<sup>3</sup> and 0.94 g/cm<sup>3</sup> to 0.97 g/cm<sup>3</sup> respectively, while the viscosity for them is equal to 600 mPa·s to 900 mPa·s and 50 mPa·s to 100 mPa·s, respectively. Unidirectional carbon and E-glass fabric were used as fibre reinforcement with weights equal to 300 g/cm<sup>2</sup> and 330 g/cm<sup>2</sup>, respectively. Both the matrix and fibre were supplied by the DOST KIMYA Company, Turkey. Finally, spherical aluminium oxide (Al<sub>2</sub>O<sub>3</sub>) nano-powder/nano-particle with a size of 48 nm, which was used as a filler reinforcement, was supplied by Nanografi Nanotechnology Company, Turkey.



**Table 4.** Flexural stiffness matrix, theoretical flexural modulus  $E_b$ , and fundamental natural frequency  $\omega_n$

Laminates	Flexural stiffness matrix [D] [Pa·m <sup>3</sup> ]	Theoretical flexural modulus, $E_b$ [GPa]	Fundamental natural frequency, $\omega_n$ [Hz]
C1	$\begin{bmatrix} 21.2 & 1.56 & 0 \\ 1.56 & 25.6 & 0 \\ 0 & 0 & 2.78 \end{bmatrix}$	31.6	23.254
C1WN	$\begin{bmatrix} 22.46 & 2.01 & 0 \\ 2.01 & 27.05 & 0 \\ 0 & 0 & 2.94 \end{bmatrix}$	33.5	22.75
C2	$\begin{bmatrix} 22.43 & 1.81 & 0 \\ 1.81 & 12.95 & 0 \\ 0 & 0 & 2.83 \end{bmatrix}$	33.3	23.78
C2WN	$\begin{bmatrix} 23.79 & 2.33 & 0 \\ 2.33 & 13.71 & 0 \\ 0 & 0 & 2.98 \end{bmatrix}$	35.1	23.29
Q1	$\begin{bmatrix} 16.21 & 3.21 & 1.65 \\ 3.21 & 27.26 & 1.65 \\ 1.65 & 1.65 & 4.43 \end{bmatrix}$	23.0	19.78
Q1WN	$\begin{bmatrix} 17.24 & 3.74 & 1.75 \\ 3.74 & 28.83 & 1.75 \\ 1.75 & 1.75 & 4.66 \end{bmatrix}$	24.4	19.42
Q2	$\begin{bmatrix} 17.7 & 3.62 & 1.46 \\ 3.62 & 14.07 & 1.46 \\ 1.46 & 1.46 & 4.64 \end{bmatrix}$	24.75	20.52
Q2WN	$\begin{bmatrix} 18.8 & 4.23 & 1.55 \\ 4.23 & 14.91 & 1.55 \\ 1.55 & 1.55 & 4.88 \end{bmatrix}$	26.0	20.05

**2.2 Laminates Manufacturing**

In this investigation, four hybrid glass/carbon laminates were used without nano-particles and the other four with it. The 2 % nano Al<sub>2</sub>O<sub>3</sub> were added to epoxy matrix by using dual mixing method, which includes both ultrasonic vibration and magnetic stirring mixing simultaneously. After that, the bubbles produced are removed by degassing the suspension mixture. The glass and carbon fibre fabrics were cut

into the required angles and dimensions, and then arranged according to the design stacking sequence in order to start the vacuum assisted resin infusion method (VARIM) by drawing the epoxy mixture into the closed system of arranged fibres and VARIM accessories [31]. A flow chart for the purpose of each fabrication stages is shown in Fig. 1.

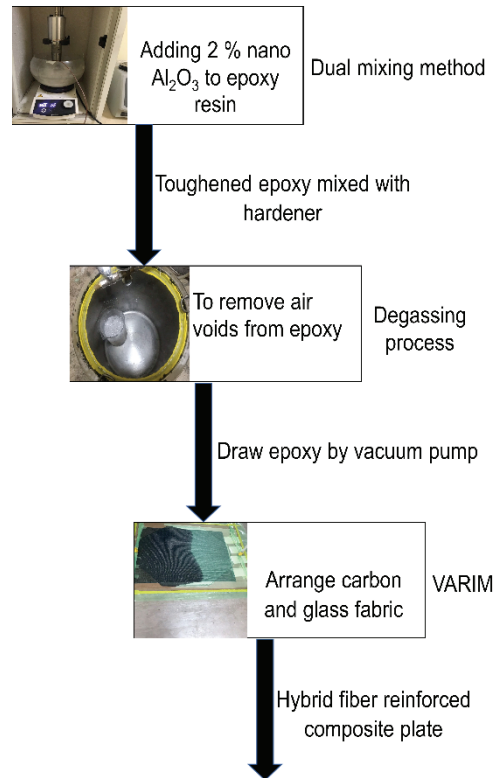


**Fig. 1.** Stages of laminated composite fabrication

**2.3 Free Vibration Test**

The dynamic properties of FRPC beam with dimensions are 250 mm length × 25 mm width and 2 mm thickness; they were measured by using the experimental set up shown in Fig. 2, which consist of the following apparatuses. Firstly, an impact hammer transducer was used to excite an impulsive force and measure it at the midpoint of the beam (Brüel & Kjær, type 8206). Secondly, a piezoelectric accelerometer was used to measure the vibration response of the excited beam (Brüel & Kjær, type 4507 B30515) positioned at the free end of the beam. Finally, the both hammer and accelerometer were connected to the Brüel & Kjær controller modules type 7539A, 5-channels, in order to analyse the collected data by using fast Fourier transform (FFT) Analyzer to obtain



the dynamic response of the free vibration test, in terms of time domain and frequency domain.

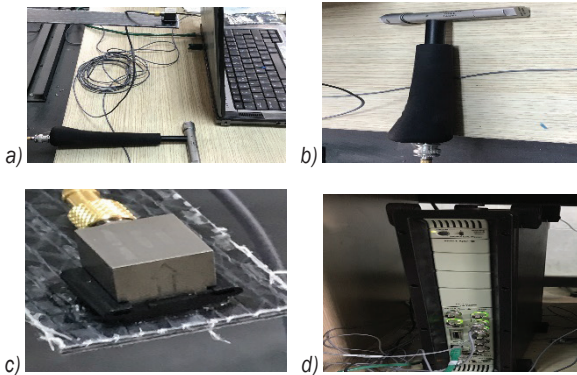


**Fig. 2.** Free vibration test set up and its parts; a) free vibration set up, b) impact hammer, c) accelerometer sensor, and d) blank module

Due to FRPC beam free vibration, the dynamic behaviour of the glass/carbon epoxy laminated composite can be found in terms of time domain (displacement-time envelope) and frequency domain (acceleration-frequency envelope). The original aspect of this paper is that the frequency response is neither represented in terms of input impulsive force with respect to frequency nor within output acceleration with respect to frequency; the new representation was in terms of output over input (acceleration/impulsive force) in the y-axis against the frequency in the x-axis, as shown in Fig. 3. The red cursor position in Fig. 3 represents the resonant frequency, for the range of frequency is between 0 Hz and 30 Hz, as represented by the critical frequency for the laminates and not necessarily the maximum frequency. If the laminate is subjected to force with excited frequency equal to this

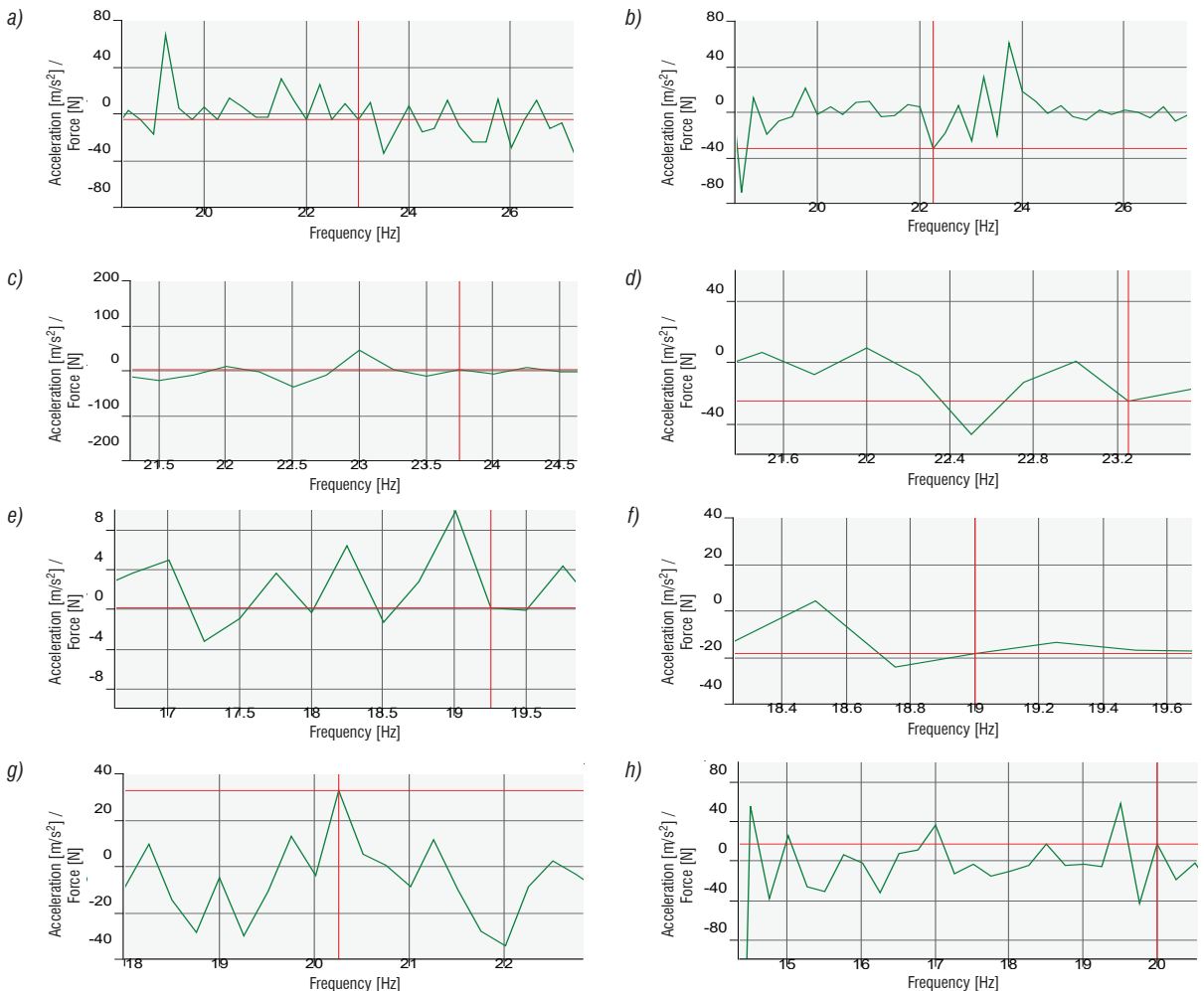


**Fig. 3.** Frequency responses of laminated epoxy composites with and without nano  $Al_2O_3$ ; a) C1, b) C1WN, c) C2, d) C2WN, e) Q1, f) Q1WN, g) Q2, and h) Q2WN

resonance frequency, then the amplitude of vibration pulse will be magnified and cause failure and presence of crack in the same laminate. The dynamic responses of all laminates are illustrated in Fig. 4 in terms of time domain. The number of peaks for cross- and quasi-group vibration response to a 400 ms time are 5 and 4 peaks respectively; this is due to the increase of natural frequency of cross group in comparison with quasi group as shown in Tables 4 and 5, similar to the results of studies [7] and [18]. The maximum natural frequency for the laminate C2 is equal to 23.5 Hz in cross group. On the other hand, the maximum one in the quasi group is for the laminate Q2 and equal to 20.25 Hz as shown in Fig. 5 because the flexural modulus of the arrangement of GGCCCCGG organized by two glass plies at the outer surface is

higher than that of the arrangement GCCGGCCG as shown in Table 5 which is different from the results of studies [6] and [17]. The element  $Q_{11}$ ,  $Q_{12}$ , and  $Q_{66}$  of  $[Q_{ij}]$  matrix for  $90^\circ$  glass fibre is higher than that for  $90^\circ$  carbon. Therefore, the presence of  $90^\circ$  glass as a second layer in the laminate leads to increase the first element of  $[D]$  matrix and then the flexural modulus. By adding 2% nano  $Al_2O_3$  to all laminated composites, the amplitude of the vibration response decreased in comparison with the original state as shown in Fig. 4. This is due to the increase of the damping ratio for the nano particle addition case in comparison with the non-addition case, similar to the results of researches [11], [13] to [17], [21], [27], and [28] as shown in Table 5 and Fig. 6. This is occurred because of the increase of the interfacial regions in composite leading to more

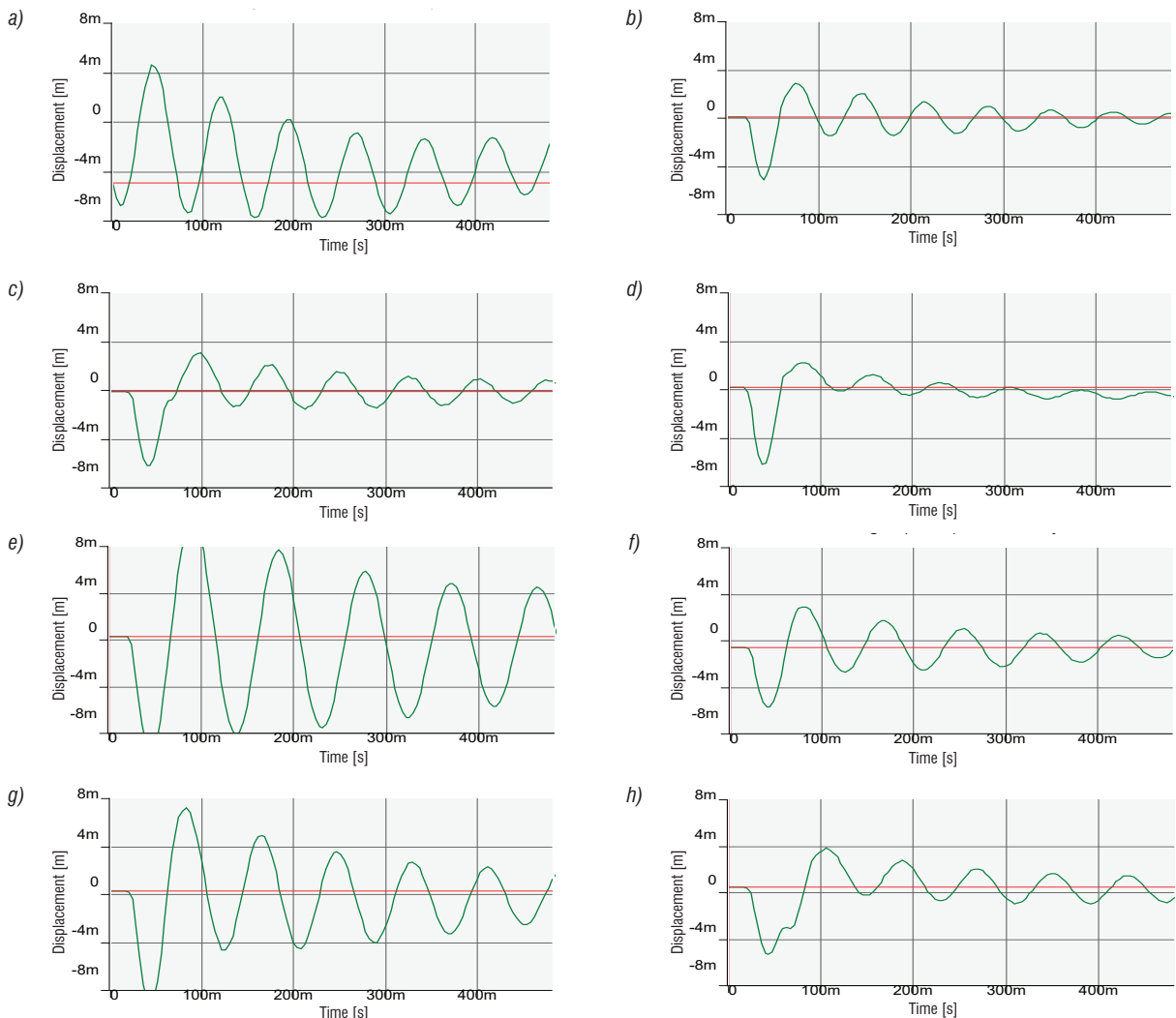


**Fig. 4.** Vibration responses of laminated epoxy composites with and without nano  $Al_2O_3$ : a) C1, b) C1WN, c) C2, d) C2WN, e) Q1, f) Q1WN, g) Q2, and h) Q2WN

energy dissipation by friction (heat) [2] and [3]. Despite the amplitude of the dynamic response for C2, C2WN, Q2, and Q2WN being lower than the amplitude for C1, C1WN, Q1 and Q1WN, respectively, as shown in Fig. 4, but the damping ratio of C2 is lower than the

**Table 5.** The experimental free vibration results (natural frequency & damping ratio)

Laminates	Natural frequency [Hz]	Damping ratio [%]
C1	22.75	0.629
C1WN	22.25	0.707
C2	23.5	0.477
C2WN	23	0.651
Q1	19	0.487
Q1WN	18.5	0.647
Q2	20.25	0.516
Q2WN	19.5	0.693

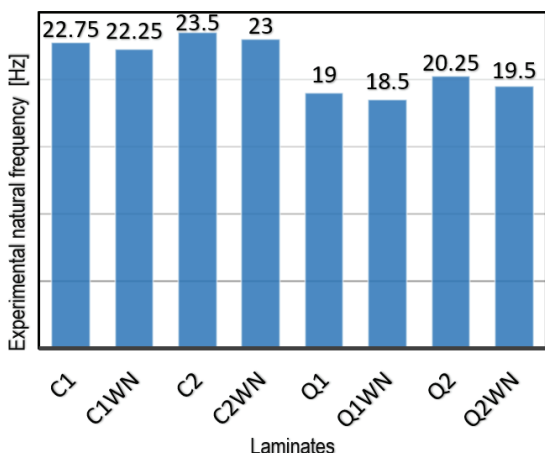


**Fig. 5.** Natural frequencies of all laminates with and without nano  $Al_2O_3$

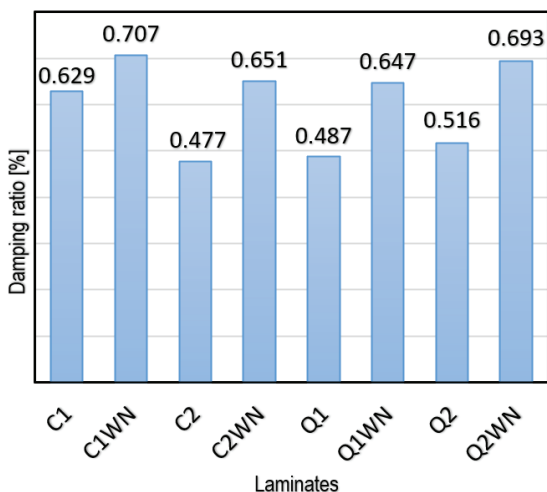


**Fig. 6.** Damping ratios of all laminates with and without nano  $Al_2O_3$

damping ratio of C1 by 24.2 %, and the damping ratio of C2WN is lower than the damping ratio of C1WN by 8 %. Its behaviour is due to the fact that the ratio of the maximum peak amplitude to the minimum peak amplitude is higher for C1 and C1WN than that for C2 and C2WN, respectively as shown in Fig. 4. The reverse situation for quasi group, where the damping ratio for Q2 is higher than damping ratio of Q1 by 5.62 % and the damping ratio for Q2WN is higher than the damping ratio of Q1WN by 6.64 % is due to the fact that the ratio of the maximum peak amplitude to the minimum peak amplitude is higher for Q2 and Q2WN than Q1 and Q1WN, respectively, as shown in Fig. 4. The stacking sequence and angle of orientation have a major effect on the value of the bending modulus, natural frequency, and damping ratio. For structural material system, it is necessary to make a balance between these properties alongside its strength. The configuration Q2 and Q2WN  $[G_0/G_{90}/C_{45}/C_{-45}]_s$  is specialized by increasing flexural modulus, natural frequency, and damping ratio simultaneously, in comparison with Q1 and Q1WN  $[G_0/C_{90}/C_{45}/G_{-45}]_s$ , respectively, as shown in Tables 4 and 5.

### 3 NUMERICAL WORKS

Ansys workbench simulation package was used to find the first six natural frequencies and its mode shape and compare it with the analytical and experimental one by using the steps shown in Fig. 7.

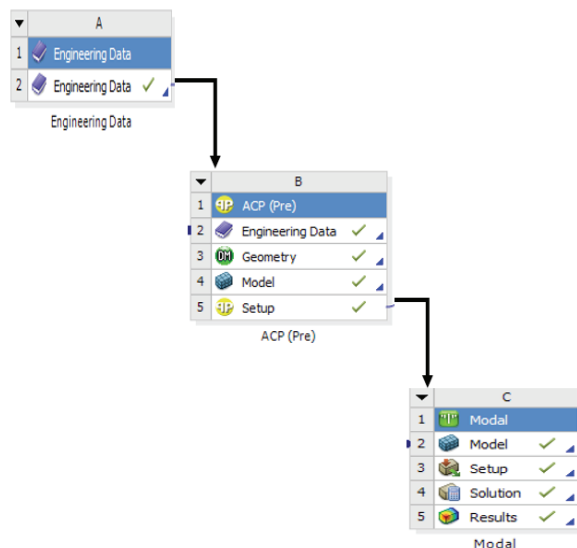


**Fig. 7.** Steps of modelling laminates in ANSYS

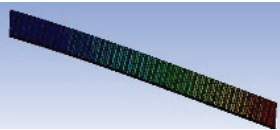
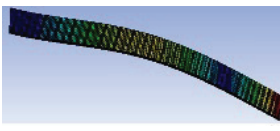
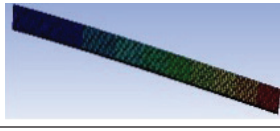
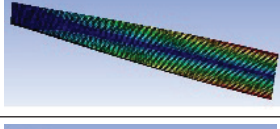
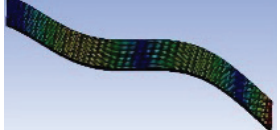
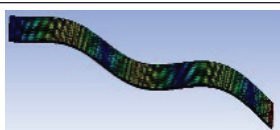
Firstly, the mechanical properties for each lamina must be entered to the engineering data. Then the arrangement of fibres in the laminated composite was

defined by using Ansys Composite PrepPost ACP (Pre) to create FEM models for different stacking sequences of laminates and finally the model analysis was used to evaluate until the first six natural frequencies with their mode's shapes are given, as shown in Table 6. It is obvious from Table 6 and Fig. 8 that all modes are bending modes, except mode 4 is torsional mode. Moreover, the maximum natural frequency for 1<sup>st</sup>, 2<sup>nd</sup>,

3<sup>rd</sup>, 5<sup>th</sup>, and 6<sup>th</sup> modes existed in C2 laminate, while for 4<sup>th</sup> mode, the maximum natural frequency existed in Q2, where in the laminates C2 and Q2 stacking sequence of G/G/C/C/C/C/G/G was utilized.

Finally, it is found that the analytical, experimental, and numerical natural frequencies are very close to each other, as shown in Fig. 9.

**Table 6.** The first six natural frequencies and its mode shapes for all laminates

No	Mode shape	Natural frequency [Hz]							
		C1	C1WN	C2	C2WN	Q1	Q1WN	Q2	Q2WN
1		23.185	22.752	23.8	23.313	19.821	19.452	20.59	20.138
2		145.16	142.45	148.98	145.94	124.08	121.77	128.9	126.07
3		263.89	258.42	265.8	260.2	218.92	214.86	231.4	225.78
4		309.84	303.71	309.75	303.59	320.66	313.71	326	318.95
5		405.87	398.29	416.45	407.94	347.04	340.58	360.5	352.71
6		793.69	778.86	808.91	791.91	679.17	666.55	705.7	690.54

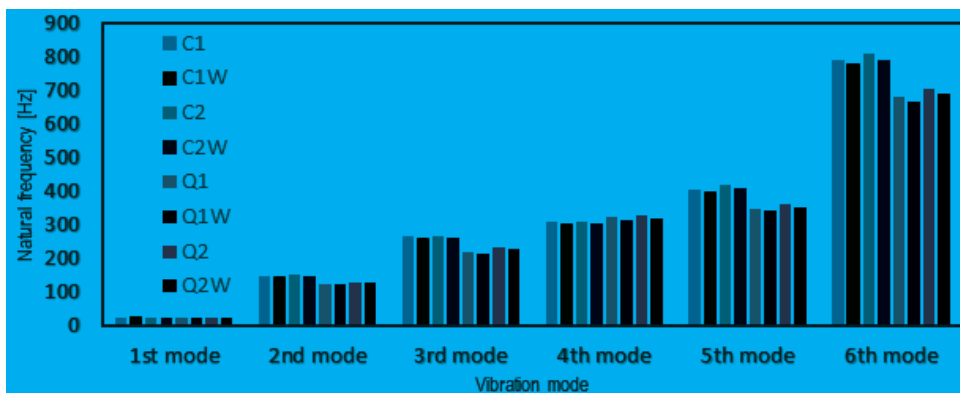


**Fig. 8.** Numerical natural frequency for all laminated composites

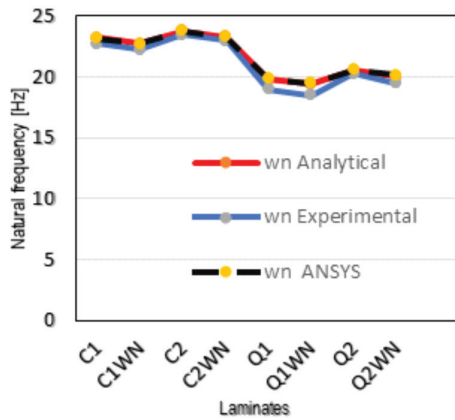


Fig. 9. Natural frequencies comparison in analytical, experimental, and numerical methods

#### 4 CONCLUSIONS

Structural components need to have high strength and stiffness along with high damping capacity. In this paper, the following conclusions can be made.

1. The maximum natural frequency for the cross- and quasi-laminate group was obtained for C2 and Q2 laminates.
2. The relationship between the natural frequency and damping ratio is inversely proportional.
3. Both flexural modulus and damping ratio were increased with addition of 2 % nano- $Al_2O_3$ , while the natural frequency was decreased.
4. The maximum damping ratio for the cross- and quasi laminate group was obtained for C1W and Q2W laminates, respectively.
5. The new aspect of this work is in the Q2 and Q2W configurations, which is appropriate to use in industry for structural element parts with higher bending modulus, natural frequency, and damping ratio properties.
6. The analytical, experimental, and numerical (ANSYS) natural frequencies are very close to each other.

#### 5 NOMENCLATURES

$D_{ij}$	flexural stiffness matrix, $[Pa \cdot m^3]$
$[Q_{ij}]$	reduced stiffness matrix, $[Pa]$
$h$	laminate thickness, $[mm]$
$D_{11}^*$	first element in the flexural compliance matrix $[1/(Pa \cdot m^3)]$
$E_b$	flexural modulus, $[GPa]$
$wn$	fundamental natural frequency, $[Hz]$
$l$	beam length, $[m]$
$I_{yy}$	moment of inertia, $[m^4]$

$\rho$  density,  $[kg/m^3]$   
 $A$  cross sectional area,  $[m^2]$

#### 6 REFERENCES

- [1] Chung, D.D. (2003). *Composite Materials: Functional Materials for Modern Technologies*. Springer Science & Business Media, DOI:10.1007/978-1-4471-3732-0.
- [2] Treviso, A., Van Genechten, B., Mundo, D., Tournour, M. (2015). Damping in composite materials: Properties and models. *Composites Part B: Engineering*, vol. 78, p. 144-152, DOI:10.1016/j.compositesb.2015.03.081.
- [3] Tang, X., Yan, X. (2020). A review on the damping properties of fiber reinforced polymer composites. *Journal of Industrial Textiles*, vol. 49, no. 6, p. 693-721, DOI:10.1177/1528083718795914.
- [4] Murugan, R., Ramesh, R., Padmanabhan, K. (2016). Investigation of the mechanical behavior and vibration characteristics of thin walled glass/carbon hybrid composite beams under a fixed-free boundary condition. *Mechanics of Advanced Materials and Structures*, vol. 23, no. 8, p909-916, DOI:10.1080/15376494.2015.1056394.
- [5] Suman, M.L.J., Murigendrappa, S.M., Kattimani, S. (2019). Experimental investigation on modal characteristics of plain woven glass/carbon hybrid composite beams with fixed-free end condition. *AIP Conference Proceedings*, vol. 2057, no. 1, art. ID 020011, DOI 10.1063/1.5085582.
- [6] Pujar, N.V., Nanjundaradhya, N.V., Sharma, R.S. (2022). Experimental investigation of the tensile and modal properties of epoxy based symmetric interlayer glass/carbon hybrid composites. *Materials Research Express*, vol. 9, no. 2, art. ID 025304, DOI:10.1088/2053-1591/ac4f88.
- [7] Aydin, M.R., Acar, V., Cakir, F., Gündoğdu, Ö., Akbulut, H. (2022). Comparative dynamic analysis of carbon, aramid and glass fiber reinforced interply and intraply hybrid composites. *Composite Structures*, vol. 291, art. ID 115595, DOI:10.1016/j.compstruct.2022.115595.
- [8] Erkljč, A., Bulut, M., and Yeter, E. (2014). The effect of hybridization and boundary conditions on damping and free vibration of composite plates. *Science and Engineering of Composite Materials*, vol. 22, no. 5, p. 565-571, DOI:10.1515/secm-2014-0070.
- [9] Zhang, J., Chaisombat, K., He, S., Wang, C.H. (2012). Hybrid composite laminates reinforced with glass/carbon woven fabrics for lightweight load bearing structures. *Materials & Design*, vol. 36, p. 75-80, DOI:10.1016/j.matdes.2011.11.006.
- [10] Swolfs, Y., McMeeking, R.M., Verpoest, I., Gorbatiikh, L. (2015). The effect of fibre dispersion on initial failure strain and cluster development in unidirectional carbon/glass hybrid composites. *Composites Part A: Applied Science and Manufacturing*, vol. 69, p. 279-287, DOI:10.1016/j.compositesa.2014.12.001.
- [11] Zhang, B., Li, Z., Wu, H., Nie, J. (2021). Research on damping performance and strength of the composite laminate. *Scientific Reports*, vol. 11, no. 1, p. 1-9, DOI:10.1038/s41598-021-97933-w.
- [12] Navaneeth, I.M., Poojary, S., Chandrashekar, A., Razak, A., Hasan, N., Almohana, A.I. (2022). Damped free vibration



- analysis of woven glass fiber-reinforced epoxy composite laminates. *Advances in Materials Science and Engineering*, vol. 2022, art. ID 6980996, DOI:10.1155/2022/6980996.
- [13] Pol, M.H., Zabihollah, A., Zareie, S., Liaghat, G. (2013). Effect of nano particles concentration on dynamic response of laminated nanocomposite beam. *Mechanics*, vol. 19, no. 1, p. 53-57, DOI:10.5755/j01.mech.19.1.3617.
- [14] Khashaba, U.A. (2015). Nanoparticle type effects on flexural, interfacial and vibration properties of GFRE composites. *Chinese Journal of Aeronautics*, vol. 29, no. 2, p. 520-533, DOI:10.1016/j.cja.2015.09.001.
- [15] Pujar, N.V., Nanjundaradhya, N.V., Sharma, R.S. (2018). Effect of graphene oxide nano filler on dynamic behavior of GFRP composites. *AIP Conference Proceedings*, vol. 1943, no. 1, art. ID 020107, DOI:10.1063/1.5029683.
- [16] Karthik, K., Rohith Renish, R., Irfan Ahmed, I., Niruban Projoth, T. (2016). Free vibration test for damping characteristics of hybrid polyester matrix composite with carbon particles. *Nano Hybrids and Composites*, vol. 11, p. 1-6, DOI:10.4028/www.scientific.net/NHC.11.1.
- [17] Utomo, J.T., Susilo, D.D., Raharja, W.W. (2017). The influence of the number and position of the carbon fiber lamina on the natural frequency and damping ratio of the carbon-glass hybrid composite. *AIP Conference Proceedings*, vol. 1788, no. 1, art. ID 030046, DOI:10.1063/1.4968299.
- [18] Singh, K., Jain, N., Bhaskar, J. (2020). Vibrational analysis of glass/carbon fiber reinforced laminate composites. *Journal of Theoretical and Applied Mechanics*, vol. 50, p. 259-277, DOI:10.7546/JTAM.50.20.03.04.
- [19] Pingulkar, P., Suresha, B. (2016). Free vibration analysis of laminated composite plates using finite element method. *Polymers and Polymer Composites*, vol. 24, no. 7, p. 529-538. DOI:10.1177/096739111602400712.
- [20] Bulut, M., Erkliğ, A., Yeter, E. (2015). Experimental investigation on influence of Kevlar fiber hybridization on tensile and damping response of Kevlar/glass/epoxy resin composite laminates. *Journal of Composite Materials*, vol. 50, no. 14, p. 1875-1886, DOI:10.1177/0021998315597552.
- [21] Alsaadi, M., Bulut, M., Erkliğ, A., Jabbar, A. (2018). Nano-silica inclusion effects on mechanical and dynamic behavior of fiber reinforced carbon/Kevlar with epoxy resin hybrid composites. *Composites Part B: Engineering*, vol. 152, p. 169-179, DOI:10.1016/j.compositb.2018.07.015.
- [22] Fairlie, G., Njuguna, J. (2020). Damping properties of flax/carbon hybrid epoxy/fibre-reinforced composites for automotive semi-structural applications. *Fibers*, vol. 8, no. 10, art. ID 64, DOI:10.3390/fib8100064.
- [23] Alexander, J., Kumar, H.A., Augustine, B. (2015). Frequency response of composite laminates at various boundary conditions. *International Journal of Engineering Science Invention*, p. 11-15.
- [24] Erkliğ, A., Bulut, M., Yeter, E. (2014). Natural frequency response of laminated hybrid composite beams with and without cutouts. *Journal of Polymer Engineering*, vol. 34, no. 9, p. 851-857, DOI:10.1515/polyeng-2014-0061.
- [25] Bulut, M., Alsaadi, M., Erkliğ, A., Alrawi, H. (2018). The effects of S-glass fiber hybridization on vibration-damping behavior of intraply woven carbon/aramid hybrid composites for different lay-up configurations. *Proceedings of the Institution of Mechanical Engineers, Part C: Journal of Mechanical Engineering Science*, vol. 233, no. 9, p. 3220-3231, DOI:10.1177/0954406218813188.
- [26] Kröger, H., Mock, S., Greb, C., Gries, T. (2022). Damping properties of hybrid composites made from carbon, vectran, aramid and cellulose fibers. *Journal of Composites Science*, vol. 6, no. 1, art. ID 13, DOI:10.3390/jcs6010013.
- [27] Senthamaraikannan, C., Ramesh, R. (2018). Evaluation of mechanical and vibration behavior of hybrid epoxy carbon composite beam carrying micron-sized CTBN rubber and nanosilica particles. *Proceedings of the Institution of Mechanical Engineers, Part L: Journal of Materials: Design and Applications*, vol. 233, no. 9, p. 1738-1752, DOI:10.1177/1464420718784315.
- [28] Bulut, M., Erkliğ, A., Kanmaz, P. (2019). Vibration-damping characterization of the basalt/epoxy composite laminates containing graphene nanopellets. *Science and Engineering of Composite Materials*, vol. 26, no. 1, p. 147-153, DOI:10.1515/secm-2017-0380.
- [29] Kaw, A.K. (2005). *Mechanics of Composite Materials*. CRC Press, Boca Raton, DOI:10.1201/9781420058291.
- [30] Reddy, J.N. (2003). *Mechanics of Laminated Composite Plates and Shells: Theory and Analysis*. CRC Press, Boca Raton, DOI:10.1201/b12409.
- [31] Goren, A., Atas, C. (2008). Manufacturing of polymer matrix composites using vacuum assisted resin infusion molding. *Archives of Materials Science and Engineering*, vol. 34, no. 2, p. 117-120.

# Experimental Study and Numerical Analysis on Windage Power Loss Characteristics of Aviation Spiral Bevel Gear with Oil Injection Lubrication

Linlin Li — Sanmin Wang

Northwestern Polytechnical University, School of Mechanical Engineering, China

*With the increasing speed of aviation spiral bevel gears, the load-independent windage power losses caused by hydrodynamic have increasingly more influence on gear transmission efficiency. Firstly, a test rig for the windage power loss of spiral bevel gear under oil-jet lubrication is established, and on this basis, a method for measuring windage torque is proposed. Next, the interactive effects of different injection lubrication parameters on the windage power loss were studied by orthogonal experiment, and the formula for calculating the windage loss was obtained by fitting the experimental data. Then, the fluid distribution, velocity field and pressure field around the gear were analysed by using a computational fluid dynamics (CFD) numerical model, and the mechanical and energy characteristics of the gear windage power loss were obtained. Finally, the dimensionless processing of the windage moment was carried out, and the variation of the dimensionless windage moment coefficient with the rotational Reynolds number is obtained. The comparison between the dimensionless windage moment coefficient of experimental data and simulation results shows that the CFD values are in good agreement with the measured data. This study provides experimental and methodological guidance for the calculation of windage power loss and windage reduction design of aviation gear pair under oil injection lubrication.*

**Key words:** spiral bevel gear, oil-jet lubrication, windage power loss, windage test

## Highlights

- A test rig for the windage power loss of spiral bevel gears under oil-jet lubrication is established.
- A method for measuring windage torque is proposed.
- The interactive effects of different injection lubrication parameters on the windage power loss were studied with orthogonal experimentation.
- The comparison between the dimensionless windage moment coefficient of experimental data and simulation results shows that the CFD values are in good agreement with the measured data.

## 0 INTRODUCTION

Aviation spiral bevel gears mainly work at high speed and high power. Therefore, the oil injection mode is mostly used to provide lubricating oil to the gear system [1]. When the fluid impacts the gear teeth, the two tooth surfaces in a tooth space are respectively represented as a suction surface and a pressure surface. The pressure differential force will produce a torque opposite to the rotation direction of gears; at the same time, the viscous force between the fluid and the gear surface will also cause the reverse torque. These two torques constitute the windage torque of the gear, thus resulting in windage power loss [2], which is a load-independent power loss. A large number of experiments show that the windage loss becomes significant with the increase of gear speed [3]. When the linear velocity of the gear is greater than 50 m/s, the windage power loss caused by hydrodynamic behaviour must be paid sufficient attention [4] to [6]. Handschuh [7] pointed out that when the linear velocity of the gear reaches 125 m/s, the windage loss of the gearbox accounts for about half of the

load-independent power loss and can dominate other loss mechanisms. At the same time, the windage effect will deflect the trajectory of lubricating oil flow, making it difficult for lubricating oil to enter the gear meshing area. This causes dry friction of the gear, and subsequent tooth surface scuffing, wear, etc. Furthermore, the additional heat generated by the windage power losses can easily aggravate the temperature rise of the gear [8] and [9].

The main methods to study the windage power loss of gearboxes are theoretical analysis, experimental measurement, and numerical simulation [10]. Physical experiments were mainly used in early literature research. Computational fluid dynamics (CFD) provides help for the visual analysis of gear windage losses and provides the possibility for the study of some complex phenomena that cannot be realized under conventional experimental conditions [11] and [12]. Researchers, such as Anderson and Loewenthal [13], Dawson [14] and Diab et al. [15], mainly used experimental methods to study the windage power loss of a single spur gear in a single-phase air flow. Considering the influence of gear

geometric parameters, working conditions, fluid properties and other factors on the windage loss, some empirical formulas for calculating the windage loss of spur and helical gears are obtained according to the experimental results. Finally, some methods to reduce windage power loss are proposed. Winfree [16] obtained a large number of experimental data on the windage loss of spiral bevel gears. The results show that the shroud can greatly reduce the windage power loss of high-speed spiral bevel gears, and a series of design principles for a gear system to reduce the windage power loss are proposed. Seetharaman and Kahraman [17] established a simplified computational fluid dynamics model to study the windage power loss of meshing spur gears to explain the suction/extrusion effect of gear meshing on windage loss. The model showed that the squeezing power loss in the meshing area contributed the most to the total windage loss. Ruzek et al. [18] used an improved test rig to study the windage power loss of disk, spur, and helical gears under various combinations through a series of experiments. Their results show that although there is coupling interaction when the two gears are engaged, the windage loss of the gear pair is about equal to the sum of the individual windage loss values when the two gears are not engaged. These findings are also verified by the sliding grid method and multi-reference rotation (MRF). Delgado and Hurrell [19] and Handschuh and Hurrell [20] performed experiments at the Glenn Research Center of NASA, US and obtained a large number of windage loss data of spur gears under different experimental conditions. The influence factors of windage power loss are studied from the aspects of gear geometry, shroud shape, different lubrication system configuration, pressure, temperature and meshing effect, and an empirical model for calculating the windage power loss of spur gears is formed.

Massini et al. [21] experimentally measured the parameters related to the windage loss of a single spur gear under free lubrication; they used particle image velocimetry (PIV) technology to measure the velocity and vector diagram of flowing fluid. This is the first experimental work to realize the visualization of flow fields near high-speed gears with PIV technology. Maccioni et al. [22] established a CFD model capable of taking aeration into consideration and developed a new solver. A dip-lubricated tapered-roller-bearing was simulated with the new solver and a standard one. The numerical predictions were compared with the experimental data obtained on a dedicated test rig using PIV. The results show that the numerical values in all rotation ranges are in good agreement with

the experimental results. Mastrone and Concli [23] presented a new mesh handling strategy specifically suited to studying the efficiency and lubrication inside gearboxes transmissions. The methodology is based on the Global Remeshing Approach with Mesh Clustering (GRAM<sup>C</sup>) process that drastically reduces the simulation time by minimizing the effort for updating the grids. Compared with the power loss measured via experimentation, the proposed method has good accuracy. Gorla et al. [24] systematically studied the effects of lubricating oil density, viscosity, gear circumferential velocity, addendum circle diameter, tooth width and other factors on the hydraulic loss of a gearbox system by CFD and carried out experimental verification. Fondelli et al. [25] used volume of fluid (VOF) model to simulate and analyse a single spur gear and adopted a mesh adaptive method to simulate the process of lubricating oil jet impacting on the tooth surface of a single high-speed gear so as to estimate the resistance moment of the lubricating oil jet and analysed the influence of the injection angle on the resistance moment and lubrication performance, thereby improving the gear transmission efficiency and saving the cost of simulation experiments. Farall et al. [26], Rapley et al. [27] and Webb et al. [28] mainly analysed the windage loss of a single spiral bevel gear in single-phase air flow by CFD. The characteristics of an air flow field around gears with and without shroud are analysed from several angles, and the influence of different configurations of the shroud on the fluid distribution around gears is analysed, which provides guidance for the optimal design to reduce windage loss. Johnson et al. [29] and Simmons et al. [30], on the basis of previous studies, used the windage test bench of the gas turbine transmission centre of Nottingham University, UK to obtain the variation law of windage power loss of a single spiral bevel gear and gear pair under different shrouds, gear rotation directions, lubrication conditions, and other parameters. Subsequently, the pressure and lubrication system are added to the bench, so that the experimental platform can form a high-pressure environment and oil mist in the gear box. The results show that the lubrication condition increases the density of fluid around the gear and Reynolds number. For gears unshrouded, the existence of lubricating oil increases the windage moment; however, the windage loss does not change much for the gear shrouded.

According to the analysis of the existing literature, there is little research on the windage power loss caused by the flow field around the spiral bevel gear pair and the two-phase flow of oil injection

lubrication, especially the theoretical analysis and experimental research on the influence of oil injection lubrication parameters on the windage loss of spiral bevel gear pair. In this paper, a test bench for measuring the windage power loss of spiral bevel gears during oil injection lubrication is established. The method for measuring the windage loss of gear pairs is proposed, and the interactive effects of different oil injection parameters on gear windage losses are obtained with orthogonal experiments. Then, based on the tooth surface movement method, the oil injection lubrication model of spiral bevel gear is established. The instantaneous distribution of two-phase fluid and the changes law of the pressure field and velocity field in the gearbox are simulated and analysed by using the Fluent software and the dynamic mesh technology. The mechanical and energy characteristics of windage losses of spiral bevel gears with oil injection lubrication are obtained, which provides a theoretical reference for the calculation of windage and windage reduction design of aviation spiral bevel gears.

## 1 EXPERIMENTAL SETUP AND MEASUREMENT

### 1.1 Test Rig

The windage power loss test experiment of spiral bevel gears adopts an open power flow gear test device, as shown in Fig. 1. The experimental equipment mainly includes a high-speed spindle, low-speed shaft, flexible coupling, bearing, variable frequency speed regulating motor, torque-speed sensor, temperature sensor, pressure sensor, eddy current brake, oil injection lubrication circuit system, and signal acquisition and processing system.

As shown in Fig. 1, the motor can rotate in both directions, and the maximum speed of the drive gear shaft can reach 10,000 rpm. The non-contact strain gauge torque sensor can measure the forward and reverse torque without zero adjustment and commutation and is not limited by the speed. At the same time, several pulse counters are integrated into the sensor, and the speed of the gear shaft can be output by calculating the number of pulses output by the photoelectric encoder. The accuracy of this sensor is  $\leq 0.2\%$  full scale, and the sensitivity drift is  $0.009\%$  per  $^{\circ}\text{C}$  in the temperature range of  $0^{\circ}\text{C}$  to  $50^{\circ}\text{C}$ .

The signal acquisition and processing system is used to collect and process all the measurement data, including shaft speed, torque, inlet and outlet oil temperature and oil pressure, as shown in Fig. 2.

The speed of the rotating shaft is set by the motor and controlled by the speed adjustment knob on the operation panel. The speed value is measured by the speed sensor and displayed on the panel. The inlet and outlet oil temperatures are measured by the temperature sensor of the oil injection lubrication system. Meanwhile, the windage torque of the gear and the friction torque on the bearing and the rotating shaft are measured by the torque sensor and also recorded on the instrument panel.

Lubrication of gears and bearings is provided by a special oil control system, as shown in Fig. 3. This system can provide lubricating oil with controlled oil temperature and oil pressure. The vacuum oil pump is connected to the pipeline system and the gate valve to adjust the oil supply pressure continuously within the range of 0 MPa to 1 MPa. The oil heater can adjust the oil temperature at any time and monitor the change

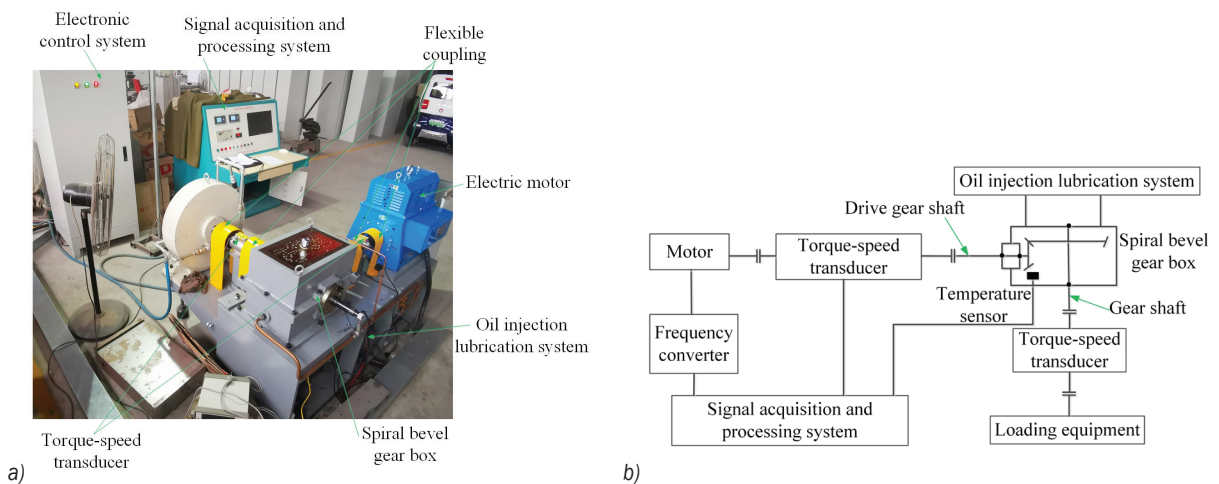


**Fig. 1.** a) View of the test rig, and b) schematic representation of test rig



of oil temperature through the thermometer on the oil tank.

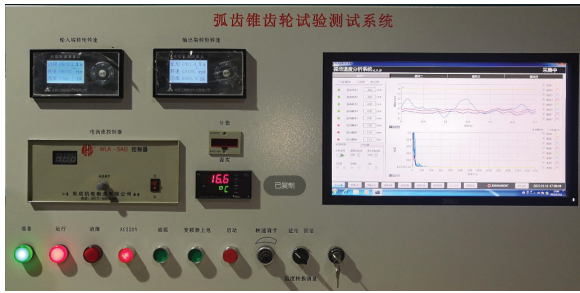


Fig. 2. Signal acquisition interface

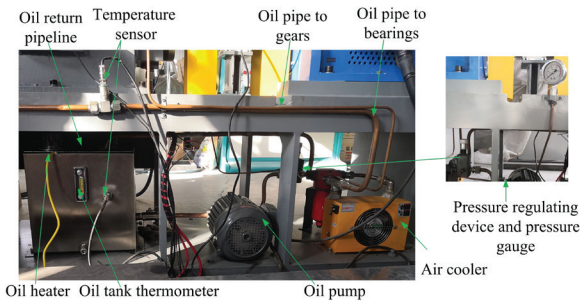


Fig. 3. Oil injection lubrication system

1.2 Experimental Measurement Scheme

At present, according to most documents on gear windage experiments [21], [29] and [30], the method to measure the rig driveline torque of rotating shafts and bearings is to measure the system torque with the gear pair removed and take this measurement value as the extra power loss caused by shafts and bearings in the gear transmission system. According to Ruzek et al. [18], gear pairs do not significantly change the additional power loss generated by bearings and rotating shafts. This is because, based on the Harris equations [31], it is found that the addition of the gear pair produces an additional power loss of less than 1 W in the entire speed range. Consequently, the effect of the gears on the rig driveline torque is considered negligible. Therefore, in this experiment, when the gear pair rotates at a low speed (input shaft speed  $\leq 1000$  rpm) and without load, the torque value measured when it is small and changes little with the increase of speed is taken as the rig driveline torque generated by the friction of the bearing, the rotating shaft, and the engagement of the gear pair without load. This is because the windage loss of the gear is small and can be ignored. At the same time, this method can eliminate the influence of the extra power loss caused by the no-load meshing of the gear pair

on the experimental measurement of the windage loss. Therefore, the windage torque of the experimental gear is the value obtained by subtracting the rig driveline torque from the measured value of the torque sensor when the system is unloaded.

When measuring the windage torque of a gear under oil injection lubrication, the friction torque of the rotating shaft, bearing and gear pair without load will change with the differences in injection temperature, injection pressure, and rotating shaft speed. According to the experimental research of Massini [21], the influence relationship is as follows:

$$M_f = a \cdot u_p^b \cdot T^c \cdot P^d, \tag{1}$$

where,  $M_f$  is the rig driveline friction moment;  $a$ ,  $b$ ,  $c$ ,  $d$  are the fitting coefficients of experimental data;  $u_p$  is the pitch circular linear speed of the rotating gear;  $T$  and  $P$  are injection temperature and pressure, respectively.

Therefore, according to different gear working conditions and oil injection lubrication conditions, the rig driveline torque in the measurement of windage loss needs to be corrected according to Eq. (1).

1.3 Measurement and Calculation of Windage Power Loss

The geometric parameters of experimental spiral bevel gears are shown in Table 1.

Table 1. Basic parameters of spiral bevel gear

Parameters	Pinion	Gear
Number of teeth	27	81
Heel module [mm]	3.85	
Pressure angle [°]	20	
Helix angle [°]	35	
Outer cone distance [mm]	164.31	
Tooth width [mm]	49	
Outside tip diameter [mm]	112.72	313.07
Rotation direction	Left	Right

The gear pair is lubricated by oil injection at the into-meshing side and out-of-meshing side at the same time. The diameter of the oil nozzle is 4 mm. According to the basic parameters of spiral bevel gears in Table 1, the tested gear pair is shown in Fig. 4.

In order to reduce the dispersion of measurement results during the test, for each test condition, run at a constant speed for ten minutes before measuring power loss. The test was repeated five times under each operating condition, and the average value was taken as the measurement value. Fig. 5 shows the



scatter plot of the average value and standard deviation of the gear windage power curve at different speeds.

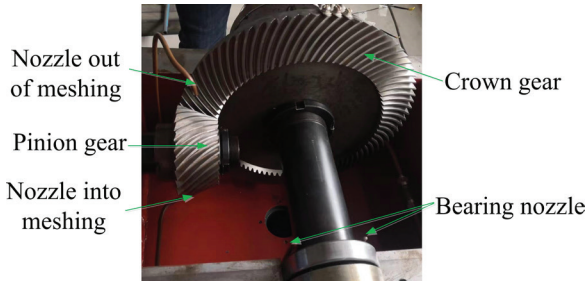


Fig. 4. Gear pair and lubrication

It can be seen from Fig. 5 that the standard deviation of the measured torque is about 2.3 % to 3.1 % of its average value, which indicates that the dispersion degree of each set of measurement data is not significant, so the repeatability of the test measurement is good.

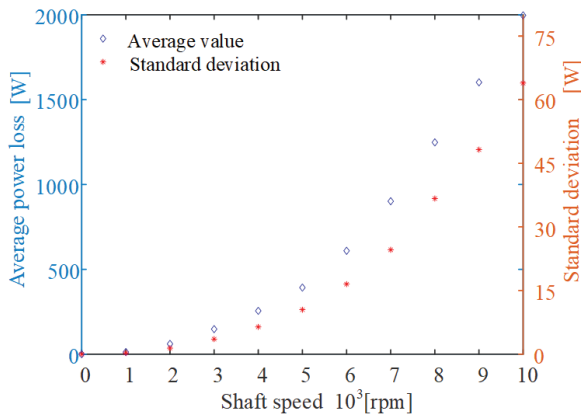


Fig. 5. Average value and standard deviation of power loss value measured by experiment

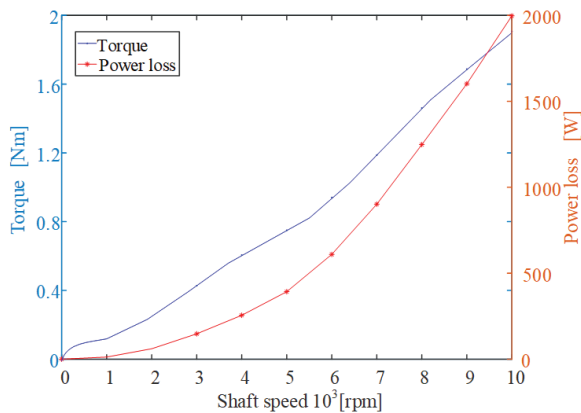


Fig. 6. Torque value and power loss value measured experimentally with different speeds

The injection temperature is set at 20 °C, the injection pressure is at 0.2 MPa, and the brake is unloaded. The motor speed button on the control panel is adjusted to continuously increase the speed from 0 rpm to 10,000 rpm. At the same time, the torque values at different speeds are recorded and the power loss values are calculated. The results are shown in Fig. 6.

As can be seen from Fig. 6, the power loss of the gear system is less than 10 W when the rotational speed is less than 800 rpm. According to the windage measurement scheme in Section 2.2, this experiment assumes that the power loss measured when the speed is lower than 800 rpm is the additional power loss caused by the friction of the gear shaft, bearing and gear pair engagement. At the same time, by changing different injection temperatures and pressures and correcting this torque according to Eq. (1), the windage torque and rig driveline torque values of the experimental gear pair at different rotational speeds are calculated, as shown in Fig. 7.

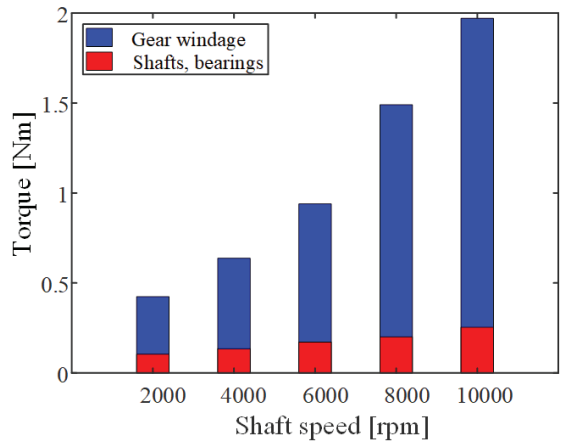


Fig. 7. Distribution of windage torque and rig driveline torque at different rotating speed

It can be seen from Fig. 7 that the windage torque of the gear pair increases sharply with the increase of the speed, but the rig driveline torque changes little with the speed. This indicates that the higher the rotational speed, the greater the proportion of the windage loss of the gear pair to the total load-independent power loss. This is because the friction force of the bearing, shaft and gear pair engagement without load is small, and the rotational speed has little effect on it. However, with the increase of the gear pair speed, the velocity of the flow field around the gear increases, and the rotating Reynolds number increases. At this time, the power consumed by gear

rotation is greater; that is, the reverse moment of fluid movement to gear rotation increases.

### 1.4 Interaction of Injection Parameters on Windage Loss

In addition to the rotational speed, the oil injection parameters are also important factors affecting the windage loss of gear pair under oil injection lubrication. Therefore, in order to seek the interaction law of injection parameters on gear windage loss, orthogonal tests are used to analyse the influence of these variables on the results. Orthogonal testing [32] can use relatively few representative data to analyse the influence of various factors on the test results. The test index of this test is the gear windage power loss calculated by subtracting the rig driveline torque from the measured torque. The shaft speed (A), oil injection pressure (B), and oil injection temperature (C) are the test factors. The level of each test factor is set as four, as shown in Table 2.

**Table 2.** Factor level

Levels	Factors		
	A Shaft speed [rpm]	B Oil-jet pressure [MPa]	C Oil-jet temperature [°C]
1	2000	0.1	20
2	4000	0.2	25
3	6000	0.3	30
4	8000	0.4	35

**Table 3.** Experiment scheme and result

Test numbers	Column (Factors)			Windage power loss [kW]
	A	B	C	
1	2000	0.1	20	0.063
2	2000	0.2	25	0.069
3	2000	0.3	30	0.075
4	2000	0.4	35	0.082
5	4000	0.1	25	0.176
6	4000	0.2	20	0.184
7	4000	0.3	35	0.197
8	4000	0.4	30	0.222
9	6000	0.1	30	0.421
10	6000	0.2	35	0.440
11	6000	0.3	20	0.478
12	6000	0.4	25	0.534
13	8000	0.1	35	1.030
14	8000	0.2	30	1.056
15	8000	0.3	25	1.123
16	8000	0.4	20	1.215

The standard orthogonal table  $L_{16}(4^3)$  is selected to carry out the experimental analysis of 16 groups of factor combinations, and the windage power loss of

each combination is obtained. The results are shown in Table 3.

The gear windage power loss of each factor at each level is added; then, its average value is calculated and recorded as  $\bar{Y}_i$ . Finally, the range of each factor was calculated and recorded as  $R_j$ . The range values are arranged in order, as shown in Table 4.

**Table 4.** Analysis of variance

Test	Column (Factors)		
	A	B	C
$\bar{Y}_1$	0.072	0.423	0.485
$\bar{Y}_2$	0.195	0.437	0.475
$\bar{Y}_3$	0.468	0.468	0.443
$\bar{Y}_4$	1.106	0.513	0.437
$R_j$	4.134	0.362	0.191

Influence order: A>B>C

From the range in Table 4, it can be seen that the interaction degree of each factor on the test results is A, B and C in descending order, among which significant factors are A and B, and C is insignificant. That is, the shaft speed has the greatest influence on the windage power loss of the gear pair, followed by the injection pressure, and both are positively correlated. The less affected is the injection temperature; it is negatively correlated.

In order to further study the interactive influence of various factors on the test indicators, the experimental data in Table 4 are fitted with polynomial curves to obtain the calculation formula of the windage power loss of spiral bevel gear pairs with test factors as independent variables. Since the polynomial objective function in the form of a power function has the least generalization and residuals, the following power function is obtained:

$$P_w = 0.0436 \cdot N^{2.71} \cdot P^{0.10} \cdot T^{-0.07}, \tag{2}$$

where  $P_w$  is the windage power loss of gears;  $N$  is the shaft speed;  $P$  the oil injection pressure;  $T$  is the oil injection temperature.

According to Eq. (2), the windage power loss of the spiral bevel gear is approximately proportional to the 2.71 power of gear speed. The empirical formulas and experiments on gear windage power losses by Anderson and Loewenthal [13], Dawson [14] and Diab et al. [15] show that the windage power loss is approximately proportional to the third power of rotational speed, and it is also related to gear parameters, fluid medium parameters and boundary

conditions. This paper is consistent with the above research conclusions. This shows that rotational speed remains the most important factor affecting the windage power loss of gear under oil injection lubrication.

In this experiment, the injection quantity is changed by adjusting the injection pressure. When the diameter of the nozzle is constant, the injection pressure is proportional to the square of the flow rate. The larger the injection pressure, the more the injection flow rate, which leads to higher injection velocity. At this time, the lubricating oil sprayed from the nozzle has greater kinetic energy and momentum, and the ability to resist the influence of high-speed fluid around the gear is stronger so that the volume fraction of the lubricating oil on the tooth surface becomes larger. Therefore, with the increase of the injection velocity, more lubricating oil can enter the meshing area of the gear pair, thereby increasing the pumping power loss of the gear pair meshing interface.

The accuracy of the calculation of windage losses significantly influences the efficiency of the gear system. At present, in engineering applications, when calculating the efficiency of the spiral bevel gear system, the power loss values mainly refer to the recommended values of AGMA standards, ISO standards or national standards [33], and there is no specific calculation formula. Therefore, the fitting formula of windage power loss based on oil injection lubrication parameters provides a theoretical reference for the efficiency calculation of spiral bevel gears. At the same time, by analysing the interactive influence law of oil injection parameters on gear windage losses, it provides theoretical and methodological guidance for the next research on the method of reducing windage power loss.

## 2 NUMERICAL SIMULATION MODEL OF SPIRAL BEVEL GEARS

### 2.1 Basic Governing Equations of Flow Field

The governing equations of the mass and momentum conservation for the fluid domain inside the gearbox are given as [21]:

$$\frac{\partial \rho}{\partial t} + \nabla \cdot (\rho \mathbf{V}) = 0, \tag{3}$$

$$\frac{\partial (\rho \mathbf{V})}{\partial t} + \nabla \cdot (\rho \mathbf{V} \mathbf{V}) = -\nabla p + \nabla \cdot [\mu (\nabla \mathbf{V} + \nabla \mathbf{V}^T)] + \rho \mathbf{g} + \mathbf{F}, \tag{4}$$

where  $\rho$  is the density.  $t$  is the time.  $\mathbf{V}$  is the velocity vector.  $\mathbf{g}$  is the gravity vector.  $\mathbf{F}$  represents the external forces.  $\mu$  is the viscosity. These basic equations should be applied to each cell.

The lubrication process of gear pair is a problem of oil-air two-phase flow, which needs to be analysed with multi-phase flow numerical calculation. Therefore, density and viscosity of the mixture are computed as

$$\rho = \alpha \rho_a + (1 - \alpha) \rho_i, \quad \mu = \alpha \mu_a + (1 - \alpha) \mu_i, \tag{5}$$

where, the subscripts  $a$  and  $i$  represent air and oil, respectively;  $\alpha$  is the volume fraction of air, and it can be calculated for all cells as

$$\frac{\partial \alpha}{\partial t} + \frac{\partial (\alpha u_i)}{\partial x_i} = 0. \tag{6}$$

### 2.2 CFD Model of Gear Pair

In order to accurately describe the hydrodynamic characteristics of the oil-gas two-phase flow in the spiral bevel gearbox. To avoid the interference of unnecessary parts in the box, a simplified geometric model of the spiral bevel gearbox was established using Unigraphics (UG) software, ignoring the web plate hole, bearings, flange structure, fixings, etc. The final three-dimensional model of the gearbox and the coordinate system are shown in Fig. 8.

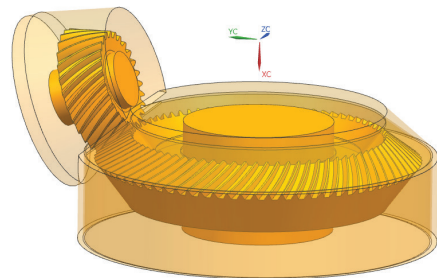


Fig. 8. 3D model of spiral bevel gearbox

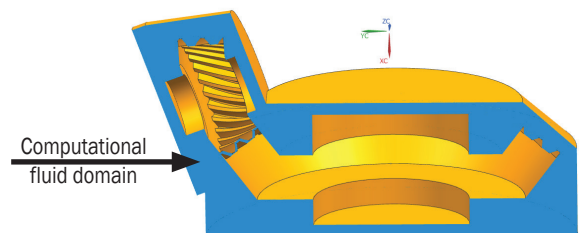
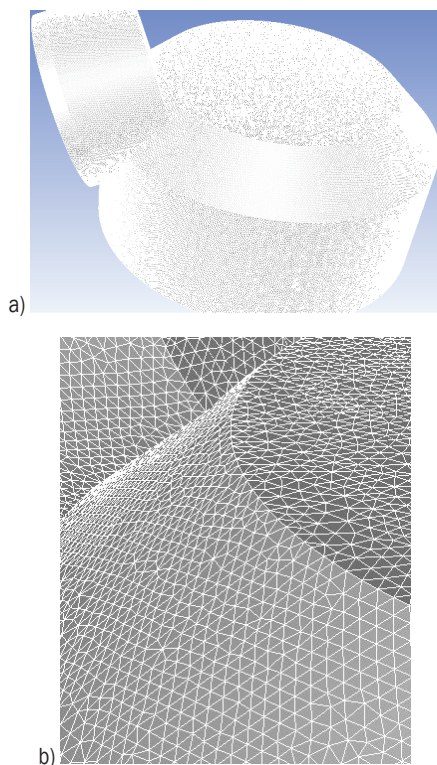


Fig. 9. Computational domain flow field model

It is necessary to calculate the interaction between the flow field and the gear with CFD simulation.

Therefore, when extracting the internal flow field of the gearbox, a closed boundary is adopted without considering the influence of the microstructure of the gearbox body. The computational fluid domain flow field model is obtained via a Boolean operation between the gearbox and the gear pair, as shown in Fig. 9.

The gearbox geometry model was imported into the pre-processing software ANSYS-ICEM CFD, and the fluid domain was discretized into unstructured tetrahedral meshes based on the finite volume method, to obtain the fluid dynamics analysis model. The mesh model of the gearbox is shown in Fig. 10.



**Fig. 10.** Mesh model of the gearbox; a) global view, and b) partial view

To improve the precision and reliability of the simulation results, a mesh independence analysis is performed to ensure that discretization errors are quantified and minimized. This was done by comparing the windage moment at a rotating speed of 8000 rpm. The number of these meshes and the windage moment values measured are shown in Table 5.

As shown in Table 5, the windage moment can be considered stable when the number of mesh elements exceeds 1,626,730. In order to ensure the accuracy of CFD calculation, reduce calculation time and save

calculation resources, it is necessary to densify and refine the mesh locally on each surface of the gear and near the oil injection nozzle. At the same time, in order to obtain high-quality mesh, it is necessary to smooth the mesh. The maximum mesh size of the fluid domain is 3 mm, the boundary layer size is 0.4 mm at tooth surface, end face and nozzle. Finally, the number of mesh elements in the entire fluid domain of the calculation model is about 1.65 million.

**Table 5.** Results of mesh independence analysis

Mesh	Total mesh elements	Windage moment [N·m]
1	357,162	2.95
2	621,376	2.13
3	916,405	1.26
4	1,457,573	1.50
5	1,626,730	1.46
6	1,912,642	1.43

### 2.3 CFD Methodology

The pre-processed model is imported into Fluent for solution. A CFD code that applies the VOF method to model free surface flow was utilized to simulate the two-phase flow. The boundary movement was defined through the UDF file, and the mesh update process was automatically completed by Fluent according to the change of the boundary in each iteration step. The solution settings are shown in Table 6.

**Table 6.** Settings of numerical calculation

Description	Parameter value
Equation control calculation method	Pressure-based separation solver
Time	Transient
Multiphase model	VOF model (implicit body force activated) Primary phase: air Secondary phase: oil
Viscous model	SST $k-\omega$
Inlet boundary	Velocity-inlet
Outlet boundary	Pressure-outlet
Wall condition	Non-slip
Dynamic mesh	Smoothing and local Remeshing
Discretization schema	Pressure velocity coupling: PIMPLE Spatial discretization: Second order upwind
Initialization	Standard initialization

### 2.4 Formation Mechanism of Gear Windage Loss

The fluid velocity vector around the tooth is shown as Fig. 11, which shows that the direction of fluid flow is opposite to the direction of gear rotation.



As can be seen from Fig. 11, when the gear rotates, the fluid around it will be separated at the tooth top. Some of the fluid flows over the top of the tooth without changing its direction. Moreover, the other part is sucked into the gap between the teeth from the position close to the tooth top and forms eddy currents in the tooth space. The tooth surface impacted by fluid appears as the pressure surface as shown in Fig. 12a, with local high pressure; Then the leeward side is shown as the suction surface as shown in Fig. 12b, and local low pressure occurs, resulting in a pressure difference between the two tooth surfaces and a pressure difference torque, which is opposite to the rotation direction of the gear.

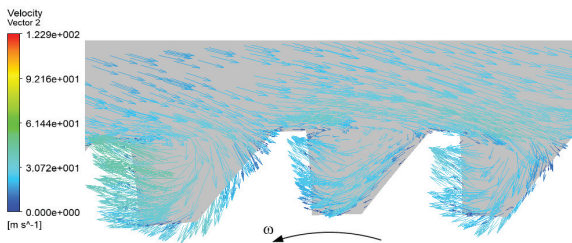


Fig. 11. Velocity vector diagram of fluid around gear [5]

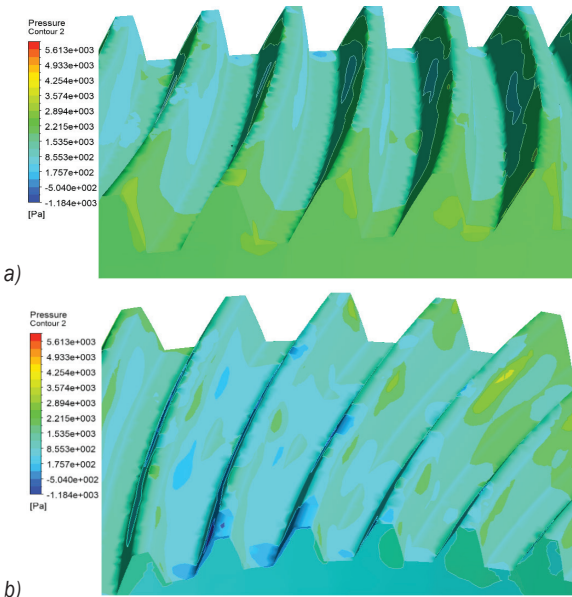


Fig. 12. Pressure distribution in tooth space; a) pressure surface, and b) suction surface [5]

Under the condition of high speed and heavy load, the aviation spiral bevel gear is lubricated by oil injection. The two gears respectively accelerate the fluid around their teeth and carry some fluid to collide and squeeze at their engagement, thus consuming the power of the gear system. Through CFD-POST, it can be calculated that the windage moment on a certain

surface of the gear is the vector sum of the pressure and viscous force on all elements of the surface to the specified axis. The calculation equation, Eq. (7) is:

$$\mathbf{M} = \sum_{i=1}^n (\mathbf{r} \times \mathbf{F}_p) + \sum_{i=1}^n (\mathbf{r} \times \mathbf{F}_v), \quad (7)$$

where  $\mathbf{M}$  is the calculated windage torque;  $\mathbf{F}_p$  and  $\mathbf{F}_v$  are the pressure and viscous force vector on the element surface, respectively;  $\mathbf{r}$  the setting axis vector;  $n$  is the number of elements on the selected wall.

Then the windage power loss of the spiral bevel gear pair is:

$$P_w = \sum_{i=1}^2 M_i \omega_i, \quad (8)$$

where  $M$  is the total windage torque value of gear;  $\omega$  is the angular speed of gear;  $i$  takes 1 or 2 to indicate the pinion or gear.

### 3 RESULTS AND DISCUSSION

#### 3.1 Dimensionless Analysis of Windage Moment

From the above analysis, it can be seen that the windage power loss of the gear with oil injection lubrication is not only related to the geometric parameters and working condition of the gear but also to the fluid characteristics, such as density and viscosity. Therefore, in order to concentrate the influence of these parameters on windage torque and enhance the comparability of calculation results, all results are dimensionless. The dimensionless coefficient  $C_M$  of windage torque is obtained with the following equation (Eq. (9)):

$$C_M = \frac{M}{1/2 \rho \omega^2 R^3}, \quad (9)$$

where  $M$  is windage torque;  $\omega$  is the gear angular velocity;  $R$  is the pitch radius of the gear;  $\rho$  is the equivalent density of oil-gas two-phase flow.

Fig. 13 shows the relationship between the dimensionless moment coefficient and the rotational Reynolds number, showing the windage torque obtained by test and numerical simulation. The rotational Reynolds number is:

$$Re = \frac{\rho_e \omega R^2}{\mu_e}, \quad (10)$$

It can be seen from Fig. 13 that the CFD numerical value is in good qualitative agreement with the experimental measurement data; however, from the quantitative perspective, the numerical

result is always lower than the experimental value. The best consistency between the two is in the range of  $Re = 2.0 \times 10^5 \sim 3.0 \times 10^5$ , where the corresponding gear shaft speed is 5500 rpm to 7500 rpm, and the percentage difference of torque value is less than 10 %. The largest difference is at 2500 rpm, when the corresponding Reynolds number is about  $0.7 \times 10^5$ , and the percentage difference is as high as 37 %. This is mainly because there are some uncertainties in the experiment, which are dominant in the lower rotation speed. It can also be found from Fig. 13 that the shape of  $C_M$  curves of the experiment and simulation is similar, all test points change near a curve, and the  $C_M$  value decreases slowly with the increase of  $Re$ , when the data with the highest uncertainty at the speed of 2000 rpm to 3000 rpm can be ignored. This is consistent with the experimental results of Massini et al. [21], Rapley et al. [27] and Johnson et al. [29].

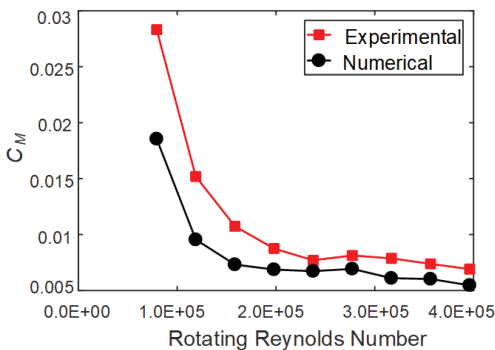


Fig. 13. Graph of  $C_M$  against Rotating Reynolds Number

### 3.2 Mechanical Characteristics of Windage Power Loss

When the gear rotates at a high speed in the oil-gas two-phase flow, in addition to the pressure action of the fluid on the gear surface, due to the viscosity of the fluid, the fluid will produce viscous resistance on each surface of the gear in contact with it, which also constitutes a small part of the windage losses of gears. The distribution of pressure and viscous force of gear pair is shown in Fig. 14.

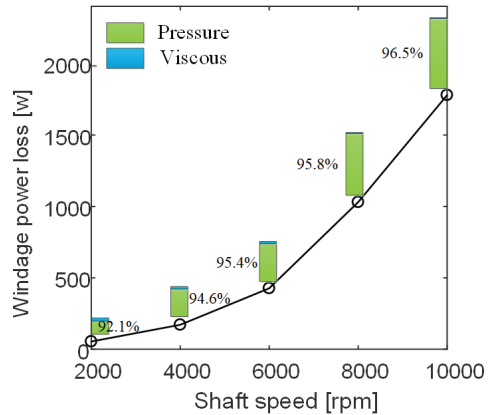


Fig. 15. Gear windage power loss of numerical investigation against rotating speed

It can be seen from Fig. 14 that there is a maximum pressure value on the into-meshing side, while the minimum pressure appears on the tooth surface and end face near the gear out-of-meshing side, and the pressure value is less than the standard atmospheric pressure, which is negative pressure. Since the spiral bevel gear is point meshing, one possible reason is that the volume between the meshing teeth shrinks

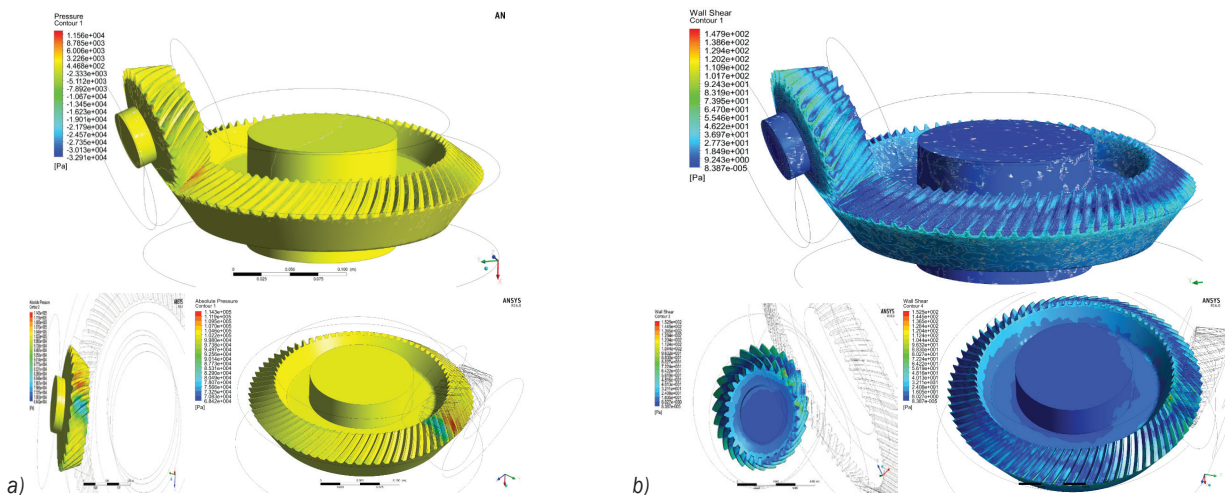


Fig. 14. The distribution of pressure and viscous force on the gears; a) pressure nephogram, and b) viscous pressure nephogram

and the fluid is squeezed during the meshing process, resulting in high pressure here. While the gear teeth on the out-of-meshing side exit from the meshing state and separate rapidly, the two-phase flow around them has been squeezed out or thrown out. Also, the space between the gear teeth increases rapidly, so that the pressure on the out-of-meshing side decreases or even becomes negative pressure. The principle of this phenomenon is similar to that of gear pump.

Fig. 15 shows the variation curve of windage power loss caused by pressure difference force and viscous force with speed. According to the mechanism of windage loss, it can be seen that the pressure difference torque and viscous torque acts on the tooth surface together, while the end face, cone surface and circumferential surface only have viscous torque. At the same time, it can be observed from Fig. 15 that the windage loss caused by pressure difference force accounts for more than 90 % of it. Therefore, from the analysis of mechanical mechanism, the windage power loss of gears is mainly determined by fluid inertia. The bar chart in the figure also shows that the percentage of power loss caused by differential pressure torque in the total windage loss increases

with the increase of speed, that is, the higher the gear speed, the more significant the pressure effect.

### 3.3 Energy Characteristics of Windage Power Loss

The above research shows that the windage power loss of the gear is the kinetic energy loss of the gear caused by the windage torque (differential pressure force and viscous force) when the gear rotates at high speed. When the gearbox is sealed, the lost kinetic energy is divided into two parts, that is, one part is converted into heat energy by the friction between the fluid and the gear surface, and the other part is converted into fluid kinetic energy. The distribution of lubricating oil inside the gearbox and on the gear surface at different time is shown in Fig. 16.

As shown in Fig. 16, due to the revolution speed of pinion is greater than that of gear, the rotation angle of pinion is larger at the same time, so more lubricating oil is carried by the pinion at the beginning of simulation. After a period of time, the lubricating oil carried by the two gears converges and collides near the meshing point, and most of the lubricating oil on the tooth surface is thrown off and falls on the wall of the gearbox.

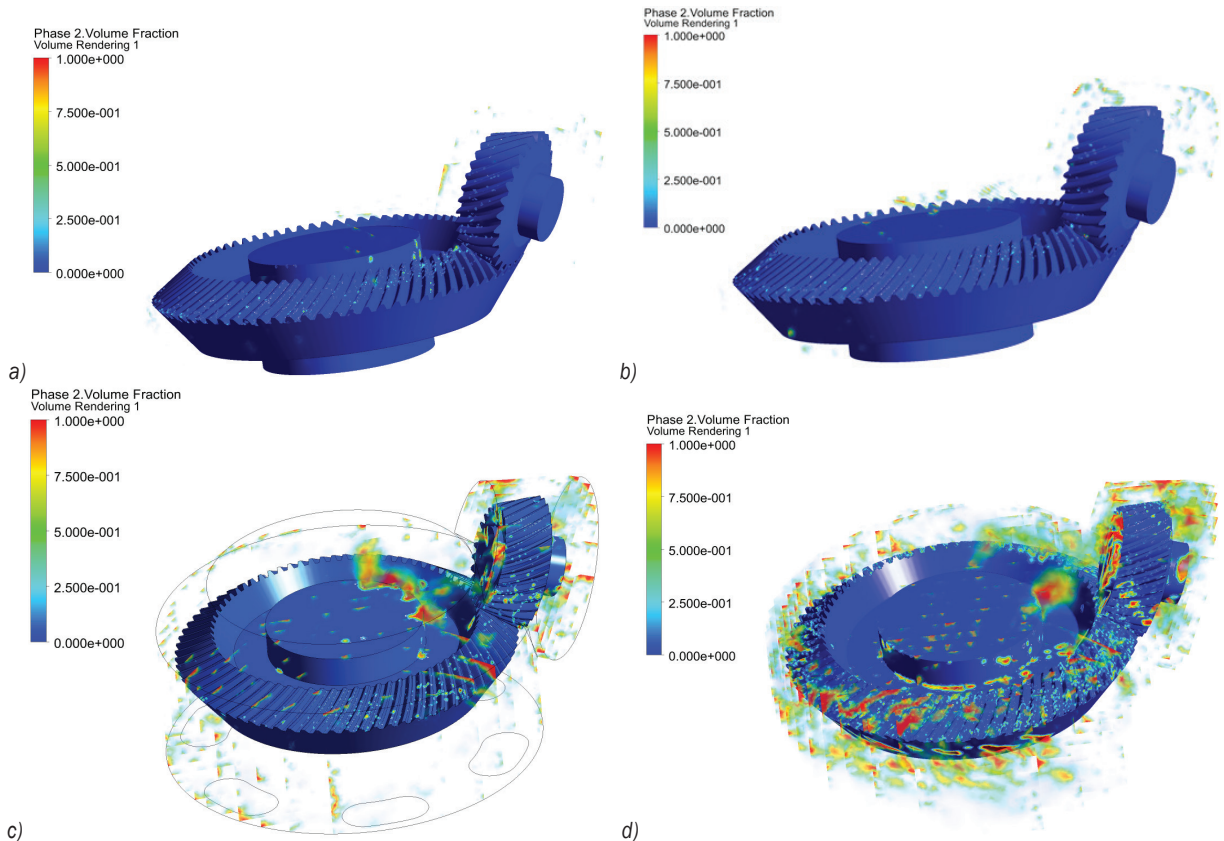


**Fig. 16.** Lubricating oil distribution of gearbox at: a)  $t = 0.005$  s, b)  $t = 0.010$  s, c)  $t = 0.015$  s, and d)  $t = 0.021$  s



Table 7 shows the turbulent kinetic energy and turbulent dissipation rate at different oil-jet velocities obtained by mass-weighted integration of the entire computational fluid domain using CFD post-processing.

**Table 7.** Turbulent kinetic energy and dissipation rate with different oil-jet velocities

Oil-jet velocity [m/s]	Turbulent kinetic energy [kg·m <sup>2</sup> /s <sup>2</sup> ]	Turbulent dissipation rate [kg·m <sup>2</sup> /s <sup>3</sup> ]
10	0.049	335.32
20	0.067	366.25
30	0.091	554.46
40	0.122	725.61
50	0.131	836.57

The turbulent kinetic energy represents the intensity of the turbulent motion inside the gear box. The turbulent dissipation rate represents the amount of fluid kinetic energy lost due to the turbulent motion of the oil-air mixture. As can be seen from Table 7, turbulent kinetic energy and the turbulent dissipation rate both increase with the increase of oil jet velocity. This indicates that the turbulent motion of oil and gas mixture in computational fluid domain becomes increasingly intense. Also, a greater amount of energy is consumed by fluid movement, resulting in the increasing of windage power loss of the gear pair. The relationship between the windage moment and the injection pressure obtained by the orthogonal experimental fitting formula, Eq. (2) in Section 2.4, shows that the results in Table 7 are consistent with the experimental conclusions.

#### 4 CONCLUSIONS

1. A method for measuring the windage losses of spiral bevel gears with oil injection lubrication is proposed by establishing an open power flow windage loss experimental rig. According to the torque values measured with experiments under different working conditions, the corresponding windage torque and rig driveline torque values of the system are calculated.
2. The interaction effect of different oil injection lubrication parameters on windage power loss is studied by orthogonal experiment. According to the experimental data, the formula for calculating the windage power loss of gear pair under oil injection lubrication is obtained. The results show that the shaft speed has the greatest influence on the windage power loss of the gear pair. The second is the injection pressure, adjusting

the injection pressure to change the injection quantity, thereby affecting the volume fraction of lubricating oil around the gear. The injection temperature has the least influence.

3. The CFD numerical model of the spiral bevel gear based on dynamic mesh is established. The fluid distribution, velocity field, and pressure field around the gear are analysed, and the mechanical and energy characteristics of windage power loss are obtained.
4. The dimensionless processing of the experimental data and simulation values of the windage torque of spiral bevel gears is carried out, and the variation law of the dimensionless windage torque coefficient with the rotational Reynolds number is obtained. The results show that the CFD values are in good agreement with the experimental data. With the increase of rotational Reynolds number, the dimensionless windage moment coefficient changes little and fluctuates on an almost horizontal line.

#### 5 REFERENCES

- [1] Dai, Y., Ma, F., Zhu, X., Su, Q., Hu, X. (2019). Evaluation and optimization of the oil jet lubrication performance for orthogonal face gear drive: Modelling, simulation and experimental validation. *Energies*, vol. 12, no. 10, p. 1935-1947, DOI:10.3390/en12101935.
- [2] Fondelli, T., Andreini, A., Facchini, B. (2018). Numerical investigation on windage losses of high-speed gears in enclosed configuration. *AIAA Journal*, vol. 56, no. 5, p. 1910-1921, DOI:10.2514/1.J055871.
- [3] Dong, C., Pei, W., Ren, Z. (2022). Experimental Research on Transmission Characteristics of Elliptic Gear Transmission Systems. *Strojniški vestnik - Journal of Mechanical Engineering*, vol. 68, no. 11, p. 702-712, DOI:10.5545/sv-jme.2022.332.
- [4] Concli, F., Gorla, C. (2017). Numerical modeling of the churning power losses in planetary gearboxes: An innovative partitioning-based meshing methodology for the application of a computational effort reduction strategy to complex gearbox configurations. *Lubrication Science*, vol. 29, no. 7, p. 455-474, DOI:10.1002/ls.1380.
- [5] Li, L., Wang, S., Zou, H., Cao, P. (2022). Windage Loss Characteristics of Aviation Spiral Bevel Gear and Windage Reduction Mechanism of Shroud. *Machines*, vol. 10, no. 5, art. ID 390, DOI:10.3390/machines10050390.
- [6] Dong, C., Liu, Y., Zhao, G. (2021). A Method for Calculating Elliptic Gear Transmission Efficiency Based on Transmission Experiment. *Strojniški vestnik - Journal of Mechanical Engineering*, vol. 67, no. 11, p. 557-569, DOI:10.5545/sv-jme.2021.7318.
- [7] Handschuh, R., Kilmain, C., Ehinger, R., Sinusas, E. (2013). Gear design effects on the performance of high speed helical

- gear trains as used in aerospace drive systems. *AHS Annual Forum and Technology Display*, No. E-18652-1, p. 668-677.
- [8] Kumar, V., Kumar, A., Yadav, S.K., Yadav, A., Prasad, L., Winczek, J. (2022). Numerical Analysis on a Constant Rate of Kinetic Energy Change Based a Two-Stage Ejector-Diffuser System. *Strojniški vestnik - Journal of Mechanical Engineering*, vol. 68, no. 5, p. 368-373, DOI:10.5545/sv-jme.2011.7538.
- [9] Li, L., Wang, S., Zhang, X., Li, Z., Li, F., Zou, H. (2022). Numerical calculation analysis and characteristic research on windage loss of oil-jet lubricated aviation gear pair. *International Journal of Aerospace Engineering*, vol. 6, no. 12, p. 1687-1699, DOI:10.1155/2022/7499587.
- [10] Ding, H., Li, H., Shao, W., Tang, J. (2021). Prediction and control for local bearing contact-based collaborative grinding of non-orthogonal aerospace spiral bevel gears. *Mechanical Systems and Signal Processing*, vol. 160, art. ID 107841. DOI:10.1016/j.ymssp.2021.107841.
- [11] Li, S., Li, L. (2021). Computational investigation of baffle influence on windage loss in helical geared transmissions. *Tribology International*, vol. 156, art. ID 106852, DOI:10.1016/j.triboint.2020.106852.
- [12] Okorn, I., Nagode, M., Klemenc, J. (2021). Operating Performance of External Non-Involute Spur and Helical Gears: A Review. *Strojniški vestnik - Journal of Mechanical Engineering*, vol. 67, no. 5, p. 256-271, DOI:10.5545/sv-jme.2020.7094.
- [13] Anderson, N., Loewenthal, S. (1981). Effect of geometry and operating conditions on spur gear system power loss. *Journal of Mechanical Design*, vol. 103, no. 1, p. 151-159, DOI:10.1115/1.3254854.
- [14] Dawson, P.H. (1984). Windage loss in larger high-speed gears. *Proceedings of the Institution of Mechanical Engineers, Part A: Power and Process Engineering*, vol. 198, no. 1, p. 51-59, DOI:10.1243/PIME\_PROC\_1984\_198\_007\_02.
- [15] Diab, Y., Ville, F., Velex, P. (2006). Investigations on power losses in high-speed gears. *Proceedings of the Institution of Mechanical Engineers, Part J: Journal of Engineering Tribology*, vol. 220, no. 3, p. 191-198, DOI:10.1243/13506501JET1.
- [16] Winfree, D.D. (2000). Reducing gear windage losses from high speed gears. *International Design Engineering Technical Conferences and Computers and Information in Engineering Conference*, p. 747-756, DOI:10.1115/DETC2000/PTG-14449.
- [17] Seetharaman, S., Kahraman, A. (2009). Load-independent spin power losses of a spur gear pair: model formulation. *Journal of Tribology*, vol. 131, no. 2, p. 181-193, DOI:10.1115/1.3085943.
- [18] Ruzek, M., Ville, F., Velex, P., Boni, J.B., Marchesse, Y. (2019). On windage losses in high-speed pinion-gear pairs. *Mechanism and Machine Theory*, vol. 132, no. 5, p. 123-132, DOI:10.1016/j.mechmachtheory.2018.10.018.
- [19] Delgado, I.R., Hurrell, M.J. (2017). Experimental investigation of shrouding on meshed spur gear windage power loss. *73rd Annual Forum and Technology Display*, NASA/TM-2017-219536.
- [20] Handschuh, R. F., Hurrell, M.J. (2010). Initial experiments of high-speed drive system windage losses. *International Conference on Gears*, art. ID 20100036224.
- [21] Massini, D., Fondelli, T., Andreini, A., Facchini, B., Tarchi, L., Leonardi, F. (2018). Experimental and numerical investigation on windage power losses in high speed gears. *Journal of Engineering for Gas Turbines and Power*, vol. 140, no. 8, DOI:10.1115/GT2017-64948.
- [22] Maccioni, L., Chernoray, V.G., Mastrone, M.N., Bohnert, C., Concli, F. (2022). Study of the impact of aeration on the lubricant behavior in a tapered roller bearing: Innovative numerical modelling and validation via particle image velocimetry. *Tribology International*, vol. 165, art. ID 107301, DOI:10.1016/j.triboint.2021.107301.
- [23] Mastrone, M.N., Concli, F. (2021). CFD simulations of gearboxes: implementation of a mesh clustering algorithm for efficient simulations of complex system's architectures. *International Journal of Mechanical and Materials Engineering*, vol. 16, no. 1, art. no. 12, DOI:10.1186/s40712-021-00134-6.
- [24] Gorla, C., Concli, F., Stahl, K., Höhn, B.R., Michaelis, K., Schultheiß, H., Stemplinger, J.P. (2013). Hydraulic losses of a gearbox: CFD analysis and experiments. *Tribology International*, vol. 66, p. 337-344, DOI:10.1016/j.triboint.2013.06.005.
- [25] Fondelli, T., Andreini, A., Da Soghe, R., Facchini, B., Cipolla, L. (2015). Numerical simulation of oil jet lubrication for high speed gears. *International Journal of Aerospace Engineering*, vol. 2015, art. ID 752457, DOI:10.1155/2015/752457.
- [26] Farrall, M., Simmons, K., Hibberd, S., Young, C. (2005). Computational investigation of the airflow through a shrouded bevel gear. *ASME Turbo Expo 2005: Power for Land, Sea, and Air*, no. 3, p. 1259-1265, DOI:10.1115/GT2005-68879.
- [27] Rapley, S., Eastwick, C., Simmons, K. (2008). Effect of variations in shroud geometry on single phase flow over a shrouded single spiral gear. *Heat Transfer, Parts A and B*, vol. 4, DOI:10.1115/gt2008-50633.
- [28] Webb, T.A., Eastwick, C., Morvan, H. (2010). Parametric modelling of a spiral bevel gear using CFD. *Proceedings of the ASME Turbo Expo*, p. 229-238, DOI:10.1115/GT2010-22632.
- [29] Johnson, G., Chandra, B., Foord, C., Simmons, K. (2009). Windage power losses from spiral bevel gears with varying oil flows and shroud configurations. *ASME Turbo Expo: Power for Land, Sea, & Air*, vol. 131, no. 4, art. ID 041019, DOI:10.1115/1.3072519.
- [30] Simmons, K., Johnson, G., Wiedemann, N. (2012). Effect of pressure and oil mist on windage power loss of a shrouded spiral bevel gear. *Journal for Engineering for Gas Turbines and Power*, vol. 134, no. 8, art. ID 081202, DOI:10.1115/1.4005984.
- [31] Harris, T.A. (1984). *Rolling Bearing Analysis*, 2<sup>nd</sup> ed., Wiley, New York.
- [32] Liang, R. (2008). Orthogonal test design for optimization of the extraction of polysaccharides from *Phascolosoma esulenta* and evaluation of its immunity activity. *Carbohydrate Polymers*, vol. 73, no. 4, p. 558-563, DOI:10.1016/j.carbpol.2007.12.026.
- [33] AGMA, (1995). *Fundamental Rating Factors and Calculation Methods for Involute Spur and Helical Gear (Metric Version)*, American Gear Manufacturers Association, 2101-C95.



# Prioritizing the Key Actors of an Organization for Business Excellence Using the Efficient Interpretive Ranking Process

Sumit Kumar\* – Pardeep Gupta

Sant Longowal Institute of Engineering & Technology, India

*Flexibilities are involved in the process of decision-making. They offer much freedom of choice in terms of the selection of suitable actors who interact with the dynamic environment of the organization. This paper presents a systematic and holistic approach to ranking key actors responsible for the business excellence of an organization. The study highlights the area where the actors of the organization should focus on achieving desired business excellence. It portrays the outcome in the form that top management is the most influential actor since it is responsible for the formulation of the vision/mission of the organization along with the setting of plant quality targets, cost-saving targets, manpower planning, and policy formulation for energy-saving. Top management is followed by cross-function teams (CFTs) and the government of India (GOI) in terms of interaction with the various processes. The novelty of this case study is that it utilizes qualitative and interpretive tools for the analysis, which does not require much statistical knowledge to produce outcomes, and the results are easy to understand. The reported results are in consensus with the results reported by various studies that are conducted using quantitative tools like Analytic Hierarchy Process (AHP), Technique for Order of Preference by Similarity to Ideal Solution (TOPSIS), total interpretive structural modelling (TISM), etc. that require statistical excellence for the calculation, interpretation, and dissemination of results to the general public and shopfloor employees.*

**Keywords:** flexibility, decision making, situation-actor-process, learning-action-performance, interpretive ranking process, business excellence, top management, Government of India, cross-functional teams

## Highlights

- Adopted qualitative and interpretive SAP-LAP framework of an organization for the identification key actors of the organization.
- The adopted methodology is qualitative and interpretive and thus easy to implement and provides understandable results.
- The efficient interpretive ranking methodology is intuitive and evolving in nature and can be effective in multiple criteria decision-making.
- The depicted methodology is a fully formed tool for shop floor implementation even by the employees without much knowledge about statistical tools.

## 0 INTRODUCTION

The business excellence of an organization can be viewed in terms of the achievement of cost competitiveness, increased productivity, the attainment of competitive quality levels, and high customer satisfaction accompanied by good customer loyalty and customer retention. The road to business excellence must involve a systematic approach to make decisions while keeping the freedom of choice in the mind. This makes decision-making a critical core process of any business excellence philosophy. The freedom of choice can be managed by ranking the variables that directly or indirectly affect the process of multi-criteria decision-making. The ranking is often carried out by the researchers and practitioners for prioritizing the variables (e.g., critical success factors, barriers, risk factors, etc.) responsible for the implementation of business excellence philosophies like total quality management (TQM), total productive maintenance (TPM), lean manufacturing, etc. Talib and Rahman [1] proposed a model based on the critical success factors (CSFs) responsible for successfully implementing TQM in the service industry and they

ranked the CSFs based on the frequency of their use. In a similar study conducted by Kumar et al. [2], the ranking of the CSFs for implementing TQM in the Indian scenario was done using the technique for order of preference by similarity to ideal solution (TOPSIS) approach. Talib and Rahman [3] adopted the analytic hierarchy process (AHP) approach for ranking the barriers to TQM implementation. Sraun and Singh [4] presented business excellence as a continuous improvement process; there are many strategies for continuous improvement, so the authors ranked the various strategies (TQM, just-in-time (JIT), leadership, TPM, customer relationship (CR), system core work, total employee involvement (TEI), supplier development) for achieving it. The authors ranked total quality management at the top position. Ojha et al. [5] presented their work on the study of the critical factors affecting manufacturing excellence using the interpretive structural modelling technique. Most of the above-mentioned studies ranked the actors that are internal to an organization (e.g., top management support or commitment, employee participation, cross-functional teams, etc.), but these studies failed to address the dynamic contextual

relationship that exists between these actors. Similarly, in managing certain issues within the organization, some external actors (e.g., government policies) play an important role, as depicted in a case study carried out in the construction industry by Taofeeq et al. [6] thus, it becomes important for an organization to incorporate the influence of changes in government policies into goal setting process through a forward-looking, anticipatory conceptualization [7]. To reduce the impact of changed government policies, the organization must modify its goal dimensions or its aspiration level [7]; thus, it can be said that the government support moderates significantly among investment strategies, financial knowledge, and organizational profitability, leading towards sustainable development goals [8].

The importance of cross-functional management has been addressed by Witcher and Butterworth [9], whose work was focused on policy deployment through *hoshin kanri* in UK subsidiaries. The authors elevated the importance of cross-functional management in deploying policies for the implementation of TQM and considered policy deployment as a prerequisite for the TQM. Further, Witcher and Chau [10] explored the concepts of policy deployment using balance score card methodology and *hoshin kanri* and found that an organization should consider both its long-term and short-term capabilities along with its core competencies. It was mandated to involve cross-functional management and top executive audits to become a strategically fit organization. In a study carried out to explore the similarities in critical success factors of *hoshin kanri* and quality management, it has been observed that many CSFs of *hoshin kanri* are similar, including top management commitment, cross-functional management, vision, strategies, etc. [11].

The above discussion presents a picture of some of the factors, such as top management, cross-functional management, and government policies, that play crucial roles in deciding the future of business excellence. Therefore, it has become vital to understand the contextual relationship among these actors. The ranking techniques can be broadly classified as quantitative or qualitative techniques. These techniques/tools have their own merits and demerits. The quantitative tools employ a suitable scale for ranking the variables, whereas the qualitative tools employ subjective interpretation by an expert about the variables for ranking, as expressed by Sushil [12]. This paper concentrates on the use of qualitative tools to address system flexibility. Interpretive structural modelling, total interpretive structural

modelling, and situation, actor, process-learning, actions, performance, etc., are some qualitative tools used to address the flexibility of the system as expressed by Sushil [13] to [15]. Sushil [13] expressed that the flexibility gaps of a managerial situation can easily be identified using the situation-actor-process-learning-action-performance (SAP-LAP) framework.

A framework based on the SAP-LAP approach has been successfully applied to investigate the supply chain issues by Arshinder [16], Banwet and Pramod [17] and Shukla et al. [18] in various Indian organizations. Further, the SAP-LAP approach has also been adopted to analyse a humanitarian supply chain to reduce the impact of a disaster on human life Lijo [19]. A study was carried out by Kumar et al. [20] to analyse the coal transportation supply chain using the SAP-LAP analysis. Shalender and Singh [21] presented a study in which they assessed the mediating effect of product flexibility on the business excellence of the organization using the SAP-LAP approach. The flexibility issues in the maintenance program for resolving the engineering support issues were studied using the SAP-LAP framework by Garg and Deshmukh [22]. Matharu and Sinha [23] and Palanisamy [24] worked on lean implementation and building information systems for small and medium enterprises using the SAP-LAP framework. The trend in India to determine whether it has enough resources to sustain a growing urban population was analysed using the SAP-LAP framework by Chavan et al. [25]. Sushil [26] expressed variable ranking as a pivoting process of management and decision-making. Sushil [26] also found that most management processes that involve the selection of the variable and decisions about the ranking of these variables are based on subjective evaluation and logic. Interpretive ranking process (IRP) utilizes the interpretive matrix and pair comparison of interpretations as a model base. The above analysis results in the development of a knowledge base. Based on this information, a dominance matrix is prepared. These dominant relationships and interpretations have been shown as an interpretive ranking model [26]. The key success factors involved in the implementation of world-class manufacturing were ranked with the help of an interpretive ranking process; the ranking model was based on the interpretive structural modelling by Haleem et al. [27]. For addressing the complexities involved in the green supply chain, Mangla et al. [28] formulated a generic SAP-LAP model addressing the strategies for reducing the risks involved. The implementation of lean is a difficult task as it has many barriers, so, Zhang et al. [29] adopted an

interpretive ranking process to rank the barriers to the implementation of lean manufacturing. Hughes et al. [30] studied the key factors responsible for the failure of information systems projects. They studied interrelationships between factors responsible for failure using an IRP approach. Narkhede et al. [31] adopted the IRP to rank various criteria and the interaction with the selection process of the third-party logistics service provider (3PLSP). Mhatre et al. [32] carried out the modelling of CSFs involved in construction projects with the help of IRP and system dynamics. Sushil [33] presented an approach named efficient-IRP (eIRP), which reduces the number of paired comparisons thus enabling it to handle a large number of variables. Malik et al. [34] carried out an analysis of the financial inclusion situation in India. The researchers adopted an efficient IRP to rank actors in the Indian economy. Parameswar et al. [35] applied the integrated total interpretive structural modelling-interpretive ranking process (TISM-IRP) approach to study the interaction for the choice of international joint venture firms after their termination. The authors presented the ranking of factors as supplier-buyer, complement, or competitor. Siva Kumar and Anbanandam [36] studied the freight transportation system in India using SAP-LAP and the e-IRP approach; they also suggested a flexible policy framework. The prioritization of actors *viz* top management, generators, retailer, consumers, government policy and regulation, and technology vendors for energy management in a smart grid system was carried out using SAP-LAP methodology by Pal & Shankar [37]. To understand the strategic issues in the integration of Industry 4.0 and the circular economy, a qualitative study has been conducted using the SAP-LAP framework by Chauhan et al. [38]. Further, both SAP-LAP and eIRP techniques have been used to prioritize the stakeholders: government policymakers, industry associations, research and academic institutions, manufacturers, and customers responsible for the implementations of Industry 4.0 [39].

This paper presents a real-life analysis of an organization using the efficient interpretive ranking process (eIRP), which is a novel approach for ranking the factors and is designed to address the limitations of other analytical and quantitative tools, such as the analytic hierarchy process (AHP) and analytic network process (ANP). Unlike AHP and ANP, the eIRP uses an alternate pair-wise comparison methodology to avoid cognitive overload on experts and generate a qualitative interpretation of the rating.

The research was conducted in the following two stages, and this paper presents the second stage.

1. Development of SAP-LAP framework of the organization for the select key business excellence issues [40].
2. Ranking of selected actors of the organization involved in the framework using the eIRP approach.

In this paper, the already developed SAP-LAP framework by Kumar and Gupta [40] has been used for further analysis with the eIRP approach. The novelty of this work lies in its application to rank the actors of a case organization responsible for business excellence. By using the eIRP, we were able to generate an interpretive database that the organization can use for future decision-making. The results of the case study were reported back to the organization.

From the above literature review, it can be established that many studies had been conducted for ranking the actors of the organization using quantitative tools like AHP, TOPSIS, etc., but there is a limited number of studies that uses a qualitative method for ranking the actors of the organization. In this paper, a qualitative ranking approach eIRP is adopted to rank the actors of an organization responsible for business excellence.

## 1 RESEARCH METHODOLOGY

### 1.1 Research Context

The study presents results from an in-depth case study of an Indian manufacturing organization: ABC Ltd. Yin [41] had selected a single organization for analysis as it can facilitate an in-depth examination of dynamics that are present in a single and unique real-life setting. This case study can be considered instrumental as it explores an in-depth examination of a particular situation and produces a knowledge base to advance understanding of more generic issues [42]. A single case study can also contribute data to examine theories to capture dynamics and complexities involved in interactions and developments over time that cannot be captured purely by the statistical analysis of any survey [43].

### 1.2 Data Collection

The qualitative data was collected by conducting semi-structured telephonic interviews with the middle and senior-level employees of the organization based on the SAP-LAP model of inquiry, as shown in Table 1. For the generalization of results, the responses were

also taken from relevant academic experts. All the respondents were informed well in advance through email about the interviews. Table 2 shows information about the number of respondents.

The data for the analysis is collected from the company’s annual reports, and business excellence newsletters and, with the help of semi-structured telephone interviews, (qualitative data) were collected from mid- and senior-level practitioners via personal interviews using the SAP-LAP model of inquiry as shown in Table 1.

**Table 1.** SAP-LAP model of enquiry

Element	Queries
Situations	What are the current issues of the organization? What are the performance parameters of the organization? What are the different initiatives adopted to improve the performance of the organization?
Actors	Who are the key actors in resolving the current issues of the organization? Who are the key actors responsible for selecting, monitoring, controlling, and improving the performance parameters?
Processes	What are the processes adopted to improve the current situation? What are the key processes adopted for selecting, monitoring, controlling, and improving the performance parameters? What could be the new key processes through which improvements of performance parameters can be done?
Learning	What are the challenges with reference to the current situation? What are the challenges with reference to various performance parameters? What are the challenges faced by various actors in improving the situations?
Actions	What are the actions that need to be taken to address the issues/challenges of improving the financial and non-financial performance parameters?
Performance parameters	How are the proposed actions going to affect the current scenario for financial parameters? How are the proposed actions going to affect the current scenario for non-financial parameters? What will be the potential impact of the actions on key actors? What will be the potential impact of the actions on various processes?

**Table 2.** Experts’ domain

S. no.	Expert domain	No. of experts	Roles
1.	Industry	65	Senior manager (05), Manager (10), Supervisors (50)
2.	Academics	11	Academic researchers

### 1.3 Error and Biasing Control

The research instrument was meticulously crafted and reviewed by experts to ensure that the questions were simple, clear, non-redundant, and free of bias. Question-ordering bias was addressed by asking first general open-ended questions and then specific questions. To eradicate confirmation bias, the data were analysed by two researchers with an unbiased perspective and followed by sharing the case study reports with the participants [41]. To avoid common method bias, the anonymity of responses was maintained, and participants were protected from evaluation apprehension [44]. Furthermore, any leading, biased, or closed-ended questions were eliminated from the questionnaire to prevent any socially desirable or agreeable responses.

### 1.4 Data Analysis

The primary data collected through the interview and secondary data collected from the organization’s newsletters, annual report, and website were clustered into categories using codes. The discussions in an iterative manner were carried out until both researchers attained consensus.

## 2 SAP-LAP FRAMEWORK

The organization ABC Ltd. is an Indian automobile manufacturer established in 1994. It manufactures medium-sized and commercial vehicles. The organization is determined to design, develop, manufacture, and market independently its commercial vehicles as per customer needs. The market share of the organization is 31.2 % in medium and heavy commercial vehicles in India in the 2019 fiscal year (FY19). The company registered a revenue of USD 2 billion in FY19. The data analysis begins with the extraction of the information as presented in Table 3. The authors identified the most influential situations in the organization along with the actors that play significant roles in these situations. The authors also identified the process required to make the transformations.

The information learning due to the existence of current situations and processes aids in understanding “why” the current state of the system exists. This further help in the identification of the most probable actions that need to be taken for the improvement of the system in ABC Ltd.

The identified actors have conflicting roles in the identified processes due to the existence of interactions



among them. The SAP-LAP framework provides a holistic way for the identification and resolution of these conflict roles. The conflict in the roles exists in the form of self-interactions (i.e., between the actors) and cross-interactions (i.e., between actors and processes). The self-interaction among the various actors can be envisioned as information, support, teamwork, knowledge sharing, and reporting whereas the cross interactions between the actors and processes can be seen as roles of actors in the currently selected process. The information obtained from the cross-interaction of actors and processes will be utilized for ranking the actors in terms of their dominance in a particular process using eLRP.

Binary and interpretive matrices were used to present the interactions between actors and processes. The selected actors and processes are defined in the following section.

**Table 3.** Elements of SAP-LAP framework

Components	Elements
Situations	SN1: High inflation
	SN2: High power cost
	SN3: Old machines and plant
	SN4: Wide range of product
	SN5: High manpower cost
Actors	ACT1: Government of India
	ACT2: Top management
	ACT3: Cross-functional Teams
Processes	PR1: Strategic Planning
	PR2: Quality assurance (QA)
	PR3: Cost management (CM)
	PR4: Human resource management (HRM)
	PR5: Energy management
Learnings	LN1: Global vision of the organization
	LN2: Technology up-gradation
	LN3: MUDA reduction program
	LN4: Capacity enhancement/Efficiency improvement
	LN5: Liaison with alternate energy resources
Actions	ACN1: Energy policy as a core objective
	ACN2: Maintenance policy
	ACN3: Technology Management
	ACN4: Use of IT in cost management
Performance	PP1: Productivity improvement
	PP2: Quality improvement
	PP3: Power consumption reduction
	PP4: Total conversion cost reduction

**2.1 Defining Actors and Processes**

**Actors (ACTs):** Actors of an SAP-LAP framework are the elements that deal with the current prevailing situation in an organization; these can be in the form

of customers, suppliers, top management, employees, etc. The identified actors are defined below. These actors can be external or internal to an organization.

**Actor 1 (ACT1): Government of India (GoI):**

The government of the country policies and these policies directly and indirectly the performance of an organization (e.g., a fiscal policy can directly affect the profits margins of an organization). In the present case study, it has been seen that inflation is a serious issue for the case organization and thus it needs to take suitable actions to counter it.

**Actor 2 (ACT2): Top management:**

In any organization the top management plays a pivotal role in crafting strategies and business objectives. It is also responsible for resource allocation and taking decisions are per the requirements. Most of the time, it is seen that the top management needs to communicate with the government for the formulation of policies as per its requirement.

**Actor 3 (ACT3): Cross-functional teams**

**(CFTs):** Cross-functional management involves persons of varied expertise to solve common issues that gave cross-linkages. Most of the issues in the case organization were found of multiple cross interactions so CFTs is selected as an actor for achieving key management indices (KMIs) or business goals by establishing relative key performance indices (KPIs) and key activity indices. The annual objectives of the organization are managed through various CFM teams. The CFM teams are led by a senior leader of the plant with members selected from various departments. The employees of the organization are included in the CFM while doing the analysis.

**Processes (PRs):**

The processes are transformational activities. The actors are involved in these activities for doing the transformations. These may represent supply chain management, outsourcing, production, and core competence building. The identified processes are defined below.

**Process 1 (PR1): Strategic planning (SP):**

Strategic planning in an organization is the foundation of its excellence. It is responsible for establishing the performance parameters along with their measurement.

**Process 2 (PR2): Quality assurance (QA):**

Quality assurance (QA) in the organization is responsible for achieving competitive quality levels. It also ensures the establishment of a quality culture from supplier to end customer. The case organization was witnessing several quality issues due to increased manufacturing complexity.

**Process 3 (PR3): Cost management (CM):**

Cost is a principal concern of every organization and needs



to be managed for optimizing the cost of end products. With twenty-year-old plants, the organization was dealing with aging assets burdened with production load. This posed threats in terms of delivering end products at a competitive price in the market.

**Process 4 (PR4): Human resource management (HRM):** HRM is selected as a process in this case study as it is responsible for the roles and responsibility distribution, employee skill development, training, rewards, recognition, etc. HRM in this organization played a striking role by contributing to increasing human productivity through total employee involvement.

**Process 5 (PR5): Energy management (EM):** from the secondary data, it was observed that the energy cost for the plant was on the higher side. This issue can be addressed in cost management, but there were some issues regarding the source of electricity, so it was decided to take up this as a new management approach.

3 EFFICIENT INTERPRETIVE RANKING PROCESS (eIRP)

The various steps involved in the interpretive ranking process are listed below [26].

1. Identification of ranking variables (X) and reference variables (Y).
2. Clarification of the contextual relationship between ranking and reference variables.
3. Identification of interactions of ranking variables (X) with reference variables (Y).
4. Development of interpretive matrix interpretation with the help of interaction matrix.
5. Pairwise comparison of ranking variables interactions with reference to variables to identify dominance matrix (interpretive logic – knowledge base-dominance interaction matrix).
6. Summary of the count of dominant interactions (with/without) weightage to the reference variables and computation of ranks (dominance matrix).

7. Validation of ranks: internal validity; cross validity; sensitivity analysis.
8. Graphical representation of ranks.
9. The decision about ranks and suggested actions.
10. Creation of knowledgebase.

**3.1 Establishing Contextual Relationships between Ranking and Reference Variables**

In the present case, the identified actors of the organization (i.e., ACT1: GoI, ACT2: Top management, and ACT3: CFTs) are the ranking variables, and they are ranked with reference to variables (i.e., processes). The contextual relationship between the various ranking variables and reference variables in binary and interpretive form is presented in Tables 4 and 5, respectively.

**Table 4.** Cross-interaction matrix for actors and processes-Binary matrix

		Actors				
External	ACT1	1	0	0	0	0
	ACT2	1	1	1	1	1
Internal	ACT3	1	1	1	1	0
	Process	PR1	PR2	PR3	PR4	PR5
					Internal	External

**3.2 Dominance Matrix: Paired-Wise Comparison**

The interpretive matrix as shown in Table 5 is used as a base to do a pair-wise comparison of ranking variables with reference to variables (i.e., actor ACT1 and ACT2 are compared for the various processes mentioned above). The outcome of this comparison is the interpretive logic of dominant interactions that exist among the actors for various processes. This interpretive dominance knowledge base is presented in Table 6.

From the information present in Tables 4 to 6, it can be seen that ACT 1: GoI interacts with other others only for processes PR1: Strategic planning as the

**Table 5.** Cross-interaction matrix for actors and processes-Interpretive matrix

		Actors				
External	ACT1	Economic policy formulators	-	-	-	-
	ACT2	Vision and plant objectives	Plant quality targets	Cost-saving targets	Manpower planning	Energy-saving project coordinator
Internal	ACT3	Key performance indicators	Quality improvement	Plant cost reduction	Skill improvement	-
	Process	PR1	PR2	PR3	PR4	PR5
					Internal	External

**Table 6.** Paired comparison with interpretations of ranking of actors with reference to processes

Paired comparison	Interaction with process	Interpretive logic
ACT1-ACT2	PR1	Formulation of economic policy and its inclusion in vision and mission statements is a must
	PR2, PR3, PR4, and PR5	ACT1 no direct role
ACT1-ACT3	PR1	The economic policies of GOI should drive the KPIs
	PR2, PR3, PR4, and PR5	ACT3 no direct role
ACT2-ACT1	PR2, PR3, PR4, and PR5	ACT1 no direct role
ACT2-ACT3	PR1	Vision statement & Plant objective should drive the KPIs
	PR2	The quality policy of the plant should drive the quality improvement projects
	PR3	The cost-saving targets should drive the plant cost-reduction projects
	PR4	Manpower planning should consider the skill improvement of employees
	PR5	ACT3 no direct role
ACT3-ACT1	PR2, PR3, PR4, and PR5	ACT1 no direct role
ACT3-ACT2	PR5	ACT3 no direct role

**Table 7.** Dominating Interaction matrix- ranking of actors with reference to processes

		Dominating		
		ACT1	ACT2	ACT3
Being dominated	ACT1	-	PR1	PR1
	ACT2	PR2, PR3, PR4, and PR5	-	PR1, PR2, PR3, PR4, and PR5
	ACT3	PR2, PR3, PR4, and PR5	-	-

organization’s economic policies will be governed by the fiscal policies of the Indian government. Similarly, it can also be seen that for process PR5: Energy management, ACT2: Top management dominates the

other two actors as top management is responsible for policy making. Table 7 shows the dominance of various actors against the selected processes in a concise manner.

**3.3 Identification of Types of Dominance Interaction**

After establishing this information, the next step is determining the type of dominance and for this, the adopted procedure is stated below.

The dominance interaction of one alternative (*m*) over the other alternative (*n*) for a criterion can be identified as follows from a binary cross-interaction matrix.

Implicit dominance: This type of dominance interaction occurs when an alternative (*m*) has a relationship whereas alternative (*n*) has no relationship: (1) and (0) in the binary matrix for a positive criterion, then the alternative (*m*) implicitly dominates the alternative (*n*) for the positive criterion and vice versa in case of negative criterion.

Implicit non-dominance: This type of dominance occurs if both (*m*) and (*n*) cells have no relationship: (0) in the binary matrix. This can also happen if both the (*m*) and (*n*) cells have a relationship: (1) in the binary matrix and the interpretations for both the factors are same in the (*m*) and (*n*) cells then there exists implicit non-dominance and then enter (0) in in the *m-n* cell.

Interpretive dominance: when both the (*m*) and (*n*) cells have a relationship (1) but their interpretations are different in both the cells, then the dominance relationship is decided by an external expert with proper justification.

Transitive dominance: This type of dominance occurs when there are entries (1) in more than two cells for a criterion but with different interpretations. Then if *m-n* is a dominant interaction, (*n-k*) and (*m-k*) will be transitive dominance. Table 8 shows the contribution of various types of dominance

**Table 8.** Various dominance comparisons for actor *x* process

Reference variables	Implicit dominance	Implicit non-dominance	Transitive dominance	Interpretive dominance	Total comparison	% Interpretive comparison
PR1	0	0	0	3	3	100
PR2	2	0	0	1	3	33.33
PR3	2	0	0	1	3	33.33
PR4	2	0	0	1	3	33.33
PR5	2	1	0	0	3	0.00
Total	8	1	0	6	15	
Percentage	53.33	6.66	0.00	53.33		

interactions in the system and it can be seen that there is no transitive dominance in the system.

For better visualization of these interactions in the various process, individual matrices for the process can be drawn as shown in Fig. 1a to e. Fig. 1 shows the type of dominance for various actors in a color-coded scheme per scheme shown in Fig. 1f.

### 3.4 Ranking of Actors

To rank the actors the steps mentioned in Section 3.3 were repeated obtaining the dominating interactions for the remaining process. for calculating the ranks of the actors following steps are adopted.

1. The overall dominance matrix was calculated by summing all possible dominance interactions.
2. Calculate, the number of all paired comparisons with their respective percentages.

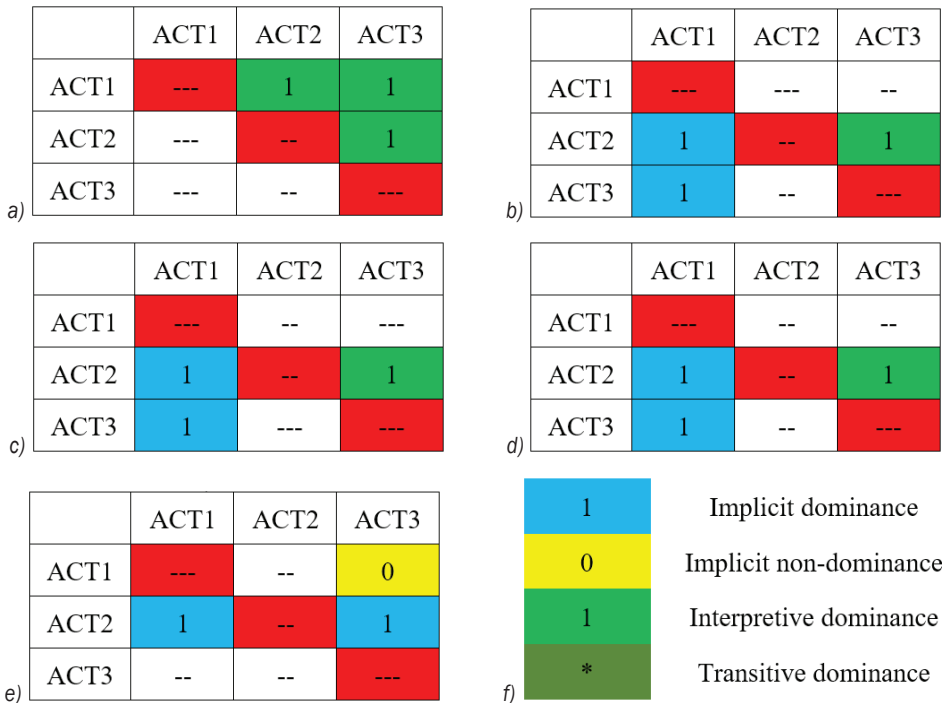


Fig. 1. Dominance of actors for various processes; a) PR1, b) PR2, a) PR3, a) PR4, a) PR5, and color-coding scheme for various dominances

Table 9. Dominance matrix- for ranking of actors w.r.t process

	ACT1	ACT2	ACT3	No. of dominating (D)	Balance dominance (D-B)	Adjusted net dominance (AND)	Dominance index (DI)	Rank dominating
ACT1	---	1	1	2	-6	0	00	III
ACT2	4	--	5	9	8	14	93.33	I
ACT3	4	0	---	4	-2	4	26.66	II
No. of being dominated (B)	8	1	6			15 Total interactions		

3. Calculate the rank of a factor based on the dominance index equation, Eq. (1) [45].

$$DI_x = \frac{AND_x}{Total\ interaction\ (TI)} \times 100. \quad (1)$$

Based on the above index, the ranks of variables are calculated and shown in Table 9. Fig. 2 shows the interpretive ranking model of actors for various processes.

## 4 RESULTS AND DISCUSSIONS

From the information presented in Table 9, it can be seen that the top management is the top-ranked actor among the others in an organization as this actor holds the responsibility for the formulation of policies related to aspects like quality, cost, and energy [1] to [4]. Also, it can be seen that the government of India

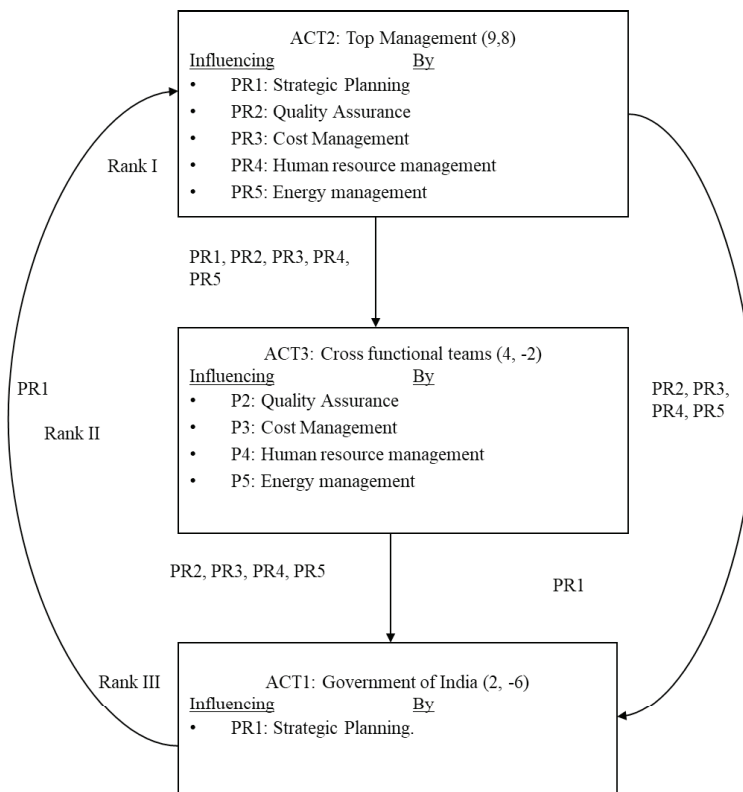


Fig. 2. Interpretive ranking model for actors with regard to processes

is the only actor that interacts with top management and the interaction happens only in the process of strategic planning where top management design its economic policies based on the economic policies of the government.

CFTs handle the issues of cross-functional management, which directly contributes to the deployment of the strategic policies formulated by top management. CFTs under cross-functional management deploy, monitor, and review the KPIs and KMIs. The importance of CFTs in an organization had been reported in several studies [9] to [11]. Therefore, the present study offers the following propositions.

Proposition 1: To curtail the situation of high inflation, the top management should frame its policies as per the fiscal policies of the government of India.

Proposition 2: To minimize the high cost of power, the top management should frame its energy policy focusing on the purchase of energy from renewable resources, cutting dependencies on diesel generators, etc.

Proposition 3a: To handle the cost of maintaining old plants and machinery, the top management should include a maintenance policy as its core policy.

Proposition 3b: The purchase of new machines to replace old low-energy-efficiency machines through cross-functional teams, which will be responsible for the achievement of associated key performance and key management indices.

Proposition 4: To produce a wide range of products, the top management should adopt a policy on manufacturing flexibilities in its core policies and implement these policies through CFTs. The CFTs will handle the KPIs and KMIs for the quality, cost, and delivery.

Proposition 5: For managing the issues related to manpower, the top management should design strategic objectives and process them through the process of human resource management.

## 5 VALIDATIONS OF THE RANKING MODEL

The ranking model can be validated through the internal validity of pair-wise comparison of actors ( $A_m - A_n$ ) through dominance system graphs for various processes ( $P_i$ ). At the very first stage, the ranking model can be validated by making certain that the net sum of all the net dominances is zero [26]. Secondly, by drawing system dominance digraphs as shown in



Fig. 3 and ensuring that there should not be a feedback loop in the digraphs as the feedback loop does not indicate clear dominance relationships. The actual validation of the model can only be done by adopting the model on the shop floor.

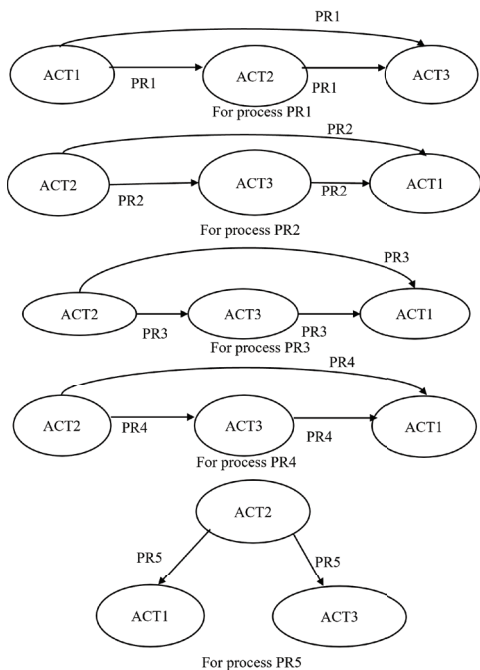


Fig. 3. Internal validation of the ranking model

## 6 CONCLUSIONS AND PRACTICAL IMPLICATIONS

This study utilizes the SAP-LAP framework developed by Kumar and Gupta [40] in building the interpretive knowledge base and in the ranking of the elements of the framework through the eIRP approach. The framework explores the freedom of choice available during the selection of the factors. The study helped in building the contextual relationships among the various elements of the framework portraying the interactions among the constituents of an organization. With the help of the efficient interpretive ranking methodology, it has been concluded that the top management is the most catalytical actor among the others and is responsible for initial push, motivation, budget allocation, etc. required for sustainable business excellence.

In contrast, the cross-functional teams are the torchbearers of the organization that are designed to resolve cross-dimensional issues. These are very much responsible for the successful implementation of total quality management [46] and other business excellence philosophies, such as TPM, six sigma, lean manufacturing, etc.

The third most influential actor in the case study is the government of India, which is responsible for framing the fiscal policies and these policies have an impact on the financial targets of the organization. The ranking obtained in the paper and the procedure adopted for the exploration of freedom of choice in decision-making may help organizations in similar situations. This study portrays an overall picture of the various situations present in the organization in an interpretive and organized manner and the ranks obtained through an efficient Interpretive Ranking Process.

The results reported in this work are consistent with the results reported by adopting both quantitative and qualitative techniques, such as AHP [3] and interpretive structural modelling (ISM) [27]. Talib and Rahman [3] reported the lack of top management commitment as a critical barrier to the implementation of TQM in an organization this result agrees with the result reported in the present study that top management is the top-ranked actor in the case organization which is responsible for policy management, budget allocation, and motivation behind carrying the activities responsible for the business excellence of the organization. Talib and Rahman [3] also reported the lack of coordination in the departments as a critical barrier that prevents the implementation of TQM; in the present case study, cross-functional management emerged as the second most critical actor responsible for the implementation, monitoring, and review of the KPIs applicable for cross-dimensional activities. The results reported in the present study are supported by the interpretive knowledge base which was not available in the previous studies.

Haleem et al. [27] adopted both ISM and IRP approaches for ranking the critical success factors responsible for the implementation of world-class manufacturing. The ISM model reported top management as the key driving factor, whereas with the IRP the authors reported a reduction in energy consumption and waste minimization as the key driving factors responsible for the implementation of world-class manufacturing. This leads to the conclusion that IRP calls for more information and yields better qualitative and realistic results than ISM.

In this paper, an efficient version of IRP has been adopted to capture and display the results in an informative manner. The results of this study are similar in a broader perspective but differ in descriptive nature from previously reported studies.

Kumar et al. [2] surveyed the TQM critical success factors in north Indian manufacturing industries

and reported that top management commitment and teamwork as a few critical success factors among others that support the implementation of TQM. The study reported that top management supports the TQM by communicating and explaining quality goals and policies to the employees of companies. In the present study, the role of top management is depicted in a much broader sense by portraying its interactions with the other actors of the organization.

Overall, this study contributes to the field by introducing the eIRP, a novel approach for ranking factors that provides a qualitative interpretation of the ratings. The eIRP has the potential to be applied to various decision-making problems in different contexts and can provide valuable insights for managers and decision-makers to improve organizational performance. The results of the case study demonstrate the practical application of the eIRP and highlight its potential to support organizations in achieving business excellence.

Furthermore, the study offers practical implications in the following manner.

1. The key actors and their interactive roles are critical to an organization and these interactions can be foreseen by the managers with the help of the SAP-LAP process.
2. The inherent flexibilities or freedom of choice in the form of interactions will be available as a knowledge base. This knowledge base can further be utilized to rank the factors of interest against a particular criterion.
3. The methodology strengthens decision-making in any managerial context.

## 7 LIMITATIONS OF THE STUDY AND FUTURE SCOPE

The work undertaken in this study has some limitations since it offers a theoretical framework based on the opinions or judgment of the expert. The subjective nature of the judgment makes the interpretive linkages volatile. However, this volatility is reduced when the weights among the opinions/judgments are very large. The results posted in the study can be tested and validated only when applied in a real situation.

This study also has some limitations as it is based on the situations found in a single organization. Therefore, the results might differ when the model is applied to another organization that has some different situations. For the generalization of the results, more empirical data should be gathered. Also, the model should be redesigned before implementing it in different scenarios. Some algorithms may be developed for carrying out interpretive paired

comparisons among the variables, which can help in addressing a large number of variables.

## 8 ACKNOWLEDGEMENTS

The authors want to thank the team of ABC Ltd., experts, and others who have contributed directly and indirectly to the development of the study.

## 9 REFERENCES

- [1] Talib, F., Rahman, Z. (2010). Critical success factors of TQM in service organizations: A proposed model. *Services Marketing Quarterly*, vol. 31. no. 3, p. 363-380, DOI:10.1080/15332969.2010.486700.
- [2] Kumar, R., Garg, D., Garg, T.K. (2011). TQM success factors in North Indian manufacturing and service industries. *TQM Journal*, vol. 23. no. 1, p. 36-46, DOI:10.1108/17542731111097470.
- [3] Talib, F., Rahman, Z. (2015). Identification and prioritization of barriers to total quality management implementation in service industry: An analytic hierarchy process approach. *TQM Journal*, vol. 27, no. 5, p. 591-615, DOI:10.1108/TQM-11-2013-0122.
- [4] Sraun, J.S., Singh, H. (2017). Continuous improvement strategies across manufacturing SMEs of Northern India: An empirical investigation. *International Journal of Lean Six Sigma*, vol. 8, no. 2, art. ID IJLSS-05-2016-0019, DOI:10.1108/IJLSS-05-2016-0019.
- [5] Ojha, R., Vij, A.K., Vrat, P. (2014). Manufacturing excellence and its critical factors. *Journal of Advances in Management Research*, vol. 11, no. 3, p. 312-332, DOI:10.1108/JAMR-06-2014-0032.
- [6] Taofeeq, M.D., Adeleke, A.Q., Lee, C.K. (2020). Government policy as a key moderator to contractors' risk attitudes among Malaysian construction companies. *Journal of Engineering, Design and Technology*, vol. 18, no. 6, p. 1543-1569, DOI:10.1108/JEDT-08-2019-0192/FULL/XML.
- [7] Shinkle, G.A., Hodgkinson, G.P., Gary, M.S. (2021). Government policy changes and organizational goal setting: Extensions to the behavioral theory of the firm. *Journal of Business Research*, vol. 129, p. 406-417, DOI:10.1016/j.jbusres.2021.02.056.
- [8] Yang, J., Liu, X. (2022). The role of sustainable development goals, financial knowledge and investment strategies on the organizational profitability: Moderating impact of government support. *Economic Research - Ekonomika Istraživanja*, vol. 36, no. 1, p. 1570-1591, DOI:10.1080/1331677X.2022.2090405.
- [9] Witcher, B.J., Butterworth, R. (2001). Hoshin Kanri: Policy management in Japanese-owned UK subsidiaries. *Journal of Management Studies*, vol. 38, no. 5, p. 651-674, DOI:10.1111/1467-6486.00253.
- [10] Witcher, B.J., Chau, V.S. (2007). Balanced scorecard and hoshin kanri: Dynamic capabilities for managing strategic fit. *Management Decision*, vol. 45, no. 3, p. 518-538, DOI:10.1108/00251740710745115.

- [11] Nicholas, J. (2016). Hoshin kanri and critical success factors in quality management and lean production. *Total Quality Management & Business Excellence*, vol. 27, no. 3-4, p. 250-264, DOI:10.1080/14783363.2014.976938.
- [12] Sushil (2012). Interpreting the interpretive structural model. *Global Journal of Flexible Systems Management*, vol. 13, p. 87-106, DOI:10.1007/S40171-012-0008-3.
- [13] Sushil (2000). SAP-LAP models of inquiry. *Management Decision*, vol. 38, no. 5, p. 347-353, DOI:10.1108/00251740010340526.
- [14] Sushil (2009). SAP-LAP linkages - A generic interpretive framework for analyzing managerial contexts. *Global Journal of Flexible Systems Management*, vol. 10, p. 11-20, DOI:10.1007/BF03396558.
- [15] Sushil (2001). SAP-LAP Framework. *Global Journal of Flexible Systems Management*, vol. 2, p. 51-55.
- [16] Arshinder, Kanda, A., Deshmukh, S.G. (2007). Supply chain coordination issues: an SAP-LAP framework. *Asia Pacific Journal of Marketing and Logistics*, vol. 19, no. 3, p. 240-264, DOI:10.1108/13555850710772923.
- [17] Banwet, D.K., Pramod, V.R. (2010). SAP-LAP Hills: A new approach for strategic change management. *Global Journal of Flexible Systems Management*, vol. 11, p. 11-20, DOI:10.1007/BF03396584.
- [18] Shukla, R.K., Garg, D., Agarwal, A. (2011). Study of select issues related to supply chain coordination: Using SAP-LAP analysis framework. *Global Journal of Enterprise Information System*, vol. 3, p. 56-69.
- [19] Lijo, J., Ramesh, A. (2012). Humanitarian supply chain management in India: a SAP-LAP framework. *Journal of Advances in Management Research*, vol. 9, no. 2, p. 217-235, DOI:10.1108/09727981211271968.
- [20] Kumar, P., Haleem, A., Qamar, F., Khan, U. (2018). Analysis of maiden modal shift in coal transportation supply chain using SAP-LAP technique. *International Journal of Logistics Systems and Management*, vol. 30, no. 4, p. 458-476, DOI:10.1504/IJLSM.2018.093585.
- [21] Shalender, K., Singh, N. (2014). Understanding product flexibility using SAP-LAP approach. *Journal of Strategic Marketing*, vol. 22, no. 2, p. 104-116, DOI:10.1080/0965254X.2013.876065.
- [22] Garg, A., Deshmukh, S.G. (2010). Engineering support issues for flexibility in maintenance: An SAP-LAP framework. *Asia Pacific Journal of Marketing and Logistics*, vol. 22, no. 2, p. 247-270, DOI:10.1108/13555851011026980.
- [23] Matharu, M., Sinha, N. (2019). Lean implementation in Indian manufacturing MSMEs: A SaP-lap analysis. *Management and Production Engineering Review*, vol. 10, p. 68-78, DOI:10.24425/mper.2019.128245.
- [24] Palanisamy, R. (2012). Building information systems flexibility in SAP-LAP framework: A case study evidence from SME sector. *Global Journal of Flexible Systems Management*, vol. 13, p. 57-74, DOI:10.1007/s40171-012-0005-6.
- [25] Chavan, M., Chandiramani, J., Nayak, S. (2019). Assessing the state of physical infrastructure in progressive urbanization strategy: SAP-LAP analysis. *Habitat International*, vol. 89, art ID. 102002, DOI:10.1016/j.habitatint.2019.102002.
- [26] Sushil (2009). Interpretive ranking process. *Global Journal of Flexible Systems Management*, vol. 10, p. 1-10, DOI:10.1007/BF03396567.
- [27] Haleem, A., Sushil, Qadri, M.A., Kumar, S. (2012). Analysis of critical success factors of world-class manufacturing practices: an application of interpretative structural modelling and interpretative ranking process. *Production Planning & Control*, vol. 23, p. 722-734, DOI:10.1080/09537287.2011.642134.
- [28] Mangla, S.K., Kumar, P., Barua, M.K. (2014). A flexible decision framework for building risk mitigation strategies in green supply chain using SAP-LAP and IRP approaches. *Global Journal of Flexible Systems Management*, vol. 15, p. 203-218, DOI:10.1007/s40171-014-0067-8.
- [29] Zhang, L., Narkhede, B.E., Chaple, A.P. (2017). Evaluating lean manufacturing barriers: an interpretive process. *Journal of Manufacturing Technology Management*, vol. 28, no. 8, p. 1086-1114, DOI:10.1108/JMTM-04-2017-0071.
- [30] Hughes, D.L., Dwivedi, Y.K., Rana, N.P. (2017). Mapping IS failure factors on PRINCE2® stages: an application of Interpretive Ranking Process (IRP). *Production Planning & Control*, vol. 28, no. 9, p. 776-790, DOI:10.1080/09537287.2017.1311431.
- [31] Narkhede, B.E., Raut, R., Gardas, B., Luong, H.T., Jha, M. (2017). Selection and evaluation of third party logistics service provider (3PLSP) by using an interpretive ranking process (IRP). *Benchmarking: An International Journal*, vol. 24, no. 6, p. 1597-1648, DOI:10.1108/BIJ-04-2016-0055.
- [32] Mhatre, T.N., Thakkar, J.J., Maiti, J. (2017). Modelling critical risk factors for Indian construction project using interpretive ranking process (IRP) and system dynamics (SD). *International Journal of Quality & Reliability Management*, vol. 34, no. 9, p. 1451-1473, DOI:10.1108/IJQRM-09-2015-0140.
- [33] Sushil (2019). Theory building using SAP-LAP linkages: an application in the context of disaster management. *Annals of Operations Research*, vol. 283, p. 811-836, DOI:10.1007/s10479-017-2425-3.
- [34] Malik, S., Maheshwari, G.C., Singh, A. (2019). Understanding financial inclusion in India: A theoretical framework building through SAP-LAP and efficient IRP. *Global Journal of Flexible Systems Management*, vol. 20, p. 117-140, DOI:10.1007/s40171-019-00207-8.
- [35] Parameswar, N., Dhir, S., Sushil (2020). Interpretive Ranking of Choice of Interaction of Parent Firms Post-International Joint Venture Termination using TISM-IRP. *Global Journal of Flexible Systems Management*, vol. 21, p. 1-16, DOI:10.1007/s40171-019-00227-4.
- [36] Siva Kumar, P., Anbanandam, R. (2020). Theory building on supply chain resilience: A SAP-LAP analysis. *Global Journal of Flexible Systems Management*, vol. 21, p. 113-133, DOI:10.1007/s40171-020-00233-x.
- [37] Pal, C., Shankar, R. (2022). A systematic inquiry of energy management in smart grid by using SAP-LAP and IRP approach. *International Journal of Energy Sector Management*, ahead-of-print, DOI:10.1108/IJESM-04-2022-0004.
- [38] Chauhan, C., Sharma, A., Singh, A. (2021). A SAP-LAP linkages framework for integrating Industry 4.0 and circular economy. *Benchmarking: An International Journal*, vol. 28, no. 5, p. 1638-1664, DOI:10.1108/BIJ-10-2018-0310.

- [39] Kumar, V., Shankar, R., Vrat, P. (2022). An analysis of Industry 4.0 implementation-variables by using SAP-LAP and e-IRP approach. *Benchmarking: An International Journal*, vol. 29, no. 5, p. 1606-1639, DOI:10.1108/BIJ-03-2021-0153.
- [40] Kumar, S., Gupta, P. (2020). Case study on business excellence issues of an Indian automobile manufacturer using SAP-LAP framework. *International Journal on Emerging Technologies*, vol. 11, p. 911-918.
- [41] Yin, R.K. (1981). The Case study as a serious research strategy. *Knowledge: Creation, Diffusion, Utilization*, vol. 3, no. 1, p. 97-114, DOI:10.1177/107554708100300106.
- [42] Stake, R.E., Denzin, N.K., Lincoln, Y.S. (1994). *Qualitative case studies in Handbook Qualitative Research*, SAGE, New York.
- [43] Siggelkow, N. (2007). Persuasion with case studies. *Academy of Management Journal*, vol. 50, no. 1, p. 20-24, DOI:10.5465/amj.2007.24160882.
- [44] Podsakoff, P.M., MacKenzie, S.B., Lee, J.-Y., Podsakoff, N.P. (2003). Common method biases in behavioral research: A critical review of the literature and recommended remedies. *Journal of Applied Psychology*, vol. 88, no. 5, p. 879-903, DOI:10.1037/0021-9010.88.5.879.
- [45] Sushil (2020). Interpretive multi-criteria ranking of production systems with ordinal weights and transitive dominance relationships. *Annals of Operations Research*, vol. 290, p. 677-695, DOI:10.1007/s10479-018-2946-4.
- [46] JUSE (2022). Union of Japanese Scientist and Engineers. from www.juse.or.jp, accessed on 2022-12-12.



# An Improved MSCNN and GRU Model for Rolling Bearing Fault Diagnosis

Teng Wang\* – Youfu Tang – Tao Wang – Na Lei

Northeast Petroleum University, Mechanical Science and Engineering Institute, China

*In this paper, a novel fault diagnosis method based on the fusion of squeeze and excitation-multiscale convolutional neural networks (SENet-MSCNN) and gate recurrent unit (GRU) is proposed to address the problem of low diagnosis rate caused by the fact that normal samples are much larger than fault samples in the vibration big data. The method takes the time-domain vibration signal as input and fuses the spatial features extracted by SENet-MSCNN. The temporal features extracted by GRU in order to bring them into the fully connected layer for identification so as to realize the intelligent diagnosis of rolling bearing adaptive feature extraction. Finally, the method is applied to the simulated signal and experimental data for testing and analysis. The results reveal that the model can reach 98.98 % and 76.44 % migration diagnostic accuracy in bearing and gearbox datasets. At the same time, it has strong noise immunity, adaptivity, and robustness, providing an effective way for intelligent diagnosis of rolling bearing vibration big data.*

**Keywords:** SENet, multiscale convolutional neural networks, gate recurrent unit, rolling bearing, fault diagnosis

## Highlights

- A novel integration method of SENet-MSCNN and GRU is proposed, which can more effectively and adaptively extract the fault features of rolling bearing and fault diagnosis.
- Based on the existing problems of convolutional neural networks (CNN), we developed MSCNN. The multiscale convolution kernel in MSCNN not only considers the global basic features of the signal but also extracts local detail features.
- The SENet is added to MSCNN to recalibrate multiscale features, which can reduce attention to irrelevant information and pay more attention to motivate important information.
- SENet-MSCNN is good at reducing frequency variance and extracting spatial features, and GRU is good at extracting long sequence time-series features. The integration model has better robustness in real working conditions and can reach 98.98 % accuracy under variable load conditions.

## 0 INTRODUCTION

As a key component in rotating machinery, rolling bearings often work in severe environments of high load and high speed, so they are highly prone to failure. Research shows that bearing faults account for the majority of the total number of faults [1]. Therefore, it is of great theoretical significance and engineering application value to research rolling bearing fault diagnosis methods to ensure the continuous and safe operation of equipment and reduce the economic loss of downtime [2].

However, the rolling bearing vibration big data caused by variable working conditions and shock excitation have typical nonlinear non-stationary complex characteristics [3] and [4], which makes the existing signal processing techniques, such as time-domain statistical analysis [5] and [6], frequency-domain spectral analysis [7] and [8], short-time Fourier transform [9], wavelet analysis [10] and [11], Hilbert-Huang transform (HHT) [12], variational mode decomposition (VMD) [13], difficult to extract fault features adaptively.

In contrast, the normal samples are much larger than the fault samples in the massive rolling bearing

vibration data collected in the field, which makes the diagnostic efficiency and recognition rate of the existing artificial intelligence diagnosis methods, such as support vector machine (SVM) [14], decision tree (DT) [15], and random forest (RF) [16], artificial neural network (ANN) [17], CNN [18] and [19], deep autoencoder (DAE) [20], deep belief network (DBN) [21], recurrent neural network (RNN) [22] and artificial immune algorithm (AIN) [23] difficult to apply in industrial contexts.

At present, researchers at home and abroad have fused signal-processing techniques with artificial intelligence diagnosis methods, such as wavelet packet decomposition and empirical mode decomposition (EMD) with back propagation (BP) network fusion [24], VMD and probabilistic neural network (PNN) [25], wavelet and CNN network fusion [26], HHT, and CNN network fusion [27]. These methods have been effective in improving the diagnostic performance of the large sample and various fault vibration data. However, vibration data is affected by different working conditions, structural parameters, fault types, fault degrees, and the number of faults. The above fusion methods have their applicability conditions

\*Corr. Author's Address: Northeast Petroleum University, Mechanical Science and Engineering Institute, China, wangteng\_1009@163.com

and need to be artificially selected based on experts' empirical knowledge, which has greater limitations.

In addition, some researchers improve fault diagnosis accuracy and robustness by fusing different artificial intelligence methods. These diagnosis methods mainly contain two parts: feature extraction and pattern recognition. A convolutional discriminative feature learning approach and support vector machine fusion method was proposed by Sun et al. [28] for fault diagnosis of induction motors; the network performance is improved. Chen et al. [29] proposed a mechanical fault diagnosis method based on CNN and extreme learning machine (ELM) by using ELM as a classifier of CNN with the advantages of fast learning speed and high generalization ability. The network performance is further improved, and the model generalization ability and convergence speed are also enhanced. Wang et al. [30] proposed a CNN-based hidden Markov model for rolling bearing fault identification by fusing the strong feature extraction capability of CNN and the excellent pattern recognition performance of the hidden Markov model. Compared with the CNN model alone, it has higher classification accuracy and robustness. Based on the excellent network performance of CNN, the above methods have achieved better performance by combining CNN with various artificial intelligence methods. However, the CNN, as a feature extraction layer, extracts high-dimensional features and contains a large amount of spatial information and sequence information. Another approach, as a classifier, classifies the spatial features extracted by the CNN without considering the connection between the features. Based on this idea, taking advantage of RNN for extracting temporal features and CNN for extracting spatial features, some researchers have combined CNN and RNN [31] for fault diagnosis and achieved better accuracy. However, RNNs are prone to gradient explosion and gradient disappearance. Gate recurrent unit (GRU) [32] and long short-term memory (LSTM) [33], as a variant of RNN, can solve gradient vanishing and gradient explosion problems. A planetary gearbox diagnosis method based on CNN and LSTM is proposed by Shi et al. [34]; the network is able to detect the type, location, and direction of gearbox faults with greater accuracy and a higher recognition rate than traditional a single CNN. Chen et al. [35] found that the features extracted by a size convolutional kernel are more singular; a multi-scale convolutional neural network and long short-term memory (MSCNN-LSTM) fault diagnosis model was proposed. The average accuracy in the experimental data reached 98.46 % and has strong noise immunity.

Li et al. [36] proposed a method that combines CNN and GRU models with vibration and acoustic emission signals for gear-pitting fault diagnosis. The method can achieve a diagnosis rate of more than 98 % and exhibits stronger robustness compared with a single CNN and GRU for different loads and learning rates. The fusion of two different deep learning methods is to take the advantage of both models and make the model representation more powerful. However, it is easy to deepen the network layer depth, leading to model overfitting.

To address these problems, a fault diagnosis method based on the fusion of SENet-MSCNN and GRU is proposed. The width of the convolutional layers of the network is increased by adding convolutional kernels of different scales to form MSCNN layers, without increasing the depth of the network structure. Convolutional kernels of different sizes can capture different perceptual field features to obtain global and local information. In addition, the features extracted by MSCNN are not all important, which can easily cause redundant information and irrelevant information to influence the classification results. Thus, the SE-Net block [37] was introduced into MSCNN to recalibrate multiscale features to reduce attention to irrelevant information and pay more attention to motivate important information. Then, the spatial features extracted by SENet-MSCNN were input to GRU to extract time-series features. Compared with other fault diagnosis methods, the method has broad application prospects in improving the accuracy of rolling bearing fault diagnosis. In addition, the method is attractive in reducing failure rates, reducing maintenance and repair costs of machinery and equipment, and preventing accidents.

## 1 FAULT DIAGNOSIS MODEL BASED ON SENet-MSCNN AND GRU METHOD

The MSCNN extracts the fault features through several convolutional kernels of different sizes and fuses the multiscale features. Then the fused features are fed into the GRU network to extract the time-series features and classify them while adding the SE-Net into the MSCNN to enable the network model to recalibrate multiscale features, which can further improve the diagnosis rate and robustness of the fault model.

### 1.1 Architecture of MSCNN

Since the rolling bearing vibration signal presents nonlinear and nonstationary characteristics, the high-

frequency features cannot be extracted by larger convolutional kernels and the low-frequency features cannot be extracted by smaller convolutional kernels. Therefore, to solve this problem, this paper uses the MSCNN structure, which includes a multiscale convolutional layer by connecting convolutional kernels of different sizes [1×1, 3×1, 5×1], whose structure is shown in Fig. 1. Convolutional kernels [3×1] extract high-frequency fault features; convolutional kernels [5×1] extract low-frequency fault features. The features extracted from several different receptive fields possess both global and local information [38] and [39]. A convolutional kernel of size [1×1] is added to each of the four branches of MSCNN, which has two advantages: first, although a [1×1] convolutional kernel cannot extract spatial features, it can extract features along the depth dimension to achieve a nonlinear feature map. Second, several [1×1] convolutional kernels are embedded in the front of [3×1, 5×1] convolutional kernels and can reduce dimensionality to reduce the computational cost. It can accelerate training and improve generalization. The calculation process of the convolution is as follows:

$$[x * g](n) = \sum_{\tau=-\infty}^{\infty} x(\tau)g(n-\tau), \quad (1)$$

where  $x$  denotes the amplitude, and  $g$  denotes the multiscale convolution kernel.

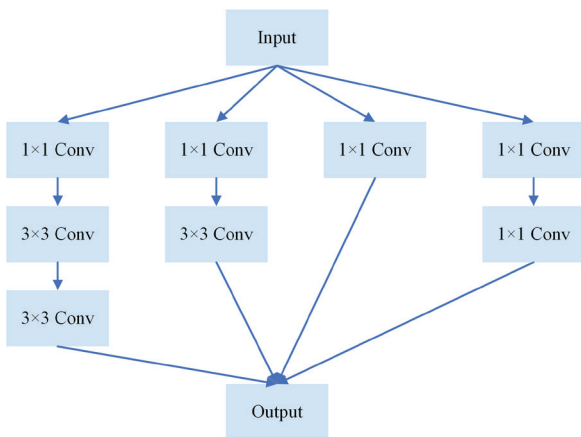


**Fig. 1.** The structure diagram of MSCNN, which includes a multiscale convolutional layer by connecting convolutional kernels of different sizes [1×1, 3×1, 5×1]

By using the scaled exponential linear units (SELU) activation function [40], the data distribution is self-normalized to satisfy a normal distribution with mean 0 and variance 1. Moreover, the SELU activation function is a non-saturated function, which can

solve the vanishing gradient and exploding gradient problem. Its function expression is as follows:

$$selu(x) = \lambda \begin{cases} x, & x > 0 \\ \alpha(e^x - 1), & x \leq 0 \end{cases} \quad (2)$$

where  $\alpha$  and  $\lambda$  denote constants.

### 1.2 Architecture of SENet

A new module is introduced in the MSCNN model: SENet, whose detailed structure is shown in Fig. 2. The biggest advantage of the SENet block is that it can construct interdependencies between channels [41]. SENet adopts a feature recalibration mechanism, which can obtain the dependency degree of each channel feature through global information. Then, by the dependency degree, the important information is selectively enhanced and the irrelevant information is squeezed to recalibrate the relationship between channel-wise features. Thus, it aids in strengthening the convolutional kernel learning capability and improve the feature representation capability of MSCNN. The formulas are as follows:

$$z_c = GAP(u_c) = \frac{1}{H \times W} \sum_{i=1}^H \sum_{j=1}^W u_c(i, j), \quad (3)$$

$$s_c = \sigma(\mathbf{W}_2 * \delta(\mathbf{W}_1 * z_c)), \quad (4)$$

$$\mathbf{M} = [m_1, m_2, m_3, \dots, m_c] = F_{scale}(s_c \bullet u_c), \quad (5)$$

where  $u_c \in R^{H \times W}$  is input feature,  $z_c = R^{1 \times c}$  the channel-wise feature vector,  $s_c = R^{H \times W}$  recalibration vectors, and  $\mathbf{M} \in R^{H \times W}$  reconstructing feature vector.  $\mathbf{W}_1 \in R^{D/r \times D}$  and  $\mathbf{W}_2 \in R^{D \times D/r}$   $z_c = R^{1 \times c}$  are weights \* convolution operator,  $\sigma$  Sigmoid function,  $\delta$  Relu function,  $r$  reduction ratio, and  $F_{scale}(\bullet)$  is scalar multiplication.

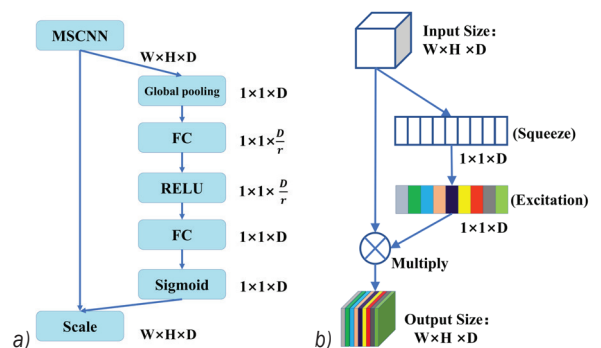


**Fig. 2.** The structure diagram of SENet; a) SENet module, and b) SENet block

### 1.3 Architecture of GRU

The GRU network is a simplified version of the LSTM, which has a simpler structure, with lower computational cost, faster iterations, and no reduction in network performance compared to the LSTM. The GRU network has only two gated units: the update gate and the reset gate. With these two gated units, it can learn, discard, and retain information in a long-term sequence and influence the output of the next iteration. As shown in Fig. 3, the input vector  $\mathbf{x}_{(t)}$  and the previous state vector  $\mathbf{h}_{(t-1)}$  are connected to two fully connected layers, through the Sigmoid function mapping the result  $z_{(t)}$  and  $r_{(t)}$  between 0 and 1.

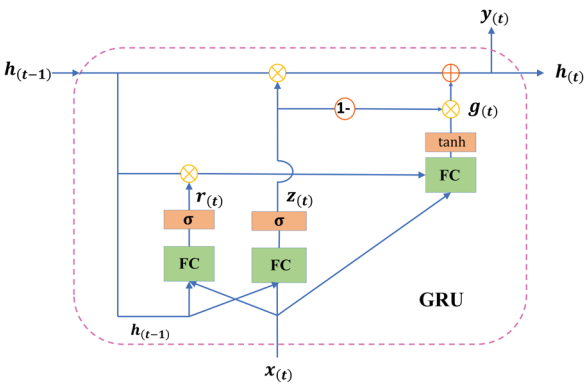


Fig. 3. The structure diagram of GRU; the GRU network has only two gated units: the update gate and the reset gate

The formulas can be given as follows:

$$z_{(t)} = \sigma(\mathbf{W}_{xz}^T \mathbf{x}_{(t)} + \mathbf{W}_{hz}^T \mathbf{h}_{(t-1)} + b_z), \quad (6)$$

$$r_{(t)} = \sigma(\mathbf{W}_{xr}^T \mathbf{x}_{(t)} + \mathbf{W}_{hr}^T \mathbf{h}_{(t-1)} + b_r), \quad (7)$$

$$g_{(t)} = \tanh(\mathbf{W}_{xg}^T \mathbf{x}_{(t)} + \mathbf{W}_{hg}^T (r_{(t)} \otimes \mathbf{h}_{(t-1)}) + b_g), \quad (8)$$

$$h_{(t)} = z_{(t)} \otimes \mathbf{h}_{(t-1)} + (1 - z_{(t)}) \otimes g_{(t)}, \quad (9)$$

where  $\sigma$  represents Sigmoid function.  $\mathbf{W}_{xz}$ ,  $\mathbf{W}_{xr}$ , and  $\mathbf{W}_{xg}$  represent the weight matrices of for their connection to the input vector  $\mathbf{x}_{(t)}$ .  $\mathbf{W}_{hz}$ ,  $\mathbf{W}_{hr}$ , and  $\mathbf{W}_{hg}$  represent the weight matrices of for their connection to the vector  $\mathbf{h}_{(t-1)}$ .  $b_z$ ,  $b_r$ , and  $b_g$  are the bias.  $\otimes$  is scalar multiplication.

### 1.4 Intelligent Fault Diagnosis Methods Based on SENet-MSCNN and GRU Model

As shown in Fig. 4, rolling bearing fault diagnosis consists of three major parts: the SENet-MSCNN layer, GRU layer, and Dense layer. The method is based on the improvement of the integration method of the CNN and LSTM, with which CNN is good at reducing the vibration frequency variance and GRU is good at extracting time-series features. Combining and improving the CNN and GRU fusion model, next the SENet-MSCNN and GRU fault diagnosis model is proposed. First, the time domain signal of bearing fault vibration is directly served as the input of SENet-MSCNN to extract multiscale features through a multiscale convolution kernel. The multiscale features are input to the SENet to recalibrate features. Then, the high dimensional multiscale features are Global Average Pooling to reduce dimensions. The low dimensional features are input to the GRU layer to extract time-series features. Finally, the features are input to the fully connected layer for classification by the Softmax function.

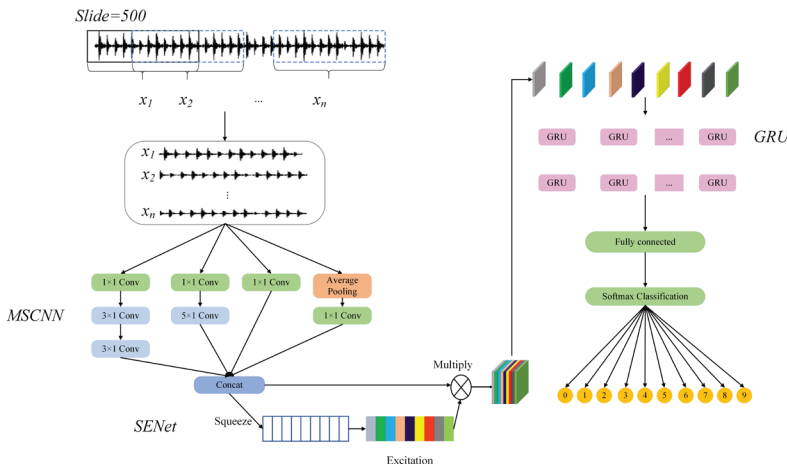


Fig. 4. The framework of the SENet-MSCNN and GRU model, which consist of three major parts SENet-MSCNN layer, GRU layer, and Dense layer



### 1.5 Signals Application of SENet-MSCNN and GRU Methods in Simulated Signals

#### 1.5.1 Construction of Simulated Signal Data Sets

The raw signal of the rolling bearing is simulated using three simplified models from the literature [42]:  $x_1(t)$ ,  $x_2(t)$ ,  $x_3(t)$ , which are:

$$x_1(t) = 0.4 \cos(2\pi f_1 t + 10), \quad (10)$$

$$x_2(t) = 0.6 \cos(2\pi f_2 t - 15), \quad (11)$$

$$x_3(t) = \sin(2\pi f_b t) [1 + \sin(2\pi f_r t)], \quad (12)$$

where  $f_1=20$  Hz,  $f_2=45$  Hz,  $f_3=100$  Hz,  $f_r=10$  Hz,  $N=2048$ , sampling frequency  $f_s=10$  Hz.

A random matrix **A** is used to construct the simulated signal and a white noise signal is added to form the simulated signal:  $x_4(t)$ ,  $x_5(t)$  and  $x_6(t)$ . As shown in Fig. 5,  $x_4(t)$ ,  $x_5(t)$  and  $x_6(t)$  are added to the Gaussian white noise to obtain the simulated signal plot with a signal-noise ratio of 2 dB; the signal-noise ratio equation is as follows:

$$SNR = 10 \log_{10} \frac{p_s}{p_n}, \quad (13)$$

$$\mathbf{A} = \begin{pmatrix} 0.5214 & 0.4555 & 0.2013 \\ 0.4278 & 0.2002 & 0.4416 \\ 0.3122 & 0.3818 & 0.6058 \end{pmatrix}, \quad (14)$$

$$\mathbf{A} \begin{pmatrix} x_1(t) \\ x_2(t) \\ x_3(t) \end{pmatrix} + \begin{pmatrix} S_{noise} \\ S_{noise} \\ S_{noise} \end{pmatrix} = \begin{pmatrix} x_4(t) \\ x_5(t) \\ x_6(t) \end{pmatrix}, \quad (15)$$

where  $p_s$  is to input signal energy,  $p_n$  noise energy, and  $S_{noise}$  Gaussian white noise.

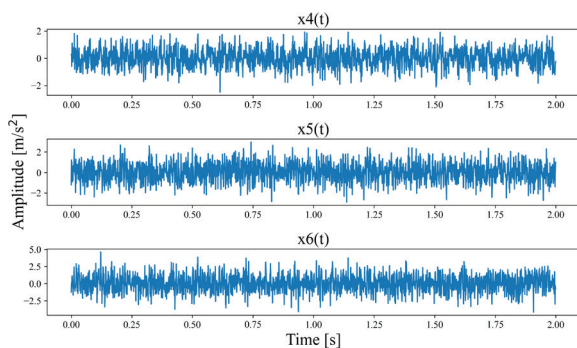


**Fig. 5.** Time-domain plots of the simulated signal, a)  $x_4(t)$ , b)  $x_5(t)$ , and c)  $x_6(t)$  are added to Gaussian white noise signals with a signal-noise ratio of -2

$x_4(t)$ ,  $x_5(t)$  and  $x_6(t)$  are added to Gaussian white noise signals with a different signal-noise ratio in the range of [-4, 8]. The numbers of training samples and test samples for each signal-noise ratio of each fault are 30 and 10, respectively, which are given in Table 1.

**Table 1.** The information of the simulated signal dataset

Signals	SNR [dB]							
	-4	-2	0	2	4	6	8	
$x_4(t)$	Train	30	30	30	30	30	30	30
	Test	10	10	10	10	10	10	10
$x_5(t)$	Train	30	30	30	30	30	30	30
	Test	10	10	10	10	10	10	10
$x_6(t)$	Train	30	30	30	30	30	30	30
	Test	10	10	10	10	10	10	10

#### 1.5.2 Network Structure and Parameters

The detailed structure and parameter settings of the SENet-MSCNN and GRU networks models are shown in Table 2. Firstly, the simulation signal is input to the SENet-MSCNN network. The number of convolutional kernels in the SENet-MSCNN network is 128, and the activation function is Selu, which induces self-normalizing data. Then the output features of SENet-MSCNN are input to global average pooling and the remaining spatial features are discarded to reduce feature dimensionality. Twenty cell numbers are set for the GRU network and the Relu function is used. The last layer is the fully connected layer and the Softmax function is applied to classify the output results into three classifications. The hyperparameters are set: the learning rate is 0.001, the batch size is 32, the number of iterations is 196, and the loss function is the cross-entropy loss function.

#### 1.5.3 Simulation Analysis

Fig. 6 is a comparison of the recognition rates in the test set between GRU, 1D-CNN, MSCNN, BP networks, and proposed methods. It can be seen that recognition rates of the SENet-MSCNN and GRU networks have stabilized at 100 % at the second iteration. The recognition rate of the GRU network has stabilized tending to 99.3 %. The BP network and MSCNN network recognition rate are stable below 99.8 %, and the 1DCNN network fluctuates more. Therefore, the recognition rate, convergence speed, and anti-noise performance of the SENet-MSCNN and GRU networks perform better in the simulation data.

**Table 2.** The parameters of the SENet-MSCNN and GRU models used in the simulated signal dataset

Layer	Kernel size/step	Kernel num	Unit	Input size	Output size	Activation
Conv_1	3×1/2	128		32×2048×1	32×1024×128	Selu
Conv_a	1×1/2	128		32×1024×128	32×512×128	Selu
Conv_b	1×1/1	128		32×1024×128	32×1024×128	Selu
Conv_b	3×1/2	128		32×1024×128	32×512×128	Selu
AveragePooling c	3×1/2			32×1024×128	32×512×128	Selu
Conv_c	5×1/1	128		32×512×128	32×512×128	Selu
Conv_d	1×1/1	128		32×1024×128	32×1024×128	Selu
Conv_d	3×1/1	128		32×1024×128	32×1024×128	Selu
Conv_d	3×1/2	128		32×1024×128	32×512×128	Selu
Concatenate				(32×512×128)×4	32×512×512	
SENet				32×512×512	32×512×512	
GlobalAverage Pooling				32×1024×512	32×512	
ExpandDim				32×512	32×512×1	
Gru_1			20	32×512×1	32×512×20	Relu
Gru_2			20	32×512×20	32×512×20	Relu
MaxPooling	3×1/2			32×512×20	32×256×20	
Flatten				32×256×20	32×5210	
Dense			3	32×5210	32×3	Softmax

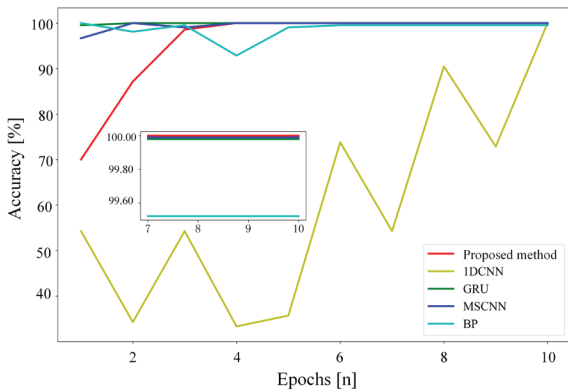


**Fig. 6.** The diagnosis rate of different methods in simulation data, several methods including SENet-MSCNN and GRU, 1DCNN, GRU, MSCNN, and BP are compared and analysed

2 APPLICATION OF SENet-MSCNN AND GRU METHODS IN ROLLING BEARING FAULT DIAGNOSIS

In this section, we first discuss the Case Western Reserve University, Cleveland, USA, bearing datasets [43] and the gearbox datasets, and our implementation details. Subsequently, the proposed method in this paper is applied to the comparative analysis of several typical methods in the two datasets. Meanwhile, we did ablation experiments to examine the effect of each model component. Finally, we design the variable working conditions experiment to analyse the migration performance of the diagnosis.

2.1 Data Preprocessing

This paper increases the data sample set through data augmentation techniques (by sliding windows and cuts) to create three different sizes of comparison test datasets of 500, 1500, and 4500 samples. As shown in Fig. 7, each sample slide window size is 2048 points, and a slide step size is 500 points, which consists of datasets.

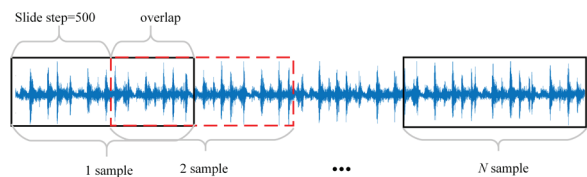


**Fig. 7.** Data augmentation with overlap where the sample length is 2048 and the sliding step is 500

2.2 Bearing Dataset

As shown in Fig. 8, the experimental platform consists of four parts: motor, torque transducer/encoder, dynamometer, and electronic control. The sampling frequency is 12 kHz, and the data ARE collected from the vibration data of the drive end (DE). There are three fault types: the inner fault, the ball fault, and the outer fault with three fault diameters (0.1778 mm, 0.3556 mm, and 0.5334 mm) and a normal state. Three fault types are shown in Fig. 9. Therefore,

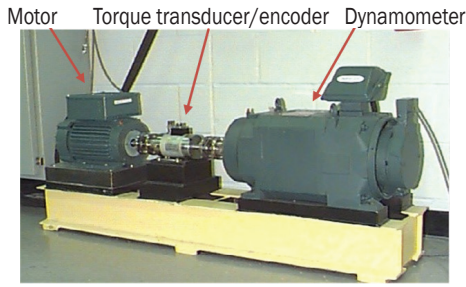


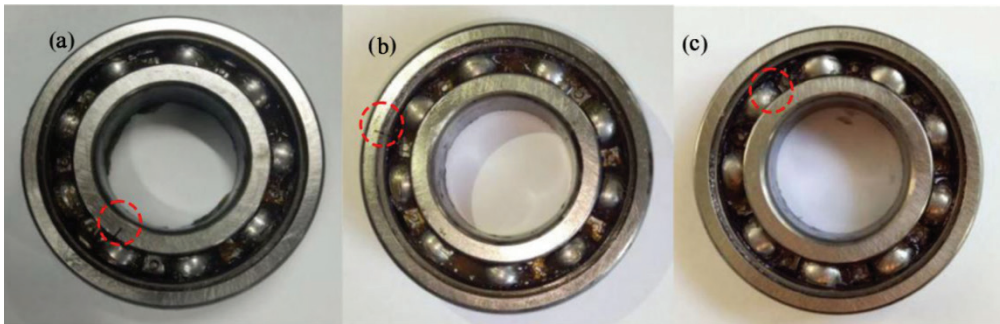
**Fig. 8.** Experiment platform for rolling bearing fault used by CWRU which consists of four parts: motor, torque transducer/encoder, dynamometer, and electronic control

there are 10 states in total and their fault time-domain waveforms are shown in Fig. 10. The rolling bearings worked at three motor loads (746 W, 1492 W, 2238 W with three motor speeds (1772 r/min, 1750 r/min, and

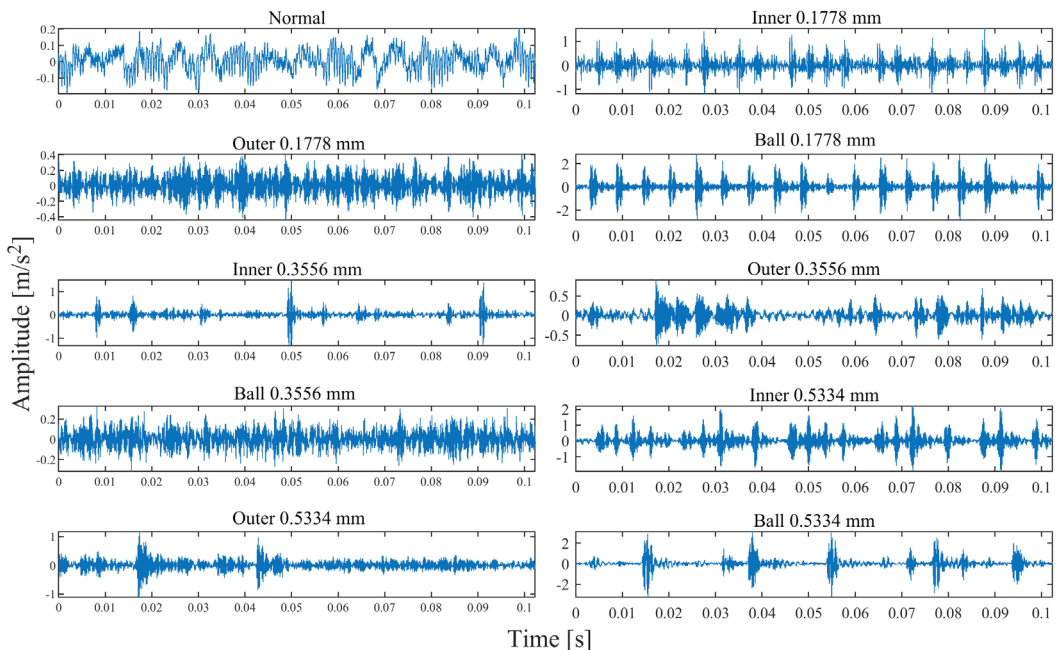
1730 r/min). The 10 states under the three working conditions (1 hp, 2 hp, 3 hp) are respectively denoted as A, B, and C. Dataset D consists of three working conditions. Details of the datasets are shown in Table 3; 80 % of the samples are extracted from the 10 states datasets under the three working conditions to form the training set and 20 % to form the test set.

### 2.3 Gearbox Dataset

The experiment in this paper used the HFZX-1 planetary gearbox fault diagnosis experimental platform, as shown in Fig. 11. The experimental platform consists of seven parts: motor, gearbox, flexible coupling, planetary gearbox, helical gearbox, torque sensor, and magnetic powder brake. Three fault states were in the experiment (gear tooth breakage,



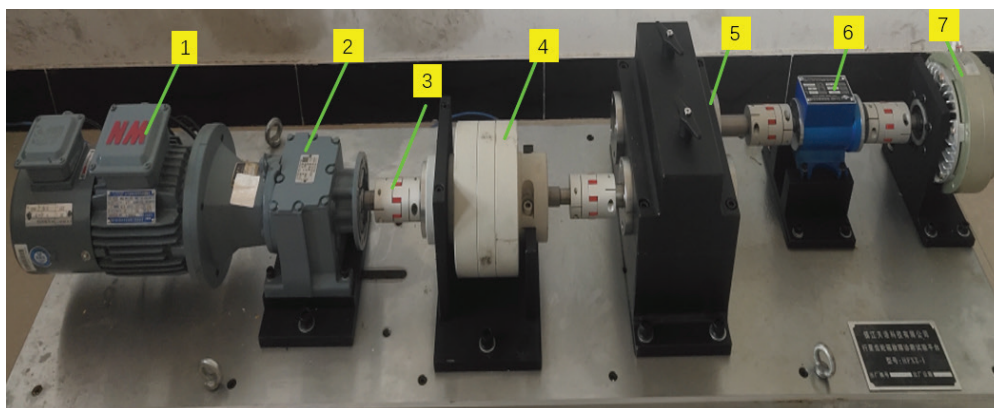
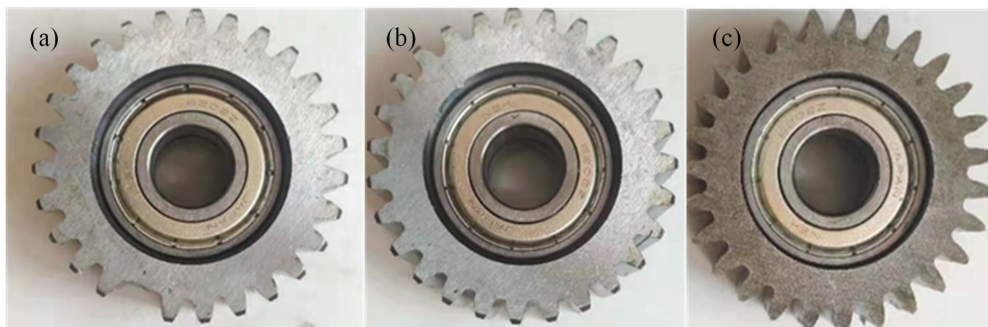
**Fig. 9.** Different faults of the rolling bearings: a) inner fault, b) outer fault, and c) ball fault



**Fig. 10.** Raw vibration signals for 10 states; rolling bearings include 10 states: Normal, Inner 0.1778 mm, Outer 0.1778 mm, Ball 0.1778 mm, Inner 0.3556 mm, Outer 0.3556 mm, Ball 0.3556 mm, Inner 0.5334 mm, Outer 0.5334 mm, and Ball 0.5334 mm

**Table 3.** The information of the rolling bearing datasets

Label		Normal		Inner			Ball			Outer	
		0	1	2	3	4	5	6	7	8	9
Fault diameter [inches]		0	0.007	0.014	0.021	0.007	0.014	0.021	0.007	0.014	0.021
A (1 hp)	Train	160	160	160	160	160	160	160	160	160	160
	Test	40	40	40	40	40	40	40	40	40	40
B (2 hp)	Train	160	160	160	160	160	160	160	160	160	160
	Test	40	40	40	40	40	40	40	40	40	40
C (3 hp)	Train	160	160	160	160	160	160	160	160	160	160
	Test	40	40	40	40	40	40	40	40	40	40
D (1 hp 2 hp 3 hp)	Train	480	480	480	480	480	480	480	480	480	480
	Test	120	120	120	120	120	120	120	120	120	120

**Fig. 11.** Planetary gearbox fault diagnosis experiment platform: 1 motor, 2 gearbox, 3 flexible coupling, 4 planetary gearbox, 5 helical gearbox, 6 torque sensor, and 7 magnetic powder brake**Fig. 12.** Different faults of the gearbox: a gear tooth breakage, b gear wear, and c gear crack

gear wear, and gear crack), as shown in Fig. 12, and one normal state.

The motor speed was set to 600 rad/min and the sampling frequency was 5120. Three loads were set: 0.1 A, 0.05 A, and 0 A corresponding to datasets A, B, and C. The acceleration sensor was installed outside the planetary gearbox to detect the vibration signal, and the time domain waveform of the original vibration signal is shown in Fig. 13.

## 2.4 Analysis of Experimental Results

The detailed structure and parameter settings of the SENet-MSCNN and GRU network models in the experimental data are shown in Table 2, which are the same as the detailed parameters under the simulated signals. The number of units in the dense layer being 10 and divided into 10 classifications. The data in A, B, C, and D working loads are used as the model input. To evaluate the superiority of the proposed method, it was compared with 1D-CNN, CNN-GRU, MSCNN,



GRU, BP, SVM, RF, and DT. The results are shown in Table 4. The proposed method outperforms the other models in various working loads. The average accuracy is improved by 1.75 %, 1.42 %, and 3.58 % compared with CNN-GRU, MSCNN, and 1DCNN, respectively. The traditional machine learning methods (SVM, RF, and DT) perform poorly, with average accuracy below 80%, which demonstrates that deep learning methods have better performance in massive vibration data. Hence, the recognition rate of the SENet-MSCNN and GRU networks is remarkably better than the other methods.

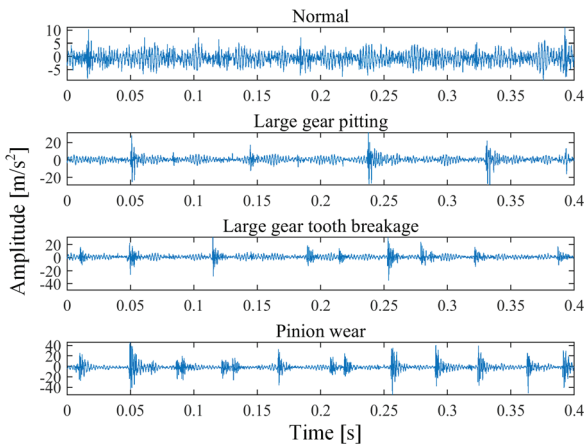


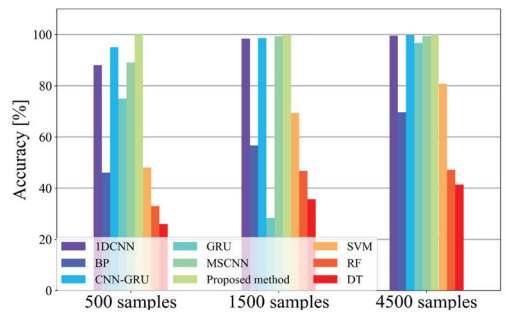
Fig. 13. Time-domain plots of vibration signals under four state modes

Table 4. The diagnosis rate of different methods in experimental data

Methods	Different working loads				Average [%]
	A	B	C	D	
Proposed method	100.00	100.00	100.00	100.00	100.00
1DCNN	98.00	94.67	93.00	100.00	96.42
CNN-GRU	97.67	99.00	97.00	99.33	98.25
MSCNN	97.33	99.00	99.00	99.00	98.58
GRU	96.33	84.67	95.66	94.00	92.64
BP	71.33	58.00	66.00	61.00	64.08
SVM	64.67	75.00	81.67	80.78	75.53
RF	47.67	60.33	49.33	47.33	51.16
DT	36.33	40.33	40.33	40.22	39.30

Considering the different performance of network models in different sizes of datasets, comparison experiments of three datasets (500 samples, 1500 samples, and 4500 samples) are established. The datasets are divided into training sets and test sets in the ratio of 4:1. The batch sizes of the three datasets are set to 16, 32, and 64, respectively. Compared with other methods,

the SENet-MSCNN and GRU model have the highest accuracy in three datasets with 100 %, 99.67 %, and 100 % respectively, which can be seen in Fig. 14. It also shows that the method has good performance in small datasets. Therefore, the accuracy and robustness of the proposed method in this paper are significantly better than others. Fig. 15 shows the time plots. The time consumed by the GRU network is the longest and the MSCNN is the shortest for each sample; the time consumed by the SENet-MSCNN and GRU networks is second. The MSCNN reduces the complexity of GRU model parameter computation and reduces the model training time. Furthermore, with the batch size increasing, the time consumed by every sample is further reduced. The consuming time of the proposed method is reduced to 19 ms/sample at 4500 samples, which further speeds up the model iteration. The SENet-MSCNN and GRU fault diagnosis models are significantly improved in terms of diagnostic accuracy, robustness, and diagnostic speed.



	500 samples	1500 samples	4500 samples
1DCNN	88.00 %	98.33 %	99.56 %
BP	46.00 %	56.67 %	69.56 %
CNN-GRU	95.00 %	98.67 %	99.78 %
GRU	75.00 %	28.33 %	96.56 %
MSCNN	89.00 %	99.33 %	99.40 %
Proposed method	100.00 %	99.67 %	100 %
SVM	48.00 %	69.33 %	80.78 %
RF	33.00 %	46.67 %	47.11 %
DT	26.00 %	35.67 %	41.33 %

Fig. 14. Diagnosis accuracy of different methods in three fault sample sets

## 2.5 Analysis of Ablation Experiments

In this section, we will do ablation experiments to compare the performance of the proposed method with several baseline methods (MSCNN, GRU, MSCNN-GRU).

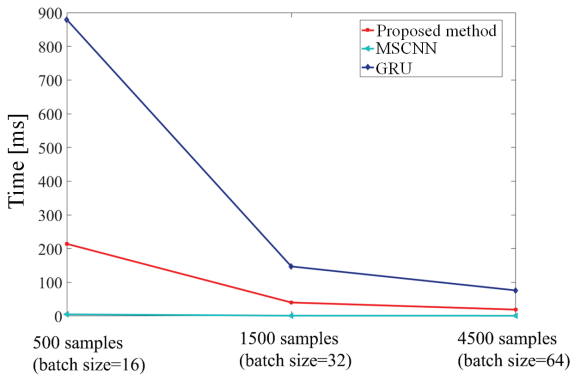


Fig. 15. Iteration speed of different methods in three datasets

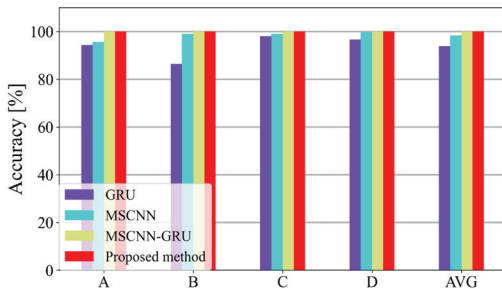


Fig. 16. Ablation study results

As Fig. 16 shows, the average accuracy of MSCNN and GRU is 93.83 % and 98.33 %, respectively. After the fusion of these two methods, MSCNN-GRU achieves 100 % accuracy in B, C, and D working conditions, with an average accuracy of 99.99 %. The proposed method adds the SENet to MSCNN-CNN, and the accuracy is further improved to reach 100 % in all four conditions. Thus, it is also

proved that the fusion of GRU, MSCNN, and SENet has a significant improvement in the recognition rate.

### 2.6 Variable Working Conditions Experiment

To further signify the migration characteristics of SENet-MSCNN and GRU models for different working conditions, the experiment datasets of A, B, C, and D working conditions are used as the input of the models. One of A, B, C, D working conditions is used as the source domain and another working condition dataset is used as the target domain, which constitutes 12 domains. Table 5 presents the accuracy of different methods in variable working conditions.

The average accuracy of BP, DT, RF, SVM models with shallow network structures is below 70 %, and the migration characteristics of these models are poor. The average accuracy of single deep network CNN, GRU, MSCNN is 91.12 %, 84.75 %, and 90.12 %, respectively. The network performance is improved. The average accuracy of the fused models, CNN-GRU, MSCNN-GRU, SENet-MSCNN and GRU are above 94.12 %. The network performance is further improved. The proposed method achieves the highest average accuracy of 98.98 %, which is 4.83 % and 2.81 % higher than CNN-GRU and MSCNN-GRU. Only in A-C, the MSCNN-GRU model performs better, with an improvement of 0.6 %. In the rest of the variable conditions, the proposed method has a significant improvement, especially in C-A, with an improvement of 11.2 %. The accuracy of all methods is reduced when C is used as the source domain or C is used as the target domain., which is explained by the fact that C enhances the cyclic shock response of rolling bearings, making the data more regular and the features learned by the network model simpler. This makes accuracy significantly reduce when testing low load data (especially 1hp working conditions), which

Table 5. Experimental diagnosis results of various methods

Methods	Variable working conditions test											Average [%]	
	A-B	A-C	A-D	B-A	B-C	B-D	C-A	C-B	C-D	D-A	D-B		D-C
1DCNN	99.60	91.40	96.60	90.00	74.80	89.00	79.40	86.40	87.00	99.20	100.00	100.00	91.12
BP	54.20	54.40	64.80	50.60	52.20	58.00	49.60	55.00	59.80	78.80	73.20	79.60	60.85
CNN-GRU	96.40	94.80	95.80	90.40	85.00	90.20	90.40	94.80	92.60	99.40	100.00	100.00	94.15
GRU	73.60	81.00	81.60	87.60	88.80	88.60	72.20	73.60	77.40	97.60	97.00	98.00	84.75
MSCNN	80.80	86.00	86.00	90.00	93.80	95.60	77.80	86.00	86.20	99.80	99.40	100.00	90.12
MSCNN-GRU	99.60	96.20	99.00	98.20	94.80	98.40	85.40	91.40	91.00	100.00	100.00	100.00	96.17
Proposed method	99.00	98.80	99.80	98.20	99.00	99.20	96.60	98.80	98.40	100.00	100.00	100.00	98.98
DT	33.60	35.80	49.60	32.00	34.20	45.20	35.20	36.80	44.80	63.80	64.20	62.80	44.83
RF	42.60	48.00	46.80	42.80	46.80	46.80	41.60	40.80	46.40	51.00	52.60	54.80	46.75
SVM	54.80	66.40	66.00	64.00	65.00	67.60	63.80	56.40	67.80	87.20	79.40	89.00	68.95

influences the migration characteristics of the model. Thus, the proposed method maintains a high accuracy under conditions with large differences, which proves that the feature extracted by the proposed method have stronger transfer characteristics.

Although the SENet-MSCNN and GRU model exhibit strong migration properties in the Western Reserve University bearing data, the bearing dataset is very transferable. Therefore, to further validate the migration properties of the method, the gearbox dataset was used to test. Table 6 presents the accuracy of different methods in variable working conditions. The SENet-MSCNN and GRU fusion model still exhibits the best performance on the gearbox dataset with an average accuracy of 76.44 %, an improvement of 4.61 %, 11.36 %, 9.77 %, and 2.69 % compared to the MSCNN, GRU, MSCNN-GRU, and CNN-GRU respectively. The average accuracy of traditional machine learning methods is below 56 %, with poor migration characteristics.

### 2.7 Visualization Results

(1) **Visualization of mid-layer activation.** A sample of the fourth fault type of rolling bearing (fault position is outer, fault diameter is 0.1778 mm) is used as input to the model; the feature map of each hidden layer output is visualized in a 2D image, which is shown in Fig. 17. The yellow parts represent the activated part and the blue parts represent the inactivated part. The features extracted by the first convolutional layer Conv 1, which is the yellow activated part, correspond to the shock component of the vibration signal. The global features extracted at different scales by the MSCNN layer are the same, while the local features are different. The convolutional kernels of  $3 \times 1$  and  $5 \times 1$  sizes are used in MSCNN\_b and MSCNN\_c. The branches are more sensitive to the shock signal and the extracted feature information has a higher resolution. As the number of network layers deepens, irrelevant information is filtered out and useful information is refined and

**Table 6.** Experimental diagnosis results of various methods

Methods	Variable working conditions test						Average [%]
	A-B	A-C	B-A	B-C	C-A	C-B	
1DCNN	69.00	53.00	61.50	100.00	48.00	89.50	70.17
BP	27.50	27.50	50.00	55.00	44.00	54.50	43.08
CNN-GRU	73.50	56.50	53.00	99.00	61.00	99.50	73.75
GRU	35.00	34.00	57.00	99.50	65.00	100.00	65.08
MSCNN	59.50	65.00	50.50	99.00	57.00	100.00	71.83
MSCNN-GRU	41.50	40.50	50.50	99.50	68.00	100.00	66.67
Proposed method	74.67	58.00	54.00	100.00	72.67	99.33	76.44
DT	28.50	26.00	33.00	42.00	34.50	28.00	32.00
RF	27.50	27.50	50.00	43.50	48.00	56.00	42.08
SVM	34.00	36.50	50.50	83.50	50.50	81.00	56.00

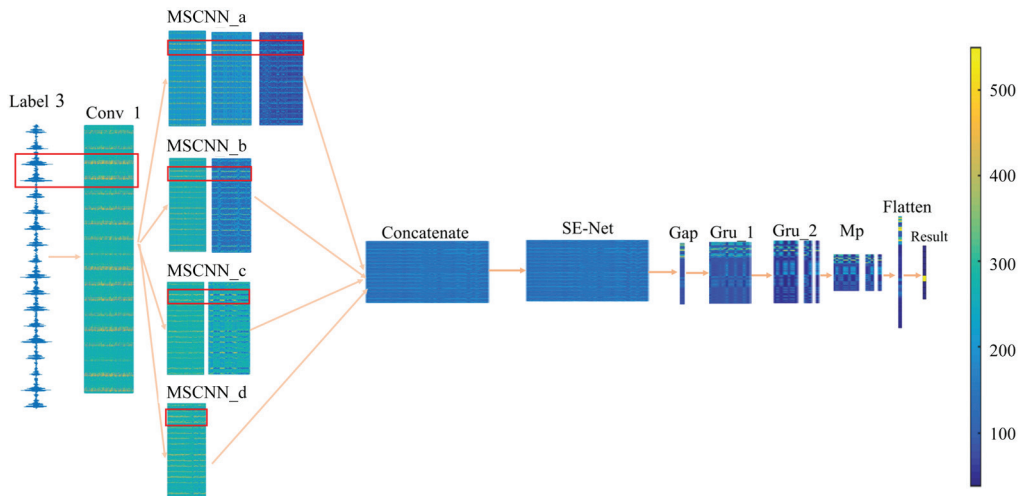


**Fig. 17.** Visualization of the hidden layer activations of SENet-MSCNN and GRU, label 3 represents the fourth fault type of rolling bearing

scaled up. The feature map becomes clearer, the extracted features are more abstract, and the source domain information is less relevant. The target domain information is gradually more relevant.

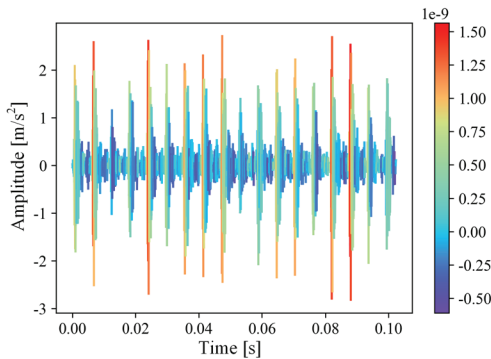


**Fig. 18.** Visualization of time-domain waveforms for class activation; the red parts represent the activated part and the blue parts represent the inactivated part

**(2) Visualization of the time-domain plot for class activation.** The time-domain waveform plot of the activation intensity of the vibration signal for the fourth fault states (fault location is the outer and the fault diameter is 0.1778 mm) is obtained by the method of class activation visualization [44]. As shown in Fig. 18, the medium and low-frequency shock signals in the red parts have a strong influence on the classification results of the fault diagnosis model, and the high-frequency signals in the blue parts have less influence on the classification results.

The part of the SENet-MSCNN and GRU model that is more sensitive to the vibration signal of the fourth fault state is similar to the characteristic frequency of the vibration signal of the fourth fault state, which further explains the fault diagnosis model to diagnose the input signal as the fourth fault state.

**(3) T-SNE Visualization.** T-SNE (T-distributed Stochastic Neighbor Embedding) is a common method used for data dimensionality reduction and visualization. In this paper, high dimension data is represented by low dimension distribution using the T-SNE method. Fig. 19 presents 1000 validation sets classified by the SENet-MSCNN and GRU models and the T-SNE visualization of their intermediate processes. The T-SNE visualization picture of raw signal through the Input Layer is confusing in the two-dimension space. The T-SNE visualization picture of raw signal through the SENet-MSCNN Layer has initial classification characteristics. GRU Layer already has obvious classification features, and the 10 states are remarkably separated from each other. The Dense Layer has even more obvious classification features, with the same state clustered at the same location and the distance between different states is larger.

### 3 CONCLUSIONS AND FUTURE WORK

In this paper, a rolling bearing fault diagnosis method based on SENet-MSCNN and GRU model is proposed. The method was applied to the comparative

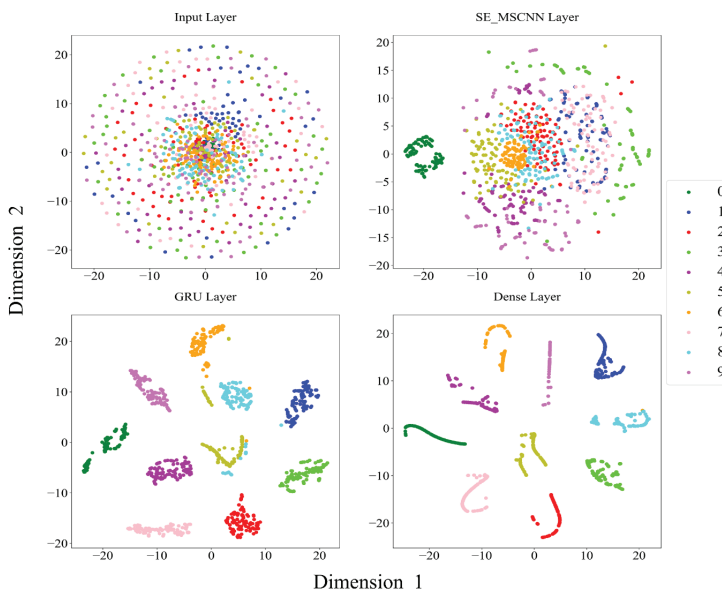


**Fig. 19.** Visualization feature distribution map using T-SNE; feature visualization of the Input Layer, SENet-MSCNN Layer, GRU Layer, and Dense Layer structures of SENet-MSCNN and GRU



analysis of the bearing data set and achieved a recognition rate of over 99.67 %. Compared with other representative fault diagnosis methods, the proposed method has significant advantages in terms of fault identification rate and robustness performance. In addition, we tested the migration capability of the model under variable working conditions in both the bearing dataset and the gearbox dataset. The method achieved recognition rates of 98.98 % and 76.44 % in the cross-service tests, respectively. The results show that the method exhibits better migration properties.

Therefore, the method is expected to provide a new method for rolling bearing fault diagnosis. In future research, we will apply the proposed fault diagnosis method to other mechanical fault types to determine its effectiveness in diagnosing a wider range of mechanical faults.

#### 4 ACKNOWLEDGEMENTS

This work was supported by the Youth Science Foundation of Northeast Petroleum University [Grant numbers 2018QNL-28].

#### 5 REFERENCES

- [1] Zhao, C., Sun, H. (2019). Dynamic distributed monitoring strategy for large-scale nonstationary processes subject to frequently varying conditions under closed-loop control. *IEEE Transactions on Industrial Electronics*, vol. 66, no. 6, p. 4749-4758, DOI:10.1109/tie.2018.2864703.
- [2] AlShorman, O., Alkahatni, F., Masadeh, M., Irfan, M., Glowacz, A., Althobiani, F., Kozik, J., Glowacz, W. (2021). Sounds and acoustic emission-based early fault diagnosis of induction motor: A review study. *Advances in Mechanical Engineering*, vol. 13, no. 2, DOI:10.1177/1687814021996915.
- [3] Gong, T., Yang, J., Liu, S., Liu, H. (2022). Non-stationary feature extraction by the stochastic response of coupled oscillators and its application in bearing fault diagnosis under variable speed condition. *Nonlinear Dynamics*, vol. 108, no. 4, p. 3839-3857, DOI:10.1007/s11071-022-07373-y.
- [4] Yun, K., Chong, Y., Enzhe, S., Liping, Y., Quan, D. (2021). Fault diagnosis method of diesel engine injector based on hierarchical weighted permutation entropy. *IEEE International Instrumentation and Measurement Technology Conference*, p. 1-6, DOI:10.1109/I2MTC50364.2021.9460083.
- [5] Li, Y., Dai, W., Zhang, W. (2020). Bearing fault feature selection method based on weighted multidimensional feature fusion. *IEEE Access*, vol. 8, p. 19008-19025, DOI:10.1109/access.2020.2967537.
- [6] Wrzochal, M., Adamczak, S., Piotrowicz, G., Wnuk, S. (2022). Industrial experimental research as a contribution to the development of an experimental model of rolling bearing vibrations. *Strojniški vestnik - Journal of Mechanical Engineering*, vol. 68, no. 9, p. 552-559, DOI:10.5545/sv-jme.2022.184.
- [7] Yi, C., Wang, H., Ran, L., Zhou, L., Lin, J. (2022). Power spectral density-guided variational mode decomposition for the compound fault diagnosis of rolling bearings. *Measurement*, vol. 199, DOI:10.1016/j.measurement.2022.111494.
- [8] Glowacz, A., Tadeusiewicz, R., Legutko, S., Caesarendra, W., Irfan, M., Liu, H., Brumerick, F., Gutten, M., Sulowicz, M., Antonino Daviu, J.A., Sarkodie-Gyan, T., Fracz, P., Kumar, A., Xiang, J. (2021). Fault diagnosis of angle grinders and electric impact drills using acoustic signals. *Applied Acoustics*, vol. 179, DOI:10.1016/j.apacoust.2021.108070.
- [9] Ribeiro Junior, R.F., dos Santos Areias, I.A., Campos, M.M., Teixeira, C.E., da Silva, L.E.B., Gomes, G.F. (2022). Fault detection and diagnosis in electric motors using convolution neural network and short-time fourier transform. *Journal of Vibration Engineering & Technologies*, vol. 10, no. 7, p. 2531-2542, DOI:10.1007/s42417-022-00501-3.
- [10] Li, Y., Cheng, G., Liu, C. (2021). Research on bearing fault diagnosis based on spectrum characteristics under strong noise interference. *Measurement*, vol. 169, DOI:10.1016/j.measurement.2020.108509.
- [11] Peng, H., Zhang, H., Fan, Y., Shangguan, L., Yang, Y. (2022). A review of research on wind turbine bearings' failure analysis and fault diagnosis. *Lubricants*, vol. 11, no. 1, DOI:10.3390/lubricants11010014.
- [12] Peng, Z., Zhike, P., Shiqian, C. (2020). Review of signal decomposition theory and its applications in machine fault diagnosis. *Journal of Mechanical Engineering*, vol. 56, no. 17, DOI:10.3901/jme.2020.17.091.
- [13] Kumar, A., Gandhi, C.P., Vashishtha, G., Kundu, P., Tang, H., Glowacz, A., Shukla, R.K., Xiang, J. (2021). Vmd based trigonometric entropy measure: A simple and effective tool for dynamic degradation monitoring of rolling element bearing. *Measurement Science and Technology*, vol. 33, no. 1, DOI:10.1088/1361-6501/ac2fe8.
- [14] Zhou, J., Xiao, M., Niu, Y., Ji, G. (2022). Rolling bearing fault diagnosis based on WGWOA-VMD-SVM. *Sensors*, vol. 22, no. 16, DOI:10.3390/s22166281.
- [15] Jiang, J., Liu, Y., Xu, C., Shen, H., Soni, M. (2022). Research on motor bearing fault diagnosis based on the adaboost algorithm and the ensemble learning with bayesian optimization in the industrial internet of things. *Security and Communication Networks*, vol. 2022, p. 1-12, DOI:10.1155/2022/4569954.
- [16] Hosseinpour-Zarnaq, M., Omid, M., Biabani-Aghdam, E. (2022). Fault diagnosis of tractor auxiliary gearbox using vibration analysis and random forest classifier. *Information Processing in Agriculture*, vol. 9, no. 1, p. 60-67, DOI:10.1016/j.inpa.2021.01.002.
- [17] Gunerkar, R.S., Jalan, A.K., Belgamwar, S.U. (2019). Fault diagnosis of rolling element bearing based on artificial neural network. *Journal of Mechanical Science and Technology*, vol. 33, no. 2, p. 505-511, DOI:10.1007/s12206-019-0103-x.
- [18] Zhang, Z., Li, H., Chen, L., Han, P., Shi, H. (2021). Rolling bearing fault diagnosis using improved deep residual shrinkage networks. *Shock and Vibration*, vol. 2021, p. 1-11, DOI:10.1155/2021/9942249.
- [19] Wang, H., Liu, Z., Peng, D., Cheng, Z. (2022). Attention-guided joint learning cnn with noise robustness for bearing fault

- diagnosis and vibration signal denoising. *ISA Transactions*, vol. 128, p. 470-484, DOI:10.1016/j.isatra.2021.11.028.
- [20] Mao, W., Feng, W., Liu, Y., Zhang, D., Liang, X. (2021). A new deep auto-encoder method with fusing discriminant information for bearing fault diagnosis. *Mechanical Systems and Signal Processing*, vol. 150, DOI:10.1016/j.ymssp.2020.107233.
- [21] Lv, D., Wang, H., Che, C. (2021). Fault diagnosis of rolling bearing based on multimodal data fusion and deep belief network. *Proceedings of the Institution of Mechanical Engineers, Part C: Journal of Mechanical Engineering Science*, vol. 235, no. 22, p. 6577-6585, DOI:10.1177/09544062211008464.
- [22] Liu, H., Zhou, J., Zheng, Y., Jiang, W., Zhang, Y. (2018). Fault diagnosis of rolling bearings with recurrent neural network-based autoencoders. *ISA Trans*, vol. 77, p. 167-178, DOI:10.1016/j.isatra.2018.04.005.
- [23] Li, D., Liu, S., Gao, F., Sun, X. (2021). Continual learning classification method for time-varying data space based on artificial immune system. *Journal of Intelligent & Fuzzy Systems*, vol. 40, no. 5, p. 8741-8754, DOI:10.3233/jifs-200044.
- [24] Bin, G.F., Gao, J.J., Li, X.J., Dhillon, B.S. (2012). Early fault diagnosis of rotating machinery based on wavelet packets-empirical mode decomposition feature extraction and neural network. *Mechanical Systems and Signal Processing*, vol. 27, p. 696-711, DOI:10.1016/j.ymssp.2011.08.002.
- [25] Lin, Y., Xiao, M., Liu, H., Li, Z., Zhou, S., Xu, X., Wang, D. (2022). Gear fault diagnosis based on cs-improved variational mode decomposition and probabilistic neural network. *Measurement*, vol. 192, DOI:10.1016/j.measurement.2022.110913.
- [26] Guo, S., Yang, T., Gao, W., Zhang, C. (2018). A novel fault diagnosis method for rotating machinery based on a convolutional neural network. *Sensors*, vol. 18, no. 5, DOI:10.3390/s18051429.
- [27] Guo, M.-F., Yang, N.-C., Chen, W.-F. (2019). Deep-learning-based fault classification using hilbert-huang transform and convolutional neural network in power distribution systems. *IEEE Sensors Journal*, vol. 19, no. 16, p. 6905-6913, DOI:10.1109/jsen.2019.2913006.
- [28] Sun, W., Zhao, R., Yan, R., Shao, S., Chen, X. (2017). Convolutional discriminative feature learning for induction motor fault diagnosis. *IEEE Transactions on Industrial Informatics*, vol. 13, no. 3, p. 1350-1359, DOI:10.1109/tii.2017.2672988.
- [29] Chen, Z., Gryllias, K., Li, W. (2019). Mechanical fault diagnosis using convolutional neural networks and extreme learning machine. *Mechanical Systems and Signal Processing*, vol. 133, DOI:10.1016/j.ymssp.2019.106272.
- [30] Wang, S., Xiang, J., Zhong, Y., Zhou, Y. (2018). Convolutional neural network-based hidden markov models for rolling element bearing fault identification. *Knowledge-Based Systems*, vol. 144, p. 65-76, DOI:10.1016/j.knsys.2017.12.027.
- [31] Hao, S., Ge, F.-X., Li, Y., Jiang, J. (2020). Multisensor bearing fault diagnosis based on one-dimensional convolutional long short-term memory networks. *Measurement*, vol. 159, DOI:10.1016/j.measurement.2020.107802.
- [32] Zhang, P., Chen, C. (2022). Wind turbine planetary gearbox fault diagnosis using circular pitch cyclic vector and a bidirectional gated recurrent unit. *Measurement Science and Technology*, vol. 34, no. 1, DOI:10.1088/1361-6501/ac95b2.
- [33] Zhu, Y., Zhu, C., Tan, J., Tan, Y., Rao, L. (2022). Anomaly detection and condition monitoring of wind turbine gearbox based on LSTM-FS and transfer learning. *Renewable Energy*, vol. 189, p. 90-103, DOI:10.1016/j.renene.2022.02.061.
- [34] Shi, J., Peng, D., Peng, Z., Zhang, Z., Goebel, K., Wu, D. (2022). Planetary gearbox fault diagnosis using bidirectional-convolutional lstm networks. *Mechanical Systems and Signal Processing*, vol. 162, DOI:10.1016/j.ymssp.2021.107996.
- [35] Chen, X., Zhang, B., Gao, D. (2020). Bearing fault diagnosis base on multi-scale cnn and lstm model. *Journal of Intelligent Manufacturing*, vol. 32, no. 4, p. 971-987, DOI:10.1007/s10845-020-01600-2.
- [36] Li, X., Li, J., Qu, Y., He, D. (2019). Gear pitting fault diagnosis using integrated cnn and gru network with both vibration and acoustic emission signals. *Applied Sciences*, vol. 9, no. 4, DOI:10.3390/app9040768.
- [37] Hu, J., Shen, L., Albanie, S., Sun, G., Wu, E. (2020). Squeeze-and-excitation networks. *IEEE Trans Pattern Anal Mach Intell*, vol. 42, no. 8, p. 2011-2023, DOI:10.1109/TPAMI.2019.2913372.
- [38] Szegedy, C., Liu, W., Jia, Y., Sermanet, P., Reed, S., Anguelov, D., Erhan, D., Vanhoucke, V., Rabinovich, A. (2015). Going deeper with convolutions. *Proceedings of the IEEE Computer Society Conference on Computer Vision and Pattern Recognition*, vol. 07-12-June, p. 1-9, DOI:10.1109/CVPR.2015.7298594.
- [39] Peng, D., Wang, H., Liu, Z., Zhang, W., Zuo, M.J., Chen, J. (2020). Multibranch and multiscale cnn for fault diagnosis of wheelset bearings under strong noise and variable load condition. *IEEE Transactions on Industrial Informatics*, vol. 16, no. 7, p. 4949-4960, DOI:10.1109/tii.2020.2967557.
- [40] Gao, T., Yang, J., Jiang, S., Yan, G. (2020). A novel fault diagnosis method for analog circuits based on conditional variational neural networks. *Circuits, Systems, and Signal Processing*, vol. 40, no. 6, p. 2609-2633, DOI:10.1007/s00034-020-01595-4.
- [41] Lv, H., Chen, J., Pan, T., Zhang, T., Feng, Y., Liu, S. (2022). Attention mechanism in intelligent fault diagnosis of machinery: A review of technique and application. *Measurement*, vol. 199, DOI:10.1016/j.measurement.2022.111594.
- [42] Lv, Y., Yuan, R., Song, G. (2016). Multivariate empirical mode decomposition and its application to fault diagnosis of rolling bearing. *Mechanical Systems and Signal Processing*, vol. 81, p. 219-234, DOI:10.1016/j.ymssp.2016.03.010.
- [43] He, X., Zhou, X., Yu, W., Hou, Y., Mechefske, C.K. (2021). Bearing fault detection and diagnosis using case western reserve university dataset with deep learning approaches: A review. *ISA Trans*, vol. 111, p. 360-375, DOI:10.1016/j.isatra.2020.10.060.
- [44] Chao, Q., Wei, X., Tao, J., Liu, C., Wang, Y. (2022). Cavitation recognition of axial piston pumps in noisy environment based on grad-cam visualization technique. *CAAI Transactions on Intelligence Technology*, DOI:10.1049/cit2.12101.

# Wear Behaviour of a Cu-Ni-Sn Hybrid Composite Reinforced with B<sub>4</sub>C prepared by Powder Metallurgy Technique

Haiter Lenin Allasi<sup>1,\*</sup> – Vettivel Singaravel Chidambaranathan<sup>2</sup> – Mary Vasanthi Soosaimariyan<sup>3</sup>

<sup>1</sup> WOLLO University, Kombolcha Institute of Technology, School of Mechanical and Chemical Engineering, Ethiopia

<sup>2</sup> Chandigarh College of Engineering and Technology, Department of Mechanical Engineering, India

<sup>3</sup> St Xavier's Catholic College of Engineering, Department of Electronics and Communication Engineering, India

*Cu matrix composites benefit from the high electrical and thermal conductivities of Cu and the mechanical wear/erosion resistance of hard reinforcement. In this study, an attempt has been made to determine the effect of the addition of reinforcement B<sub>4</sub>C in Cu-Ni-Sn. The B<sub>4</sub>C is reinforced to form a hybrid Cu matrix composite with powder metallurgy technique. The hybrid composites are obtained by milling, blending, and compacting the powders to obtain a fine grain-sized particle without aggregation. The grain size and particle nature were characterized using scanning electron microscope (SEM) and X-ray diffraction (XRD) techniques, respectively. The microstructure, density, hardness, and wear rate of the composites were studied. The pin-on-disc method is equipped to study the wear behaviour and coefficient of friction. The sintered density of the prepared Cu-15%Ni is 98.25 %, Cu-8%Sn is 98.20 %, Cu-15%Ni-8%Sn is 98.10 % and Cu-15%Ni-8%Sn-2%B<sub>4</sub>C is 95.26 % and lower specific wear rate has been recorded for Cu-15Ni-8Sn-2B<sub>4</sub>C 121×10<sup>-6</sup> mm<sup>3</sup>/(Nm) and the addition of reinforcement B<sub>4</sub>C in Cu-Ni-Sn displays remarkable changes in wear rate and friction coefficient.*

**Keywords:** powder metallurgy, copper, wear, characterization, density, composites

## Highlights

- The sintered density of the prepared Cu-15%Ni is 98.25 %, Cu-8%Sn is 98.20 %, Cu-15%Ni-8%Sn is 98.10 % and Cu-15%Ni-8%Sn-2%B<sub>4</sub>C is 95.26 %.
- The addition of reinforcement B<sub>4</sub>C in Cu-Ni-Sn displays remarkable changes in wear rate and friction coefficient.
- The lower specific wear rate has been recorded for Cu-15Ni-8Sn-2B<sub>4</sub>C is 121×10<sup>-6</sup> mm<sup>3</sup>/(Nm).
- The severe plastic deformation and cracks are reduced with the addition of B<sub>4</sub>C.

## 0 INTRODUCTION

Metal matrix composites (MMCs) are newer materials made in response to increased demand due to emerging applications in the fields of aircraft, space, defence, automotive, and transport because of their good strength and light weight [1] to [4]. The MMCs of different varieties are prepared with powder metallurgy techniques, which is suitable for bulk production. However, due to the existence of residual porosity and exhibited poor mechanical properties, it is used because of its non-wetting behaviour of MMCs.

Cu matrix composites benefit from the high electrical and thermal conductivities of Cu and the mechanical wear/erosion resistance of the reinforcement, such as WC. In addition to Cu–WC, other potential materials for similar applications are Cu–Mo, Cu–Al<sub>2</sub>O<sub>3</sub>, Ag–Mo, Ag–W, Cu–SiC, Cu–TiC, Cu–Sn, Cu–Ni and Ag–CdO [5].

Senthil Kumar et al. studied the tribological behaviours of Cu–6Sn–6Zn–3Pb alloy sliding against AISI 321 stainless steel under sea water, distilled water and dry sliding conditions are studied on a pin-on-disc tester. Generally, the friction coefficient in

distilled water is the largest and the smallest in dry sliding. The wear mechanism is a micro-plough and plastic deformation in distilled water and under dry sliding [6].

Vettivel et al. studied the development of Cu-reinforced SiC particulate composites; SiC particles as reinforcement were blended with unmilled and as-milled Cu powder with reinforcement contents of 10 vol. %, 20 vol. %, 30 vol. %, and 40 vol. % using powder metallurgy. X-ray diffraction of all the composites was done in order to determine the various phases in the composites. Scanning electron microscopy (SEM) and EDS (electron diffraction X-ray spectroscopy) were carried out for the microstructure analysis of the composites. Cu–SiC composites containing higher vol. % of the SiC show better wear resistance [7].

The microstructure and tensile properties of Cu alloy reinforced with boron carbide (B<sub>4</sub>C) using a stir-casting technique. The hardness of the composites increased gradually by adding the reinforcement compared to the base alloy properties. The yield strength also increases by adding the B<sub>4</sub>C particulates into the Cu alloy matrix [8]. Another study confirmed that mechanical and thermal properties of multi-

\*Corr. Author's Address: Wollo University, Kombolcha Institute of Technology, School of Mechanical and Chemical Engineering, Ethiopia, drahlenin@kiot.edu.et



walled carbon nanotubes (CNT) reinforced Cu–10Sn alloy composites. Microstructural observations showed that CNTs were retained in the composite matrix after laser processing. The addition of CNTs showed improvement in strain hardening, mechanical, and thermal properties of Cu–10Sn alloy. Composites with 12 vol. % CNTs showed more than an 80 % increase in the Young's modulus and a 40 % increase in the thermal conductivity of Cu–10Sn alloy [9] and [10].

Cu is used as a primary matrix and Ni and Sn as a secondary matrix and 2 %  $B_4C$  as reinforcement added to the alloy (Cu-15%Ni-8%Sn). These spindle alloys cover excellent bearing properties and are thus used in a wide range of applications [11]. Copper an electrolytic ally processed and precipitated metal is taken and coated with nickel and tin with volume fractions of 15 % and 8 % respectively. Nickel is compatible and provides better reinforcement and adhesion to the carbide materials [12].

In this study, copper, nickel, tin and boron carbide are reinforced to form hybrid MMCs via a

powder metallurgy technique. The hybrid composites are obtained by milling, blending, and compacting powders to obtain a fine grain-sized particle without aggregation. The effect of the addition of  $B_4C$  in mechanical and tribological behaviour has been studied.

## 1 METHODS

Electrolytic copper powder with density  $8.92 \text{ g/cm}^3$  at  $20 \text{ }^\circ\text{C}$ , nickel with  $8.9 \text{ g/cm}^3$  at  $20 \text{ }^\circ\text{C}$  and tin with  $7.3 \text{ g/cm}^3$  at  $20 \text{ }^\circ\text{C}$ , whereas boron carbide  $2.52 \text{ g/cm}^3$  at  $20 \text{ }^\circ\text{C}$  is reinforced to the metals. These are mechanically alloyed to the micron range and the samples are fabricated with a powder metallurgy technique to prepare MMCs. Then, the obtained MMC is sintered to high temperature of about  $900 \text{ }^\circ\text{C}$ . The sintered density of the Cu-15%Ni is 98.25 %, Cu-8%Sn is 98.20 %, Cu-15%Ni-8%Sn is 98.10 % and Cu-15%Ni-8%Sn-2% $B_4C$  is 95.26 %.

The morphology and size of the particles are examined for individual metals and alloys, also after

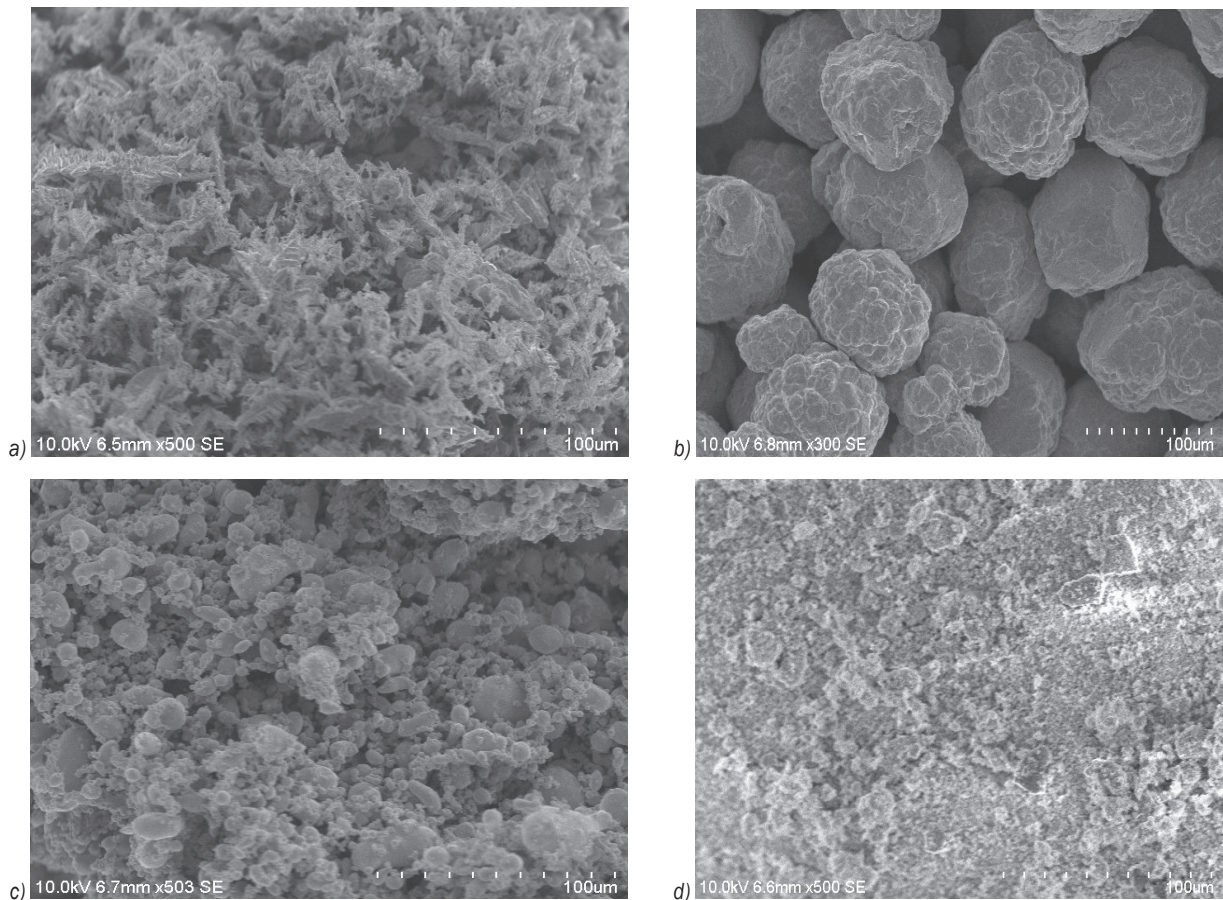


**Fig. 1.** SEM image of unreinforced materials: a) Copper (Cu), b) Nickel (Ni), c) Tin (Sn), and d) 2% Boron carbide ( $B_4C$ )



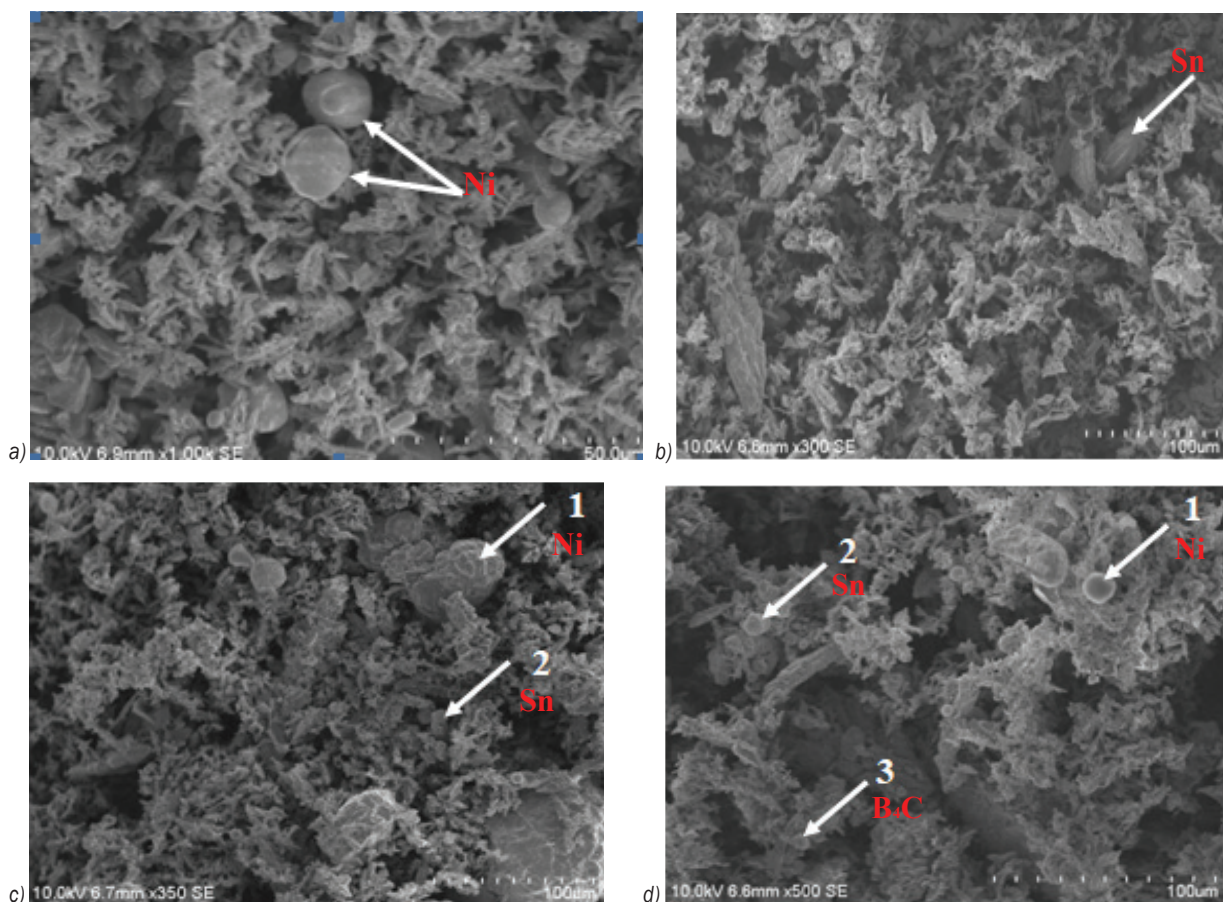
reinforcement added to the materials (i.e., MMC using SEM). The crystal structure and the phase change of the materials are studied using an X-ray diffractometer (XRD) with respect to the intensity peaks and materials diffraction angle  $2\theta$ . The hardness, strength and wear of the composites are determined using a pin-on-disc apparatus with which the sliding distance, sliding velocity, load, and speed are applied to the composites by varying these parameters.

The SEM image shows the particle sizes are 100  $\mu\text{m}$ , 30  $\mu\text{m}$ , 20  $\mu\text{m}$ , and 10  $\mu\text{m}$  for all metals such as Cu, Ni, Sn and  $\text{B}_4\text{C}$ , respectively. The MMCs Cu-15%Ni, Cu-8%Sn, Cu-15%Ni-8%Sn and Cu-15%Ni-8%Sn-2% $\text{B}_4\text{C}$  also exhibit smaller sizes. The morphology and grain nature of the materials are visualized using SEM and are obtained in different morphological forms. The Cu metal looks like cylindrical short tubes and have a slightly adhesive nature, whereas Ni, Sn and  $\text{B}_4\text{C}$  show solid spherical balls with much less agglomeration.

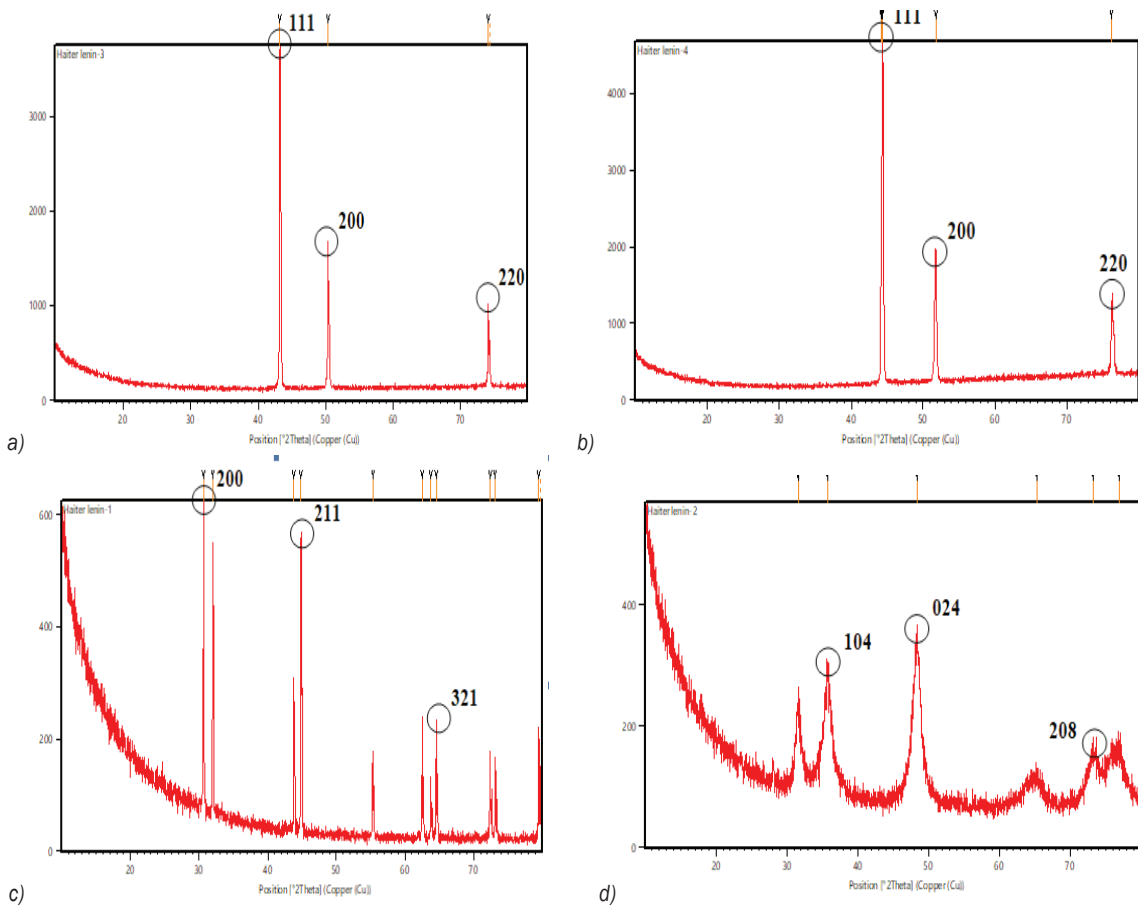
The mixed MMCs after 2 %  $\text{B}_4\text{C}$  is reinforced exhibit good morphology and fine-grain nature.

Fig. 2a and b show the SEM images of Cu and Ni, respectively. and the diameter of the particles ranges from 5  $\mu\text{m}$  to 20  $\mu\text{m}$ , whereas Fig. 2c and d exhibit foamy and short fibrous materials, respectively. The MMC of Cu-15%Ni-8%Sn-2% $\text{B}_4\text{C}$  exhibits improved shape, with cylindrical tubes and spherical balls compressed against one another more evenly and resembling a very fine dispersion of particles with diameters ranging from 1  $\mu\text{m}$  to 10  $\mu\text{m}$ . The composites are well mixed, while the powders are crushed and blended to obtain good compaction of materials.

The X-ray diffractometer analysis of the particles in Fig. 3 reveals good crystal structure and phase development in the lattice fringes. Cu and Ni have a peak that corresponds to the (111) hkl lattice plane (Fig. 2a and b) and shows pure materials that have not been reacted with by the atmosphere, but Sn and  $\text{B}_4\text{C}$  have illogical peaks that show fewer impurities. For Sn and  $\text{B}_4\text{C}$ , the hkl lattice planes are 200 and 024, respectively, due to the amorphous nature of the particles.



**Fig. 2.** SEM images of reinforced materials; a) Cu-Ni, b) Cu-Sn, c) Cu-Ni-Sn, and d) Cu-Ni-Sn-2% $\text{B}_4\text{C}$



**Fig. 3.** XRD patterns for unreinforced materials; a) Copper (Cu), b) Nickel (Ni), c) Tin (Sn), and d) Boron carbide ( $B_4C$ )

The materials have incorporated each other into copper metal and then  $B_4C$  is reinforced to the composites and the composites are structurally characterized by XRD, which explores the hkl lattice planes with respect to the intensities and  $2\theta$  shown in Fig. 4. The materials are produced by mechanically alloying and composites are fabricated by Powder Metallurgy PM technique, milled, crushed, and then blended. Finally, the compaction of the material is well fitted by uniform dispersion of particles and sintered to a high temperature of about  $900\text{ }^\circ\text{C}$  to avoid further grain growth. Thus, the lattice parameters of the composites are uniformly distributed for Cu-Ni, Cu-Sn and Cu-Ni-Sn. While the reinforced composites contain carbon particles ( $B_4C$ ), the peaks point at another  $2\theta$  position and all other materials represent peaks in the same  $2\theta$  position.

## 2.1 Wear test

The pin-on-disc instrument is equipped to study the hardness and wear rate of the composites. Ultra-hard

materials are used for wear-resistant applications because they have good sliding interaction with the abrasive particles [13]. This research describes the wear rate of metals Cu, Ni and Sn individually and then alloy Cu-Ni-Sn and also for MMCs Cu-Ni-Sn- $B_4C$ , which exhibits better resistance to wear compared to alloy. The wear rate varies according to the variable parameters and contribution of the materials volume concentration.

The specific wear rates of the unreinforced and reinforced composites are analysed by changing the process parameters, mainly weight percentage or volume concentration, sintering temperature, load, sliding distance, sliding velocity, friction coefficient and volume loss of the composite material. Vettivel et al. [14], analysed the friction coefficient and specific wear rate by ANOVA (Analysis of Variance) method and found that the result mainly depends on the type and size of the reinforcement phase of the particles. Also, the metal-on-metal contact that takes place at the initial stage is relatively low at the steady state [15].

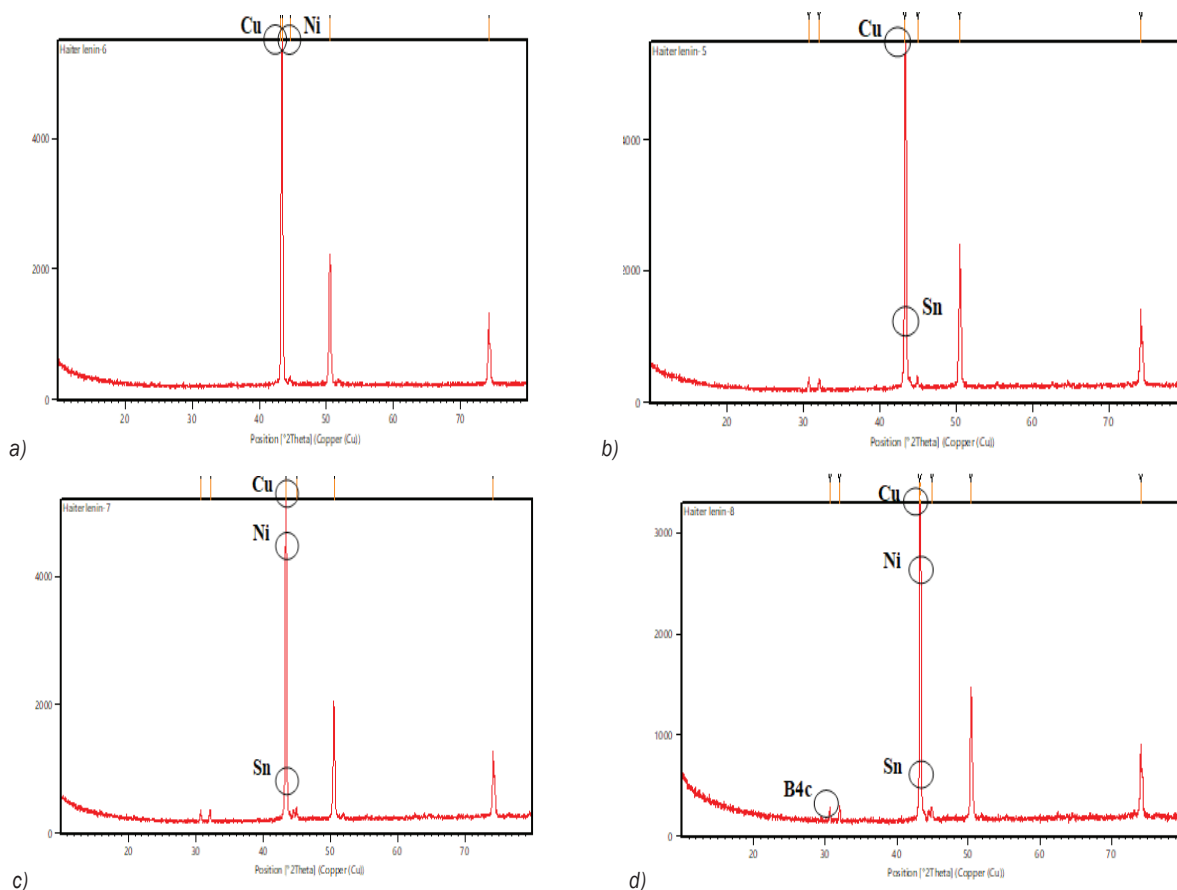


Fig. 4. XRD patterns of reinforced composites; a) Cu-Ni, b) Cu-Sn, c) Cu-Ni-Sn, and d) Cu-Ni-Sn-2%B<sub>4</sub>C

## 2 RESULTS AND DISCUSSION

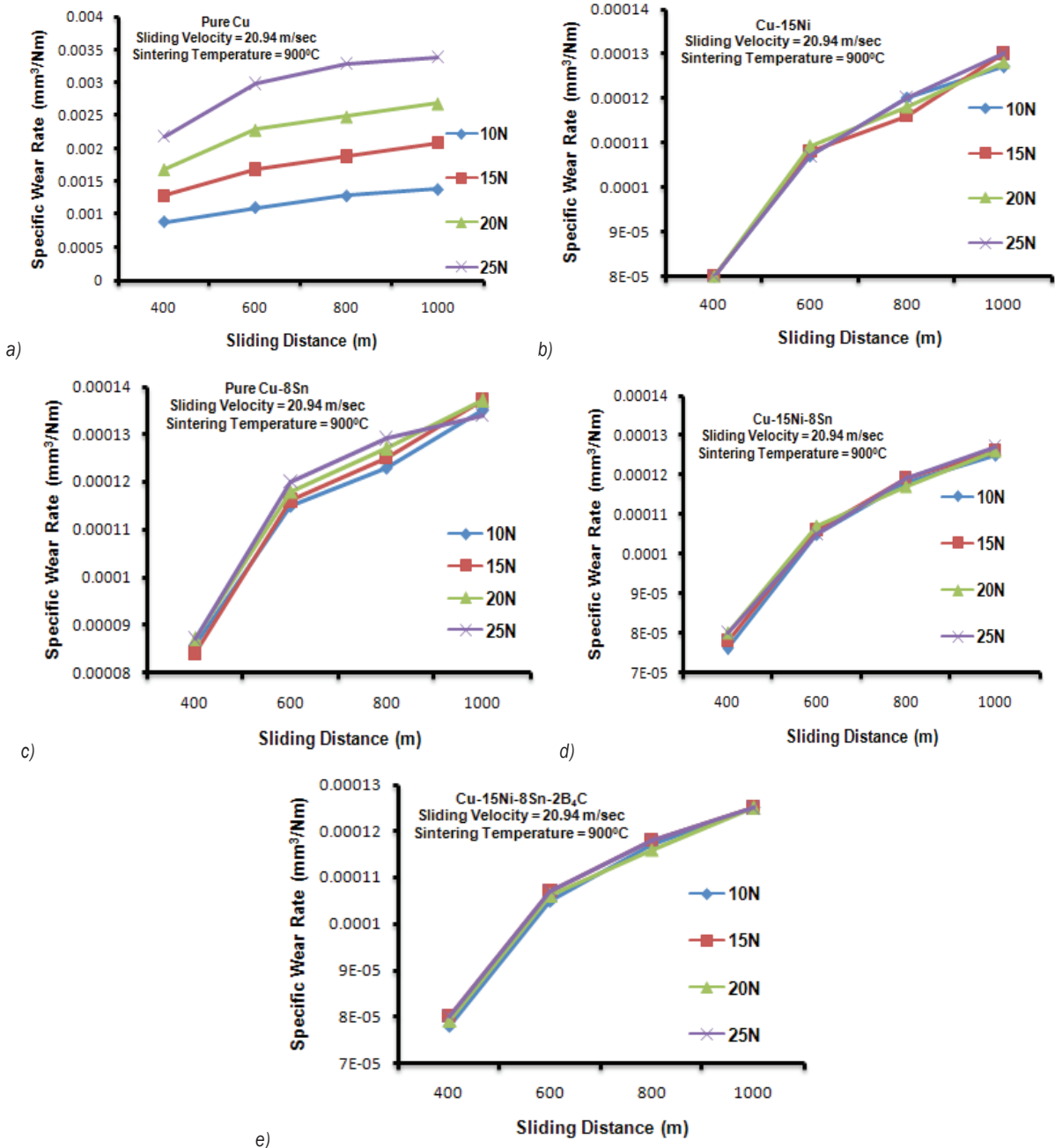
### 2.1 Effect of Sliding Distance on Specific Wear Rate

Fig. 5 represents the specific wear rate increases with the sliding distance significantly. There is a gradual and linear raise in specific wear rate due to the hardness of the composites according to the constituents added to it [16] to [18]. From Fig. 5a, pure copper metal is tested for a specific wear rate, which shows  $78 \times 10^{-5} \text{ mm}^3/(\text{Nm})$  to  $340 \times 10^{-6} \text{ mm}^3/(\text{Nm})$ , at a constant sintering temperature of  $900^\circ\text{C}$  and sliding speed  $20.94 \text{ m/s}$  and variable parameters like sliding distance and load applied is  $400 \text{ m}$  to  $1000 \text{ m}$  and  $10 \text{ N}$  to  $25 \text{ N}$ , correspondingly. Also, a specific wear rate is experienced for alloy Cu-15Ni and Cu-8Sn, which reveals that  $130 \times 10^{-6} \text{ mm}^3/(\text{Nm})$ , also for Cu-15Ni-8Sn alloy shows  $127 \times 10^{-6} \text{ mm}^3/(\text{Nm})$  with that a constant temperature and sliding speed and variable parameters of sliding distance at  $1000 \text{ m}$  and load applied of about  $25 \text{ N}$ . Here, we can infer that the alloy can have the intense effect in specific wear

rate compared to pure metal, which is at very heavy loading and high sliding distance. If the reinforcement B<sub>4</sub>C is added to that matrix alloy, the composite Cu-15Ni-8Sn-2B<sub>4</sub>C exhibits a reduced wear rate of about  $121 \times 10^{-6} \text{ mm}^3/(\text{Nm})$ . In this work, only 2%B<sub>4</sub>C is added as reinforcement resulted with a good reduction in specific wear rate compared to metal and matrix alloy. The lower specific wear rate has been recorded for Cu-15Ni-8Sn-2B<sub>4</sub>C. The decrement in specific wear rate is due to the addition of B<sub>4</sub>C in the Cu-15Ni-8Sn. The results are in good agreement with other studies [9] and [14].

### 2.2 Worn Surface and Microstructure

The worn surface analysis of the MMCs in various volume fractions was investigated using SEM. The samples were tested by placing it in a holder inside the vacuum chamber. The image displayed information about the composites after the load was applied to it. Along the sliding direction, the materials withstand and prevent deformation and formation of oxide



**Fig. 5.** The effect of sliding distance on specific wear rate of metal, matrix and composites; a) Cu, b) Cu-15Ni, c) Cu-8Sn, d) Cu-15Ni-8Sn, e) Cu-15Ni-8Sn-2B<sub>4</sub>C

debris at the interface region or at the contact surface; thus grooves, shear wedges, depth of penetration to wear, ploughing, and cracks can be observed. Due to the wear, the materials are abraded [19].

The worn surface of the unreinforced specimen is caused by the removal of material from the surface during the wear test. To avoid the rolling of the specimen, during the test the material was held in the

testing machine [20]. Ling. et al. [20] analysed the microstructure nature of the Al-SiC composites; they found that while adding reinforcement to the matrix, big pores were found, due to the low volume fraction and grain size of the reinforcement added to the composites [21]. The particles are in heterogeneous distribution and are so large that the worn surface can be seen; the durable bonding between the



reinforcement and matrix resulted in particle accumulation and grain boundaries [22] and [23].

The worn surface of the unreinforced Cu at constant load and wearing time is shown in Fig. 6a, it has long smooth patches consisting of cracks and wear grooves. At the centre of the specimen, long shear wedges can be seen. Copper shows short and discontinuous pitting steps because of the unreinforced and heterogeneous distribution of particles with irregular size. From Fig. 6b and c, it can be inferred that Cu-Ni and Cu-Sn are unreinforced;

the worn surface can be seen with shear wedges and wear grooves. Fig. 6d shows matrix alloy Cu-15Ni-8Sn exhibiting wear at constant load, time and sliding direction. Here also carbide material is not reinforced with this matrix and exhibits long and continuous smooth patches, cracks, and reduced wear grooves; it can withstand stress at high temperatures. Fig. 6e shows the morphology of the worn surface of the composite (reinforcement of carbide materials) Cu-15Ni-8Sn-2B<sub>4</sub>C at constant load and time. The wear occurs according to the sliding direction and has

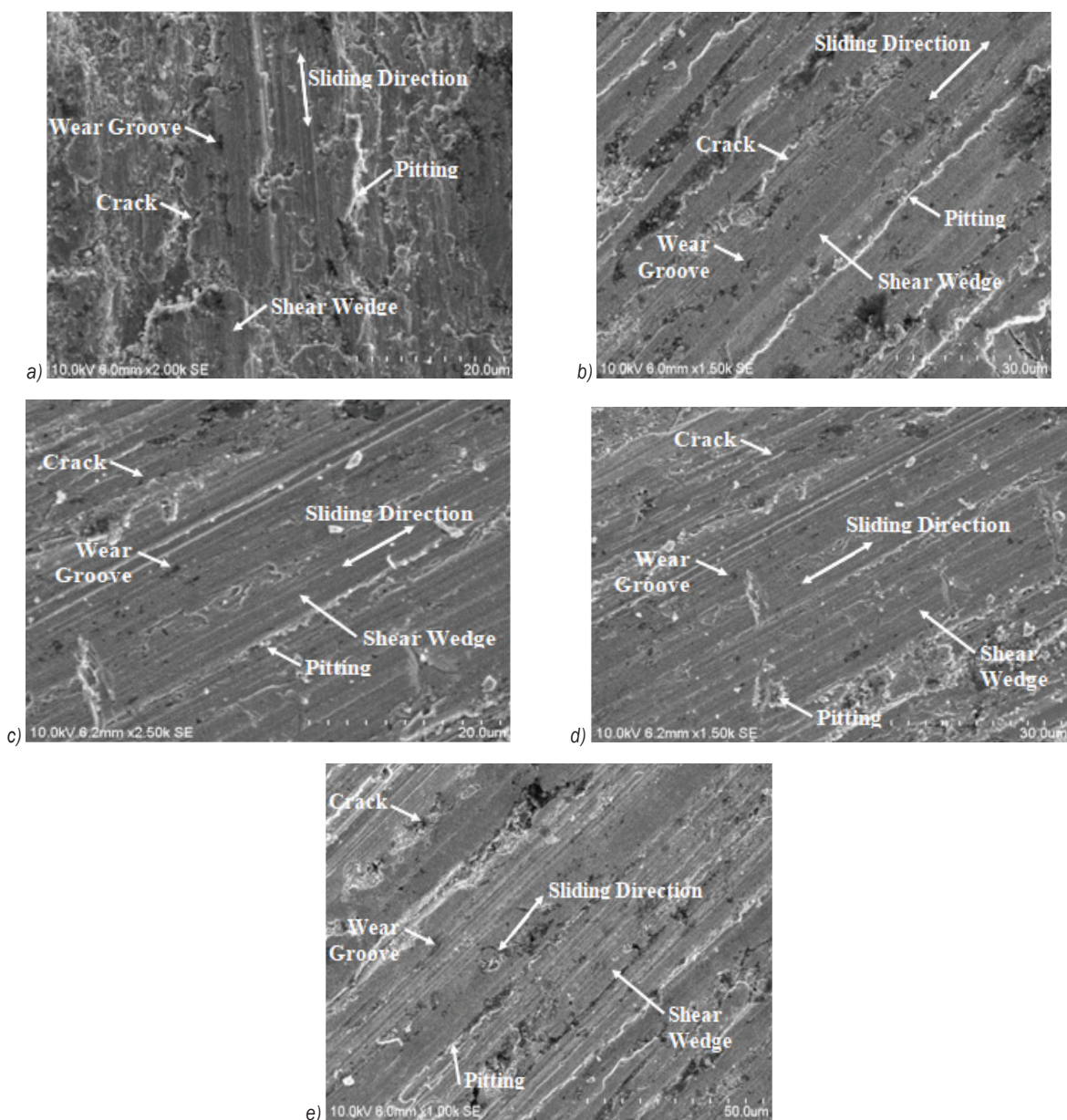


**Fig. 6.** SEM image of worn surface for unreinforced and reinforced composites; a) Cu-Ni, b) Cu-15Ni, c) Cu-8Sn, d) Cu-15Ni-8Sn, and e) Cu-15Ni-8Sn-2B<sub>4</sub>C

rough patches with large amounts of wear grooves compared to unreinforced material and matrix alloy. The morphology clearly infers that cracks are fewer, and pitting is continuous with long shear wedges and so it withstands wear resistance, and the surface is not damaged while increasing the temperature. The composite after reinforcing with B<sub>4</sub>C with less volume fraction at 2 % resulted in a negative effect on the wear of the material and provided hardness and strength to the composite.

## 2.2 Sintered Density Test

Sintering is the principal factor for controlling the density of the composite materials; sintering time and temperature play major roles. When there is a huge variation in load and temperature, the density affects extensively [17]. The increase in experimental density is a consequence of enhancing the mechanical property of the specimen. The higher the density, the better the strength of the composites; this is because the reduced size of pores reduces the defect of the material.

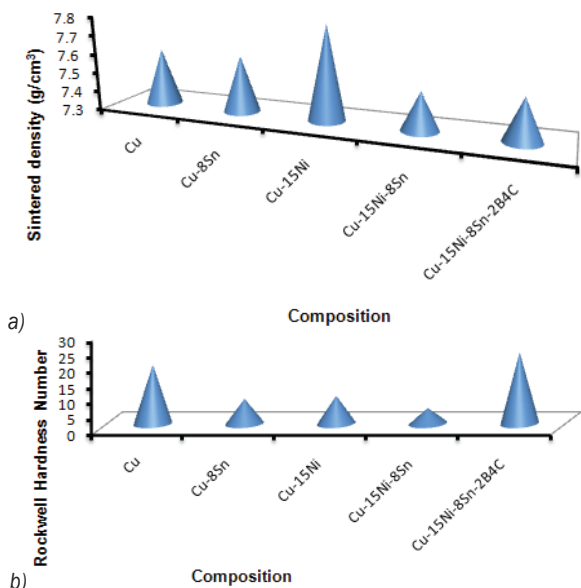


Fig. 7. Effect of composition on: a) sintered density, and b) hardness

In this work, the performance of the composite is good, but the experimental density is less for MMC Cu-15Ni-8Sn-2B<sub>4</sub>C. Here, the contribution of carbide is less (volume fraction 2 %), but the copper matrix contribution is normal, so better in other performances and meagre in experimental density. The bar plot shown in Fig. 7a represent the effect of sintered density at 900 °C. The unreinforced copper and Cu-8Sn show

approximately 7.6 g/cm<sup>3</sup> density. The matrix Cu-15Ni display 7.8 g/cm<sup>3</sup>, while the metal matrix and composite (Cu-15Ni-8Sn and Cu-15Ni-8Sn-2B<sub>4</sub>C) are at 7.5 g/cm<sup>3</sup> and 7.52 g/cm<sup>3</sup> respectively. From this, we can infer that the higher the weight fraction, the better the density of the material.

## 2.3 Hardness Test

The Rockwell hardness is a test method, and ASTM E-18 is the commonly used method to be equipped. The hardness is determined with the help of an indenter present in equipment that measures the size of impression and depth of penetration of the indenter, performed by the composite material at the surface of the material to be loaded for testing. The Rockwell hardness test method is more accurate than other types of testing methods and is used for all metals and composites.

The present study investigated integrated the various compositions and tested for hardness and found the Rockwell hardness number. The material is heated to a sintering temperature of 900 °C, the powders were compacted, and the load is applied to it. Based on the hardness of the material, it withstands the load. From Fig 7b, hardness number is high for the reinforced material. Even though, the addition of boron carbide volume fraction is less, the hardness of the composite is enhanced. The Rockwell hardness number of the unreinforced Cu-15Ni-8Sn and MMC Cu-15Ni-8Sn-2B<sub>4</sub>C is 5 and 23, respectively.

## 3 CONCLUSIONS

The unreinforced copper, Cu-Ni, Cu-Sn and Cu-Ni-Sn-B<sub>4</sub>C composites were prepared using the powder metallurgy technique. The morphology, grain size and uniform dispersion of the composites were characterized using SEM and XRD. The tribological, hardness and density of the specimens were tested, and the following conclusions are drawn.

- The SEM images confirm that the Sn, Ni and B<sub>4</sub>C particles are distributed uniformly throughout the matrix.
- The sintered density of the prepared Cu-15%Ni is 98.25 %, Cu-8%Sn is 98.20 %, Cu-15%Ni-8%Sn is 98.10 % and Cu-15%Ni-8%Sn-2%B<sub>4</sub>C is 95.26 %
- Cu-15Ni-8Sn-2B<sub>4</sub>C exhibits lower wear rate of about 121 × 10<sup>-6</sup> mm<sup>3</sup>/(Nm) compared to the other prepared samples. It is mainly due to the nature and the addition of hard reinforcement B<sub>4</sub>C in the Cu-15Ni-8Sn.

- Worn surface confirmed that there is a reduction of plastic deformation and cracks due to the addition of B4C.

## 5 REFERENCES

- [1] Karthikeyan, G., Jinu, G. R. (2016). Dry sliding wear behavior optimization of stir cast LM6/ZrO<sub>2</sub> composites by response surface methodology analysis. *Transactions of the Canadian Society for Mechanical Engineering*, vol. 40, no. 3, p. 351-369, DOI:10.1139/tcsme-2016-0026.
- [2] Palanikumar, K., Karthikeyan, R. (2007). Assessment of factors influencing surface roughness on the machining of Al/SiC particulate composites. *Materials & Design*, vol. 28, no. 5, p. 1584-1591, DOI:10.1016/j.matdes.2006.02.010.
- [3] Moustafa, S.F., Abdel-Hamid, Z., Abd-Elhay, A. M. (2002). Copper matrix SiC and Al<sub>2</sub>O<sub>3</sub> particulate composites by powder metallurgy technique. *Materials Letters*, vol. 53, no. 4-5, p. 244-249, DOI:10.1016/S0167-577X(01)00485-2.
- [4] Kaczmar, J.W., Pietrzak, K., Włosiński, W. (2000). The production and application of metal matrix composite materials. *Journal of Materials Processing Technology*, vol. 106, no. 1-3, p. 58-67, DOI:10.1016/S0924-0136(00)00639-7.
- [5] Singh, J.B., Cai, W., Bellon, P. (2007). Dry sliding of Cu-15 wt% Ni-8 wt% Sn bronze: Wear behaviour and microstructures. *Wear*, vol. 263, no. 1-6, p. 830-841, DOI:10.1016/j.wear.2007.01.061.
- [6] Narayanasamy, P., Balaji, A.N., Vettivel, S.C. (2018). Microstructural, electrical, thermal and tribological studies of copper-fly ash composites through powder metallurgy. *Bulletin of the Polish Academy of Sciences: Technical Sciences*, vol. 66, no. 6, p. 935-940, DOI:10.24425/bpas.2018.125941.
- [7] Senthil Kumar, P., Manisekar, K., Vettivel, S.C. (2016). Effect of extrusion on the microstructure and tribological behavior of copper-tin composites containing MoS<sub>2</sub>. *Tribology Transactions*, vol. 59, no. 6, p. 1016-1030, DOI:10.1080/10402004.2015.1131347.
- [8] Vettivel, S.C., Selvakumar, N., Ponraj, N.V. (2013). Tribological behaviour of Cu-5W sintered powder composite. *Advanced Materials Research*, vol. 622, p. 1300-1304, DOI:10.4028/www.scientific.net/AMR.622-623.1300.
- [9] Ponraj, N.V., Azhagurajan, A., Vettivel, S.C., Sahaya Shajan, X., Nabhiraj, P.Y., Haiderlenin, A. (2019). Modeling and optimization of the effect of sintering parameters on the hardness of copper/graphene nanosheet composites by response surface methodology. *Metal Science and Heat Treatment*, vol. 60, p. 611-615, DOI:10.1007/s11041-019-00327-z.
- [10] Vijay Ponraj, N., Azhagurajan, A., Vettivel, S.C., Sahaya Shajan, X., Nabhiraj, P.Y. (2018). Study of processing and microstructure of copper composite reinforced with graphene nanosheet by powder metallurgy technique. *Powder Metallurgy and Metal Ceramics*, vol. 56, p. 523-534, DOI:10.1007/s11106-018-9925-9.
- [11] Manohar, G., Dey, A., Pandey, K.M., Maity, S. R. (2018). Fabrication of metal matrix composites by powder metallurgy: A review. *AIP Conference Proceedings*, vol. 1952, no. 1, art. ID 020041, DOI:10.1063/1.5032003.
- [12] Meignanamoorthy, M., Ravichandran, M. (2018). Synthesis of metal matrix composites via powder metallurgy route: a review. *Mechanics and Mechanical Engineering*, vol. 22, no. 1, p. 65-76, DOI:10.2478/mme-2018-0007.
- [13] Lieblich, M., Corrochano, J., Ibáñez, J., Vadillo, V., Walker, J.C., Rainforth, W.M. (2014). Subsurface modifications in powder metallurgy aluminium alloy composites reinforced with intermetallic MoSi<sub>2</sub> particles under dry sliding wear. *Wear*, vol. 309, no. 1-2, p. 126-133, DOI:10.1016/j.wear.2013.11.012.
- [14] Vettivel, S.C., Selvakumar, N., Narayanasamy, R., Leema, N. (2013). Numerical modelling, prediction of Cu-W nano powder composite in dry sliding wear condition using response surface methodology. *Materials & Design*, vol. 50, p. 977-996, DOI:10.1016/j.matdes.2013.03.072.
- [15] Johnyames, S., Annamalai, A.R. (2017). Fabrication of aluminium metal matrix composite and testing of its property. *Mechanics, Materials Science & Engineering*, vol. 9, DOI:10.2412/mmse.62.86.695.
- [16] Kumar, T.R., Swamy, R.P., Chandrashekar, T.K. (2013). An experimental investigation on wear test parameters of metal matrix composites using Taguchi technique. *Indian Journal of Engineering and Materials Sciences*, vol. 20, p. 329-333
- [17] Radhika, N., Sasikumar, J., Jojith, R. (2021). Effect of grain modifier on mechanical and tribological properties of al-si alloy and composite. *Silicon*, vol. 13, p. 841-855, DOI:10.1007/s12633-020-00476-4.
- [18] Cao, F., Chen, C., Wang, Z., Muthuramalingam, T., Anbuhezhiyan, G. (2019). Effects of silicon carbide and tungsten carbide in Aluminium metal matrix composites. *Silicon*, vol. 11, p. 2625-2632, DOI:10.1007/s12633-018-0051-6.
- [19] Kumar, C.R., Malarvannan, R.R.R., JaiGanesh, V. (2020). Role of SiC on mechanical, Tribological and thermal expansion characteristics of B4C/Talc-reinforced Al-6061 hybrid composite. *Silicon*, vol. 12, p. 1491-1500, DOI:10.1007/s12633-019-00243-0.
- [20] Ling, G., Shui, Z., Sun, T., Gao, X., Wang, Y., Sun, Y., Wang, G., Li, Z. (2018). Rheological behavior and microstructure characteristics of SCC incorporating metakaolin and silica fume. *Materials*, vol. 11, no. 12, art. ID 2576, DOI:10.3390/ma11122576.
- [21] Tjong, S.C., Lau, K.C. (2000). Abrasive wear behavior of TiB<sub>2</sub> particle-reinforced copper matrix composites. *Materials Science and Engineering: A*, vol. 282, no. 1-2, p. 183-186, DOI:10.1016/S0921-5093(99)00752-2.
- [22] Öksüz, K.E. (2015). A study on Al<sub>2</sub>O<sub>3</sub>/SiC/B4C reinforced Cu-Sn matrix composite by warm compaction powder metallurgy. *Advanced Materials Research*, vol. 1128, p. 123-126, DOI:10.4028/www.scientific.net/AMR.1128.123.
- [23] Saminatharaja, D., Periyakounder, S., Selvaraj, M., Elangandhi, J. (2021). Performance study of EDM process parameters using TiC/ZrSiO<sub>4</sub> particulate-reinforced copper composite electrode. *Strojniški vestnik - Journal of Mechanical Engineering*, vol. 67, no. 11, p. 547-556, DOI:10.5545/sv-jme.2021.7254.



# Diffusion Equation Generalized for Modeling of Chladni Patterns

Igor Grabec<sup>1,\*</sup> – Nikolaj Sok<sup>2</sup>

<sup>1</sup>University of Ljubljana, Faculty of Mechanical Engineering, Slovenia

<sup>2</sup>University of Ljubljana, Faculty of Computer and Information Science, Slovenia

*Random walk of particles during Chladni pattern formation is macroscopically treated as a diffusion process. The corresponding generalized diffusion equation is formulated based upon the generator of vibration driven random walk by following Einstein's treatment of Brownian motion.*

**Keywords:** Chladni patterns, vibration driven random walk, diffusion process

## Highlights

- Formation of Chladni patterns is macroscopically treated as a diffusion process.
- The diffusion coefficient is expressed by the parameters of driven random walk generator.
- The corresponding generalized diffusion equation is formulated.
- A generalization of Einstein's description of random walk phenomenon is performed.
- A new basis for the macroscopic description of Chladni pattern formation is given.
- A very complex physical phenomenon is rather simply described.

## 1 INTRODUCTION

Experimental research of sound and mechanical vibrations by Ernst Chladni at the end of the eighteenth century was supported by observation of patterns formed by tiny particles on vibrating surfaces [1] and [2]. Although this phenomenon has significantly contributed to the development of acoustics, its analytical model has been formulated only recently [3]. For this purpose trajectories of bouncing particles were optically recorded, numerically analyzed and described by a new model of vibration driven random walk [3] and [4]. In this walk the horizontal displacement  $\Delta \mathbf{r} = (\Delta x, \Delta y)$  during a single bounce is comprised of two statistically independent and normally distributed stochastic components. Since the standard deviation of each component is approximately proportional to the amplitude  $A(\mathbf{r})$  of the surface vibration at the position  $\mathbf{r} = (x, y)$ , the generator of the corresponding random walk displacement  $\Delta \mathbf{r}$  can be modeled by the Eq. (1):

$$\Delta \mathbf{r} = CA(\mathbf{r})\mathbf{G}. \quad (1)$$

Here  $\mathbf{G} = (G(s_x), G(s_y))$  denotes the Gaussian random vector generator comprised of two Gaussian random number generators with seeds  $(s_x, s_y)$ . The constant  $C$  determines the relation between the vibration amplitude  $A$  and the magnitude of the horizontal displacement  $\Delta \mathbf{r}$  that can be statistically characterized by its probability distribution [3] and [4].

Applicability of the random walk model in Eq. (1) is here demonstrated by calculating the pattern

formed on a square plate that is initially uniformly covered by the sand particles and then excited in the middle of its edge. Fig. 1 shows the distribution of the vibration amplitude  $A(\mathbf{r})$  and some typical trajectories of particles during formation of the Chladni pattern, while Fig. 2 shows the evolution of pattern distribution. Its properties are in a good agreement with examples published in the literature about Chladni patterns and demonstrations of vibrations excited by sound [1] to [5].

Development of particle distribution in Fig. 2 reveals that during the formation of a Chladni pattern the particles are on average moving from intensively vibrating regions of the plate to the calm regions at the nodal lines. This happens because the random walk displacement  $\Delta \mathbf{r}$  is on average proportional to the vibration amplitude  $A(\mathbf{r})$  as described by Eq. (1). Consequently, the initially uniform distribution of particles is transformed into a pattern that exhibits the nodal lines. Similarly as in this case also several other Chladni patterns simulated by Eq. (1) reveal remarkably good agreement with corresponding experimental observations [3] to [5].

## 2 MACROSCOPIC DESCRIPTION OF CHLADNI PATTERN FORMATION

Since the random walk of bouncing particles resembles the Brownian motion, it can be macroscopically described by the diffusion equation as formulated by Einstein [6]. Transition from the microscopic description of a single particle movement to the



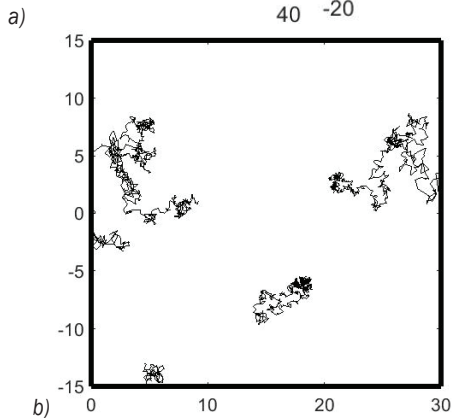
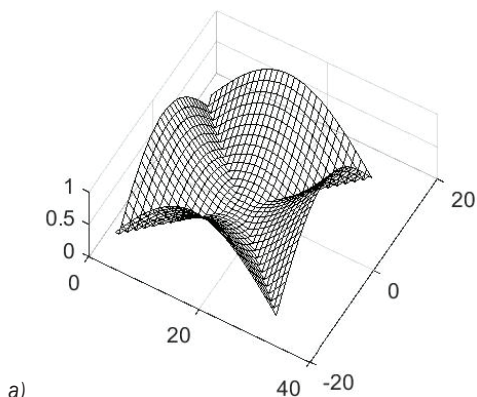


**Fig. 1.** a) Distribution of the vibration amplitude  $A(\mathbf{r})$ , and b) typical trajectories comprised of 1000 random walk jumps of particles during the formation of the Chladni pattern (shown in Fig. 2)

macroscopic description of the particle distribution is based upon the relation between the mean square displacement of particles  $\langle |\Delta \mathbf{r}|^2 \rangle$  in the time interval  $\tau$  and the diffusion coefficient  $D = \langle |\Delta \mathbf{r}|^2 \rangle / 2\tau$ . Our model in Eq. 1 characterizes a single displacement during the vibration period  $\tau$  by the mean square value  $\langle |\Delta \mathbf{r}|^2 \rangle$  proportional to  $A(\mathbf{r})^2$ .

Consequently, the diffusion coefficient:

$$D(\mathbf{r}) = C^2 A(\mathbf{r})^2 \langle |\mathbf{G}|^2 \rangle / 2\tau, \quad (2)$$

depends on the position  $\mathbf{r}$  and the evolution of the particle density  $\rho(\mathbf{r}, t)$  in time  $t$  has to be described by the diffusion equation of the generalized form:

$$\partial \rho(\mathbf{r}, t) / \partial t = \text{div}[D(\mathbf{r}) \text{grad} \rho(\mathbf{r}, t)]. \quad (3)$$

This equation is applicable for the determination of the particle density  $\rho(\mathbf{r}, t)$  during formation of a Chladni pattern when the geometric form of the plate and the amplitude distribution  $A(\mathbf{r})$  are given. For this purpose a numerical treatment is generally needed since the diffusion coefficient  $D(\mathbf{r})$  is not a constant.

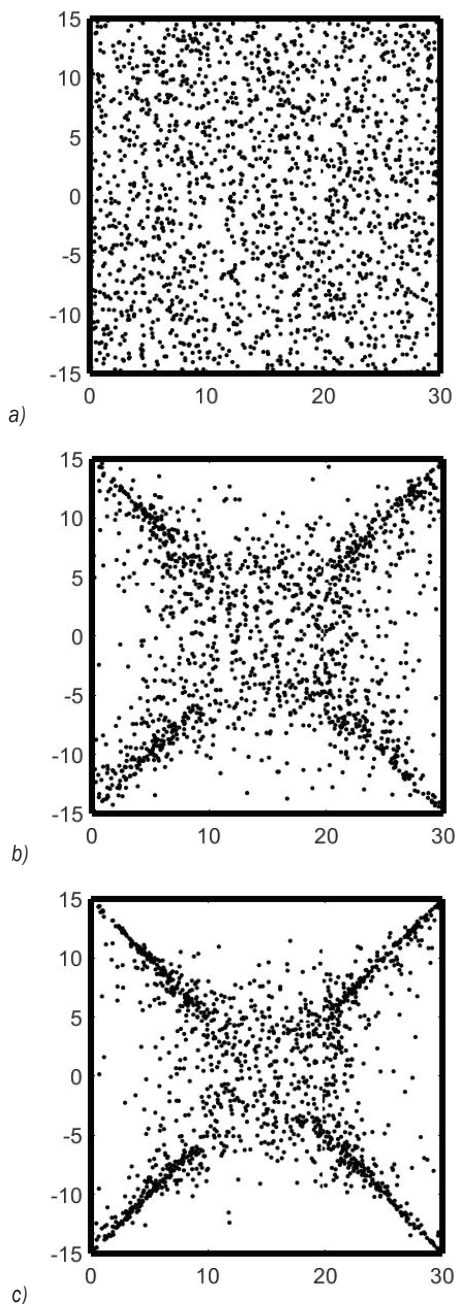


**Fig. 2.** Chladni pattern formed from 2000 particles by a) 0 jumps, b) 500 jumps and c) 1000 jumps

### 3 DISCUSION AND CONCLUSIONS

Some properties of very complex diffusion process during the formation of Chladni patterns can be predicted based upon general properties of the vibration driven random walk. Since the diffusion coefficient  $D(\mathbf{r})$  is proportional to the square of the vibration amplitude  $A(\mathbf{r})^2$  the particles diffuse

from the regions of high amplitude to the regions of low amplitude. Consequently, the initially uniform distribution of particles is changed as indicated by the evolving Chladni pattern. At nodal lines the vibration amplitude  $A(\mathbf{r})$  as well as the diffusion coefficient  $D(\mathbf{r})$  is negligible, and therefore the diffusing particles are there accumulating. From the knowledge of nodal lines some basic characteristics of the particle density  $\rho(\mathbf{r},t)$  in an evolving Chladni pattern can thus be predicted without solving the corresponding generalized diffusion equation.

When the surface vibration is caused by the interference of travelling waves the Chladni pattern can also be utilized to describe the properties of wave interference [7]. However, this is a bit surprising, since such a treatment corresponds to the macroscopic description of wave interference by the generalized diffusion equation. We therefore expect that a more detailed description of the phenomenon is needed for the modeling of random walk driven by the travelling waves. For this purpose a consideration of quantum-mechanical description of particle movement could be helpful.

#### 4 ACKNOWLEDGEMENTS

The authors would like to thank Prof. Tomaž Klinc for his comments and acknowledge the cooperation

with the Laboratory of Synergetics at the Faculty of Mechanical Engineering, University of Ljubljana, Slovenia supported by the Slovenian Research Agency through the research core funding No. P2-0241.

#### 5 REFERENCES

- [1] Smilansky, U., Stöckmann, H.-J. (2007). Nodal patterns in physics and mathematics – From Chladni's seminal work to modern applications – A historic-scientific perspective. *EU Physical Journal - Special Topics*, vol. 145, p. 103-123.
- [2] Chladni, E.F.F. (1787). *Entdeckungen über die Theorie des Klanges*, Leipzig.
- [3] Grabec, I. (2017). Vibration driven random walk in a Chladni experiment. *Physics Letters A*, vol. 381, no. 2, p. 59-64, DOI:10.1016/j.physleta.2016.10.059.
- [4] Grabec, I., Sok, N. (2019). Formation of Chladni patterns by vibration driven random walk of particles. *Nonlinear Phenomena in Complex Systems*, vol. 22, no. 1, p. 75-83.
- [5] Forrister, T. (2018). How do Chladni plates make it possible to visualize sound? from <https://www.comsol.com/blogs/how-do-chladni-plates-make-it-possible-to-visualize-sound>, accessed on 2022-12-23.
- [6] Einstein, A. (1905). Über die von der molekular-kinetischen Theorie der Wärme geforderte Bewegung von in ruhenden Flüssigkeiten suspendierten Teilchen. *Annalen der Physik*, vol. 322, no. 8, p. 549-560, DOI:10.1002/andp.19053220806.
- [7] Grabec I., Sok N. (2021). Demonstration of interference patterns by the random walk of particles. *Strojniški vestnik - Journal of Mechanical Engineering*, vol. 67, no. 1-2, p. 67-69, DOI:10.5545/sv-jme.2020.6950.

# Vsebina

**Strojniški vestnik - Journal of Mechanical Engineering**  
**letnik 69, (2023), številka 5-6**  
**Ljubljana, maj-junij 2023**  
**ISSN 0039-2480**

**Izhaja dvomesečno**

## **Razširjeni povzetki (extended abstracts)**

- Goran Vorotović, Jela Burazer, Aleksandar Bengin, Časlav Mitrović, Miloš Januzović, Nebojša Petrović, Đorđe Novković: Študija primera metodološkega pristopa k verifikaciji zmogljivosti propelerjev brezpilotnih letalnikov SI 21
- Ali Celik, Bayram Sahin, Eyüphan Manay, Abit Balin: Uporaba hibridne mehke metode AHP&TOPSIS pri adaptaciji stavbe izobraževalne ustanove s certifikatom LEED v hladni regiji v skoraj ničenergijsko stavbo SI 22
- Ava A.K. Mohammed, Gailan Ismail Hassan, Younis Khalid Khdir: Dinamične lastnosti simetrično laminiranih nanokompozitov, ki vključujejo enako število steklenih in ogljikovih vlaken SI 23
- Linlin Li, Sanmin Wang: Eksperimentalna študija in numerična analiza izgub moči zaradi ventiliranja pri letalskih stožčastih zobniških prenosnikih s spiralnimi zobmi, mazanih z vbrizgavanjem olja SI 24
- Sumit Kumar, Pardeep Gupta: Določanje ključnih akterjev za poslovno odličnost v organizacijah po procesu učinkovitega razlagalnega rangiranja (eIRP) SI 25
- Teng Wang, Youfu Tang, Tao Wang, Na Lei: Diagnosticiranje napak kotalnih ležajev na podlagi izboljšanih modelov MSCNN in NRU SI 26
- Haiter Lenin Allasi, Vettivel SingaravelChidambaranathan, Mary Vasanthi Soosaimariyan: Obrabne lastnosti hibridnega kompozita Cu-Ni-Sn, ojačenega z B<sub>4</sub>C in pripravljenega po postopkih metalurgije prahov SI 27
- Igor Grabec, Nikolaj Sok: Difuzijska enačba posplošena za modeliranje Chladnijevih vzorcev SI 28





# Študija primera metodološkega pristopa k verifikaciji zmogljivosti propelerjev brezpilotnih letalnikov

Goran Vorotović\* – Jela Burazer – Aleksandar Bengin – Časlav Mitrović –  
Miloš Januzović – Nebojša Petrović – Đorđe Novković

Univerza v Beogradu, Fakulteta za strojništvo, Srbija

V članku so predstavljene možnosti za analizo statične zmogljivosti in vibracij propelerjev letal majhne moči. Letala majhne moči kot »potrošni« material so danes realnost, glavni cilj raziskovalcev pa je zagotavljanje njihove varne uporabe.

Pričujoči članek zato predstavlja predlog metodologije za preizkušanje krakov propelerjev letal majhne moči v atmosferi. Metoda bi bila primerna tudi za letala večje moči, kakor tudi za letalnike na drugih nebesnih telesih, ki še niso bili preizkušeni. Predstavljeno je preizkuševališče za kvantifikacijo potiska, navora in vibracij propelerjev majhnih brezpilotnih letalnikov. Preizkuševališče omogoča realistične meritve kompleksnega vedenja propelerjev med delovanjem ter zagotavlja dragocene podatke za izboljševanje konstrukcije in delovanja propelerjev. Analizirane so bile lastnosti statične zmogljivosti in vibracij propelerjev za letala majhne moči za vpogled v njihovo vedenje in izboljšanje varnostnih ukrepov.

Vedenje propelerjev kljub intenzivnim raziskavam ostaja kompleksen izziv v letalstvu. Preizkuševališče je izvedeno kot aluminijasta konstrukcija, ki sprejme propelerje premera do 550 mm za varno preizkušanje. Podporna konstrukcija preizkuševališča je izdelana iz aluminijastih L-profilov dimenzij 30 mm × 50 mm × 5 mm. Preliminarni izračuni statične in dinamične nosilnosti konstrukcije so dali zadovoljive rezultate v skladu z dobrimi tehničnimi praksami, z varnostnim faktorjem 1,6. Za zajem podatkov v sklopu vzporednih statičnih in dinamičnih meritev je bila uporabljena večkanalna enota HBM QuantumX MX840A. Osemkanalna enota zabeleži 20.000 meritev na sekundo na kanal s 24-bitno ločljivostjo. Potisk je bil izmerjen s konzolnim merilnim pretvornikom za silo, število vrtljajev pa je bilo izmerjeno z optičnim digitalnim dajalnikom. Za meritve vibracij sta bila uporabljena dva pospeškometra: prvi je bil postavljen na premičnem delu konstrukcije preizkuševališča, ki je pod vplivom potiska propelerja, drugi pa na fiksnem delu preizkuševališča. Za meritve navora je bil konstruiran in izdelan poseben konzolni nosilec.

Zajeti eksperimentalni podatki realistično opisujejo kompleksno vedenje propelerjev med delovanjem.

Rezultati eksperimentov so osnova za določanje parametrov, ki povzročajo nepravilno delovanje propelerjev med letom, kakor tudi za postopke karakterizacije kakovosti, s katerimi se določa doba uporabnosti propelerjev v prvi fazi razvoja.

Raziskava potrjuje potrebo po verifikaciji analitičnih in eksperimentalnih rezultatov s preizkuševališča v realnih obratovalnih pogojih s kombinacijo strojne in programske opreme.

Avtorji so zato mnenja, da je potrebna potrditev rezultatov na realnih letalnikih v vseh atmosferskih pogojih, ne glede na to, na katerem planetu se izvajajo eksperimenti.

**Ključne besede: propeler, dinamične lastnosti vleka, oscilacije, zajem podatkov, dinamika**

# Uporaba hibridne mehke metode AHP&TOPSIS pri adaptaciji stavbe izobraževalne ustanove s certifikatom LEED v hladni regiji v skoraj ničenergijsko stavbo

Ali Celik<sup>1,\*</sup> – Bayram Sahin<sup>1</sup> – Eyüphan Manay<sup>1</sup> – Abit Balin<sup>2</sup>

<sup>1</sup> Tehniška univerza v Erzurumu, Oddelek za strojništvo, Turčija

<sup>2</sup> Univerza v Istanbulu, Šola za transport in logistiko, Turčija

Cilj pričujoče študije je bil izboljšanje energijske učinkovitosti za znižanje stroškov po pristopu skoraj ničenergijske stavbe na modelu stavbe Fakultete za strojništvo in arhitekturo s certifikatom LEED (*Leadership in Energy and Environmental Design*) Tehniške univerze v Erzurumu, ki se nahaja v hladni podnebni regiji Turčije. Namen je bil tudi ustvariti realističen model za podporo pri odločanju o gradnji energijsko učinkovitih stavb, ki ne potrebujejo tujih certifikatov. Med cilji študije so bili tudi zmanjšanje rabe energije, pridobivanje energije in zmanjšanje izpustov CO<sub>2</sub>. Univerze imajo velik delež v skupni rabi energije javnega sektorja, zato se z zmanjšanjem rabe energije razbremeni proračun.

Adaptacija referenčne stavbe v skoraj ničenergijsko stavbo vključuje naslednje korake:

- Izračun rabe primarne energije in izpustov referenčne stavbe s certifikatom LEED-SILVER.
- Opredelitev rezultatov posamičnih in mešanih scenarijev za povečanje energijske učinkovitosti z modeliranjem stavbe.
- Opredelitev posamičnih in mešanih scenarijev za povečanje energijske učinkovitosti ter izvedba energijske in stroškovne analize.
- Izračun emisij ogljika in dobe odplačila za scenarije izboljšanja energijske učinkovitosti.
- Vrednotenje rezultatov scenarijev izboljševanja energijske učinkovitosti z večkriterijskimi metodami odločanja.

Študija podaja pristop h gradnji energijsko učinkovitih stavb za izobraževalne institucije v hladnih podnebnih regijah po načelih skoraj ničenergijskih stavb ter brez tujih certifikatov za zaščito energijskih virov in gospodarskih interesov države.

V letih 2017 do 2019 so bile opravljene terenske meritve porabe zemeljskega plina in električne energije v referenčni stavbi. Analizirani so bili dejavniki, ki vplivajo na doseganje skoraj ničelne rabe energije. Cilj je bil doseči stroškovno optimalne ravni energijske učinkovitosti s scenariji za zmanjšanje rabe energije v stavbi Fakultete za strojništvo in arhitekturo Tehniške univerze v Erzurumu s certifikatom LEED. Rezultati posamičnih in mešanih scenarijev za povečanje energijske učinkovitosti so bili določeni z energijskim modeliranjem stavbe. Najprimernejši posamični in mešani scenarij sta bila določena s sistematičnim hibridnim modelom, ki povezuje mehki analitični hierarhični proces (AHP) in tehniko razvrstitve po podobnosti z idealno rešitvijo (TOPSIS) kot večkriterijski metodi za odločanje.

Z uporabo posamičnih in mešanih scenarijev energijske učinkovitosti so bili doseženi 85,6-odstotni letni prihranek primarne energije, 83,6-odstotno znižanje skupnih stroškov in 86,4-odstotno zmanjšanje izpustov CO<sub>2</sub> v primerjavi z referenčno stavbo. Doba odplačila scenarijev je med 3,8 in 14,53 leta. Rezultati kažejo, da so ekonomski kriteriji odločilni pri določanju najprimernejšega scenarija za hladne podnebne regije.

V študiji so določeni parametri, ki bi usmerjali zakonsko regulativo z uporabo metod večkriterijskega odločanja (MCDM) pri identifikaciji stroškovnega optimuma za skoraj ničenergijsko raven rabe. Študija je pomembna za gradnjo energetske in stroškovno učinkovitih stavb v univerzitetnih kampusih. Rezultati študije so uporabni kot realističen model za podporo pri odločanju o izbiri scenarijev za izboljševanje energetske učinkovitosti stavb.

**Ključne besede:** zelena stavba, skoraj ničenergijska stavba, analiza rabe energije in stroškovnega optimuma, mehki analitični hierarhični proces (FAHP), TOPSIS

# Dinamične lastnosti simetrično laminiranih nanokompozitov, ki vključujejo enako število steklenih in ogljikovih vlaken

Ava A.K. Mohammed – Gailan Ismail Hassan – Younis Khalid Khdir  
Tehniški kolidž v Erbilu, Politehnika v Erbilu, Erbil, Irak

Cilj raziskave je povečanje modula elastičnosti pri upogibu, lastne frekvence in faktorja dušenja s posebno razporeditvijo steklenih in ogljikovih vlaken ter z dodatkom 2 % nanodelcev  $Al_2O_3$  v epoksidni osnovi hibridnega kompozita G/C.

Povečanje modula elastičnosti pri upogibu spremlja povečanje lastne frekvence in zmanjšanje faktorja dušenja. Ena od možnosti za povečanje omenjenega modula je dodajanje enakega števila steklenih in ogljikovih vlaken v osnovo kompozita in razporeditev vlaken za večji faktor dušenja. Drugi način za povečanje modula elastičnosti pri upogibu in faktorja dušenja je z dodatkom pribl. 2 % nanodelcev  $Al_2O_3$  v osnovo polimernega kompozita, ojačenega z vlakni.

Za teoretično oceno modula elastičnosti pri upogibu in osnovne lastne frekvence laminatov je bila uporabljena klasična teorija laminiranih plošč. Laminati so bili izdelani po metodi infuzije smole s pomočjo vakuumu, njihove dinamične lastnosti (lastna frekvenca in faktor dušenja) pa so bile določene eksperimentalno s prostim vibracijskim testom. Končno je bilo izvedeno še modeliranje laminatov v paketu Ansys Workbench za določitev prvih šestih lastnih frekvenc in oblike vibracij ter njihova primerjava z rezultati analitičnih in eksperimentalnih metod.

Lastne frekvence, ki so bile določene analitično, eksperimentalno in numerično, se dobro ujemajo. Križni vzorec 2 in kvazi vzorec 2 sta imela največjo lastno frekvenco med križno in kvazi laminiranimi skupinami: 23,5 Hz in 20,25 Hz. Modul elastičnosti pri upogibu pri razporeditvi GGCCCCGG z dvema steklenima slojema na zunanji površini je namreč višji kot pri razporeditvi GCCGGCCG. Modul elastičnosti pri upogibu in faktor dušenja sta se povečala z dodatkom 2 % nanodelcev  $Al_2O_3$ , medtem ko se je lastna frekvenca zmanjšala. Večji faktor dušenja je bil dosežen pri križnem vzorcu 1 z nanodelci  $Al_2O_3$  in pri kvazi vzorcu 2 z nanodelci  $Al_2O_3$ : 0,707 % in 0,693 %.

Rezultati raziskave se nanašajo na osem-slojni kompozit s 50 % steklenih in 50 % ogljikovih vlaken v osnovi iz epoksi smole ter z dodatkom 2 % nanodelcev  $Al_2O_3$  in brez njega. Predlogi za nadaljnje raziskave:

1. Povečanje števila kompozitnih slojev na deset ter sprememba odstotnih deležev ogljikovih in steklenih vlaken na 40 % / 60 %.
2. Sprememba vrstnega reda zlaganja simetričnih križnih in kvazi laminatov, najprej s slojem steklenih vlaken in nato s slojem ogljikovih vlaken na zunanji površini.
3. Sprememba deleža dodanih nanodelcev v osnovi na 3 %.

Kot se je izkazalo pri kvazi vzorcu 2/kvazi vzorcu 2 z dodatkom nanodelcev  $Al_2O_3$  v primerjavi s kvazi vzorcem 1/kvazi vzorcem z dodatkom nanodelcev  $Al_2O_3$ , se z dodajanjem dveh steklenih slojev na zunanjo površino skupine kvazi laminatov hkrati povečajo upogibni modul elastičnosti, lastna frekvenca in faktor dušenja.

**Ključne besede:** križni laminat, kvazi laminat, modul elastičnosti pri upogibu, lastna frekvenca, faktor dušenja, nanodelci  $Al_2O_3$

# Eksperimentalna študija in numerična analiza izgub moči zaradi ventiliranja pri letalskih stožčastih zobniških prenosnikih s spiralnimi zobmi, mazanih z vbrizgavanjem olja

Linlin Li – Sanmin Wang

Severozahodna politehnika, Šola za strojništvo, Kitajska

Pri izgubah ventiliranja gre za pojav, ko vrtenje zobnikov povzroči pospeševanje fluida, s katerim so obdani zobniki. Izguba moči zaradi ventiliranja je moč, ki je potrebna za vrtenje zobnikov v fluidu in se prišteva k izgubam moči zaradi ubiranja. Moč, ki se izgublja v sistemu prenosnika, se kaže v povečanju turbulentnosti in segrevanju fluida. Zaradi izboljševanja izkoristka prenosa in varčevanja z gorivom obstaja stalna potreba po omejevanju izgub in povečanju obremenljivosti prenosnikov, zlasti v aeronavtiki.

Z vse večjimi vrtilnimi hitrostmi stožčastih zobnikov s spiralnim ozobjem v letalstvu na izkoristek prenosnikov vedno bolj vplivajo od obremenitve neodvisne izgube ventiliranja, ki jih povzročajo hidrodinamični pojavi.

Glavne metode preučevanja izgub ventiliranja pri zobnikih so teoretična analiza, numerične simulacije in eksperimentalna verifikacija. Teoretična analiza omogoča preučevanje osnovnih zakonitosti problema in daje jasne smernice. Eksperimentalne raziskave so bila glavna znanstvena metoda pred razvojem tehnologije simulacij in omogočajo neposredno preverjanje teorije. Numerične simulacije omogoča simuliranje in analizo tokov fluida v prenosnikih po metodi CFD. Ta metoda omogoča vizualno analizo pretočnih polj in nekatere kompleksnejše eksperimentalne študije, ki v običajnih pogojih niso izvedljive.

Izdelano je bilo preizkuševališče za merjenje izgub ventiliranja pri stožčastih zobnikih s spiralnim ozobjem, mazanih z vbrizgavanjem olja. Predstavljen je predlog metode za merjenje izgub ventiliranja pri zobniških dvojicah. Z ortogonalnimi eksperimenti so bili preučeni interaktivni vplivi različnih parametrov vbrizgavanja olja na izgube ventiliranja. Nato je bil na podlagi metode premika površine zoba postavljen model mazanja omenjenih zobniških dvojic z vbrizgavanjem olja. Trenutna porazdelitev dvofaznega fluida ter spremembe tlačnega in hitrostnega polja v prenosniku so bile simulirane in analizirane s pomočjo programske opreme Fluent in tehnologije dinamičnega mreženja. Opredeljene so bile mehanske in energijske značilnosti izgub ventiliranja pri stožčastih zobnikih s spiralnim ozobjem in mazanjem z vbrizgavanjem olja.

Na podlagi izmerjenih vrednosti momenta v različnih delovnih pogojih sta bila izračunana moment ventilacijskih izgub in moment pogonske gredi preizkuševališča. Rezultati so pokazali, da ima največji vpliv na ventilacijske izgube zobniške dvojice vrtilna hitrost gredi. Drugi dejavnik po vrsti je tlak vbrizgavanja, s prilagajanjem katerega se spreminja količina vbrizga, ki vpliva na volumski delež mazalnega olja v okolici zobnikov. Najmanjši vpliv ima temperatura vbrizgavanja. Opravljena je bila brezdimenzijska analiza momenta ventiliranja in izračunana je bila variabilnost brezdimenzijskega količnika momenta ventiliranja z rotacijskim Reynoldsovim številom. Primerjava med brezdimenzijskim količnikom momenta ventiliranja na podlagi eksperimentalnih podatkov in simulacij je pokazala, da se rezultati simulacij dobro ujemajo z izmerjenimi podatki.

Pričujoča raziskava tako ne pripomore le k razvoju teorije in metod za analizo izgub moči ventiliranja pri letalskih visokohitrostnih stožčastih zobnikih s spiralnim ozobjem in mazanjem z vbrizgavanjem olja, temveč podaja tudi teoretično osnovo za snovanje pristopov k zmanjšanju izgub ventiliranja. To pa ima veliko uporabno vrednost pri razvoju tehnologije visokoučinkovitih zobniških prenosnikov.

**Ključne besede:** stožčasti zobnik s spiralnimi zobmi, mazanje z oljnim curkom, izgube zaradi ventiliranja, preizkus ventiliranja, eksperimentalna potrditev, računalniška dinamika fluidov, mehanizem oblikovanja, lastnosti ventiliranja



# Določanje ključnih akterjev za poslovno odličnost v organizacijah po procesu učinkovitega razlagalnega rangiranja (eIRP)

Sumit Kumar\* – Pardeep Gupta

Inštitut za inženiring in tehnologijo Sant Longowal (SLIET), Indija

V pričujočem članku je predstavljen kvalitativni pristop za določanje ključnih akterjev v organizacijah v različnih življenjskih situacijah: proces učinkovitega razlagalnega rangiranja (eIRP). Analiza rangiranja temelji na razlagalnem modelu organizacije, postavljenem s tehniko modeliranja situacija – akter – proces – učenje – dejanja – uspešnost (SAP–LAP). Predstavljen je sistematični pristop k razreševanju konfliktov, ki se običajno pojavljajo pri dinamičnem večkriterijskem odločanju v organizacijah. Cilj je izvedba kvalitativne raziskave v organizaciji za rangiranje njenih ključnih akterjev v različnih situacijah kot podpora pri odločanju. Za potrebe analize in predstavitve pristopa je bila izbrana vzorčna organizacija za rangiranje njenih ključnih akterjev, kot so najvišje vodstvo in medfunkcijski timi (CFT), ter zunanjega akterja – indijske vlade. Vloga teh ključnih akterjev v procesih kot so strateško planiranje (SP), zagotavljanje kakovosti (QA), upravljanje stroškov (CM), upravljanje človeških virov (HRM) in upravljanje energije (EM) je bila rangirana za določene situacije v okolju organizacije, kot so visoka inflacija, visoki stroški energije, stari stroji in oprema, široka paleta izdelkov in visoki stroški delovne sile.

Kvalitativni podatki so bili zbrani v semistrukturiranih telefonskih intervjujih s srednjim in višjim nivojem zaposlenih v organizaciji po modelu zbiranja podatkov SAP-LAP. Zaradi posplošitve rezultatov so bili pridobljeni tudi odzivi od ustreznih strokovnjakov iz akademske sfere. Ti odgovori so osnova za primerjalno kvalitativno razlagalno logiko, ki je potrebna za učinkovit proces razlagalnega rangiranja.

Analiza je razkrila, da je pri večini obravnavanih procesov najvišje rangirani akter najvišje vodstvo, sledijo pa mu medfunkcijski timi in indijska vlada. Podani so bili naslednji predlogi za poslovno odličnost organizacije:

- Predlog 1: Za zmanjšanje vpliva visoke inflacije mora vrhovno vodstvo oblikovati lastne politike v skladu s fiskalnimi politikami indijske vlade.
- Predlog 2: Za zmanjšanje visokih stroškov energije mora vrhovno vodstvo oblikovati svojo energetska politiko s poudarkom na nabavi energije iz obnovljivih virov, odpravi odvisnosti od dizelskih generatorjev itd.
- Predlog 3a: Za obvladovanje stroškov vzdrževanja starih strojev in opreme mora najvišje vodstvo v svojo temeljno politiko vključiti tudi politiko vzdrževanja.
- Predlog 3b: Nabava novih strojev za zamenjavo starih, energetska potratnih strojev s strani večfunkcijskih timov, ki bodo odgovorni za doseganje ključnih kazalnikov uspešnosti in vodenja.
- Predlog 4: Najvišje vodstvo mora za izdelavo široke palete izdelkov v svojih temeljnih politikah sprejeti politiko fleksibilnosti proizvodnje in jo izvajati prek večfunkcijskih timov. Ti timi bodo odgovorni za ključne kazalnike uspešnosti in vodenja na področju kakovosti, stroškov in dobave.
- Predlog 5: Za obvladovanje vprašanj, povezanih s človeškimi viri, mora najvišje vodstvo oblikovati strateške cilje in jih izvajati skozi proces upravljanja človeških virov. Rezultati pričujoče študije so omejeni glede na to, da študija podaja teoretični okvir na podlagi mnenj in ocen strokovnjakov. Razlagalne povezave so nestabilne zaradi subjektivne narave ocen. Novost dela je v rangiranju tistih akterjev znotraj vzorčne organizacije, ki so odgovorni za poslovno odličnost. Z uporabo eIRP je bilo mogoče ustvariti razlagalno podatkovno bazo, ki jo lahko organizacija v prihodnosti uporabi pri sprejemanju odločitev. Organizacija je bila obveščena o rezultatih študije primera, ki jih bo lahko uporabila glede na svoje potrebe.

**Ključne besede: prilagodljivost, odločanje, SAP-LAP, e-IRP, poslovna odličnost, najvišje vodstvo, indijska vlada, medfunkcijski timi (CFT)**

# Diagnosticiranje napak kotalnih ležajev na podlagi izboljšanih modelov MSCNN in NRU

Teng Wang\* – Youfu Tang – Tao Wang – Na Lei

Severovzhodna univerza za naftno industrijo, Inštitut za tehniške vede in strojništvo, Kitajska

Kotalni ležaji so poglavitni sestavni del rotacijskih strojev in pogosto obratujejo v težavnih razmerah velikih obremenitev in visokih hitrosti, zaradi česar so nagnjeni k odpovedim. Raziskave so pokazale, da so prav odpovedi ležajev najpogostejši vzrok za okvare. Raziskave metod za diagnosticiranje napak na kotalnih ležajih imajo tako teoretično in praktično vrednost za zagotavljanje neprekinjenega in varnega obratovanja opreme ter zmanjševanje gospodarskih izgub zaradi prekinitev obratovanja.

Množični podatki o vibracijah kotalnih ležajev pod vplivom spremenljivih obratovalnih pogojev in vzbujanj v obliki udarcev imajo značilno kompleksne nelinearne in nestacionarne lastnosti, zaradi česar je težko izkoristiti obstoječe tehnike obdelave signalov za adaptivno izločanje značilk napak. Normalni vzorci so po drugi strani veliko večji od vzorcev napak v množičnih podatkih o vibracijah kotalnih ležajev, zbranih na terenu, zaradi česar diagnostična učinkovitost in stopnja prepoznavne v obstoječih diagnostičnih metodah na podlagi umetne inteligence težko dosežeta zahtevano raven za industrijsko rabo. Raziskovalci doma in v tujini trenutno zlivajo tehnike obdelave signalov z diagnostičnimi metodami na podlagi umetne inteligence. Te metode so učinkovite za izboljševanje učinkovitosti diagnostike pri velikih vzorcih in raznovrstnih podatkih o vibracijah zaradi napak. Na podatke o vibracijah vplivajo različni obratovalni pogoji, strukturni parametri, vrste napak, stopnje napak in njihovo število. Omenjene metode zlivanja so lahko uporabne v določenih pogojih, izbira pa je odvisna od empiričnega znanja strokovnjakov, ki ima vedno svoje omejitve.

Za razrešitev teh izzivov je predstavljen predlog nove metode za diagnosticiranje napak z zlivanjem metod SENet-MSCNN (Squeeze and Excitation-Multiscale Convolutional Neural Networks) in GRU (Gate Recurrent Unit), ki naslavlja problem nizke stopnje diagnosticiranja zaradi normalnih vzorcev, ki so bistveno večji od vzorcev napak v množičnih podatkih o vibracijah. Metoda uporablja kot vhod signal vibracij v časovni domeni in ga zliva s prostorskimi značilkami, pridobljenimi po metodi SE-MSCNN. Časovne značilke so izločene po metodi GRU in uporabljene v popolnoma povezanem sloju za identifikacijo s ciljem realizacije pametne diagnostike z adaptivnim pridobivanjem značilk kotalnih ležajev. Metoda je bila nato preizkušena in analizirana na simuliranem signalu in na eksperimentalnih podatkih. Rezultati kažejo, da lahko model pri podatkovnih setih za ležaje in prenosnike doseže 98,98- in 76,44-odstotno migracijsko diagnostično točnost. Poleg tega izkazuje dobro imunost pred šumom, prilagodljivost in robustnost, s tem pa predstavlja učinkovito sredstvo za pametno diagnostiko na podlagi množičnih podatkov o vibracijah kotalnih ležajev.

**Ključne besede:** SENet, MSCNN, GRU, kotalni ležaj, diagnosticiranje napak

# Obrabne lastnosti hibridnega kompozita Cu-Ni-Sn, ojačenega z B<sub>4</sub>C in pripravljenega po postopkih metalurgije prahov

Haiter Lenin Allasi<sup>1,\*</sup> – Vettivel Singaravel Chidambaranathan<sup>2</sup> – Mary Vasanthi Soosaimariyan<sup>3</sup>

<sup>1</sup> Univerza WOLLO, Inštitut za tehnologijo v Kombolči, Šola za strojništvo in kemijsko tehnologijo, Etiopija

<sup>2</sup> Kolidž za inženiring in tehnologijo v Čandigarju, Oddelek za strojništvo, Indija

<sup>3</sup> Katoliški kolidž za inženiring Sv. Ksavierja, Oddelek za elektroniko in komunikacije, Indija

Kompozitni materiali s kovinsko osnovo so razmeroma nova skupina lahkih gradiv, ki se s svojo visoko trdnostjo vse bolj uveljavljajo v letalski, vesoljski, obrambni, avtomobilski industriji in transportu. Kompoziti s Cu osnovo izkoriščajo visoko električno in toplotno prevodnost bakra ter mehansko obstojnost trde ojačitve proti obrabi in eroziji. V pričujoči študiji so bili uporabljeni baker za osnovo ter Ni in Sn za sekundarno osnovo, zlitini pa je bil dodan še B<sub>4</sub>C v deležu 2 % za ojačitev (Cu-15%Ni-8%Sn). Ta zlitina ima odlične ležajne lastnosti in je zato prisotna v najrazličnejših aplikacijah. Elektrolitski baker je bil prevlečen z nikljem in kositrom v volumskem deležu 15 % in 8 %. Nikelj je združljiv ter zagotavlja boljšo ojačitev in adhezijo na karbidne materiale. Cilj študije je primerjava obrabne obstojnosti in mehanskih lastnosti gradiv Cu-15%Ni, Cu-8%Sn, Cu-15%Ni-8%Sn in Cu-15%Ni-8%Sn-2%B<sub>4</sub>C.

Predstavljena je analiza vpliva ojačitve Cu-Ni-Sn z B<sub>4</sub>C. Za ojačitev z B<sub>4</sub>C in oblikovanje hibridnih kompozitov s Cu osnovo so bili uporabljeni postopki metalurgije prahov. Hibridni kompoziti so bili pridobljeni z mletjem, mešanjem in kompaktiranjem prahov. Rezultat so drobna zrna, ki se ne skepljajo. Uporabljen je bil prah elektrolitskega bakra z gostoto 8,92 g/cm<sup>3</sup>, niklja z gostoto 8,9 g/cm<sup>3</sup> in kositra z gostoto 7,3 g/cm<sup>3</sup>, za ojačitev pa je bil uporabljen prah borovega karbida z gostoto 2,52 g/cm<sup>3</sup> (vse gostote pri 20 °C). Prahovi so bili mehansko obdelani in pripravljeni so bili vzorci kompozitnega materiala s kovinsko osnovo. Velikosti zrn in lastnosti delcev so bile analizirane po metodi vrstične elektronske mikroskopije in rentgenske difrakcije. Preučene so bile mikrostruktura, gostota, trdota in stopnja obrabe kompozitov. Obrabne lastnosti in količnik trenja so bili določeni s tehniko valjčka na disku. Kristalna struktura in fazne spremembe v materialih (vrhovi intenzitete in difrakcijski kot 2θ) so bile analizirane z rentgenskim difraktometrom. Trdota, trdnost in obraba kompozitov so bile določene s tribometrom tipa valjček na disku pri spremenljivi drsni razdalji, drsni hitrosti, obremenitvi in hitrosti.

Posnetki SEM potrjujejo enakomerno porazdelitev delcev Sn, Ni in B<sub>4</sub>C v osnovi. Sintrana gostota pripravljenih vzorcev: Cu-15%Ni – 98,25 %, Cu-8%Sn – 98,20 %, Cu-15%Ni-8%Sn – 98,10 % in Cu-15%Ni-8%Sn-2%B<sub>4</sub>C – 95,26 %. Cu-15Ni-8Sn-2B<sub>4</sub>C ima v primerjavi z ostalimi vzorci manjšo stopnjo obrabe, ta pa znaša približno 121×10<sup>-6</sup> mm<sup>3</sup>/(Nm). To je mogoče pripisati predvsem trdim dodatkom B<sub>4</sub>C v osnovi Cu-15Ni-8Sn. Pregled obrabne površine je potrdil zmanjšanje plastične deformacije in razpok zaradi dodatka B<sub>4</sub>C. Prispevek študije je ugotovitev, da se z dodatkom B<sub>4</sub>C v Cu-Ni-Sn znatno spremenita stopnja obrabe in količnik trenja.

**Ključne besede:** metalurgija prahov, baker, obraba, karakterizacija, gostota, hibridni kompoziti, vrstični elektronski mikroskop, rentgenska difrakcija

# Guide for Authors

All manuscripts must be in English. Pages should be numbered sequentially. The manuscript should be composed in accordance with the Article Template given above. The suggested length of contributions is 10 to 20 pages. Longer contributions will only be accepted if authors provide justification in a cover letter. For full instructions see the Information for Authors section on the journal's website: <http://en.sv-jme.eu>.

## SUBMISSION:

Submission to SV-JME is made with the implicit understanding that neither the manuscript nor the essence of its content has been published previously either in whole or in part and that it is not being considered for publication elsewhere. All the listed authors should have agreed on the content and the corresponding (submitting) author is responsible for having ensured that this agreement has been reached. The acceptance of an article is based entirely on its scientific merit, as judged by peer review. Scientific articles comprising simulations only will not be accepted for publication; simulations must be accompanied by experimental results carried out to confirm or deny the accuracy of the simulation. Every manuscript submitted to the SV-JME undergoes a peer-review process.

The authors are kindly invited to submit the paper through our web site: <http://ojs.sv-jme.eu>. The Author is able to track the submission through the editorial process - as well as participate in the copyediting and proofreading of submissions accepted for publication - by logging in, and using the username and password provided.

## SUBMISSION CONTENT:

The typical submission material consists of:

- A **manuscript** (A PDF file, with title, all authors with affiliations, abstract, keywords, highlights, inserted figures and tables and references),
- Supplementary files:
  - a **manuscript** in a WORD file format
  - a **cover letter** (please see instructions for composing the cover letter)
  - a ZIP file containing **figures** in high resolution in one of the graphical formats (please see instructions for preparing the figure files)
  - possible **appendices** (optional), cover materials, video materials, etc.

Incomplete or improperly prepared submissions will be rejected with explanatory comments provided. In this case we will kindly ask the authors to carefully read the Information for Authors and to resubmit their manuscripts taking into consideration our comments.

## COVER LETTER INSTRUCTIONS:

Please add a **cover letter** stating the following information about the submitted paper:

1. Paper **title**, list of **authors** and their **affiliations**. **One** corresponding author should be provided.
2. **Type of paper**: original scientific paper (1.01), review scientific paper (1.02) or short scientific paper (1.03).
3. A **declaration** that neither the manuscript nor the essence of its content has been published in whole or in part previously and that it is not being considered for publication elsewhere.
4. State the **value of the paper** or its practical, theoretical and scientific implications. What is new in the paper with respect to the state-of-the-art in the published papers? Do not repeat the content of your abstract for this purpose.
5. We kindly ask you to suggest at least two **reviewers** for your paper and give us their names, their full affiliation and contact information, and their scientific research interest. The suggested reviewers should have at least two relevant references (with an impact factor) to the scientific field concerned; they should not be from the same country as the authors and should have no close connection with the authors.

## FORMAT OF THE MANUSCRIPT:

The manuscript should be composed in accordance with the Article Template. The manuscript should be written in the following format:

- A **Title** that adequately describes the content of the manuscript.
- A list of **Authors** and their **affiliations**.
- An **Abstract** that should not exceed 250 words. The Abstract should state the principal objectives and the scope of the investigation, as well as the methodology employed. It should summarize the results and state the principal conclusions.
- 4 to 6 significant **key words** should follow the abstract to aid indexing.
- 4 to 6 **highlights**; a short collection of bullet points that convey the core findings and provide readers with a quick textual overview of the article. These four to six bullet points should describe the essence of the research (e.g. results or conclusions) and highlight what is distinctive about it.
- An **Introduction** that should provide a review of recent literature and sufficient background information to allow the results of the article to be understood and evaluated.
- A **Methods** section detailing the theoretical or experimental methods used.
- An **Experimental section** that should provide details of the experimental set-up and the methods used to obtain the results.
- A **Results** section that should clearly and concisely present the data, using figures and tables where appropriate.
- A **Discussion** section that should describe the relationships and generalizations shown by the results and discuss the significance of the results, making comparisons with previously published work. (It may be appropriate to combine the Results and Discussion sections into a single section to improve clarity.)
- A **Conclusions** section that should present one or more conclusions drawn from the results and subsequent discussion and should not duplicate the Abstract.
- **Acknowledgement** (optional) of collaboration or preparation assistance may be included. Please note the source of funding for the research.
- **Nomenclature** (optional). Papers with many symbols should have a nomenclature that defines all symbols with units, inserted above the references. If one is used, it must contain all the symbols used in the manuscript and the definitions should not be repeated in the text. In all cases, identify the symbols used if they are not widely recognized in the profession. Define acronyms in the text, not in the nomenclature.
- **References** must be cited consecutively in the text using square brackets [1] and collected together in a reference list at the end of the manuscript.
- **Appendix(-ices)** if any.

## SPECIAL NOTES

**Units:** The SI system of units for nomenclature, symbols and abbreviations should be followed closely. Symbols for physical quantities in the text should be written in italics (e.g.

$v$ ,  $T$ ,  $n$ , etc.). Symbols for units that consist of letters should be in plain text (e.g.  $\text{ms}^{-1}$ , K, min, mm, etc.). Please also see: <http://physics.nist.gov/cuu/pdf/sp811.pdf>.

**Abbreviations** should be spelled out in full on first appearance followed by the abbreviation in parentheses, e.g. variable time geometry (VTG). The meaning of symbols and units belonging to symbols should be explained in each case or cited in a **nomenclature** section at the end of the manuscript before the References.

**Figures** (figures, graphs, illustrations digital images, photographs) must be cited in consecutive numerical order in the text and referred to in both the text and the captions as Fig. 1, Fig. 2, etc. Figures should be prepared without borders and on white grounding and should be sent separately in their original formats. If a figure is composed of several parts, please mark each part with a), b), c), etc. and provide an explanation for each part in Figure caption. The caption should be self-explanatory. Letters and numbers should be readable (Arial or Times New Roman, min 6 pt with equal sizes and fonts in all figures). Graphics (submitted as supplementary files) may be exported in resolution good enough for printing (min. 300 dpi) in any common format, e.g. TIFF, BMP or JPG, PDF and should be named Fig1.jpg, Fig2.tif, etc. However, graphs and line drawings should be prepared as vector images, e.g. CDR, AI. Multi-curve graphs should have individual curves marked with a symbol or otherwise provide distinguishing differences using, for example, different thicknesses or dashing.

**Tables** should carry separate titles and must be numbered in consecutive numerical order in the text and referred to in both the text and the captions as Table 1, Table 2, etc. In addition to the physical quantities, such as  $t$  (in italics), the units [s] (normal text) should be added in square brackets. Tables should not duplicate data found elsewhere in the manuscript. Tables should be prepared using a table editor and not inserted as a graphic.

## REFERENCES:

A reference list must be included using the following information as a guide. Only cited text references are to be included. Each reference is to be referred to in the text by a number enclosed in a square bracket (i.e. [3] or [2] to [4] for more references; do not combine more than 3 references, explain each). No reference to the author is necessary.

References must be numbered and ordered according to where they are first mentioned in the paper, not alphabetically. All references must be complete and accurate. Please add DOI code when available. Examples follow.

### Journal Papers:

Surname 1, Initials, Surname 2, Initials (year). Title. *Journal*, volume, number, pages, DOI code.

- [1] Hackenschmidt, R., Alber-Laukant, B., Rieg, F. (2010). Simulating nonlinear materials under centrifugal forces by using intelligent cross-linked simulations. *Strojnikski vestnik - Journal of Mechanical Engineering*, vol. 57, no. 7-8, p. 531-538, DOI:10.5545/sv-jme.2011.013.

Journal titles should not be abbreviated. Note that journal title is set in italics.

### Books:

Surname 1, Initials, Surname 2, Initials (year). Title. Publisher, place of publication.

- [2] Groover, M.P. (2007). *Fundamentals of Modern Manufacturing*. John Wiley & Sons, Hoboken.

Note that the title of the book is italicized.

### Chapters in Books:

Surname 1, Initials, Surname 2, Initials (year). Chapter title. Editor(s) of book, book title. Publisher, place of publication, pages.

- [3] Carbone, G., Ceccarelli, M. (2005). Legged robotic systems. Kordić, V., Lazinica, A., Merdan, M. (Eds.), *Cutting Edge Robotics*. Pro literatur Verlag, Mammendorf, p. 553-576.

### Proceedings Papers:

Surname 1, Initials, Surname 2, Initials (year). Paper title. Proceedings title, pages.

- [4] Stefančić, N., Martinčević-Mikić, S., Tošanović, N. (2009). Applied lean system in process industry. *MOTSP Conference Proceedings*, p. 422-427.

### Standards:

Standard-Code (year). Title. Organisation. Place.

- [5] ISO/DIS 16000-6:2.002. *Indoor Air - Part 6: Determination of Volatile Organic Compounds in Indoor and Chamber Air by Active Sampling on TENAX TA Sorbent, Thermal Desorption and Gas Chromatography using MSD/FID*. International Organization for Standardization. Geneva.

### WWW pages:

Surname, Initials or Company name. Title, from <http://address>, date of access.

- [6] Rockwell Automation. Arena, from <http://www.arenasimulation.com>, accessed on 2009-09-07.

## EXTENDED ABSTRACT:

When the paper is accepted for publishing, the authors will be requested to send an **extended abstract** (approx. one A4 page or 3500 to 4000 characters or approx. 600 words). The instruction for composing the extended abstract are published on-line: <http://www.sv-jme.eu/information-for-authors/>.

## COPYRIGHT:

Authors submitting a manuscript do so on the understanding that the work has not been published before, is not being considered for publication elsewhere and has been read and approved by all authors. The submission of the manuscript by the authors means that the authors automatically agree to publish the paper under CC-BY 4.0 Int. or CC-BY-NC 4.0 Int. when the manuscript is accepted for publication. All accepted manuscripts must be accompanied by a Copyright Agreement, which should be sent to the editor. The work should be original work by the authors and not be published elsewhere in any language without the written consent of the publisher. The proof will be sent to the author showing the final layout of the article. Proof correction must be minimal and executed quickly. Thus it is essential that manuscripts are accurate when submitted. Authors can track the status of their accepted articles on <https://en.sv-jme.eu/>.

## PUBLICATION FEE:

Authors will be asked to pay a publication fee for each article prior to the article appearing in the journal. However, this fee only needs to be paid after the article has been accepted for publishing. The fee is 380 EUR (for articles with maximum of 6 pages), 470 EUR (for articles with maximum of 10 pages), plus 50 EUR for each additional page. The additional cost for a color page is 90.00 EUR (only for a journal hard copy; optional upon author's request). These fees do not include tax.





<http://www.sv-jme.eu>

# Contents

## Papers

- 199 Goran Vorotović, Jela Burazer, Aleksandar Bengin, Časlav Mitrović, Miloš Januzović, Nebojša Petrović, Đorđe Novković:  
**A Case Study of a Methodological Approach to the Verification of UAV Propeller Performance**
- 208 Ali Celik, Bayram Sahin, Eyüphan Manay, Abit Balin:  
**A Study Using the Hybrid Fuzzy AHP&TOPSIS Method in the Conversion of a LEED-Certified Education Building into a Nearly Zero-Energy Building in a Cold Climate**
- 223 Ava A.K. Mohammed, Gailan Ismail Hassan, Younis Khalid Khdir:  
**The Dynamic Behaviour of Symmetrical Laminated Nano-composite Containing Equal Numbers of Glass and Carbon Fibre Layers**
- 234 Linlin Li, Sanmin Wang:  
**Experimental Study and Numerical Analysis on Windage Power Loss Characteristics of Aviation Spiral Bevel Gear with Oil Injection Lubrication**
- 247 Sumit Kumar, Pardeep Gupta:  
**Prioritizing the Key Actors of an Organization for Business Excellence Using the Efficient Interpretive Ranking Process**
- 260 Teng Wang, Youfu Tang, Tao Wang, Na Lei:  
**An Improved MSCNN and GRU Model for Rolling Bearing Fault Diagnosis**
- 275 Haiter Lenin Allasi, Vettivel Singaravel Chidambaranathan, Mary Vasanthi Soosaimariyan:  
**Wear Behaviour of a Cu-Ni-Sn Hybrid Composite Reinforced with B<sub>4</sub>C prepared by Powder Metallurgy Technique**
- 284 Igor Grabec, Nikolaj Sok:  
**Diffusion Equation Generalized for Modeling of Chladni Patterns**